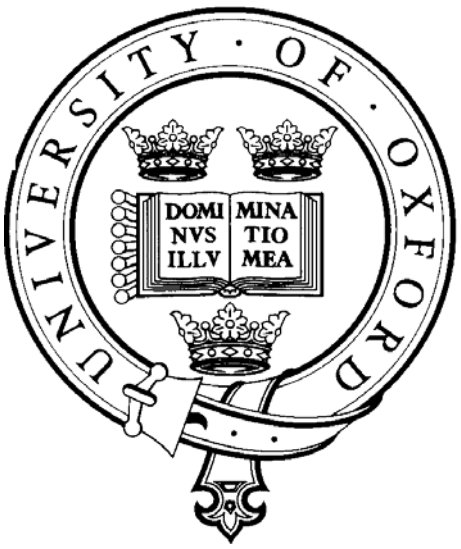

ANALYSIS OF INCOMPLETE AND COMPLETE CONTACTS IN SLIDING AND PARTIAL SLIP

Thesis submitted to the Department of Engineering Science of Oxford University in partial fulfilment of the requirements for the degree of Doctor of Philosophy

by

SARAVANAN KARUPPANAN

GREEN COLLEGE

OXFORD

Michaelmas Term, 2007

Analysis of incomplete and complete contacts in sliding and partial slip

Saravanan Karuppanan
Doctor of Philosophy in Engineering Science
Green College, Oxford, Michaelmas Term 2007

Abstract

Fretting fatigue is a type of contact fatigue which causes premature failure in a number of engineering assemblies subjected to vibration or other forms of cyclic loading. It is concerned with the nucleation of cracks due to oscillatory micro slip between contacting bodies. Therefore, a detailed knowledge of the interface conditions and the means of quantifying crack nucleation are very important, and will be the ultimate goal of this thesis. The analysis of an incomplete contact (Herzian contact) is considered first followed by various complete contacts.

Fretting fatigue tests employing a Hertzian contact are analysed accurately by introducing several modifications needed to the classical formulation. With the total state of stress in a strip established, the crack tip stress intensity factor for a crack growing inward from the trailing edge of the contact is determined by the distributed dislocation technique. The results are then correlated with local solutions for the contact stress field which enable an estimate of the crack nucleation life, and hence a characteristic material property quantifying initiation, to be found.

The interfacial contact pressure distribution beneath a complete sliding contact between elastically similar components, in the presence of friction, has been studied in detail, with particular reference to contacts whose edge angles are 60^0, 90^0 and 120^0. The possible types of behaviour at the edge of contacts, namely power order singularity, power order bounded and square root bounded, are discussed. A full understanding of the behaviour requires a detailed study of a characteristic equation, and this shows the kinds of pressure distribution to be anticipated, which can vary very markedly. The transition from power order behaviour to local separation and bounded behaviour is examined, and an appropriate asymptotic form developed.

The problem of trapezium shaped punches pressed into a frictional, elastically similar half-plane, and subject to sequential normal and shear loading, under partial slip, is studied. Detailed considerations have again been given to the specific cases of 60^0, 90^0 and 120^0 punches, and maps have been developed showing the initial mix of stick, slip and separation regions, together with the steady state response when the shearing force is cycled. Conditions for full stick are established.

Dedication

To my wife, children and parents, with love and gratitude.

Acknowledgements

I would like to thank my supervisor, Professor David Hills for his excellent guidance and support. It has been a great honour and an inspiration to work with such a distinguished academic and scientist. I have gained invaluable experience from a humble, caring and hardworking person as himself. My thanks are also extended to Professor Alexander Korsunsky, my co-supervisor, for all the fruitful discussions in the earlier stage of my DPhil.

I acknowledge the financial support from Universiti Teknologi Petronas which enabled me to complete my DPhil.

I would also like to extend my appreciation to Professor A. Sackfield, Professor J.R. Barber and Professor E. Giner who have helped me during my DPhil.

I am privileged to have met and engaged in numerous technical and general discussions with Dr. Chris Churchman, Dr. Qiu Hui, Mr. Robert Paynter, Dr. Daniele Dini and Dr. Ramesh Rajasekaran. Thank you very much for your invaluable ideas.

Last but no means least, I would like to thank everyone who have contributed in one way or another to the completion of my DPhil.

Preface

This thesis is an account of the research programme carried out by the author in the Department of Engineering Science, University of Oxford, under the supervision of Professor David A. Hills. The research is original and no part of it has been submitted for a degree at this university or elsewhere. The work of other authors has been drawn freely though with due acknowledgement in the text.

Some of the work described in this thesis has been published in the following papers:

1. Karuppanan, S. and Hills, D. A. (2007), Stress intensity factor for a crack within a strip under arbitrary loading, *Journal of Strain Analysis*, **42**, 39-45.
2. Karuppanan, S., Dini, D. and Hills, D. A. (2007), Fretting fatigue test analysis of contact, *Fatigue Fract. Engng. Mater. Struct.*, **30(6)**, 499–509.
3. Karuppanan, S., Churchman, C.M., Hills, D. A. and Giner, E. (2007), Sliding frictional contact between a square block and an elastically similar half-plane, *European Journal of Mechanics A/Solids*, in press.
4. Karuppanan, S. and Hills, D. A. (2007), Sliding of general frictional complete contacts, *International Journal of Mechanical Sciences*, under review.
5. Karuppanan, S. and Hills, D. A. (2007), Frictional complete contacts between elastically similar bodies subject to normal and shear load, *International Journal of Solids and Structures*, under review.
6. Karuppanan, S. and Hills, D. A. (2007), An edge dislocation in a semi-infinite elastic wedge, *Journal of Strain Analysis*, under review.

Contents

Chapter 1

Introduction

1.1 General introduction

Engineering failures are often associated with fatigue. Any catastrophic engineering failure is a major concern because it not only involves economic losses and disruption of services but it may also involve loss of human lives which is very unfortunate. Therefore designing against fatigue failure has been an important design criterion adopted by engineers. Fatigue failures may occur in different forms, namely mechanical fatigue, contact fatigue, creep fatigue, corrosion fatigue and others. Fretting fatigue is a type of contact fatigue which reduces the fatigue endurance limit and promotes premature fatigue crack nucleation and enhances early propagation.

Fretting is a contact damage process due to oscillatory micro-slip that occurs between machine components subjected to a clamping pressure and vibratory excitation or an oscillatory tangential force. Fretting damage can be classified into fretting fatigue, fretting wear and fretting corrosion. Fretting fatigue is associated with partial slip contact conditions, where the contact area between the components in contact consists of a stick region in between slip regions.

Components subjected to fretting fatigue experience severe stress gradients at the edge of contact which contributes to premature crack nucleation and accelerated short-crack propagation. This reduces the fatigue lives of the components significantly compared to plain fatigue. Fretting fatigue is one of the most important considerations in designing structures and components in the aerospace and nuclear industries.

It is clear that the fretting fatigue phenomenon has significant industrial and economic relevance. Therefore, the motivation of this work is to understand in more detail the response of incomplete and complete contacts to fretting conditions. As part of our attempts to understand the latter, some attention will also be given to the corresponding sliding problem.

1.2 Contact mechanics

The birth of contact mechanics is associated with the paper by Hertz (1882). Since then many researchers have made significant contributions to the field of contact mechanics. Contact is an essential part of solid mechanics because it is the principal means of applying external loads to a deformable body. The resulting stresses due to the contact are often most critical in the body. Generally contacts can be put into one of several different classes depending on the geometry of the contacting bodies (Hills *et al.*, 1993 and Hills and Nowell, 1994).

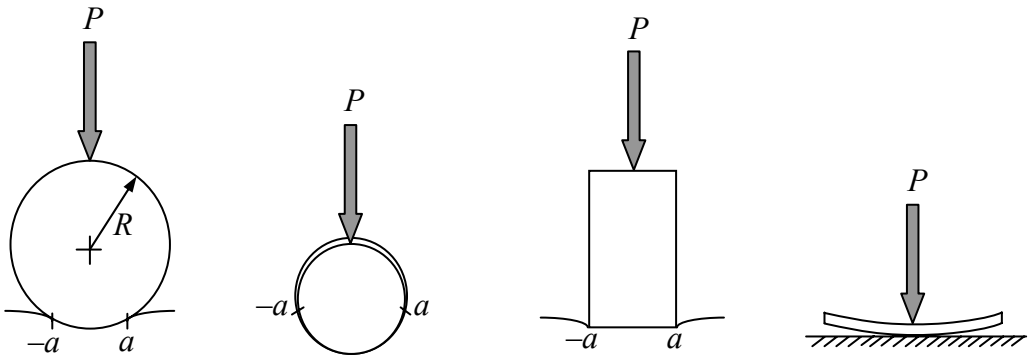

Figure 1.1 : The various types of contact (a) Incomplete and non-conformal (b) Incomplete and conformal (c) Complete (d) Receding

The first type of contact is known as incomplete contact and is shown in "plane" form in Figure 1.1(a) and Figure 1.1(b). In this type of contact, when two contacting bodies

are brought together, contact is made along a line, and as the load is increased, this line will grow to form a narrow strip. Therefore, in incomplete contact, the contact extent is dependent on the applied load and is not fixed by the geometry of the contacting bodies. Also, in incomplete contacts, the contact pressure falls continuously to zero towards the edges of the contacts. Examples of incomplete contact are seen in gears, railway wheels and rolling element bearings.

Incomplete contacts can be further divided into conformal or non-conformal contact. If the contact half-width a, is very small compared to the radius of the cylinder R, i.e. $a << R$, Figure 1.1(a), the contact is considered as non-conformal. In this case, the cylinder may be approximated as a half-plane during the calculation of deformation and stresses. In contrast, for the case of conformal contact as shown in Figure 1.1(b), the contact half-width is not negligible in comparison with the radius of the cylinder and hole. Therefore neither of the bodies can be approximated as a half-plane.

The second type of contact is known as complete contact. Figure 1.1(c) shows a complete contact, where a flat-ended punch is pressed into an elastic plane. In this case, the size of the contact is independent of the contact load. The two contacting bodies do not have a common tangent at the edges of the contact. In complete contacts, the corresponding contact pressure is singular at the edges of the contacts. Complete contacts arise in many practical fretting problems such as in some spline joints and in bolted flange connections.

The third type of contact that is very rare in practice is known as a receding contact. Figure 1.1(d) shows a thin elastic plate placed on an elastic plane. The edges of this plate will lift if a normal load is applied to the plate causing the contact patch to recede.

1.3 Literature review

1.3.1 Historical background of fretting fatigue

The occurrence of fretting was first reported in 1911 by Eden *et al*. (1911). They noticed the formation of fretting debris, interpreted as iron oxide, between the fatigue test specimen and the grips which hold the test specimen at the contact region. The first systematic study of fretting was conducted by Tomlinson (1927). He claimed that fretting resulted from 'molecular attrition', which was later discounted. Further investigations (Tomlinson, 1939), led to the conclusion that fretting is a purely mechanical process associated with microslip. Warlow-Davies (1941) found that fretted steel specimens experienced a reduction in fatigue strength of up to 17%. McDowell (1953) showed that the combined effects of fretting and fatigue have a significant effect on the fatigue strength, decreasing it by a factor of 2-5 or even more.

In the 1950s several theories of fretting were proposed. Godfrey *et al.* (1950, 1952, 1953, 1954, 1956) in their attempt to characterize the nature of fretting and establish its mechanism, concluded that adhesion resulted from contact, and fine particles were subsequently broken loose and oxidised. They also concluded that cyclic motion was not necessary for fretting. Feng and Rightmire (1952, 1953, 1955, 1956) hypothesised fretting as a multi-stage process consisting of initial stage, transition period, declining stage and steady-state stage. They believed that the fretting process consisted of the breakaway of particles, subsequent oxidation, and abrasion. Halliday and Hirst (1956), in their attempt to define the relationship between fretting and magnitude of slip amplitude, concluded that the magnitude of relative slip influences fretting result. Uhlig (1953, 1954) suggested that fretting wear occurs due to the combined effect of mechanical and chemical factors. Waterhouse (1955) believed that fretting involves adhesion, the breaking of welds and transfer of metal. Wright (1952a, 1952b) emphasised that oxygen was an important factor in causing fretting damage.

In the late 1960s and early 1970s, Nishioka *et al*. (1968, 1969a, 1969b, 1969c, 1969d, 1972) conducted a series of experiments using cylindrical steel pads and steel specimens to investigate the possible factors that may influence the fretting fatigue strength. Their conclusions, amongst others, were the existence of non-propagating fretting fatigue cracks, the varying effect of the amount of relative slip between the surfaces on the fatigue life, the occurrence of crack initiation in a region of high stress near the contact edge, and the increase of coefficient of friction during the experiments. They also found that the mean stress applied to the specimen had little effect on the initiation of cracks, and the development of micro-slip zones at both edges of the contact when a tangential force less than that necessary to cause sliding was applied. Also, they stated that material hardness has little effect on the fretting fatigue life.

Hoeppner and Goss (1974) demonstrated the existence of a damage threshold. They suggested that a certain amount of fretting damage was necessary to have any detrimental effect on the fatigue strength. The existence of a fretting damage threshold was also proposed by Waterhouse (1972) and by Endo and Goto (1976). Endo and Goto (1976), through their experiments, found that the initial propagation of fretting fatigue cracks, which is dependent on the fretting conditions, was faster than plain fatigue cracks. Hoeppner and Goss (1974), Endo and Goto (1976) and more recently Alic and Kantimathi (1979) suggested that after the initiation of fatigue cracks from fretting damage, the fretting has no further role in propagating these fatigue cracks. A series of experiments carried out by Bramhall (1973) and later by Nowell (1988) demonstrated that the existence of a critical contact size below which contacts ‘last forever’, whilst larger contacts experiencing an identical spatial stress distribution have a finite life.

Several books on fretting fatigue have also been published for better understanding of this subject. In 1981, Waterhouse published a book that includes a collection of recent work by several researchers during that time. The book contains ideas on forecasting fretting fatigue damage, recognising that, if it does occur and appropriate measures that can be taken

to avoid it. More recently Hills and Nowell (1994) published a book that includes, among other items, the modelling of contact problems, the modelling of short cracks and the experimental simulation of fretting fatigue.

1.3.2 Crack nucleation criteria

In the past decade or so, several researchers have attempted to quantify nucleation of fretting fatigue cracks by using numerous approaches, mostly those developed for plain fatigue, namely critical plane analysis, short crack methods and crack-notch analysis. The main difference is the use of a contact stress field due to fretting conditions instead of a stress field due to plain fatigue condition. Some of these approaches will be briefly described in this section.

Critical plane analysis

In fretting fatigue, the state of stress in the contact region is multiaxial and non-proportional in nature. This suggests the application of multiaxial fatigue models to describe fretting fatigue crack nucleation. The critical plane approach is a multi-axial formulation, where cracks are expected to nucleate along a preferential plane referred to as a critical plane. Empirical relationships are normally used to predict the most severely loaded plane or critical plane.

Ruiz *et al*. (1984, 1986) proposed a parameter, κ_R, which includes the effects of localized tensile stress, shear traction and slip amplitude as a possible parameter to quantify initiation. This parameter, that is applicable only to the fretting fatigue conditions, is also known as Ruiz' parameter. It is defined as

$$\kappa_R = \sigma_T \tau \delta , \tag{1.1}$$

where σ_T is the tangential stress, τ is the shear traction and δ is the value of the microslip between the contacting surfaces. This parameter is a maximum at the locations where cracks

were observed experimentally. Therefore, it can be used to predict the crack nucleation site in the contact.

A model which is widely used to correlate crack nucleation observations is the Smith-Watson-Topper or *SWT* equation. The *SWT* parameter Γ is the product of the maximum stress σ_{max} and strain amplitude $\Delta\varepsilon/2$ during a complete loading cycle. The equation can be expressed as

$$\Gamma = \sigma_{\max}\frac{\Delta\varepsilon}{2} = \frac{(\sigma_f)^2}{E}(2N_i)^{2b} + \sigma_f\,\varepsilon_f\,(2N_i)^{b+c}, \tag{1.2}$$

where σ_f and b are the fatigue strength coefficient and exponent, ε_f and c are the fatigue ductility coefficient and exponent, E is Young's modulus and N_i is the number of fatigue cycles to nucleate a crack to a particular length. The crack is said to be most likely to nucleate on the plane which experiences the maximum *SWT* parameter. Several researchers have attempted to use this model to analyse fretting fatigue tests, including Swolwinski and Farris (1996, 1998), Lykins *et al.* (2000), Araujo and Nowell (2002) and Fridrici *et al.* (2005).

Socie (1987) suggested the use of *SWT* parameter for the case where the cracks grow on high tensile strain planes. Fatemi and Socie (1988) proposed a variant on this model for cracks that grow on high shear strain planes. The model can be expressed as

$$FS = \frac{\Delta\gamma}{2}\left(1+\alpha\,\frac{\sigma_{\max}}{\sigma_y}\right) = \frac{\tau_f}{G}(2N_i)^b + \gamma_f\,(2N_i)^c, \tag{1.3}$$

where $\Delta\gamma/2$ is the shear strain amplitude during a complete loading cycle, σ_y is the yield strength, α is a constant which is dependent on fatigue life, G is the shear modulus, τ_f and b are the shear fatigue strength coefficient and exponent and γ_f and c are the shear fatigue ductility coefficient and exponent. The critical plane in this approach is that having the maximum value of the *FS* parameter.

Short crack method

The concept of linear elastic fracture mechanics (LEFM) implies that, for a long crack, there is a threshold stress intensity factor range ΔK_{th} which is independent of crack length,

$$\Delta K_{th} = \Delta K_o \quad \text{for} \quad l > l_o . \tag{1.4}$$

Long cracks are assumed to propagate only if the stress intensity factor range at the tip of a crack in a body ΔK is above this threshold value ΔK_o, i.e. $\Delta K > \Delta K_o$. However, many authors have observed the growth of short fatigue cracks at a nominal stress intensity level below the long crack threshold value (Miller, 1993). Pearson (1975) reported that the growth of short cracks is significantly faster than long cracks subjected to the same ΔK. Kitagawa and Takahashi (1976) observed that, for short cracks, there is a critical crack size l_o below which the threshold stress intensity range ΔK_{th} decreases with decreasing crack length l. Furthermore, for short cracks, the initiation and propagation of cracks can take place at $\Delta K < \Delta K_o$ if the tensile stress range $\Delta\sigma$ experienced by the crack is greater than the fatigue limit of the material $\Delta\sigma_{fl}$,

$$\Delta\sigma > \Delta\sigma_{fl} \quad \text{for} \quad l < l_o . \tag{1.5}$$

Equation (1.5) can be expressed in terms of the stress intensity factor as

$$\Delta K > Y\Delta\sigma_{fl}\sqrt{\pi l} , \tag{1.6}$$

where Y is the geometrical factor. The critical crack size l_o at the transition between the two regimes may be found by setting

$$l_o = \frac{1}{\pi}\left(\frac{\Delta K_o}{Y\Delta\sigma_{fl}}\right)^2 . \tag{1.7}$$

Substitution of equation (1.7) into equation (1.6) gives

$$\Delta K > \Delta K_o\sqrt{\frac{l}{l_o}} \quad \text{for} \quad l < l_o . \tag{1.8}$$

The variation of the threshold stress intensity factor range with crack size is conveniently plotted in Figure 1.2, using equation (1.4) and equation (1.8). This is known as a Kitagawa-Takahashi (K-T) diagram, which shows a sharp transition between short and long crack behaviour, which is unlikely in practice. However, experimental results by Tanaka *et al.* (1981) showed that the approximation is reasonably accurate. An alternative approach was suggested by El Haddad *et al.* (1979a, 1979b). Using this approach, the crack propagation threshold is expressed by

$$\Delta K_{th} = \Delta K_o \sqrt{\frac{l}{l + l_o}} \,. \tag{1.9}$$

This plot gives a smoother transition between short and long crack behaviour and is also shown in Figure 1.2.

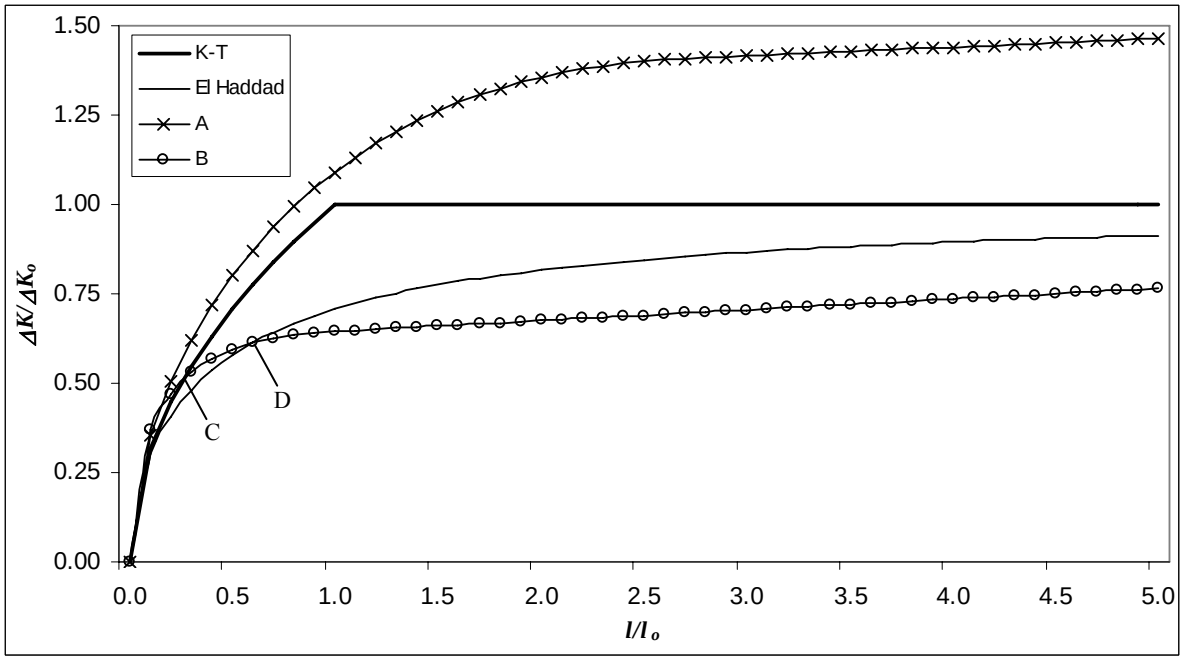

Figure 1.2 : Crack growth trajectories in the Kitagawa-Takahashi (K-T) and El Haddad diagram.

The short crack methodology uses this diagram to investigate the propagation and arrest of cracks. The nucleating crack can be represented by a stress intensity factor (SIF) curve on this diagram. If the SIF curve is always above the threshold values, curve A on

Figure 1.2, cracks will initiate and propagate. However, if the curve is initially above the threshold values and falls below it after a certain length, curve B on Figure 1.2, cracks will initiate and then cease growth (at point C – K-T, or point D – El Haddad).

1.3.3 Complete contacts studies

Complete contacts are those where one body defines the size of the contact by virtue of having abrupt edges to the contacting face. It is very difficult to analyse contacts of this class analytically, because in most cases it is not possible to use a formulation for an elastic half-plane (space) to represent the internal displacement and stress fields within the contact-defining body.

Khadem and O'Connor (1969) studied the complete contact problem numerically. They attempted to represent the solution in series form, and that proved to be mathematically taxing exercise. Most recent attacks on problems of this class have been made using an experimental approach in conjunction with a commercial finite element package.

Giannakopoulus *et al.* (1998) recognized the similarities between the stress fields near to the edge of a flat rigid punch and that at the tip of an elastic crack. By using an asymptotic expansion of the stress fields at the edge of the sharp contact, they showed the similarities with the asymptotic fields around the tip of a crack. Therefore, it was concluded that the crack growth in fretting fatigue at the edge of a flat contact can be represented by this 'crack analogue' model. Xie and Hills (2003) successfully used *S*-theory to predict the crack initiation angle from the contact surface of rectangular rigid punch and flat substrate.

Mugadu *et al.* (2002a) modified the in-line form of the fretting-fatigue test apparatus by introducing a self-aligning pad fixture that enables experimental investigation of complete contacts. He also carried out an experimental investigation of complete contact in his attempt to quantify their fretting fatigue strength (Mugadu, 2002). Fretting fatigue tests using complete contacts have also been conducted at Kyushu University (Kondo and Bodai,

2001; Kondo *et al.*, 2004; Kondo *et al.*, 2005) and by Pape and Neu (1999) to name a few. Mugadu *et al.* (2002b) proposed an asymptotic approach to study the state of stress near the corner of a complete contact subject to fretting loads. The state of stress was encapsulated in a single parameter known as the generalised stress intensity factor. It was suggested that, if the profile of the pad in a fretting test matched with the edge of a prototype being studied, the state of stress and strain will also be the same for the same loading and friction conditions. Mugadu and Hills (2003) studied the problem of a rigid punch pressed against an incompressible half-plane by a constant normal load and subsequently subjected to both a cyclically varying shear load, and a synchronously varying bulk load. The possible slip/stick distributions found and the conditions under which they might exist were explicitly defined.

Tur *et al.* (2002) considered the application of special singular finite elements, using the technique developed by Lin and Tong (1980), to model the singular state of stress at the edge of complete contacts. They concluded that these special elements gave a higher convergence rate as compared to isoparametric elements.

Navarro *et al.* (2003) also investigated the problem of a rigid square ended punch pressed onto an incompressible half-plane, and subjected to a monotonically increasing proportional shear force and bulk tension but with particular attention to the effect of the tension in stabilising the partial slip regime. A summary of the possible responses for various combinations of shearing force and normalised bulk tension were given, and it was shown that the presence of bulk tension allows for a stable partial slip regime.

Churchman and Hills (2006a) considered in detail the problem of a square block on an elastically similar half-plane and subjected to fretting loading. They developed a general interfacial characteristics map for the case of a monotonically increasing shear load and then an oscillatory shear load. They also employed wedge asymptotics extensively to complement finite element analysis in order to add detail at the edge of a complete contact. This problem was also considered independently by Bohorquez and Dominguez (2005) with more emphasis on the finite element analysis to determine the behaviour of the contact.

Some complete contacts subjected to cyclic loading were predicted to shake down in the sense that frictional slip ceases after a few loading cycles (Banerjee and Hills, 2006; Churchman and Hills, 2006a). Klarbring *et al.* (2007) proved that complete contact problems do 'shake down' for uncoupled systems using discrete formulation.

1.4 Summary of thesis

Considerable progress has been made in the field of fretting fatigue since the first reported work by Eden *et al.* (1911). The vast majority of research has been concentrated on experimental investigation of the fretting phenomenon, and on the analysis of associated crack propagation. Despite some recent efforts to quantify the nucleation of fretting cracks, more work is still required to reduce the level of uncertainty and conservatism involved in the current lifing methodologies. It was also noticed from the literature review that research on complete contacts has only been carried out extensively in the last a decade or so, and therefore requires more attention. In this thesis, the focus will be on the areas where less research seems to have been done.

The main aim of this thesis is to analyse incomplete and complete contacts subject to fretting loads. The scope of incomplete contacts is restricted to Hertzian type contacts where an attempt to analyse accurately fretting fatigue tests results available in the literature will be carried out with the tools developed, and also with those readily available. An attempt to quantify nucleation of cracks by using an asymptotic approach will be made.

The scope of complete contacts will be on the interfacial characteristics of elastically similar complete contacts under sliding and partial slip conditions, the latter with a monotonically increasing and cyclic shear. A general interfacial behaviour map for the conditions mentioned above will be developed with particular reference to contact angles of 60^0, 90^0 and 120^0. Wedge asymptotics will be used, where appropriate, to add detail at the contact edge.

Chapter 2

Fretting fatigue test analysis tools

2.1 Introduction

Fretting contact normally involves a constant normal force P, an oscillatory tangential force Q with an amplitude less than the frictional force ($Q < fP$), and the presence of bulk stress in one or both contacting bodies. A typical fretting fatigue experimental set up which is able to simulate this condition is shown in Figure 2.1. This arrangement was used by Nishioka and Hirakawa (1969a), Bramhall (1973), Nowell (1988) and more recently it has been used at Purdue (Szolwinski and Farris, 1996) and Wright-Patterson Air Force Base (Cortez *et al.*, 2000).

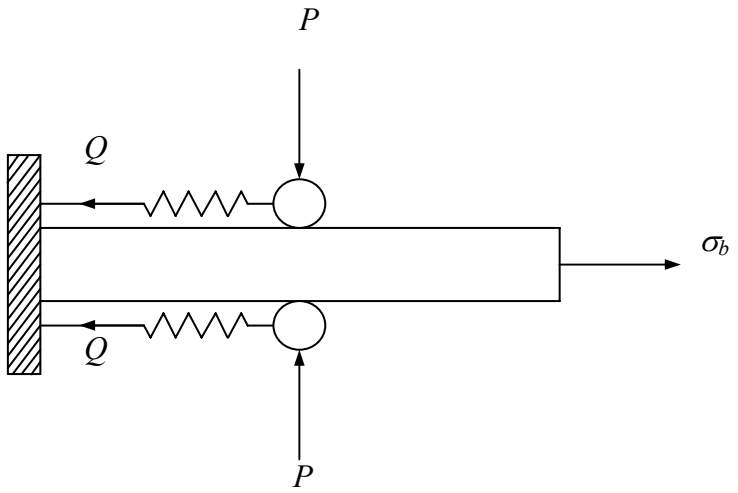

Figure 2.1 : Schematic representation of fretting fatigue experiment

In this configuration, the fretting pads are clamped to a flat specimen of finite thickness by a normal force P. These pads are restrained by springs so that the application of bulk stress to one end of the specimen will cause a tangential force Q to be applied to the contact in phase

with the bulk stress. The stiffness of the spring is normally adjusted to ensure that the contact remains in partial slip condition.

More recently, fretting fatigue tests employing a two-actuator arrangement have become very popular and the essentials of the arrangement are shown in Figure 2.2. In this setup, for greater versatility, two actuators are used: one to exert a shearing force and one to apply a bulk load to the test specimen. Details of the mechanics of the apparatus are given in Mugadu *et al.* (2002a).

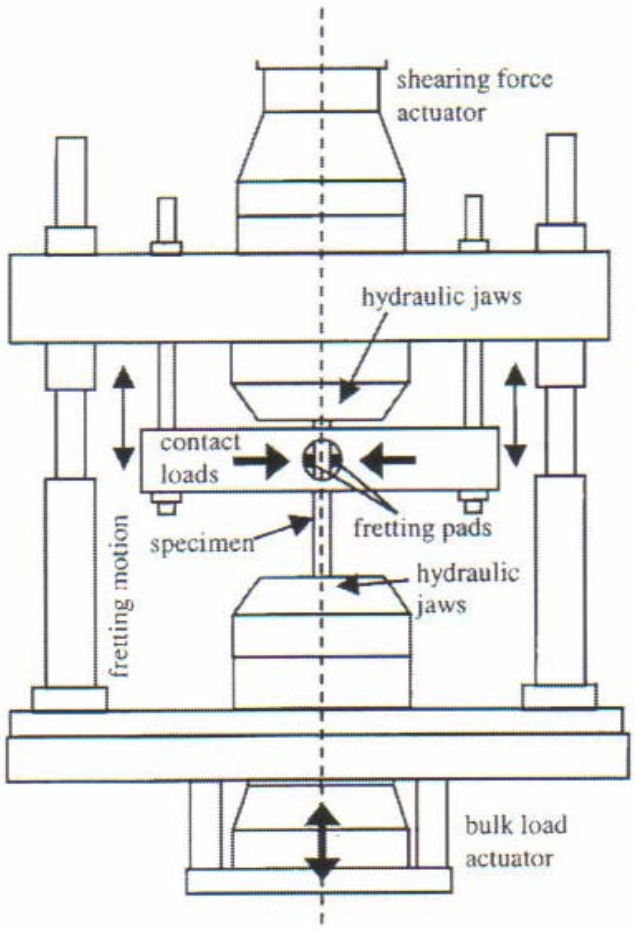

Figure 2.2 : Schematic representation of the fretting fatigue test using a two-actuator arrangement

Cylindrical fretting pads are a popular choice because the contact stress distribution can be determined using well defined techniques which will be described in later sections. In most tests, attempts to measure the crack growth as a function of number of cycles of loading have not been made, so that all that is really known is whether a test produced a 'run-out' (normally a life of greater than 10^7 cycles), or the number of cycles required to cause failure by fracture. Although the tests are notionally 'Hertzian' in geometry, because they comprise a cylinder pressed onto a test specimen, there are several features which make the problem different from the classical Hertz test. Therefore, in this chapter, the necessary tools and the appropriate modifications needed to the classical formulation that will enable accurate analysis of fretting tests will be presented. These will then be applied to the original tests conducted by Nowell (1988) and Szolwinski (1998) and will be discussed in chapter 3.

2.2 Surface tractions : Hertz-Cattaneo contact

The first step in solving a contact problem is to find the surface tractions. The technique often used for finding the surface tractions in plane problems is to establish and solve integral equations (Hills *et al*., 1993). This is a well defined technique and only the results of the surface traction distributions will be presented in the following sections.

2.2.1 The effect of mild bulk tension

The traction on the test specimen under partial slip conditions, subject to fretting loading and an oscillatory bulk load for the example problem of two cylinders in contact, which was first solved by Cattaneo (1938) and independently by Mindlin (1949) is now given.

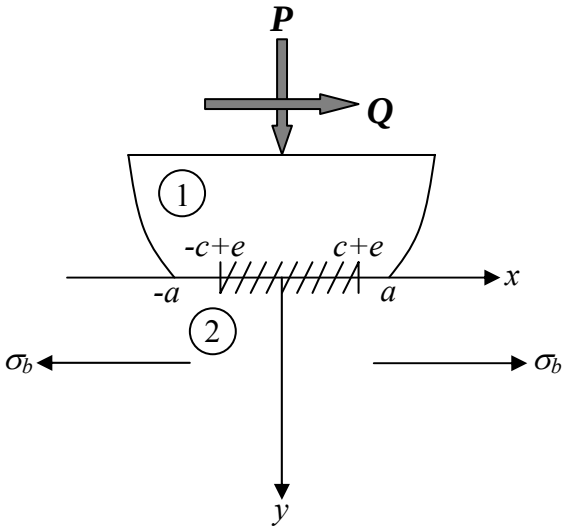

Figure 2.3 : Typical Hertz-Cattaneo contact problem

The bulk tension is expected to shift the position of the stick zone (Nowell and Hills, 1987a). In the case where the bulk tension is mild compared with the shear load, both the normal and shear surface tractions, *p(x)* and *q(x)*, maybe solved in closed form. With the loading condition and axis set as in Figure 2.3, the results are

$$p(x) = p_o\sqrt{1-\left(\frac{x}{a}\right)^2} \qquad |x| \le a\,, \tag{2.1a}$$

$$\begin{aligned} q(x) &= fp(x) \qquad\qquad -a \le x \le e-c \cup e+c \le x \le a \\ &= fp(x) - \frac{fp_o}{a}\sqrt{c^2-(x-e)^2} \qquad |x-e| \le c \end{aligned}\,, \tag{2.1b}$$

where

$$c = a\sqrt{1-\frac{Q}{fP}}\,, \tag{2.2a}$$

$$e = \frac{a\sigma_b}{4fp_o}\,, \tag{2.2b}$$

$$p_o = \frac{2P}{\pi a}\,, \tag{2.2c}$$

a is the contact half-width, c is the stick region half-width, e is the shift in stick region due to bulk load, f is the coefficient of friction, p_o is the maximum contact pressure, P is the normal load per unit length, Q is the shear load per unit length and σ_b is the bulk stress. The shear traction is valid only if $\sigma_b / fp_o < 4(1-\sqrt{1-Q/fP})$.

2.2.2 The effect of strong bulk tension

For the case where strong bulk tension is applied, $\sigma_b / fp_o > 4(1-\sqrt{1-Q/fP})$, reverse slip will take place at one edge of the contact. The shear traction for this case is therefore

$$\begin{aligned} q(x) &= fp(x) && -a \le x \le e-c \\ &= fp(e-c) - \frac{x-(e-c)}{2c}\{fp(e+c)+fp(e-c)\} + fp_o q'(x) && |x-e| \le c, \\ &= -fp(x) && e+c \le x \le a \end{aligned} \qquad (2.3)$$

where $q'(x)$ is the function to be determined to describe the shear traction in the stick region. To solve for $q'(x)$, first consider the surface strains for body 1 (contact pad) and body 2 (test specimen) (Hills *et al*., 1993)

$$\frac{\partial u_1}{\partial x} = -\frac{(1-2\nu)(1+\nu)p(x)}{E} - \frac{2(1-\nu^2)}{\pi E}\int_{-a}^{a}\frac{q(\xi)}{(x-\xi)}d\xi, \qquad (2.4a)$$

$$\frac{\partial u_2}{\partial x} = -\frac{(1-2\nu)(1+\nu)p(x)}{E} + \frac{2(1-\nu^2)}{\pi E}\int_{-a}^{a}\frac{q(\xi)}{(x-\xi)}d\xi + \frac{\sigma_b}{E}(1-\nu^2), \qquad (2.4b)$$

where $\partial u/\partial x$ is the surface strain, ν is Poisson's ratio and E is Young's modulus. There is no slip in the stick zone: therefore the relative tangential strain is zero, i.e.

$$\frac{\partial g}{\partial x} \equiv \frac{\partial u_1}{\partial x} - \frac{\partial u_2}{\partial x} = 0 \qquad e-c < x < e+c, \qquad (2.5)$$

giving

$$\int_{-a}^{a}\frac{q(\xi)}{(x-\xi)}d\xi = -\frac{\sigma_b \pi}{4},$$

$$\int_{e-c}^{e+c}\frac{q'(\xi)}{(x-\xi)}d\xi=-\frac{\sigma_b\pi}{4fp_o}-\int_{-a}^{e-c}\frac{\sqrt{1-(\xi/a)^2}}{(x-\xi)}d\xi+\int_{e+c}^{a}\frac{\sqrt{1-(\xi/a)^2}}{(x-\xi)}d\xi$$
$$-\int_{e-c}^{e+c}\frac{\sqrt{1-\left((e-c)/a\right)^2}-\dfrac{\xi-(e-c)}{2c}\left\{\sqrt{1-\left((e+c)/a\right)^2}+\sqrt{1-\left((e-c)/a\right)^2}\right\}}{(x-\xi)}d\xi, \quad (2.6)$$
$$=-\frac{\sigma_b\pi}{4fp_o}-I_1(x,c,e)+I_2(x,c,e)-I_3(x,c,e)$$

where $I_1(x,c,e)$, $I_2(x,c,e)$ and $I_3(x,c,e)$ are given in Appendix *A*. Normalise the interval of integration by setting $u = (\xi - e)/c$ and $v = (x - e)/c$ giving

$$\int_{-1}^{1}\frac{q'(u)}{(v-u)}du=-\frac{\sigma_b\pi}{4fp_o}-I_1(v,c,e)+I_2(v,c,e)-I_3(v,c,e). \quad (2.7)$$

Equation 2.7 can be expressed as

$$\int_{-1}^{1}\frac{w(u)\phi(u)}{(v-u)}du=-\frac{\sigma_b\pi}{4fp_o}-I_1(v,c,e)+I_2(v,c,e)-I_3(v,c,e), \quad (2.8)$$

where $\phi(u)$ is a bounded function and $w(u)$ is an appropriate fundamental function. The solution for $q'(u)$ is expected to be bounded at ± 1, so $w(u) = (1- u^2)^{1/2}$. Integral equation (2.8) maybe represented using Gauss-Chebyshev quadrature, and in discretized form is

$$\sum_{i=1}^{n}\frac{W(u_i)\phi(u_i)}{(v_k-u_i)}=-\frac{\sigma_b\pi}{4fp_o}-I_1(v_k,c,e)+I_2(v_k,c,e)-I_3(v_k,c,e), \quad (2.9)$$

where

$$u_i=\cos\left(\frac{\pi i}{n+1}\right) \qquad \text{for } i = 1, \ldots.., n \quad (2.10a)$$

$$v_k=\cos\left(\frac{\pi(2k-1)}{2(n+1)}\right) \qquad \text{for } k = 1, \ldots.., n+1 \quad (2.10b)$$

$$W(u_i)=\frac{\pi(1-u_i^2)}{n+1} \qquad \text{for } i = 1, \ldots.., n. \quad (2.10c)$$

This will give rise to a set of $(n + 1)$ linear simultaneous equations for $\phi(u_1), \ldots., \phi(u_n)$. The additional equation corresponds to an additional unknown, viz. the location of one of the

boundaries of the stick region. A choice has to be made to omit one equation, and in this case the $(n + 1)th$ equation can be left out. Once the solution is found, a check should be made to check whether the $(n + 1)th$ equation is satisfied. This will be achieved if a consistent choice of c and e is made.

Another equation, indirectly for $q'(x)$, which must be satisfied, is

$$Q = \int_{-a}^{a} q(\xi) d\xi , \tag{2.11a}$$

and hence

$$\begin{aligned} \frac{Q}{fp_o} &= \int_{-a}^{e-c} \sqrt{1-(\xi/a)^2}\, d\xi - \int_{e+c}^{a} \sqrt{1-(\xi/a)^2}\, d\xi + \int_{e-c}^{e+c} q'(\xi) d\xi \\ &+ \int_{e-c}^{e+c} \left\{ \sqrt{1-\left((e-c)/a\right)^2} - \frac{\xi-(e-c)}{2c}\left(\sqrt{1-\left((e+c)/a\right)^2} + \sqrt{1-\left((e-c)/a\right)^2} \right) \right\} d\xi , \\ &= J_1(c,e) - J_2(c,e) + J_3(c,e) + J_4(c,e) \end{aligned} \tag{2.11b}$$

where again $J_1(c,e)$, $J_2(c,e)$, $J_3(c,e)$ and $J_4(c,e)$ are given in Appendix *A*. Equations (2.6) and (2.11) are solved to determine the shear traction in the stick region.

2.3 Stress formulation in a strip

2.3.1 Stress in a half-plane

The internal stress field in a plane contact problem capable of half-plane representation is often determined by using Muskhelishvili potential. For a particular loading condition, once the Muskhelishvili potential is determined, the stresses in the half-plane may be deduced from (Muskhelishvili, 1953)

$$\sigma_{yy}^{H}(x,y) = \mathrm{Re}[\overline{\phi}(\bar{z}) - \overline{\phi}(z) + (\bar{z} - z)\phi'(z)], \tag{2.12a}$$

$$\sigma_{xx}^{H}(x,y) = 2[\phi(z) - \overline{\phi}(\bar{z})] - \sigma_{yy}^{H}(x,y) + \sigma_b , \tag{2.12b}$$

$$\sigma_{xy}^{H}(x,y) = \mathrm{Im}[\overline{\phi}(\bar{z}) - \overline{\phi}(z) + (\bar{z} - z)\phi'(z)]. \tag{2.12c}$$

The potential ϕ is a function of position z which is a complex coordinate ($z = x + iy$). The notation $\phi'(z)$ implies differentiation of potential $\phi(z)$ with respect to z, $\overline{\phi}(z)$ implies taking the conjugate of ϕ and $\overline{\phi}(\bar{z})$ implies taking the conjugate of ϕ and replacing the argument by $\bar{z}$. The first task is to determine the Muskhelishvili potential.

The Muskhelishvili potential for partial slip conditions in the presence of mild bulk tension, $\sigma_b / fp_o < 4(1-\sqrt{1-Q/fP})$, is obtained in closed form by substituting equation (2.1a) and equation (2.1b) into the contour integral along the line of contact

$$\phi(z) = \frac{1}{2\pi i}\int_{contact} \frac{p(t) - iq(t)}{t - z} dt \,, \tag{2.13}$$

giving

$$\phi(z) = -\frac{p_o i}{2a}\left[z - \sqrt{z^2 - a^2}\right] + \frac{p_o f}{2a}\left[\sqrt{z^2 - a^2} - \sqrt{(z-e)^2 - c^2} - e\right]. \tag{2.14}$$

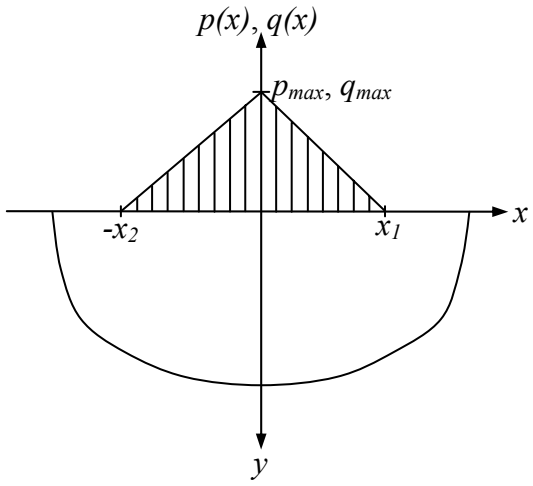

Figure 2.4 : Loading of a half-plane by a triangular distribution of traction

The Muskhelishvili potential for partial slip conditions in the presence of strong bulk tension, $\sigma_b / fp_o > 4(1-\sqrt{1-Q/fP})$, cannot be derived in closed form. The common practice for this case is to use a piecewise linear representation of the actual traction distribution by the means of overlapping triangular distributions of tractions. The

Muskhelishvili potential for a triangular traction element, however, can be derived in closed form (Hills *et al.*, 1993). The triangular traction profile shown in Figure 2.4 may be represented by

$$\frac{p(x)}{p_{\max}} = \frac{q(x)}{q_{\max}} = 1 - \frac{x}{x_1} \qquad 0 < x < x_1, \tag{2.15a}$$

$$\frac{p(x)}{p_{\max}} = \frac{q(x)}{q_{\max}} = 1 + \frac{x}{x_2} \qquad -x_2 < x < 0. \tag{2.15b}$$

The Muskhelishvili potentials for the triangular traction distribution above are

$$\frac{2\pi i\phi(z)}{-p_{\max} + iq_{\max}} = \left(1 - \frac{z}{x_1}\right)\ln\left(\frac{z - x_1}{z}\right) - \left(1 + \frac{z}{x_2}\right)\ln\left(\frac{z + x_2}{z}\right), \tag{2.16a}$$

$$\frac{2\pi i\phi'(z)}{-p_{\max} + iq_{\max}} = -\frac{1}{x_1}\ln\left(\frac{z - x_1}{z}\right) - \frac{1}{x_2}\ln\left(\frac{z + x_2}{z}\right), \tag{2.16b}$$

$$\frac{2\pi i\overline{\phi}(z)}{p_{\max} + iq_{\max}} = \left(1 - \frac{z}{x_1}\right)\ln\left(\frac{z - x_1}{z}\right) - \left(1 + \frac{z}{x_2}\right)\ln\left(\frac{z + x_2}{z}\right), \tag{2.16c}$$

$$\frac{2\pi i\overline{\phi}(\overline{z})}{p_{\max} + iq_{\max}} = \left(1 - \frac{\overline{z}}{x_1}\right)\ln\left(\frac{\overline{z} - x_1}{\overline{z}}\right) - \left(1 + \frac{\overline{z}}{x_2}\right)\ln\left(\frac{\overline{z} + x_2}{\overline{z}}\right). \tag{2.16d}$$

The internal stress field is determined by superposition of contributions from the triangular elements. The triangular traction distribution is suitable for incomplete contacts where the tractions fall continuously to zero at the edge of the contact.

Figure 2.5 is a typical plot of the normalised stress components at the surface of the specimen using a half-plane formulation, for the case, $Q/P = 0.45$, $f = 0.75$ and $\sigma_b = 0$. The direct stress component acting parallel to the free surface σ_{xx}, which is primarily responsible for the propagation of transverse cracks, is observed to be a maximum at the trailing edge of contact.

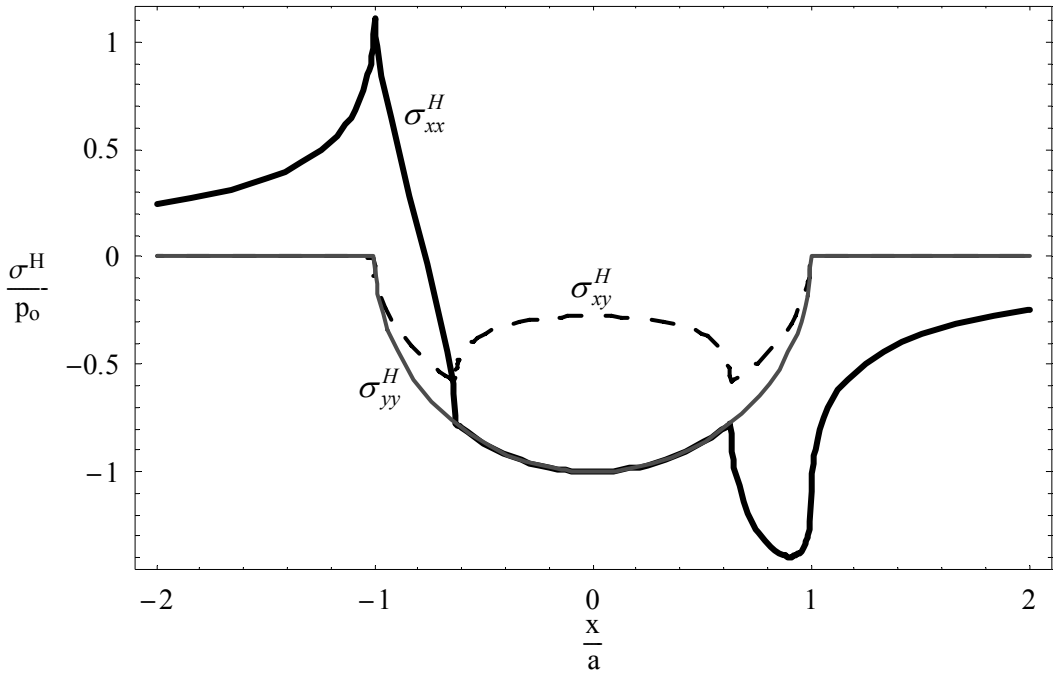

Figure 2.5 : Normalised stress components at the surface of the specimen by using half-plane formulation, for the case, $Q/P = 0.45$, $f = 0.75$ and $\sigma_b = 0$.

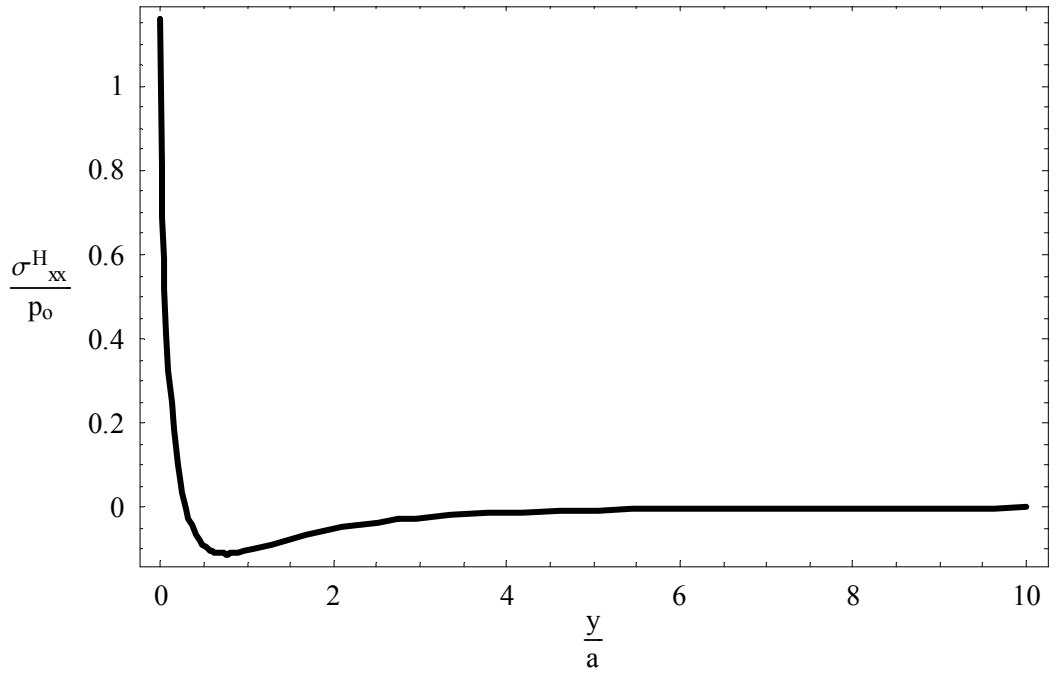

Figure 2.6 : Normalised subsurface σ_{xx} component at the trailing edge of the contact determined by using half-plane formulation, for the case, $Q/P = 0.45$, $f = 0.75$ and $\sigma_b = 0$.

Figure 2.6 is a typical plot of the normalised subsurface σ_{xx} component at the trailing edge of the contact using a half-plane formulation, for the case, $Q/P = 0.45$, $f = 0.75$ and $\sigma_b = 0$. The value of σ_{xx} is a maximum at the surface, becomes compressive just below the surface and then approaches zero deep into the surface.

2.3.2 Corrective stress in a strip

Most fretting fatigue test configurations do not allow the problem to be treated using the conventional half-plane approximation. It has been reported by Fellows *et al*. (1995) that the effect of the finite specimen thickness on the surface traction distribution is not much different from that predicted using a half-plane formulation if the ratio of specimen thickness to contact width is greater than 5. However, the effect of the specimen thickness *on the stress distribution* could not be neglected and must be taken into account in developing crack initiation and propagation models in fretting fatigue.

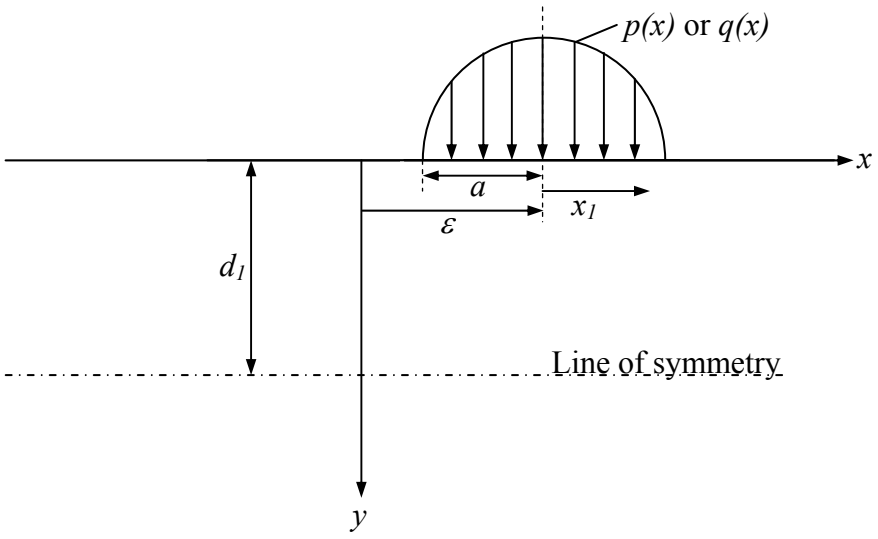

Figure 2.7 : Geometry and variables for deriving stresses in a strip

The corrective stress components, $\sigma_{ij}^{C}(x,y)$ at an arbitrary point (*x*,*y*) within a strip due to the traction distributions *p*(*x*) and *q*(*x*) shown in Figure 2.7 are (Sneddon, 1951)

$$\begin{aligned}\sigma_{xx}^{C}(x,y) = p_{avg}\frac{2}{\pi}\int_0^{\infty}\left[\frac{G_{xxp}}{\Delta(\lambda)} - (\bar{y}\lambda - 1)e^{-\bar{y}\lambda}\right]\tilde{p}(\lambda)\cos(\lambda\bar{x}_1)d\lambda \\ + q_{avg}\frac{2}{\pi}\int_0^{\infty}\left[\frac{G_{xxq}}{\Delta(\lambda)} - (\bar{y}\lambda - 2)e^{-\bar{y}\lambda}\right]\tilde{q}(\lambda)\sin(\lambda\bar{x}_1)d\lambda\end{aligned}, \tag{2.17a}$$

$$\begin{aligned}\sigma_{yy}^{C}(x,y) = p_{avg}\frac{2}{\pi}\int_0^{\infty}\left[\frac{G_{yyp}}{\Delta(\lambda)} + (\bar{y}\lambda + 1)e^{-\bar{y}\lambda}\right]\tilde{p}(\lambda)\cos(\lambda\bar{x}_1)d\lambda \\ + q_{avg}\frac{2}{\pi}\int_0^{\infty}\left[\frac{G_{yyq}}{\Delta(\lambda)} + \bar{y}\lambda e^{-\bar{y}\lambda}\right]\tilde{q}(\lambda)\sin(\lambda\bar{x}_1)d\lambda\end{aligned}, \tag{2.17b}$$

$$\begin{aligned}\sigma_{xy}^{C}(x,y) = p_{avg}\frac{2}{\pi}\int_0^{\infty}\left[\frac{G_{xyp}}{\Delta(\lambda)} - \bar{y}\lambda e^{-\bar{y}\lambda}\right]\tilde{p}(\lambda)\sin(\lambda\bar{x}_1)d\lambda \\ + q_{avg}\frac{2}{\pi}\int_0^{\infty}\left[\frac{G_{xyq}}{\Delta(\lambda)} + (\bar{y}\lambda - 1)e^{-\bar{y}\lambda}\right]\tilde{q}(\lambda)\cos(\lambda\bar{x}_1)d\lambda\end{aligned}, \tag{2.17c}$$

where $\bar{y} = y/a$, $\bar{d} = d_1/a$, $\bar{x}_1 = (x_1 - \varepsilon)/a$, a is the contact semi-width, p_{avg} and q_{avg} are the average normal and shear loads acting over the contact area, ε is the offset of the contact patch centre from $x = 0$ and d_1 is the specimen half-thickness. Fourier cosine transforms of *p*(*x*) and *q*(*x*) with respect to the transform variable λ are

$$\tilde{p}(\lambda) = \int_0^1 \left(\frac{p(\bar{x}_1)}{p_{avg}}\right)\cos(\lambda\bar{x}_1)\,d\bar{x}_1, \tag{2.18a}$$

$$\tilde{q}(\lambda) = \int_0^1 \left(\frac{q(\bar{x}_1)}{q_{avg}}\right)\cos(\lambda\bar{x}_1)\,d\bar{x}_1. \tag{2.18b}$$

The dimensionless stress influence functions, G_{ijp} and G_{ijq} are given by

$$G_{xxp} = \cosh\left(\lambda\left(\bar{d} - \bar{y}\right)\right)\left(A_p + 2B_p\right) + \sinh\left(\lambda\left(\bar{d} - \bar{y}\right)\right)\left(\lambda\left(\bar{d} - \bar{y}\right)B_p\right), \tag{2.19a}$$

$$G_{yyp} = -\left\{\cosh\left(\lambda\left(\bar{d} - \bar{y}\right)\right)\left(A_p\right) + \sinh\left(\lambda\left(\bar{d} - \bar{y}\right)\right)\left(\lambda\left(\bar{d} - \bar{y}\right)B_p\right)\right\}, \tag{2.19b}$$

$$G_{xyp} = \cosh\left(\lambda\left(\bar{d} - \bar{y}\right)\right)\left(\lambda\left(\bar{d} - \bar{y}\right)B_p\right) + \sinh\left(\lambda\left(\bar{d} - \bar{y}\right)\right)\left(A_p + B_p\right), \tag{2.19c}$$

$$G_{xxq} = \cosh\left(\lambda\left(\bar{d} - \bar{y}\right)\right)\left(A_q + 2B_q\right) + \sinh\left(\lambda\left(\bar{d} - \bar{y}\right)\right)\left(\lambda\left(\bar{d} - \bar{y}\right)B_q\right), \tag{2.19d}$$

$$G_{yyq} = -\left\{\cosh\left(\lambda\left(\bar{d} - \bar{y}\right)\right)\left(A_q\right) + \sinh\left(\lambda\left(\bar{d} - \bar{y}\right)\right)\left(\lambda\left(\bar{d} - \bar{y}\right)B_q\right)\right\}, \tag{2.19e}$$

$$G_{xyq} = -\left\{\cosh\left(\lambda\left(\bar{d} - \bar{y}\right)\right)\left(\lambda\left(\bar{d} - \bar{y}\right)B_q\right) + \sinh\left(\lambda\left(\bar{d} - \bar{y}\right)\right)\left(A_q + B_q\right)\right\}, \tag{2.19f}$$

and the functions A_p, B_p, A_q, B_q, $\Delta(\lambda)$ are

$$A_p = \left(\lambda\bar{d}\right)\cosh\left(\lambda\bar{d}\right) + \sinh\left(\lambda\bar{d}\right), \tag{2.20a}$$

$$A_q = \left(\lambda\bar{d}\right)\sinh\left(\lambda\bar{d}\right), \tag{2.20b}$$

$$B_p = -\sinh\left(\lambda\bar{d}\right), \tag{2.20c}$$

$$B_q = -\cosh\left(\lambda\bar{d}\right), \tag{2.20d}$$

$$\Delta(\lambda) = \left(\lambda\bar{d}\right)\sinh\left(\lambda\bar{d}\right)\cosh\left(\lambda\bar{d}\right). \tag{2.20e}$$

The integrals in equations (2.17a) – (2.17c) were evaluated numerically. A choice has to be made to truncate these integrals evaluated over semi-infinite ranges to finite integrals by setting appropriate upper limits of integration. A value of 20 as the upper limit of integration was found to be sufficient for the integrals to converge satisfactorily. Note that the corrective stresses are symmetric about the specimen half-width.

Figure 2.8 is a plot of the corrective σ_{xx} component at the trailing edge of the contact, due to the effect of normal traction $p(x)$ and shear traction $q(x)$, for the case, d_1/a = 5, Q/P = 0.45, f = 0.75 and σ_b = 0. The effect of shear traction, $q(x)$, on the corrective σ_{xx} component is observed to be negligible compared to the effect of normal traction $p(x)$.

Figure 2.9 is a plot of the corrective σ_{xx} component at the trailing edge of the contact, due to the effect of normal traction $p(x)$ for different ratios of strip thickness to contact width d_1/a, for the case, Q/P = 0.45 and f = 0.75. The magnitude of the corrective σ_{xx} component is observed to increase as the d_1/a ratio decreases.

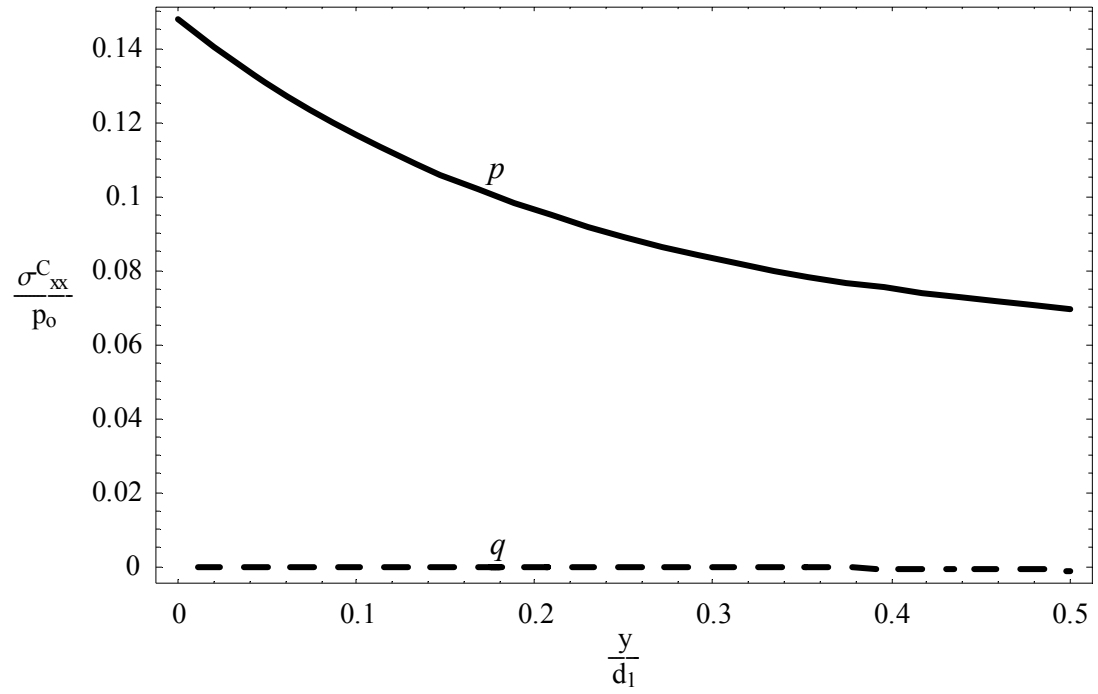

Figure 2.8 : Corrective σ_{xx} component at the trailing edge of the contact, due to the effect of normal traction $p(x)$ and shear traction $q(x)$, for the case, $d_1/a = 5$, $Q/P = 0.45$, $f = 0.75$ and $\sigma_b = 0$.

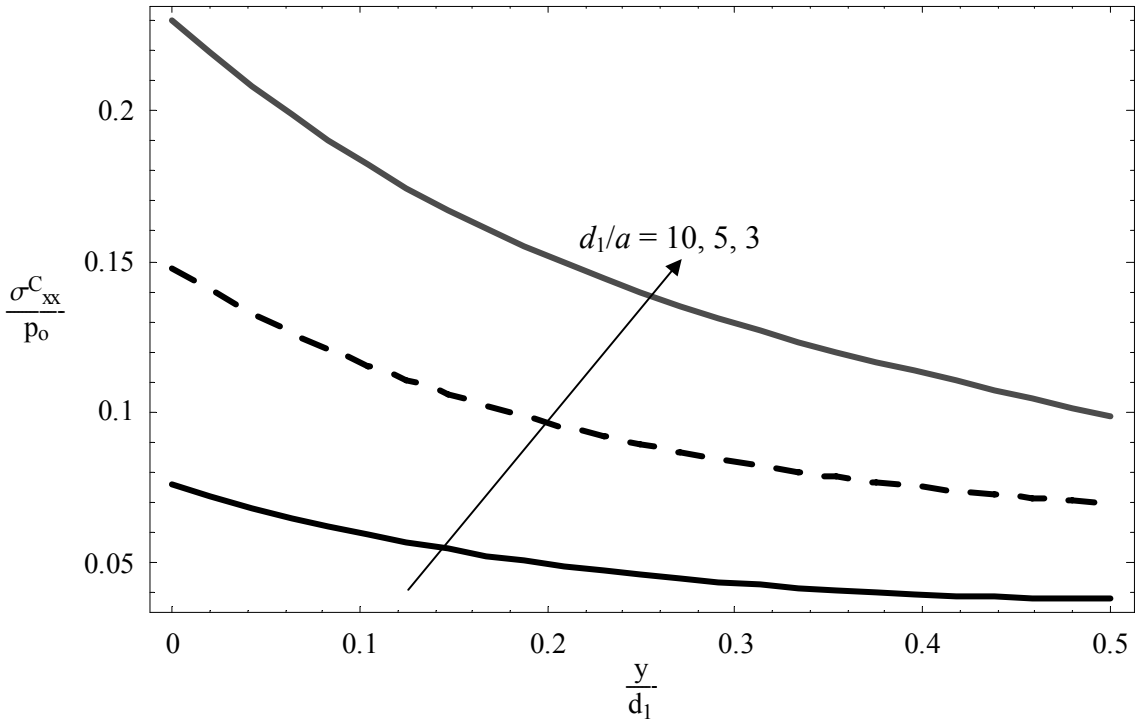

Figure 2.9 : Corrective σ_{xx} component at the trailing edge of the contact, due to the effect of normal traction $p(x)$ for different ratios of strip thickness to contact width d_1/a, for the case, $Q/P = 0.45$ and $f = 0.75$.

2.3.3 Resultant stress in a strip

The resultant stress in a strip, $\sigma_{ij}^{T}(x,y)$, is given by

$$\sigma_{ij}^{T}(x,y) = \sigma_{ij}^{H}(x,y) + \sigma_{ij}^{H}(x,d-y) + \sigma_{ij}^{C}(x,y) \qquad 0 \le y \le d/2\,, \qquad (2.21a)$$

$$\sigma_{ij}^{T}(x,y) = \sigma_{ij}^{H}(x,y) + \sigma_{ij}^{H}(x,d-y) + \sigma_{ij}^{C}(x,d-y) \qquad d/2 \le y \le d\,, \qquad (2.21b)$$

where $\sigma_{ij}^{H}(x,y)$ is the state of stress implied by a half-plane solution and $\sigma_{ij}^{C}(x,y)$ is the corrective stress due to the finite width of the specimen.

Figure 2.10 is a plot of the resultant σ_{xx} component in a strip, at the trailing edge of the contact, for the case, $Q/P = 0.45$, $f = 0.75$, $\sigma_b = 0$ and $d_1/a = 5$. Note that the total stress in the strip is symmetric about the specimen half-width.

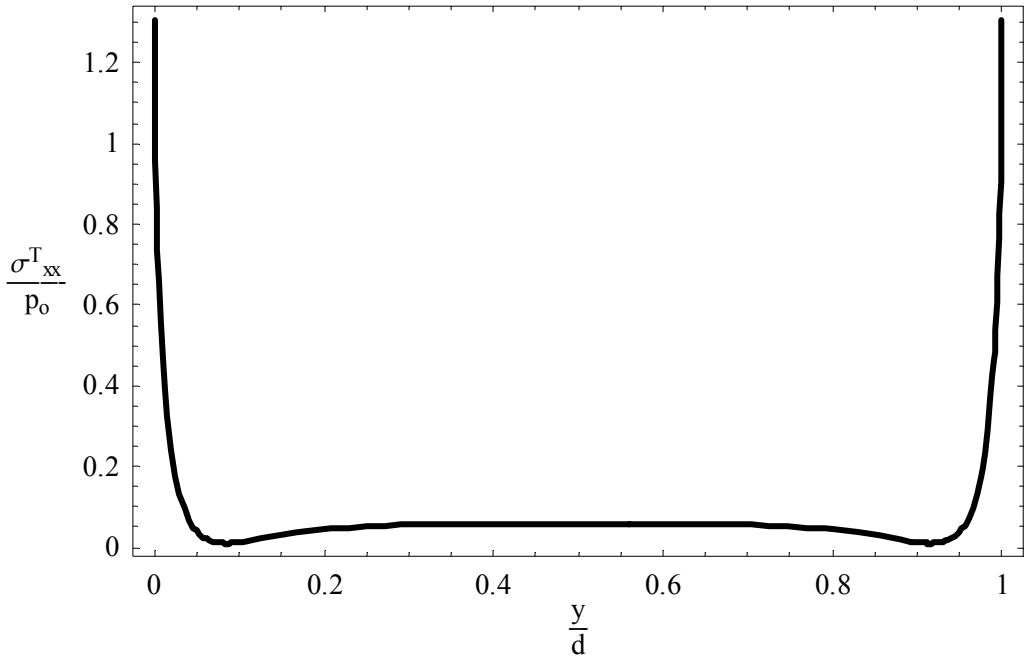

Figure 2.10 : Resultant σ_{xx} component in a strip, at the trailing edge of the contact, for the case, $Q/P = 0.45$, $f = 0.75$, $\sigma_b = 0$ and $d_1/a = 5$.

For this example case, the maximum σ_{xx} stress component at the trailing edge was found to be 12.5% more than that found using a half-plane formulation (Figure 2.6).

2.4 Stress intensity factor for a crack within a strip

2.4.1 Introduction

Problems of a crack in a strip occur very widely in engineering problems. The particular application which is the subject of this investigation is a crack in a tensile test specimen subject not only to oscillatory bulk loading but also fretting (contact fatigue) loading, as shown in Figure 2.11a. A particular additional difficulty which exists here compared with more conventionally loaded problems is that the notional stress field, in the crack's absence, produced by the contact stress field, has very steep gradients, and these are not easy to treat. The logical choice is then between the finite element method, for which the disadvantage is that the effect of different crack lengths relative to the contact half-width must be treated by re-modelling the problem, and the distributed dislocation technique (Hills *et al.*, 1996). The former is very cumbersome if the crack tip stress intensity is needed as a function of crack length, in order to determine fatigue life. A precursor analysis needed in the latter case is that for a dislocation in a domain of the correct form - in this case, a semi-infinite strip - and this is itself quite challenging if done by Fourier transform methods (Sneddon, 1951). Here, this step is bypassed and a simple solution derived for the dislocation, which makes the solution technique more accessible, and easier to programme. The thrust of this section is to demonstrate the simple procedure, to describe its implementation, and to show that it is both efficient and accurate.

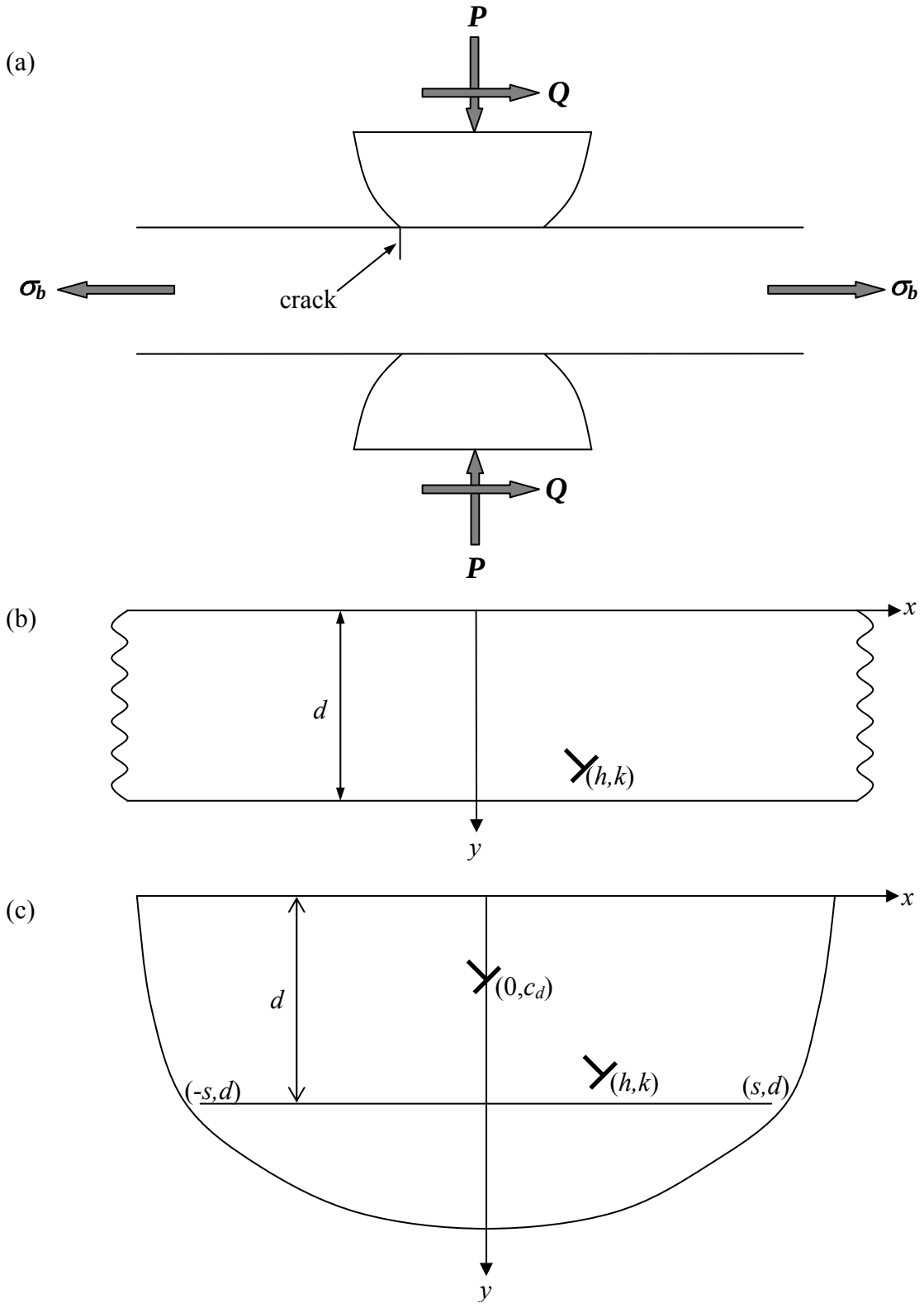

Figure 2.11 : Geometry of the problem to be solved; (a) actual problem - dogbone specimen subject to fretting loads, (b) enabling problem - the solution for a dislocation within a semi-infinite strip, (c) strategy used to find the solution for a dislocation within a semi-infinite strip.

The sub-problem to be solved first is therefore to derive the state of stress for a dislocation in a strip, of infinite longitudinal extent, Figure 2.11(b), and the procedure developed makes use of the solution for a dislocation within a half-plane, which is widely available, and relatively simple (Hills *et al.*, 1996; Nowell and Hills, 1987b). Note that, whilst the dislocation provides a strain kernel, it has no long range resultant, and hence the stresses decay quickly (like $1/r$), and so will produce little residual traction on a remote boundary. Thus, if the dislocation, positioned at $y = c_d$, is very close to one edge of the strip, i.e. $c_d << d$, the half-plane solution by itself will prove adequate, as the effect of the far boundary, at $y = d$, will be small. Similarly, if the dislocation is close to the far boundary, a solution based on the half-plane having the line $y = d$ as its free surface may suffice. Usually, however, neither of these conditions is satisfied, and we must allow for the presence of both free surfaces. The strategy used here, depicted in Figure 2.11(c), is to create one strip surface (usually the one further from the dislocation), by the installation of a large crack. The kernel function for the dislocation forming the crack is that for a dislocation in a half-plane, so that the 'other' edge of the strip is correctly represented. The basic idea of finding a dislocation solution in an arbitrary shaped body is also available in the literature (Hills *et al.*, 1996).

2.4.2 Formulation - dislocation solution in a strip

With the axis set as shown in Figure 2.11(c), the state of stress produced in the half-plane $y > 0$ at a general point, $\tilde{\sigma}_{ij}(x,y)$ by a dislocation having Burgers vector components, (b_x,b_y) located at an arbitrary point (h,k) is (Hills *et al.*, 1996)

$$\tilde{\sigma}_{ij}(x,y) = \frac{2\mu}{\pi(\kappa+1)}\left\{b_x(h,k)G_{xij}(x,y,h,k) + b_y(h,k)G_{yij}(x,y,h,k)\right\}, \qquad (2.22)$$

where G_{xxx}, G_{yxx}, G_{xyy}, G_{yyy}, G_{xxy} and G_{yxy} are given in section 2.4.7, μ is the modulus of rigidity and κ is Kolosov's constant. Now, a solitary dislocation, the object dislocation,

i.e. that being modelled, is installed at $(0,c_d)$, whilst an array of dislocations is placed along the line of the 'crack' ($y = d$, and $-s \le x \le s$), to represent the free surface. The tractions, $\bar{\sigma}_{ij}(x,d)$, induced over the trace line denoting the 'crack' by the distribution of dislocations are given by

$$\bar{\sigma}_{yy}(x,d) = \frac{2\mu}{\pi(\kappa+1)}\left\{\int_{-s}^{s} B_x(h,d)\,G_{xyy}(x,d,h,d)\,dh + \int_{-s}^{s} B_y(h,d)\,G_{yyy}(x,d,h,d)\,dh\right\}, \quad (2.23a)$$

$$\bar{\sigma}_{xy}(x,d) = \frac{2\mu}{\pi(\kappa+1)}\left\{\int_{-s}^{s} B_x(h,d)\,G_{xxy}(x,d,h,d)\,dh + \int_{-s}^{s} B_y(h,d)\,G_{yxy}(x,d,h,d)\,dh\right\}, \quad (2.23b)$$

where $B_i(h,d)$ is the dislocation density ($= db_i/dh$) evaluated at the point (h,d). If the object dislocation, positioned at $(0,c_d)$ produces a state of stress along the crack trace line

$$\tilde{\sigma}_{ij}(x,d) = \frac{2\mu}{\pi(\kappa+1)}\left\{b_x(0,c_d)\,G_{xij}(x,d,0,c_d) + b_y(0,c_d)\,G_{yij}(x,d,0,c_d)\right\}, \quad (2.24)$$

the requirement that the crack face be traction-free is given by

$$\sigma_{yy}(x,d) = \tilde{\sigma}_{yy}(x,d) + \bar{\sigma}_{yy}(x,d) = 0 \qquad y = d \qquad -s \le x \le s\,, \quad (2.25a)$$

$$\sigma_{xy}(x,d) = \tilde{\sigma}_{xy}(x,d) + \bar{\sigma}_{xy}(x,d) = 0\,. \quad (2.25b)$$

In practice the two possible Burgers vector orientations for the object dislocation are dealt with separately, to avoid undue coupling; each gives rise to two simultaneous coupled singular integral equations of the first kind, expressing the requirement that the 'crack' faces, representing the remote edge of the strip, be traction-free. The limits of these integral equations (i.e. the length of the 'crack' representing the far strip boundary) have to be decided. The quantity s/d must be set to a large value, and 65 has been found suitable. It is convenient to normalise the interval of the integration from $-s \le h \le s$ to $-1 \le u \le 1$ by substituting $u = h/s$. The observation points are transformed in a similar way by setting $v = x/s$. An assumption must also be made about the end-point behaviour of the 'crack', and

this is chosen to be bounded at both ends (even though formally there is a singularity). This is because better convergence can be achieved as the notional stress state is very weak at these distances. The appropriate quadrature, based on a Gauss-Chebyshev procedure, is given by Erdogan, Gupta and Cooke (1973), and the discretized form of the equations is

$$G_{xyy}(v_k,d,0,c_d)+s\sum_{i=1}^{n}W(u_i)\left\{G_{xyy}(v_k,d,u_i,d)\phi_x(u_i)+G_{yyy}(v_k,d,u_i,d)\phi_y(u_i)\right\}=0, \quad (2.26a)$$

$$G_{xxy}(v_k,d,0,c_d)+s\sum_{i=1}^{n}W(u_i)\left\{G_{xxy}(v_k,d,u_i,d)\phi_x(u_i)+G_{yxy}(v_k,d,u_i,d)\phi_y(u_i)\right\}=0, \quad (2.26b)$$

where

$$u_i=\cos\left(\frac{\pi i}{n+1}\right) \qquad \text{for } i = 1, \ldots.., n \quad (2.27a)$$

$$v_k=\cos\left(\frac{\pi(2k-1)}{2(n+1)}\right) \qquad \text{for } k = 1, \ldots.., n+1 \quad (2.27b)$$

$$W(u_i)=\frac{\pi(1-u_i^2)}{n+1} \qquad \text{for } i = 1, \ldots.., n. \quad (2.27c)$$

This will give rise to a linear set of $2n + 2$ simultaneous equations for $\phi_x(u_1),....,\phi_x(u_n)$ and $\phi_y(u_1),....,\phi_y(u_n)$. There are two surplus equations because of the assumption of bounded end-points behaviour. A choice has to be made of which two over-specified equations to omit. In this case, the last equation in equation (2.26a) and equation (2.26b) were omitted. The unknown functions $\phi_x(u_i)$ and $\phi_y(u_i)$ are then determined by solving the simultaneous equations above, where the primary unknowns are the dislocation densities $\phi_j(u_i)$. When once these have been found the state of stress anywhere within the strip may be deduced as the sum of that caused by the object dislocation, together with the effect of the dislocation array forming the crack. Of particular interest is the state of stress arising on the line $x = 0$, where the real crack is to be installed. This is given by

$$\sigma_{ij}(0,y)=\frac{2\mu}{\pi(\kappa+1)}\left\{\begin{array}{l} b_x(0,c_d)G_{xij}(0,y,0,c_d)+b_y(0,c_d)G_{yij}(0,y,0,c_d)+ \\ \int_{-s}^{s}B_x(h,d)G_{xij}(0,y,h,d)\,dh+\int_{-s}^{s}B_y(h,d)G_{yij}(0,y,h,d)\,dh \end{array}\right\}, \qquad (2.28)$$

and, as the observation point never lies on the interval of integration, these integrals are regular, so that there is a free choice of the observation point.

2.4.3 Results - dislocation solution in a strip

The state of stress induced by the dislocation on the line $x = 0$ may be found from equation (2.28). The effect of the object dislocation is subtracted, thereby removing the Cauchy singularity, and leaving a bounded correction. A plot for an example dislocation is shown in Figure 2.12. The stress component which produces mode I loading for a crack lying normal to the surface, σ_{xx}, was chosen as the example here. As there are two length scales in this problem viz. the position of object dislocation, c_d and the width of the strip, d, the results for different ratios of c_d/d are required.

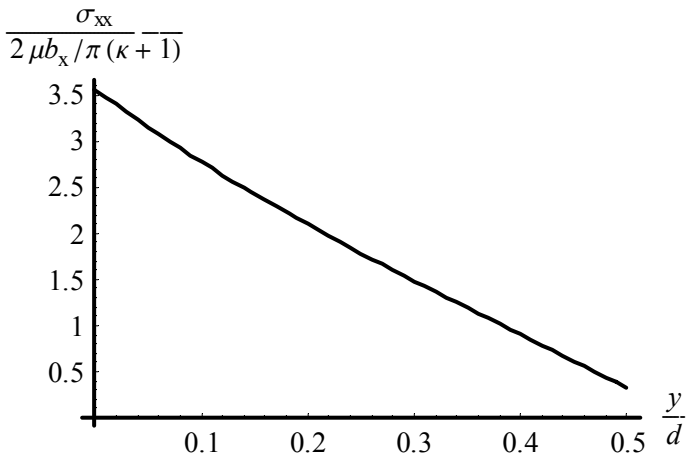

(a)

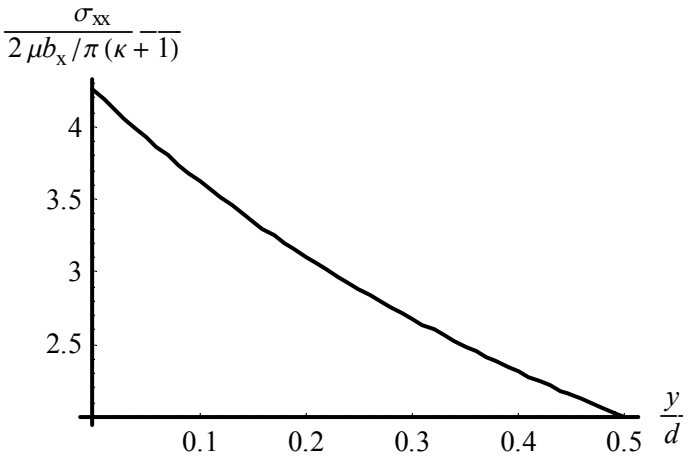

(b)

Figure 2.12 : Correction to the half-plane solution due to the remote edge, when (a) $c_d/d = 0.2$ (b) $c_d/d = 0.8$, for an edge dislocation located at a depth c_d in a strip of width d.

To assist in using the results, curves were fitted through evaluated data points. The choice that was made was to fit a cubic equation for each plot and the coefficients determined by a standard least-squares procedure. The resulting function is the correction due to the presence of a far free boundary and is in the following form

$$S_{kij}(y, c_d, d) = \frac{1}{d}\left[C_1 + C_2\left(\frac{y}{d}\right) + C_3\left(\frac{y}{d}\right)^2 + C_4\left(\frac{y}{d}\right)^3 \right], \tag{2.29a}$$

$$C_n = A_{n1} + A_{n2}\left(\frac{c_d}{d}\right) + A_{n3}\left(\frac{c_d}{d}\right)^2 + A_{n4}\left(\frac{c_d}{d}\right)^3, \tag{2.29b}$$

where the values of the constants C_n, A_{n1}, A_{n2}, A_{n3} and A_{n4} for n = 1,..,4 are given in Table 2.1.

Table 2.1 : Constants in equations (2.29a) and (2.29b)

S_{kij}	A_{11}	A_{12}	A_{13}	A_{14}	A_{21}	A_{22}	A_{23}	A_{24}
S_{xxx}	0.4	18.9	–14.5	–3.9	–1.6	–40.1	25.4	20.3
S_{yxy}	0	0	0	0	0.1	–0.2	22.4	–13.2
S_{kij}	A_{31}	A_{32}	A_{33}	A_{34}	A_{41}	A_{42}	A_{43}	A_{44}
S_{xxx}	3.6	12.7	29.4	–49.6	–3.4	–7.6	–32.4	50.7
S_{yxy}	0	–1.2	–27.5	14.0	–0.4	5.2	0.7	10.9

Note : The constants for S_{xxy} and S_{yxx} are 0.

Therefore the state of stress in the strip arising on the line $x = 0$ may also be written as

$$\hat{\sigma}_{ij}(0,y) = \frac{2\mu}{\pi(\kappa+1)} \left\{ \begin{array}{l} b_x(0,c_d)\left(G_{xij}(0,y,0,c_d) + S_{xij}(y,c_d,d)\right) \\ + b_y(0,c_d)\left(G_{yij}(0,y,0,c_d) + S_{yij}(y,c_d,d)\right) \end{array} \right\}. \tag{2.30}$$

2.4.4 Stress intensity factor formulation

The solution for the physical crack itself, when lying normal to the free surface, is, in fact, simpler than that for the dislocation, because the solution is inherently uncoupled, i.e. shearing tractions produce a mode II loading only, and opening tractions produce mode I loading only. This property is clear from the form of the solution for the dislocations. Figure 2.13 shows a surface-breaking crack of length l, lying normal to the free surface of a strip, and loaded by arbitrary stress of magnitude $\sigma_T(x,y)$. For this particular example, the remote loading produces mode I loading only, so that only climb dislocations are needed. The total direct stress, $\sigma_{xx}(0,y)$, due to both the external loading and the influence of an array of climb dislocations along the crack face is set to zero, to render the crack faces traction-free. The integral equation for the problem above is given by

$$\sigma_T(0,y) + \frac{2\mu}{\pi(\kappa+1)} \int_0^l B_x(0,c_d)\left(G_{xxx}(0,y,0,c_d) + S_{xxx}(y,c_d,d)\right) dc_d = 0, \tag{2.31}$$

where

$$B_x = db_x / dc_d . \tag{2.32}$$

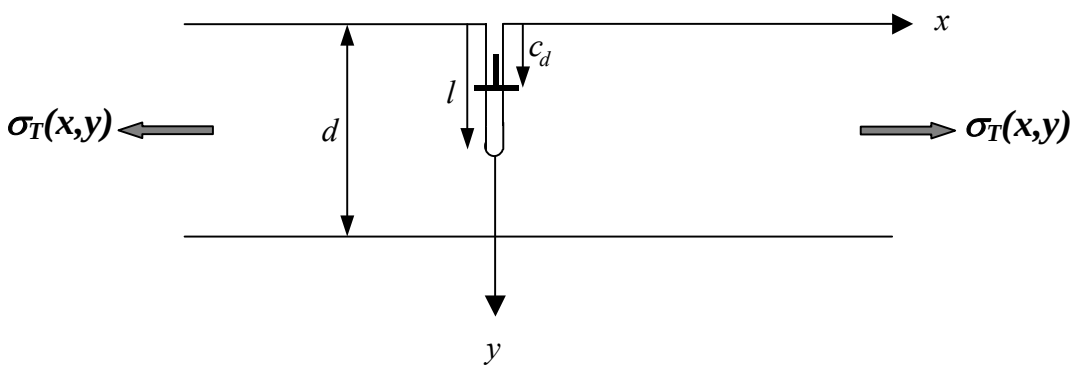

Figure 2.13 : A surface-breaking crack perpendicular to the free surface loaded by arbitrary stress

Once again, it is convenient to normalise the interval of integration from $0 \le c_d \le l$ to $-1 \le u \le 1$, this time by substituting $u = 2c_d/l - 1$. The observation points are transformed in a similar way giving $v = 2y/l - 1$. An assumption must be made about the end-point behaviour of the crack, and this is singular at $y = l$ and bounded at $y = 0$. The same quadrature as that cited above is used (but this time the singular-bounded form is required) giving

$$\sigma_T(0,v_k) + l\sum_{i=1}^{n} W(u_i)\{G_{xxx}(0,v_k,0,u_i) + S_{xxx}(v_k,u_i,d)\}\hat{\phi}(u_i) = 0\,, \tag{2.33}$$

where

$$u_i = \cos\left(\frac{2i-1}{2n+1}\pi\right) \qquad \text{for } i = 1, \ldots, n \tag{2.34a}$$

$$v_k = \cos\left(\frac{2k}{2n+1}\pi\right) \qquad \text{for } k = 1, \ldots, n \tag{2.34b}$$

$$W(u_i) = \frac{2(1+u_i)}{2n+1} \qquad \text{for } i = 1, \ldots, n. \tag{2.34c}$$

$$\hat{\phi}(u_i) = \frac{\mu}{(\kappa+1)}\phi(u_i)\,. \tag{2.34d}$$

When once the function $\hat{\phi}(u_i)$ is known, the stress intensity factor can be found by interpolation from (Hills *et al.*,1996)

$$K_I = 2\sqrt{2}\sqrt{\pi l}\,\frac{\mu}{(\kappa+1)}\phi(1) = 2\sqrt{2}\sqrt{\pi l}\,\hat{\phi}(1)\,, \tag{2.35a}$$

$$\hat{\phi}(1) = \frac{2}{(2n+1)}\sum_{i=1}^{n}\cot\left(\frac{2i-1}{2(2n+1)}\pi\right)\sin\left(\frac{2i-1}{2n+1}\pi n\right)\hat{\phi}(u_i)\,. \tag{2.35b}$$

2.4.5 Stress intensity factor comparison

To test the validity of the solution and its rate of convergence, a comparison was made with the relevant strip solutions given in the literature. The solution by Brown and Srawley (Brown and Srawley, 1966; Murakami, 1987) in the notation used here is given by

$$\frac{K_I}{\sigma\sqrt{\pi l}} = 1.12 - 0.231\left(\frac{l}{d}\right) + 10.55\left(\frac{l}{d}\right)^2 - 21.72\left(\frac{l}{d}\right)^3 + 30.39\left(\frac{l}{d}\right)^4, \qquad (2.36)$$

and that by Paris and Sih (Paris and Sih, 1965; Lampman, 1997) is

$$\frac{K_I}{\sigma\sqrt{\pi l}} = \sec\beta\sqrt{\frac{\tan\beta}{\beta}}\left[0.752 + 2.02\left(\frac{l}{d}\right) + 0.37(1-\sin\beta)^3\right];\ \beta = \frac{\pi l}{2d}. \qquad (2.37)$$

Equation 2.36 is said to have accuracy of ±0.5% for ratios of crack length to strip width, *l*/*d*, less than 0.6, whereas the accuracy of equation 2.37 is ±0.5% for any *l*/*d* ratio.

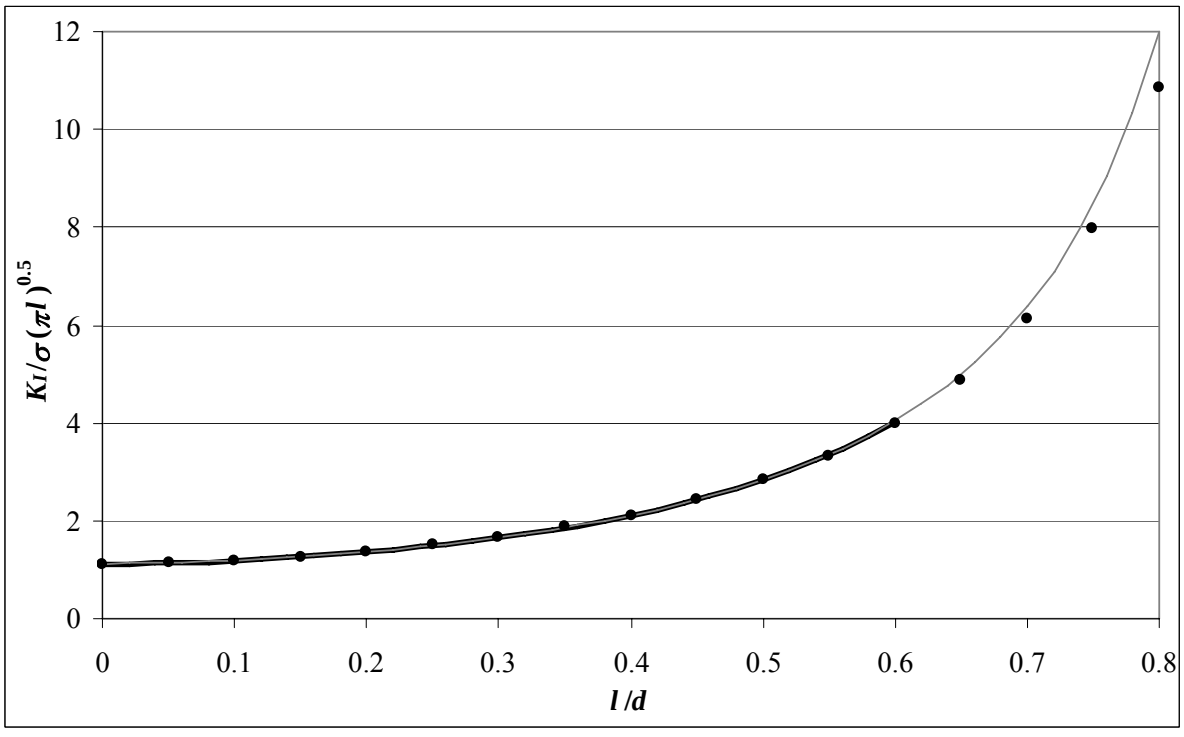

Figure 2.14 : Comparison of stress intensity factor calibrations for an edge cracked specimen in a uniform field. The black line is the result by Brown and Srawley, the grey line is by Paris and Sih, and the dots are the results obtained by using distributed dislocation method.

Plots of stress intensity factor calibrations for an edge cracked specimen for different ratios of l/d is shown in Figure 2.14. The distributed dislocation method gives results in very close agreement with the previously published results (Brown and Srawley, 1966; Murakami, 1987; Paris and Sih, 1965; Lampman, 1997). The divergence in the results in the literature occurs when the l/d ratio is greater than 0.6 and the present method is well adapted to treat such cases. It is reliable at much larger values of l/d. Also, in practical applications, a fracture length of more than half of the specimen width is very unlikely.

2.4.6 Conclusions

The distributed dislocation technique for solving for crack tip stress intensity factors is very efficient and ideal when the crack exists in a relatively simple domain but with steep notional stress gradients. However, a drawback is that the solution for an edge dislocation in the domain is needed before the solution can be found, and this can be challenging and time-consuming in itself. The solution for a dislocation in a strip or layer is a good example of where there is a big overhead in finding the dislocation solution, and the technique described here shows how this may be circumvented in a very straightforward way. The technique introduced involves some approximations, namely the assumption that the 'other' specimen boundary may be represented by a finite crack length, the application of Gauss-Chebyshev procedure to solve the singular integral equations and the curves fitting to the correction solutions, which may introduce errors. Nevertheless this technique gives results in very close agreement with the reference solutions in the literature and is very useful when solving problems involving steep stress gradients.

2.4.7 Functions used to calculate stresses in a half-plane

$$G_{xxx}(x,y,h,k)=\left\{\begin{array}{l}\dfrac{3(y-k)}{r_1^2}-\dfrac{2(y-k)^3}{r_1^4}-\dfrac{3(y+k)}{r_2^2}+\dfrac{2(y+k)^3}{r_2^4}-\dfrac{2k}{r_2^2}\\ +\dfrac{16k(y+k)^2}{r_2^4}-\dfrac{16k(y+k)^4}{r_2^6}-\dfrac{12k^2(y+k)}{r_2^4}+\dfrac{16k^2(y+k)^3}{r_2^6}\end{array}\right\}, \tag{2.38a}$$

$$G_{yxx}(x,y,h,k)=(x-h)\left\{\begin{array}{l}-\dfrac{1}{r_1^2}+\dfrac{2(y-k)^2}{r_1^4}+\dfrac{1}{r_2^2}-\dfrac{2(y+k)^2}{r_2^4}+\dfrac{12k(y+k)}{r_2^4}\\ -\dfrac{16k(y+k)^3}{r_2^6}-\dfrac{4k^2}{r_2^4}+\dfrac{16k^2(y+k)^2}{r_2^6}\end{array}\right\}, \tag{2.38b}$$

$$G_{xyy}(x,y,h,k)=\left\{\begin{array}{l}-\dfrac{(y-k)}{r_1^2}+\dfrac{2(y-k)^3}{r_1^4}+\dfrac{(y+k)}{r_2^2}-\dfrac{2(y+k)^3}{r_2^4}-\dfrac{2k}{r_2^2}\\ -\dfrac{8k(y+k)^2}{r_2^4}+\dfrac{16k(y+k)^4}{r_2^6}+\dfrac{12k^2(y+k)}{r_2^4}-\dfrac{16k^2(y+k)^3}{r_2^6}\end{array}\right\}, \tag{2.38c}$$

$$G_{yyy}(x,y,h,k)=(x-h)\left\{\begin{array}{l}-\dfrac{1}{r_1^2}-\dfrac{2(y-k)^2}{r_1^4}+\dfrac{1}{r_2^2}+\dfrac{2(y+k)^2}{r_2^4}-\dfrac{4k(y+k)}{r_2^4}\\ +\dfrac{16k(y+k)^3}{r_2^6}+\dfrac{4k^2}{r_2^4}-\dfrac{16k^2(y+k)^2}{r_2^6}\end{array}\right\}, \tag{2.38d}$$

$$G_{xxy}(x,y,h,k)=(x-h)\left\{\begin{array}{l}-\dfrac{1}{r_1^2}+\dfrac{2(y-k)^2}{r_1^4}+\dfrac{1}{r_2^2}-\dfrac{2(y+k)^2}{r_2^4}-\dfrac{4k(y+k)}{r_2^4}\\ +\dfrac{16k(y+k)^3}{r_2^6}+\dfrac{4k^2}{r_2^4}-\dfrac{16k^2(y+k)^2}{r_2^6}\end{array}\right\}, \tag{2.38e}$$

$$G_{yxy}(x,y,h,k)=\left\{\begin{array}{l}-\dfrac{(y-k)}{r_1^2}+\dfrac{2(y-k)^3}{r_1^4}+\dfrac{(y+k)}{r_2^2}-\dfrac{2(y+k)^3}{r_2^4}-\dfrac{2k}{r_2^2}\\ +\dfrac{16k(y+k)^2}{r_2^4}-\dfrac{16k(y+k)^4}{r_2^6}-\dfrac{12k^2(y+k)}{r_2^4}+\dfrac{16k^2(y+k)^3}{r_2^6}\end{array}\right\}, \tag{2.38f}$$

$$r_1^2=(x-h)^2+(y-k)^2 \qquad r_2^2=(x-h)^2+(y+k)^2. \tag{2.38g}$$

2.5 Asymptotic solutions

2.5.1 Introduction

Asymptotic analysis is based on the idea of reducing the complexity of the problem to be studied by representing it by some known local function. It is the first order approximation of the overall problem to be studied and is able to describe accurately the stress/displacement fields only within a region very close to the feature of interest, i.e. crack tip or contact edge. The accuracy of the solution decreases as one moves away from the feature of interest.

The idea of using an asymptotic solution to characterize the state of stress in the crack nucleation regions of slipping complete contact was developed by Mugadu *et al*. (2002b). Dini *et al*. (2004; 2005) suggested that the asymptotic approach could be extended to incomplete contacts. The asymptotic approach is a convenient way of encapsulating the whole local stress state. This gives a simple means of comparing fatigue strength measured in a simple fretting test and using it to predict the strength of a complex prototype.

2.5.2 Surface tractions

Figure 2.15 shows the Hertz-Cattaneo contact with coordinate x measured from the contact edge. It was shown by Dini *et al*. (2004; 2005) that the contact pressure adjacent to the edge of this contact may be defined by

$$\begin{aligned} p(x) &= K_N\sqrt{x} \qquad x > 0 \\ &= 0 \qquad\qquad x < 0 \end{aligned}, \tag{2.39}$$

if the two bodies in contact are elastically similar and can be represented by half-planes. K_N is the normal load multiplicative constant which has dimensions of $FL^{-5/2}$.

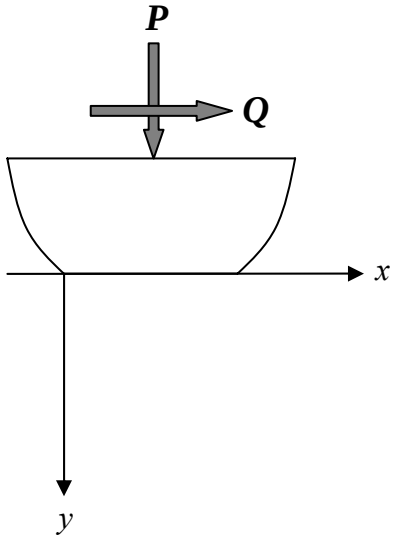

Figure 2.15 : Hertz-Cattaneo contact with local coordinate system at the contact edge

Similarly, the shear traction distribution under partial-slip conditions is deduced from the Hertz-Cattaneo solution by considering the contact to be semi-infinite ($a \rightarrow \infty$) whilst keeping the slip zone size, d_o, finite. The shear traction is expected to produce a constant tangential displacement remote from the contact edge. Therefore the shear traction can be expressed as

$$q(x) = \frac{K_T}{\sqrt{x}} \qquad x >> d_o, \tag{2.40}$$

where K_T is the shear load multiplicative constant with dimensions of $FL^{-3/2}$. The complete shear traction distribution is defined by

$$\begin{aligned} q(x) &= \frac{2K_T}{d_o}\sqrt{x} && 0 < x < d_o \\ &= \frac{2K_T}{d_o}\left(\sqrt{x} - \sqrt{x - d_o}\right) && x > d_o \\ &= 0 && x < 0. \end{aligned} \tag{2.41}$$

The shear traction in the slip zone can be also written as

$$q(x) = fK_N\sqrt{x} \qquad 0 < x < d_o, \tag{2.42}$$

where f is the coefficient of friction. Therefore by equating the shear traction distribution in the slip zone, the multiplicative constants K_N and K_T are shown to be related by

$$\frac{K_T}{K_N} = \frac{fd_o}{2}. \tag{2.43}$$

The normal load multiplicative constant, for a Hertzian contact of half-width a and peak contact pressure p_o is given by

$$\begin{aligned} K_N &= p_o\sqrt{\frac{2}{a}} \\ &= \frac{2\sqrt{2}P}{\pi\sqrt{a^3}}. \end{aligned} \tag{2.44}$$

Once the slip zone size is determined, the shear load multiplicative constant can be determined from the relationship given in equation (2.43). In the case where mild bulk tension is applied, $\sigma_b / fp_o < 4(1-\sqrt{1-Q/fP})$, the slip zone size can be expressed in closed form as

$$d_o = a\left(1-\sqrt{1-Q/fP}+\frac{\sigma_b}{4fp_o}\right). \tag{2.45}$$

Therefore the shear load multiplicative constant is

$$\begin{aligned} K_T &= \frac{\sqrt{2a}fp_o}{2}\left(1-\sqrt{1-Q/fP}+\frac{\sigma_b}{4fp_o}\right) \\ &= \frac{\sqrt{2}fP}{\pi\sqrt{a}}\left(1-\sqrt{1-Q/fP}+\frac{\sigma_b\pi a}{8fP}\right). \end{aligned} \tag{2.46}$$

However, if a strong bulk tension is applied, $\sigma_b / fp_o > 4(1-\sqrt{1-Q/fP})$, the size of slip zone cannot be expressed in a closed form. In this case the size of the slip zone is determined by using the numerical approach described in section 2.2.2. K_T in this case is given by

$$K_T = \frac{K_N f d_o}{2}. \tag{2.47}$$

2.5.3 Internal state of stress

The complete internal stress field may be found from Muskhelishvili potentials. These potentials are summarized below (Dini *et al*., 2004; 2005)

$$\Phi_p(w) = \frac{K_N}{2}\sqrt{w}, \tag{2.48a}$$

$$\Phi_q(w) = \frac{iK_T}{d_o}\left(\sqrt{w} - \sqrt{w-d_o}\right), \tag{2.48b}$$

$$\Phi_b(w) = \frac{\sigma_b}{8}, \tag{2.48c}$$

where $w = x + iy$ and $i = \sqrt{-1}$. $\Phi_p(w)$, $\Phi_q(w)$ and $\Phi_b(w)$ correspond to the effects of normal load, shear load and remote bulk tension, respectively.

Chapter 3

Fretting fatigue test analysis of Herzian contact

3.1 Introduction

The fretting fatigue test results to be processed are those which have been published by Nowell (1988) and Szolwinski (1998). The material employed by Nowell was an aluminium alloy with 4% copper present, and has the designation HE15-TF. A very similar material employed by Szolwinski has the designation Al2024-T351. Some of the important mechanical properties of both materials are given in Table 3.1.

Table 3.1 : Mechanical properties of HE15-TF and Al2024-T351

Property	HE15-TF	Al2024-T351
Tensile Strength, σ_{uts} (MPa)	500	490 – 520
Yield Strength, σ_y (MPa)	465	325 – 340
Fatigue Limit, σ_{fl} (MPa)	124	135 – 140
Elastic Modulus, E (GPa)	74	74.1
Fracture Toughness, K_{IC} ($MPa\ m^{0.5}$)	24	31 – 34

3.2 Crack analysis

For each experiment conducted the state of stress was found, using a combination of the techniques described in section 2.3. The state of stress in a strip was found to be a maximum at the trailing edge of the contact. Therefore, it was assumed that a crack started precisely at the extreme trailing edge of the contact, and grew inwards into the material. Note that the crack initially grows into a decreasing stress field, as it grows out of the influence of the first

contact stress field, but then, if the component survives with the crack tip beyond the centreline, it grows *into* the influence of the opposing pad.

The fracture crack length l_f is determined by setting the stress intensity factor at the tip of a crack, equation (2.35a), to the fracture toughness of the material K_{IC}, giving

$$l_f = \frac{1}{8\pi}\left(\frac{K_{IC}}{\hat{\phi}(1)}\right)^2 . \tag{3.1}$$

This calculation was carried out for all tests, *including those which produced no failure*. The values of the fracture crack length are included in section 3.5. It is noted that the critical length is of order 35 – 50% of the test specimen thickness.

Crack growth is assumed to be governed by a simple Paris law

$$\frac{dl}{dN} = A(\Delta K)^m \tag{3.2}$$

where l is the crack length, ΔK is the range of (mode I) stress intensity factor and N is the number of cycles. Paris crack-growth constants for these materials are given in Table 3.2, where the units employed are consistent with crack growth rate. The crack growth rate for HE15-TF is in *m*/*cycle* and ΔK is in $MPa\sqrt{m}$ whereas the crack growth rate for Al2024-T351 is in *in*/*cycle* and ΔK is in $ksi\sqrt{in}$.

Table 3.2 : Paris crack-growth constants for HE15-TF and Al2024-T351

Paris Data	HE15-TF	Al2024-T351
Paris law coefficient, A	1.74×10^{-10}	3.59×10^{-9}
Paris law exponent, m	4	3.387

A useful calculation to perform is to deduce the length of the crack as a function of the number of cycles of loading. In order to do this it is strictly necessary to take into account deviations from Paris behaviour at either end of the crack's life, but here the

sweeping simplification will be made that Paris' law is valid throughout the propagation phase. An example of the normalized crack length as a function of the normalized number of cycles of loading, for Nowell's Test No. 4, is shown in Figure 3.1, and it will be observed that the vast majority of the life of the component is consumed while the crack is extremely short or, indeed, undergoing nucleation. Standard practice at some companies is to assume that the *entire* life of the crack is correctly described by the propagation equation, and hence to find the 'effective initial flaw size', l_{eff}, and these, too, are tabulated in section 3.5. These are found by integrating Paris' law (equation (3.2)) numerically

$$\int_{l_{eff}}^{l_f} \frac{dl}{A(\Delta K)^m} = \int_0^{N_f} dN \tag{3.3}$$

where N_f is the number of cycles to failure. Of course, in the very early stages of crack development the process is more correctly described as being one of nucleation, but the usual difficulties arise when trying to decide when the nucleation phase ends and propagation takes over: this is quite separate from the question of contact-enhanced propagation, which can satisfactorily be treated using Paris' law.

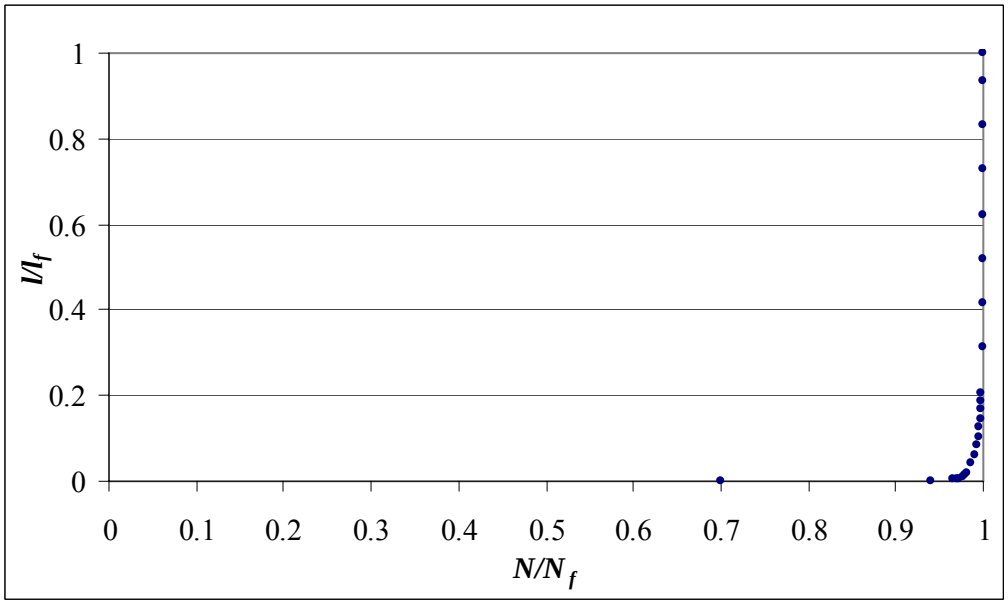

Figure 3.1 : Normalized crack length as a function of normalized number of cycles of loading, for Nowell's Test No.4.

3.3 Nucleation Criteria

In the traditional description of fatigue, an '$S - N_f$' diagram is used to correlate the 'stress' (S) to the number of cycles to cause failure (N_f). The classical Wöhler procedure cannot satisfactorily take stress gradients into account, and, if we applied it to these fretting fatigue tests, the most logical thing to do would be to treat 'S' as the component of stress (σ_{xx}) present at the trailing edge of the contact. This may readily be found using the contact stress analysis already described, and an $S - N_f$ plot obtained using this approach is given in Figure 3.2 (Karuppanan *et al.*, 2007a). There is a very considerable spread of results. This is, perhaps, not completely surprising because it has been observed that the *size* of the contact, and hence the size of the region sustaining a high contact stress, has a profound influence on contact fatigue life: this information is completely absent if simply a component of stress, at the point of nucleation, is employed.

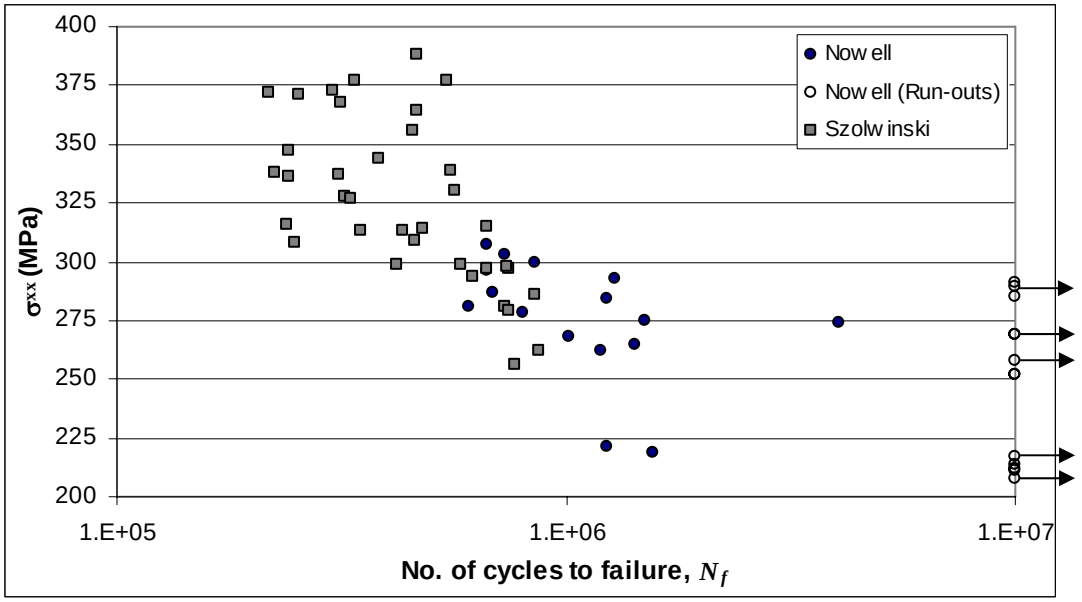

Figure 3.2 : Maximum stress at the trailing contact edge as a function of cycles to failure

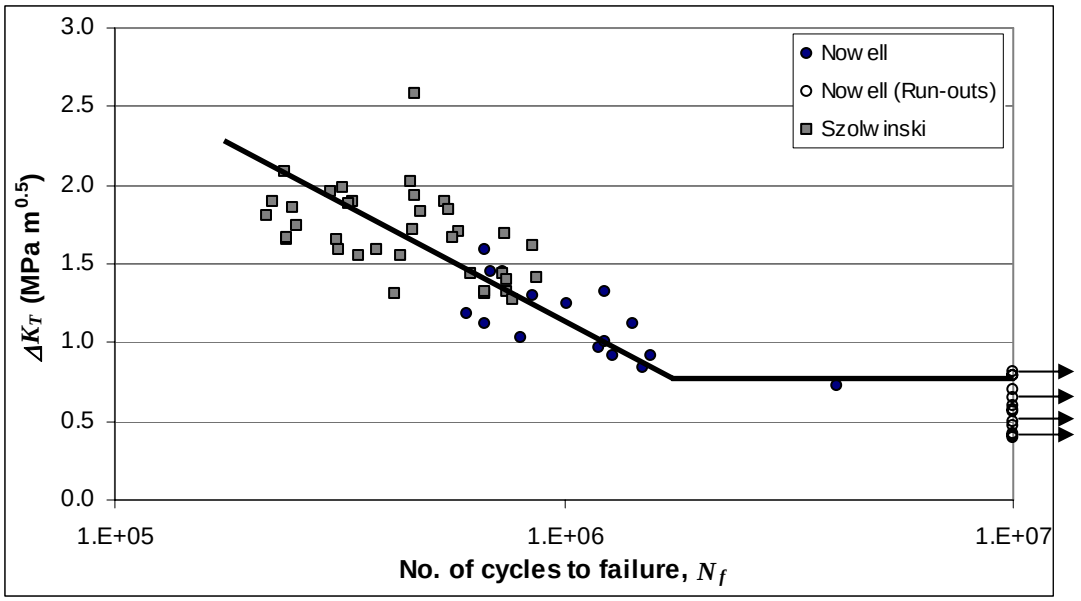

Figure 3.3 : ΔK_T as a function of cycles to failure

The second approach is to employ an asymptotic solution to represent the stress field at the edge of contact. It is straightforward to find the values of the normal load multiplicative constant and the shear load multiplicative constant for the geometry being studied. As the normal load is constant and, to a first approximation, will therefore have no effect on nucleation characteristics, we shall focus on the effect of oscillatory shear. It should be noted that this procedure effectively correlates local **whole** stress fields, i.e. it takes into account both the spatial distribution of stresses and their gradients. The multiplicative factors K_N, K_T which scale the fields are dimensional ($K_N : FL^{-5/2}$, $K_T : FL^{-3/2}$) and hence include information about the extent of the loaded region or equivalently, about stress gradients. The obvious first correlation to attempt is therefore one in which ΔK_T is plotted against N_f, and this set of results is displayed in Figure 3.3 (Karuppanan *et al.*, 2007a). Although there is still some spread, the clustering of results nearer the threshold is much better than in the $S - N_f$ plot (Figure 3.2). Naturally neither plot tells the story rigorously: in Figure 3.2 it is assumed that the entire life is controlled by the state of stress at a particular point, whilst in Figure 3.3 it is assumed that the whole of the life is consumed in nucleation of the crack, as the generalised stress intensity K_T applies only in the

neighbourhood of nucleation. Each therefore reflects the dominant effect of early development on the total life, but in rather different ways. Note that those points plotted at $N = 1\times10^7$ actually denote lives which are greater than this, but unquantified, i.e. 'run-outs'. It is also worth noting that the $\Delta K_T - N_f$ plot displays a fretting fatigue limit at high number of cycles (10^7), even though non-ferrous alloys do not usually exhibit this response in plain fatigue conditions.

The concept of using a local 'full field' correlation of state of stress with the early life of the crack is very appealing, because it means that a single factor encapsulates the entire field, and hence it controls the behaviour of 'cracks' from negligible to finite, if short, length, in just the same way that the crack tip stress intensity factor controls long crack propagation rate. A general problem is that the asymptotic field and the actual contact field diverge as the observation point moves away from the contact corner. The rate of divergence restricts the range of applicability of the asymptote. Figure 3.4 shows a comparison between a finite Hertzian contact (solid lines) and the bounded asymptote (dashed lines), for the case $Q/fP = 0.2$, $d_o/a = 0.106$ and $\sigma_b = 0$, according to the system of reference shown in Figure 2.15. Although something like the second deviatoric invariant $\left(\sqrt{J2}\right)$ is probably the responsible quantity for material degradation when no actual crack is present, as soon as a crack of finite length is present, it is the stress component σ_{xx} which is likely to have most influence on the early rate of growth, and this diverges more quickly than the other components of stress. For this stress component, it is noted that the rate of divergence of the asymptote is particularly rapid along a line perpendicular to the free surface, and starting from the contact edge. In practice cracks often grow inwards along a 45° line before turning to grow perpendicular to the free surface, and in this region the contact stress field is better encapsulated by the asymptote.

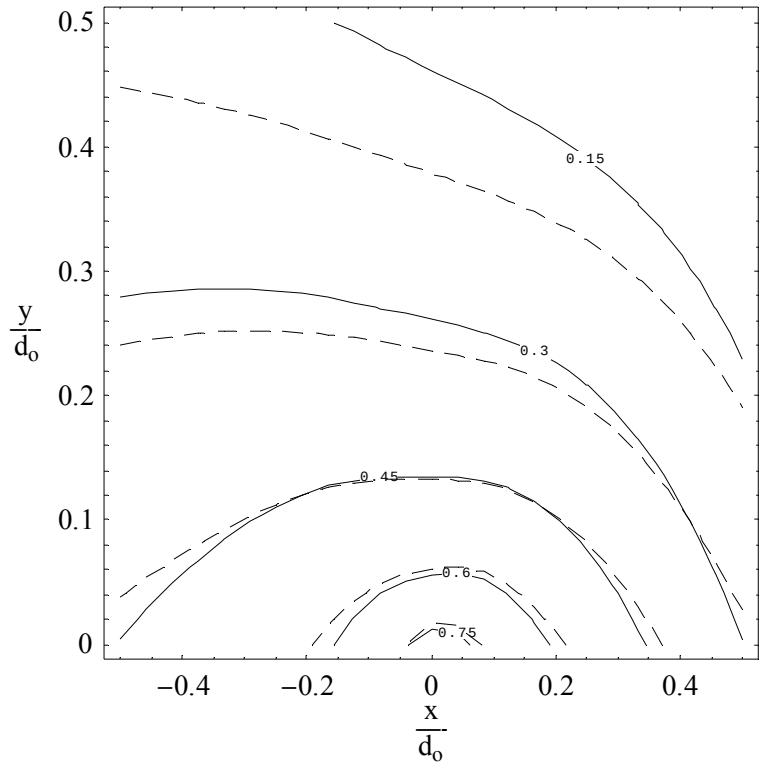
0.5
0.4
0.3
0.2
0.1
0
y/d_o
0.15
0.3
0.45
0.6
0.75
−0.4
−0.2
0
0.2
0.4
x/d_o

(a)

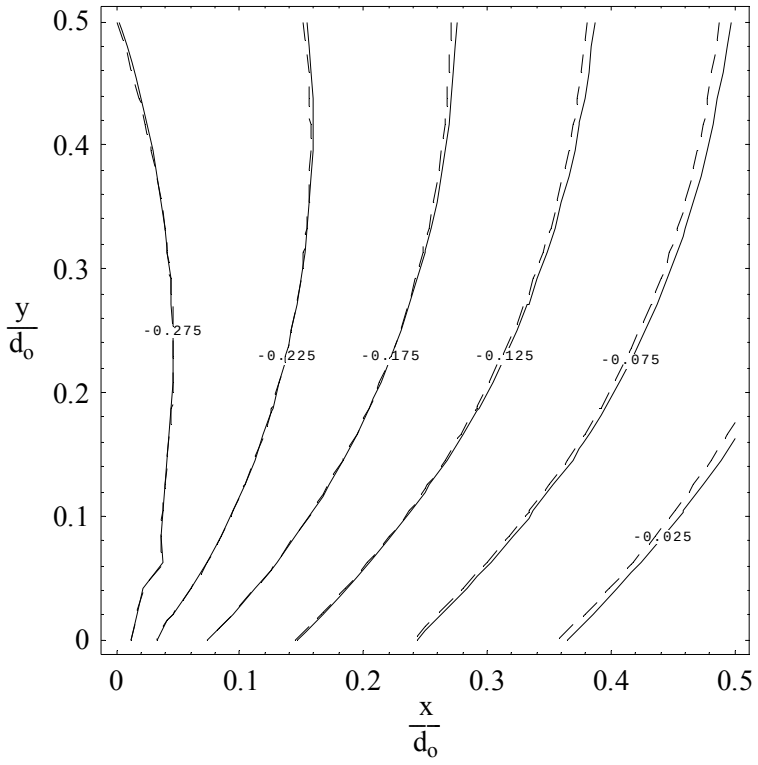
0.5
0.4
0.3
0.2
0.1
0
y/d_o
-0.275
-0.225
-0.175
-0.125
-0.075
-0.025
0
0.1
0.2
0.3
0.4
0.5
x/d_o

(b)

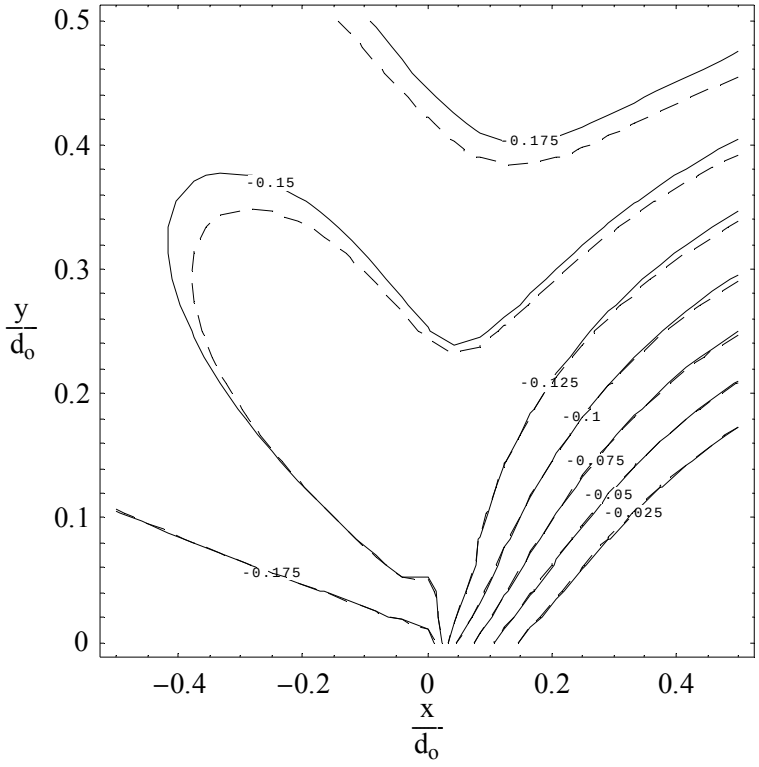

(c)

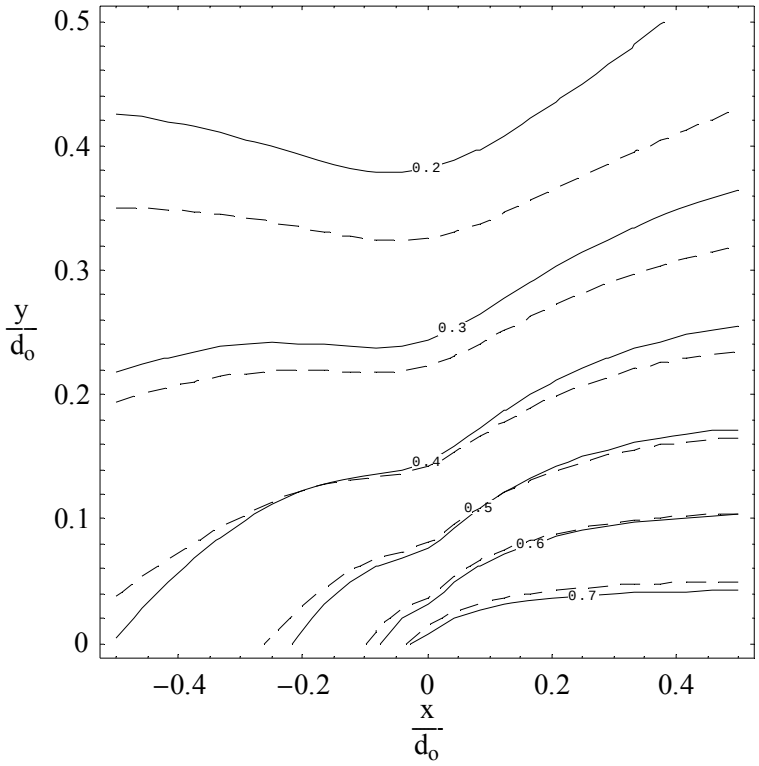

(d)

Figure 3.4 : Contour plots of; (a) σ_{xx}/p_o (b) σ_{yy}/p_o (c) σ_{xy}/p_o (d) $\sqrt{J2}/p_o$ stress components comparison between finite Hertzian contact (solid lines) and the bounded asymptote (dashed lines), for the case $Q/fP = 0.2$, $d_o/a = 0.106$ and $\sigma_b = 0$.

A disappointing property of the incomplete contact asymptote is the rate of divergence, because it means that it is not feasible to 'wrap up' the later stages of nucleation within the asymptotic form. Thus, the asymptotic solution provides an excellent measure of the boundary between finite and infinite lives, but has yet to be developed as a satisfactory parameter that can be used to correlate nucleation life in the 'finite life' regime. Although, from the scientific point of view, this limits the usefulness of the asymptotic approach, in practice it is the boundary between finite and infinite life which is of paramount importance, as it is important to design assemblies to have an infinite life. The generalised stress intensity approach is extremely useful in this regard, because it means that it is possible to carry out laboratory tests with a very simple piece of apparatus to determine experimentally the threshold value of ΔK_T for the material being used. Providing that the surface finish and coefficient of friction are also the same as in the prototype, the threshold value will continue to apply for contacts of **any** (incomplete) geometry, and it is therefore possible to design the contact explicitly to ensure that the threshold is never actually achieved.

3.4 Conclusions

The fretting fatigue tests conducted by Nowell and Szolwinski have been analysed thoroughly, and the lives determined using both classical total life and nucleation based criteria, the latter using local or 'asymptotic' solutions. It has been shown that the nucleation threshold condition is much better described by the asymptotic approach, which has several fundamental advantages: the first is that the whole of the local stress state is fully encapsulated in asymptote, and this is a quantity which can be determined under simple fretting conditions. It is important to draw a distinction between this approach, in which it is recognised that the presence of the slipping interface has an important effect on the nucleation process, and 'analogies' based on either critical plane approaches or notch analogies, which normally use calibrations obtained from monolithic components, and in

which the important slipping interface is not present. Secondly, the technique explains the 'size effect'.

3.5 Fretting fatigue test results

3.5.1 Nowell's test results

No	p_o	σ_b	Q/P	a	N_f	l_f	ΔK_T	d_o	$\sigma_{xx,max}$	l_{eff}
1	157	92.7	0.45	0.10	∞	4.94	0.47	0.056	285	–
2	157	92.7	0.45	0.19	∞	4.87	0.65	0.107	289	–
3	157	92.7	0.45	0.28	∞	4.84	0.79	0.158	291	–
4	157	92.7	0.45	0.38	1.29	4.81	0.92	0.214	293	3.27
5	157	92.7	0.45	0.57	0.67	4.75	1.12	0.322	296	3.65
6	157	92.7	0.45	0.76	0.85	4.70	1.30	0.429	300	3.12
7	157	92.7	0.45	0.95	0.73	4.63	1.45	0.536	303	3.11
8	157	92.7	0.45	1.14	0.67	4.56	1.59	0.643	307	3.06
9	143	92.7	0.24	0.09	∞	4.96	0.28	0.035	238	–
10	143	92.7	0.24	0.18	∞	4.93	0.40	0.070	238	–
11	143	92.7	0.24	0.36	∞	4.89	0.56	0.141	244	–
12	143	92.7	0.24	0.54	∞	4.87	0.69	0.211	247	–
13	143	92.7	0.24	0.72	5.06	4.85	0.80	0.282	250	2.25
14	143	92.7	0.24	0.90	1.22	4.82	0.89	0.352	253	3.44
15	143	92.7	0.24	1.08	1.28	4.80	0.97	0.422	256	3.22
16	143	92.7	0.45	0.09	∞	4.94	0.42	0.053	269	–
17	143	92.7	0.45	0.18	∞	4.90	0.59	0.105	269	–
18	143	92.7	0.45	0.27	4.04	4.85	0.73	0.158	274	2.61
19	143	92.7	0.45	0.36	1.50	4.83	0.84	0.210	275	3.36
20	143	92.7	0.45	0.54	0.80	4.78	1.03	0.315	278	3.73
21	143	92.7	0.45	0.72	0.61	4.72	1.19	0.420	281	3.80
22	143	92.7	0.45	0.90	1.24	4.70	1.33	0.525	284	2.83

23	143	92.7	0.45	1.08	0.69	4.61	1.45	0.630	287	3.30
24	143	77.2	0.45	0.09	∞	5.52	0.39	0.049	252	–
25	143	77.2	0.45	0.18	∞	5.47	0.56	0.099	252	–
26	143	77.2	0.45	0.36	∞	5.38	0.79	0.197	258	–
27	143	77.2	0.45	0.54	1.20	5.32	0.96	0.296	262	3.65
28	143	77.2	0.45	0.72	1.42	5.26	1.11	0.394	265	3.18
29	143	77.2	0.45	0.90	1.02	5.20	1.25	0.493	268	3.35
30	120	61.8	0.45	0.14	∞	6.17	0.41	0.075	208	–
31	120	61.8	0.45	0.21	∞	6.09	0.50	0.113	211	–
32	120	61.8	0.45	0.28	∞	6.06	0.57	0.151	212	–
33	120	61.8	0.45	0.42	∞	6.02	0.70	0.226	214	–
34	120	61.8	0.45	0.57	∞	5.97	0.82	0.307	217	–
35	120	61.8	0.45	0.71	1.57	5.93	0.91	0.383	219	4.03
36	120	61.8	0.45	0.85	1.23	5.88	1.00	0.458	221	4.18

Note : Coefficient of friction, $f = 0.75$; Thickness of the specimen, $d = 12.5\ mm$; Units used are as follows:- p_o, σ_b, $\sigma_{xx,max}$: MPa; a, l_f, d_o: mm; N_f : $\times 10^6$ cycles; ΔK_T : $MPa\sqrt{m}$; l_{eff} : μm

3.5.2 Szolwinski's test results

No	p_o	σ_b	Q/P	a	N_f	l_f	ΔK_T	d_o	$\sigma_{xx,max}$	l_{eff}
1	246.0	110.3	0.22	1.54	314000	5.15	1.59	0.553	368	4.25
2	197.8	84.7	0.28	1.24	422000	5.92	1.31	0.509	299	5.52
3	208.4	110.3	0.31	1.31	241475	5.11	1.67	0.629	347	5.21
4	202.7	100.7	0.35	1.21	241016	5.36	1.66	0.619	336	5.64
5	230.6	110.3	0.31	1.37	217061	5.07	1.81	0.631	372	4.93
6	155.7	111.7	0.43	1.76	238000	4.92	1.08	1.222	316	5.37
7	155.3	112.9	0.37	1.75	249574	4.96	1.86	1.091	308	5.50
8	223.2	84.8	0.23	1.40	668277	5.92	1.31	0.479	315	4.02
9	189.2	100.0	0.27	1.66	349520	5.39	1.55	0.728	313	4.92
10	189.2	100.0	0.27	1.66	433780	5.39	1.55	0.728	313	4.43

11	207.3	88.4	0.35	1.30	563946	5.69	1.66	0.630	330	3.86
12	240.4	101.9	0.31	1.51	545489	5.24	1.89	0.664	377	3.12
13	240.4	101.9	0.31	1.51	337934	5.24	1.89	0.664	377	3.89
14	174.2	85.8	0.38	1.53	582922	5.73	1.71	0.834	299	4.16
15	166.3	97.0	0.32	1.88	739250	5.41	1.70	0.962	298	3.59
16	199.9	113.1	0.34	1.75	455759	4.90	2.03	0.922	356	3.44
17	166.9	85.4	0.32	1.88	856524	5.76	1.61	0.910	286	3.64
18	204.0	115.8	0.52	1.28	465000	4.74	2.59	0.987	388	3.05
19	201.2	85.2	0.21	1.77	665073	5.90	1.32	0.602	297	4.12
20	201.2	85.2	0.21	1.77	749093	5.90	1.32	0.602	297	3.89
21	177.3	81.8	0.24	2.00	747135	5.96	1.40	0.766	279	4.08
22	177.3	81.8	0.25	2.00	729719	5.94	1.43	0.786	281	4.07
23	223.0	109.2	0.35	1.40	302804	5.04	1.95	0.713	373	4.09
24	153.4	81.0	0.31	1.73	867330	5.97	1.41	0.830	262	4.20
25	153.8	82.9	0.26	1.74	768364	5.98	1.28	0.753	256	4.63
26	203.6	99.4	0.31	1.79	552250	5.30	1.84	0.832	339	3.46
27	176.4	109.5	0.34	1.99	320864	4.99	1.98	1.091	328	4.43
28	237.8	108.8	0.27	1.49	253883	5.12	1.74	0.613	371	4.59
29	165.8	110.8	0.33	1.87	479540	5.02	1.83	1.039	314	3.96
30	224.0	98.2	0.36	1.40	464166	5.32	1.93	0.701	364	3.53
31	178.3	97.9	0.24	2.01	463324	5.46	1.53	0.837	295	4.44
32	187.9	84.7	0.27	1.65	621442	5.86	1.43	0.674	294	4.25
33	174.3	97.4	0.36	1.53	459882	5.40	1.71	0.837	309	4.36
34	192.1	106.4	0.34	1.69	225535	5.11	1.90	0.883	338	5.23
35	174.9	110.6	0.38	1.53	330695	5.02	1.88	0.916	327	4.55
36	209.0	97.1	0.33	1.31	311516	5.45	1.66	0.625	337	4.92
37	238.6	85.4	0.27	1.50	381535	5.80	1.58	0.560	344	4.47

Note : Coefficient of friction, $f = 0.65$; Thickness of the specimen, $d = 12.7\ mm$; Units used are as follows:- p_o, σ_b, $\sigma_{xx,max}$: MPa; a, l_f, d_o: mm; N_f : cycles; ΔK_T : $MPa\sqrt{m}$; l_{eff} : μm.

Chapter 4

Introduction to wedge theory

4.1 Williams asymptotic method

The problem considered by Williams (1952) is a notch of included angle 2ψ (or wedge if $2\psi < 180^0$) subjected to tractions on the remote boundaries, as shown in Figure 4.1. Williams developed a method to investigate the nature of the stress field near the apex of the notch by using plane polar coordinates (r,θ) centred on the corner and expanding the stress field as an asymptotic series in powers of r. Here the emphasis is on the stress components for a very small value of r so that other surfaces of the body, including the loaded boundaries, are so far away for the wedge that it may be considered as semi-infinite, with 'loading at infinity'.

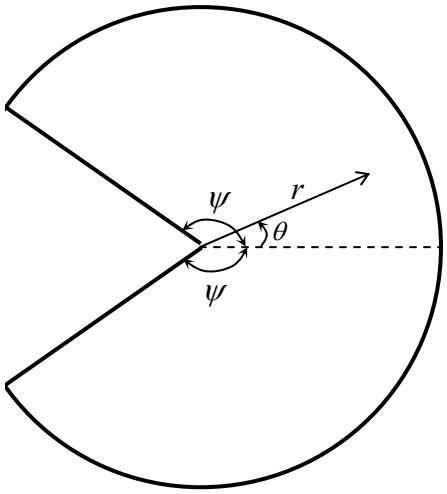

Figure 4.1 : Semi-infinite notch geometry with included angle 2ψ

The general stress field at the notch is a complicated function of r and θ, but as the asymptotic field is being considered only the dominant term in the series of expansion is

required. In order to find the stress and displacement distribution near the apex, an appropriate Airy stress function is required. The Airy stress function chosen that satisfies the biharmonic equation

$$\nabla^4\phi = \nabla^2\nabla^2\phi = \left(\frac{\partial^2}{\partial r^2} + \frac{1}{r}\frac{\partial}{\partial r} + \frac{1}{r^2}\frac{\partial^2}{\partial \theta^2}\right)^2 \phi = 0, \tag{4.1}$$

is in the form

$$\phi = r^{\lambda+1}\left[A_1\cos(\lambda+1)\theta + A_2\cos(\lambda-1)\theta + A_3\sin(\lambda+1)\theta + A_4\sin(\lambda-1)\theta\right], \tag{4.2}$$

where A_1, A_2, A_3 and A_4 are the constants to be determined. The stress components in polar coordinates are determined by substituting the Airy stress function into equations

$$\sigma_{rr} = \frac{1}{r}\frac{\partial\phi}{\partial r} + \frac{1}{r^2}\frac{\partial^2\phi}{\partial\theta^2}, \tag{4.3a}$$

$$\sigma_{\theta\theta} = \frac{\partial^2\phi}{\partial r^2}, \tag{4.3b}$$

$$\sigma_{r\theta} = -\frac{1}{r}\frac{\partial^2\phi}{\partial r\partial\theta} + \frac{1}{r^2}\frac{\partial\phi}{\partial\theta}, \tag{4.3c}$$

giving the following results

$$\sigma_{rr} = \lambda r^{\lambda-1}\begin{bmatrix} -A_1(\lambda+1)\cos(\lambda+1)\theta - A_2(\lambda-3)\cos(\lambda-1)\theta \\ -A_3(\lambda+1)\sin(\lambda+1)\theta - A_4(\lambda-3)\sin(\lambda-1)\theta \end{bmatrix}, \tag{4.4a}$$

$$\sigma_{\theta\theta} = \lambda r^{\lambda-1}\begin{bmatrix} A_1(\lambda+1)\cos(\lambda+1)\theta + A_2(\lambda+1)\cos(\lambda-1)\theta \\ +A_3(\lambda+1)\sin(\lambda+1)\theta + A_4(\lambda+1)\sin(\lambda-1)\theta \end{bmatrix}, \tag{4.4b}$$

$$\sigma_{r\theta} = \lambda r^{\lambda-1}\begin{bmatrix} A_1(\lambda+1)\sin(\lambda+1)\theta + A_2(\lambda-1)\sin(\lambda-1)\theta \\ -A_3(\lambda+1)\cos(\lambda+1)\theta - A_4(\lambda-1)\cos(\lambda-1)\theta \end{bmatrix}. \tag{4.4c}$$

The general form of the polar displacements can be derived from the following stress function-displacement relationships

$$\frac{\partial u_r}{\partial r} = \frac{1}{2\mu}\left[\frac{1}{r}\frac{\partial \phi}{\partial r} + \frac{1}{r^2}\frac{\partial^2 \phi}{\partial \theta^2} - \left(\frac{3-\kappa}{4}\right)\nabla^2 \phi\right], \tag{4.5a}$$

$$\frac{\partial u_\theta}{\partial r} - \frac{u_\theta}{r} + \frac{1}{r}\frac{\partial u_r}{\partial \theta} = \frac{1}{\mu}\left[-\frac{1}{r}\frac{\partial^2 \phi}{\partial r \partial \theta} + \frac{1}{r^2}\frac{\partial \phi}{\partial \theta}\right], \tag{4.5b}$$

giving

$$2\mu u_r = r^\lambda \begin{bmatrix} -A_1(\lambda+1)\cos(\lambda+1)\theta + A_2(\kappa-\lambda)\cos(\lambda-1)\theta \\ -A_3(\lambda+1)\sin(\lambda+1)\theta + A_4(\kappa-\lambda)\sin(\lambda-1)\theta \end{bmatrix}, \tag{4.6a}$$

$$2\mu u_\theta = r^\lambda \begin{bmatrix} A_1(\lambda+1)\sin(\lambda+1)\theta + A_2(\kappa+\lambda)\sin(\lambda-1)\theta \\ -A_3(\lambda+1)\cos(\lambda+1)\theta - A_4(\kappa+\lambda)\cos(\lambda-1)\theta \end{bmatrix}, \tag{4.6b}$$

where μ is the modulus of rigidity, κ is the Kolosov constant (= $3 - 4\nu$ in plane strain) and ν is Poisson's ratio.

The boundary condition for this problem is that the free surface of the notch is required to be traction-free, so that

$$\sigma_{\theta\theta}(r,\psi) = \sigma_{r\theta}(r,\psi) = 0\text{, and} \tag{4.7a}$$

$$\sigma_{\theta\theta}(r,-\psi) = \sigma_{r\theta}(r,-\psi) = 0. \tag{4.7b}$$

Application of these boundary conditions leads to a set of four homogeneous equations with four constants A_1, A_2, A_3 and A_4 which have a non-trivial solution. The equations can be simplified by cancelling the common factor, $\lambda r^{\lambda-1}$ and by taking sums and differences in pairs which will display the symmetry of the system, and can be expressed as two independent matrix equations

$$\begin{bmatrix} (\lambda+1)\sin(\lambda+1)\psi & (\lambda-1)\sin(\lambda-1)\psi \\ (\lambda+1)\cos(\lambda+1)\psi & (\lambda+1)\cos(\lambda-1)\psi \end{bmatrix} \begin{Bmatrix} A_1 \\ A_2 \end{Bmatrix} = \begin{bmatrix} 0 \\ 0 \end{bmatrix}, \tag{4.8a}$$

$$\begin{bmatrix} (\lambda+1)\cos(\lambda+1)\psi & (\lambda-1)\cos(\lambda-1)\psi \\ (\lambda+1)\sin(\lambda+1)\psi & (\lambda+1)\sin(\lambda-1)\psi \end{bmatrix} \begin{Bmatrix} A_3 \\ A_4 \end{Bmatrix} = \begin{bmatrix} 0 \\ 0 \end{bmatrix}. \tag{4.8b}$$

The symmetric terms A_1 and A_2 have a non-trivial solution if the determinant of the coefficient matrix in equation (4.8a) is equal to zero, leading to

$$\lambda \sin 2\psi + \sin 2\lambda\psi = 0\,, \tag{4.9a}$$

whilst the antisymmetric terms A_3 and A_4 have a non-trivial solution if the determinant of the coefficient matrix in equation (4.8b) is equal to zero, giving

$$\lambda \sin 2\psi - \sin 2\lambda\psi = 0\,. \tag{4.9b}$$

Equations (4.9a) and (4.9b) are implicit functions of λ that can be solved using numerical methods and the strength of singularity, λ, for a range of wedge included angle, 2ψ, is shown in Figure 4.2. The strength of singularity found from equation (4.9a) is denoted λ_I (for mode I loading case) and those found from equation (4.9b) is denoted λ_{II} (for mode II loading case).

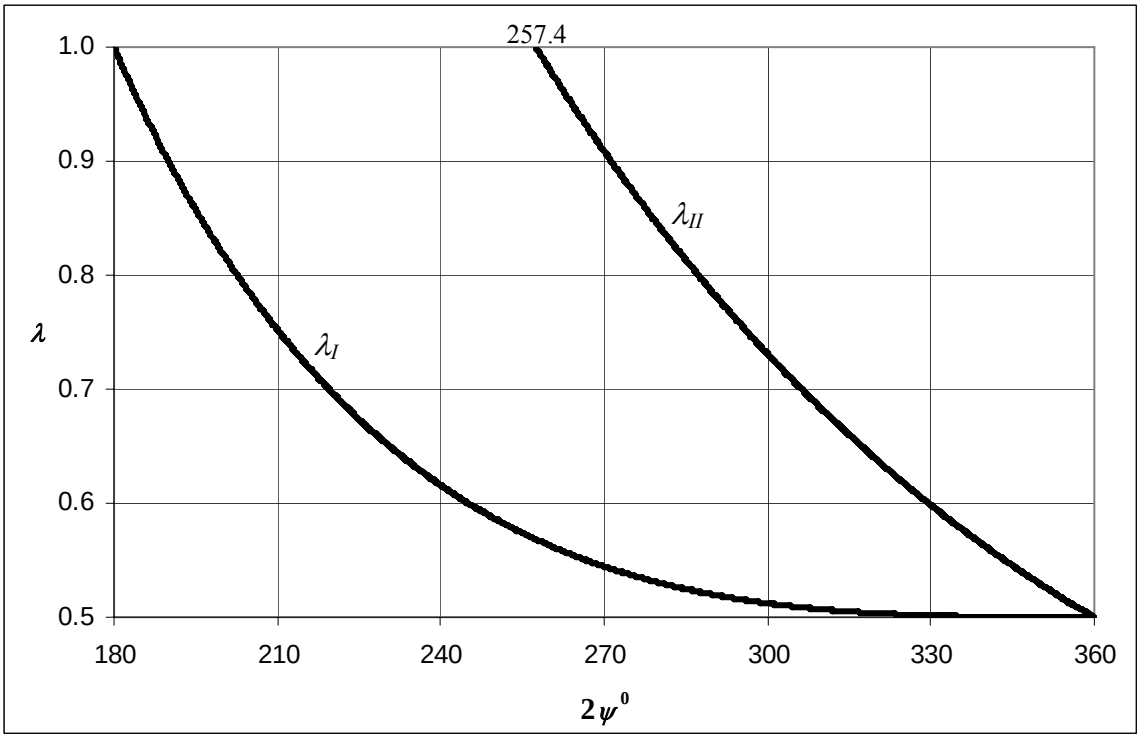

Figure 4.2 : Strength of the singularity, λ, as a function of the wedge included angle, 2ψ

Once the values of the eigenvalues λ are found, the unknown constants A_1, A_2, A_3 and A_4 can be determined. The stress components are then completely defined from equations (4.4a) – (4.4c). If the notch stress intensity factors, under mode I and mode II loading, which are uncoupled along the bisector of the notch are respectively defined as

$$K_I = \frac{\sigma_{\theta\theta}(r,0)}{r^{\lambda_I - 1}} \quad Lt \quad r \to 0\,, \tag{4.10a}$$

$$K_{II} = \frac{\sigma_{r\theta}(r,0)}{r^{\lambda_{II} - 1}} \quad Lt \quad r \to 0\,, \tag{4.10b}$$

the stresses from equations (4.4a) – (4.4c) can be written as (Churchman, 2006)

$$\sigma_{rr}(r,\theta) = K_I r^{\lambda_I - 1} f_{rr}^{I}(\theta) + K_{II} r^{\lambda_{II} - 1} f_{rr}^{II}(\theta)\,, \tag{4.11a}$$

$$\sigma_{\theta\theta}(r,\theta) = K_I r^{\lambda_I - 1} f_{\theta\theta}^{I}(\theta) + K_{II} r^{\lambda_{II} - 1} f_{\theta\theta}^{II}(\theta)\,, \tag{4.11b}$$

$$\sigma_{r\theta}(r,\theta) = K_I r^{\lambda_I - 1} f_{r\theta}^{I}(\theta) + K_{II} r^{\lambda_{II} - 1} f_{r\theta}^{II}(\theta)\,, \tag{4.11c}$$

where

$$f_{rr}^{I}(\theta) = \frac{\cos\left[(\lambda_I - 1)\psi\right]\cos\left[(\lambda_I + 1)\theta\right] - \dfrac{(\lambda_I - 3)}{(\lambda_I + 1)}\cos\left[(\lambda_I + 1)\psi\right]\cos\left[(\lambda_I - 1)\theta\right]}{\cos\left[(\lambda_I + 1)\psi\right] - \cos\left[(\lambda_I - 1)\psi\right]}\,, \tag{4.12a}$$

$$f_{rr}^{II}(\theta) = \frac{\sin\left[(\lambda_{II} - 1)\psi\right]\sin\left[(\lambda_{II} + 1)\theta\right] - \dfrac{(\lambda_{II} - 3)}{(\lambda_{II} + 1)}\sin\left[(\lambda_{II} + 1)\psi\right]\sin\left[(\lambda_{II} - 1)\theta\right]}{\sin\left[(\lambda_{II} - 1)\psi\right] - \dfrac{(\lambda_{II} - 1)}{(\lambda_{II} + 1)}\sin\left[(\lambda_{II} + 1)\psi\right]}\,, \tag{4.12b}$$

$$f_{\theta\theta}^{I}(\theta) = \frac{\cos\left[(\lambda_I - 1)\psi\right]\cos\left[(\lambda_I + 1)\theta\right] - \cos\left[(\lambda_I + 1)\psi\right]\cos\left[(\lambda_I - 1)\theta\right]}{\cos\left[(\lambda_I - 1)\psi\right] - \cos\left[(\lambda_I + 1)\psi\right]}\,, \tag{4.12c}$$

$$f_{\theta\theta}^{II}(\theta) = \frac{\sin\left[(\lambda_{II} - 1)\psi\right]\sin\left[(\lambda_{II} + 1)\theta\right] - \sin\left[(\lambda_{II} + 1)\psi\right]\sin\left[(\lambda_{II} - 1)\theta\right]}{-\sin\left[(\lambda_{II} - 1)\psi\right] + \dfrac{(\lambda_{II} - 1)}{(\lambda_{II} + 1)}\sin\left[(\lambda_{II} + 1)\psi\right]}\,, \tag{4.12d}$$

$$f_{r\theta}^{I}(\theta)=\frac{\sin\left[(\lambda_I-1)\psi\right]\sin\left[(\lambda_I+1)\theta\right]-\sin\left[(\lambda_I+1)\psi\right]\sin\left[(\lambda_I-1)\theta\right]}{\sin\left[(\lambda_I-1)\psi\right]-\dfrac{(\lambda_I+1)}{(\lambda_I-1)}\sin\left[(\lambda_I+1)\psi\right]}, \tag{4.12e}$$

$$f_{r\theta}^{II}(\theta)=\frac{\cos\left[(\lambda_{II}-1)\psi\right]\cos\left[(\lambda_{II}+1)\theta\right]-\cos\left[(\lambda_{II}+1)\psi\right]\cos\left[(\lambda_{II}-1)\theta\right]}{\cos\left[(\lambda_{II}-1)\psi\right]-\cos\left[(\lambda_{II}+1)\psi\right]}. \tag{4.12f}$$

In the same manner, the displacement fields can be written as

$$u_r(r,\theta)=\frac{1}{2\mu}\left[K_I r^{\lambda_I}u_r^I(\theta)+K_{II}r^{\lambda_{II}}u_r^{II}(\theta)\right], \tag{4.13a}$$

$$u_\theta(r,\theta)=\frac{1}{2\mu}\left[K_I r^{\lambda_I}u_\theta^I(\theta)+K_{II}r^{\lambda_{II}}u_\theta^{II}(\theta)\right], \tag{4.13b}$$

where

$$u_r^I(\theta)=-\left[\frac{-(\lambda_I-1)\cos[(\lambda_I+1)\theta]\dfrac{\sin[(\lambda_I-1)\psi]}{\sin[(\lambda_I+1)\psi]}-(\kappa-\lambda_I)\cos[(\lambda_I-1)\theta]}{\lambda_I(\lambda_I+1)\left[1-\dfrac{\cos[(\lambda_I-1)\psi}{\cos[(\lambda_I+1)\psi}\right]}\right], \tag{4.14a}$$

$$u_r^{II}(\theta)=-\left[\frac{(\lambda_{II}-1)\sin[(\lambda_{II}+1)\theta]\dfrac{\cos[(\lambda_{II}-1)\psi]}{\cos[(\lambda_{II}+1)\psi]}+(\kappa-\lambda_{II})\sin[(\lambda_{II}-1)\theta]}{\lambda_{II}(\lambda_{II}-1)\left[1-\dfrac{\cos[(\lambda_{II}-1)\psi}{\cos[(\lambda_{II}+1)\psi}\right]}\right], \tag{4.14b}$$

$$u_\theta^I(\theta)=-\left[\frac{(\lambda_I-1)\sin[(\lambda_I+1)\theta]\dfrac{\sin[(\lambda_I-1)\psi]}{\sin[(\lambda_I+1)\psi]}-(\kappa+\lambda_I)\sin[(\lambda_I-1)\theta]}{\lambda_I(\lambda_I+1)\left[1-\dfrac{\cos[(\lambda_I-1)\psi}{\cos[(\lambda_I+1)\psi}\right]}\right], \tag{4.14c}$$

$$u_\theta^{II}(\theta)=-\left[\frac{(\lambda_{II}-1)\cos[(\lambda_{II}+1)\theta]\dfrac{\cos[(\lambda_{II}-1)\psi]}{\cos[(\lambda_{II}+1)\psi]}-(\kappa+\lambda_{II})\cos[(\lambda_{II}-1)\theta]}{\lambda_{II}(\lambda_{II}-1)\left[1-\dfrac{\cos[(\lambda_{II}-1)\psi}{\cos[(\lambda_{II}+1)\psi}\right]}\right]. \tag{4.14d}$$

4.2 Wedge bonded to a half plane

The solution to the problem of two wedges bonded together was developed by Bogy (1968, 1971). The geometry of the problem solved is shown in Figure 4.3 where two elastically dissimilar wedges of angles φ_1 and φ_2 are bonded together. The appropriate Airy stress functions are of the form used in Williams' solution and are given by

$$\phi_1 = r^{\lambda+1}\left[A_{11}\cos(\lambda+1)\theta + A_{12}\cos(\lambda-1)\theta + A_{13}\sin(\lambda+1)\theta + A_{14}\sin(\lambda-1)\theta\right], \qquad (4.15a)$$

$$\phi_2 = r^{\lambda+1}\left[A_{21}\cos(\lambda+1)\theta + A_{22}\cos(\lambda-1)\theta + A_{23}\sin(\lambda+1)\theta + A_{24}\sin(\lambda-1)\theta\right], \qquad (4.15b)$$

where A_{11}, A_{12}, A_{13}, A_{14} and A_{21}, A_{22}, A_{23}, A_{24} are constants for body 1 and body 2, respectively. The stress components for this problem are determined by substituting these Airy stress functions into equations (4.3a) – (4.3c).

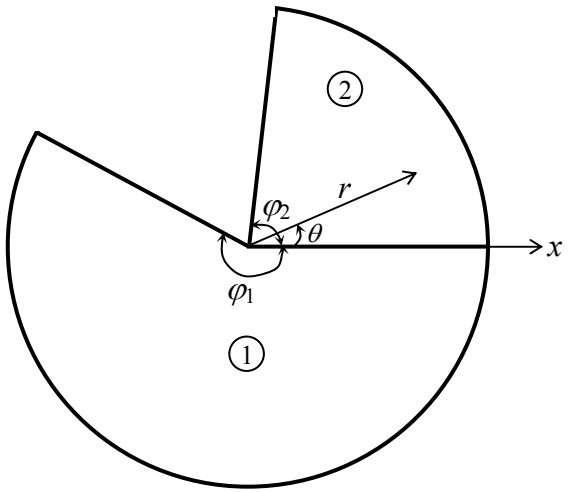

Figure 4.3 : Two bonded wedges of internal angles φ_1 and φ_2

There are eight constants to be determined in the expressions for the stresses and therefore solution requires eight independent boundary conditions. The free surfaces are required to remain traction-free giving

$$\sigma_{r\theta 1}(r,-\varphi_1)=\sigma_{\theta\theta 1}(r,-\varphi_1)=0\,, \tag{4.16a}$$

$$\sigma_{r\theta 2}(r,\varphi_2)=\sigma_{\theta\theta 2}(r,\varphi_2)=0\,. \tag{4.16b}$$

Continuity of traction and displacement at the common boundary give the remaining four boundary conditions

$$\sigma_{\theta\theta 1}(r,0)=\sigma_{\theta\theta 2}(r,0)\,, \tag{4.17a}$$

$$\sigma_{r\theta 1}(r,0)=\sigma_{r\theta 2}(r,0)\,, \tag{4.17b}$$

$$u_{\theta 1}(r,0)=u_{\theta 2}(r,0)\,, \tag{4.17c}$$

$$u_{r1}(r,0)=u_{r2}(r,0)\,. \tag{4.17d}$$

The determinant of the boundary condition matrix can be written as (Bogy, 1971)

$$\begin{aligned}\nabla(\varphi_1,\varphi_2,\alpha,\beta;\lambda)=A(\varphi_1,\varphi_2;\lambda)\beta^2+2B(\varphi_1,\varphi_2;\lambda)\alpha\beta+C(\varphi_1,\varphi_2;\lambda)\alpha^2\\ +2D(\varphi_1,\varphi_2;\lambda)\beta+2E(\varphi_1,\varphi_2;\lambda)\alpha+F(\varphi_1,\varphi_2;\lambda)=0\,,\end{aligned} \tag{4.18}$$

where

$$A(\varphi_1,\varphi_2;\lambda)=4K(\lambda,\varphi_1)K(\lambda,\varphi_2)\,, \tag{4.19a}$$

$$B(\varphi_1,\varphi_2;\lambda)=2\lambda^2\sin^2(\varphi_1)K(\lambda,\varphi_2)+2\lambda^2\sin^2(\varphi_2)K(\lambda,\varphi_1)\,, \tag{4.19b}$$

$$C(\varphi_1,\varphi_2;\lambda)=4\lambda^2(\lambda^2-1)\sin^2(\varphi_1)\sin^2(\varphi_2)+K(\lambda,(\varphi_1-\varphi_2))\,, \tag{4.19c}$$

$$D(\varphi_1,\varphi_2;\lambda)=2\lambda^2[\sin^2(\varphi_1)\sin^2(\lambda\varphi_2)-\sin^2(\varphi_2)\sin^2(\lambda\varphi_1)]\,, \tag{4.19d}$$

$$E(\varphi_1,\varphi_2;\lambda)=-D(\varphi_1,\varphi_2;\lambda)+K(\lambda,\varphi_2)-K(\lambda,\varphi_1)\,, \tag{4.19e}$$

$$F(\varphi_1,\varphi_2;\lambda)=K(\lambda,(\varphi_1+\varphi_2))\,, \tag{4.19f}$$

in which the auxiliary function $K(\lambda,x)$ is defined by

$$K(\lambda,x)=\sin^2(\lambda x)-\lambda^2\sin^2(x)\,, \tag{4.20}$$

and α, β are the Dundurs parameters which describe the elastic mismatch between the two bodies. The Dundurs parameters are defined as

$$\alpha = \frac{(\mu_2/\mu_1)(\kappa_1+1)-(\kappa_2+1)}{(\mu_2/\mu_1)(\kappa_1+1)+(\kappa_2+1)}, \tag{4.21a}$$

$$\beta = \frac{(\mu_2/\mu_1)(\kappa_1-1)-(\kappa_2-1)}{(\mu_2/\mu_1)(\kappa_1+1)+(\kappa_2+1)}, \tag{4.21b}$$

where μ_1, μ_2 and κ_1, κ_2 are the modulus of rigidity and Kolosov's constant for bodies 1 and 2, respectively.

For elastically similar bonded wedges (i.e. for the case $\alpha = \beta = 0$), the characteristic equation (4.18) simplifies to

$$\nabla(\varphi_1,\varphi_2,0,0;\lambda) = \sin^2\big(\lambda(\varphi_1+\varphi_2)\big) - \lambda^2\sin^2\big(\varphi_1+\varphi_2\big) = 0\,. \tag{4.22}$$

If $\varphi_1 + \varphi_2 = 2\psi$ (for a notch with included internal angle 2ψ), equation (4.22) can be expressed as

$$\sin^2(2\lambda\psi) - \lambda^2\sin^2(2\psi) = 0\,, \tag{4.23}$$

which is the same as the product of equations (4.9a) and (4.9b) of the Williams solution, i.e.

$$(\lambda\sin 2\psi + \sin 2\lambda\psi)(\lambda\sin 2\psi - \sin 2\lambda\psi) = 0\,,$$
$$\sin^2(2\lambda\psi) - \lambda^2\sin^2(2\psi) = 0\,. \tag{4.24}$$

Therefore, Williams solution (1952), for a monolithic notch may be applied to the problem of a wedge bonded to an elastically similar half-plane. The included notch angle, 2ψ, is taken as the sum of the wedge angle φ and the half-plane angle π as shown in Figure 4.4.

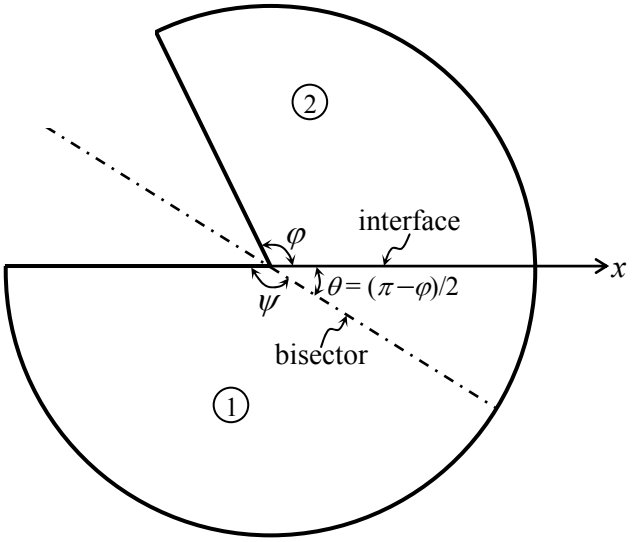

Figure 4.4 : Wedge of internal angle, φ, bonded to a half-pane

Of particular interest are the tractions along the adhered interface, where $\theta = (\pi - \varphi)/2$. The tractions are therefore defined as (Churchman, 2006)

$$-p(x) = \sigma_{\theta\theta}\left(x, \frac{\pi-\varphi}{2}\right) = K_I x^{\lambda_I - 1} f_{\theta\theta}^{I}\left(\frac{\pi-\varphi}{2}\right) + K_{II} x^{\lambda_{II} - 1} f_{\theta\theta}^{II}\left(\frac{\pi-\varphi}{2}\right), \tag{4.25a}$$

$$q(x) = \sigma_{r\theta}\left(x, \frac{\pi-\varphi}{2}\right) = K_I x^{\lambda_I - 1} f_{r\theta}^{I}\left(\frac{\pi-\varphi}{2}\right) + K_{II} x^{\lambda_{II} - 1} f_{r\theta}^{II}\left(\frac{\pi-\varphi}{2}\right), \tag{4.25b}$$

or

$$-p(x) = K_I^o x^{\lambda_I - 1} + K_{II}^o x^{\lambda_{II} - 1}, \tag{4.26a}$$

$$q(x) = K_I^o x^{\lambda_I - 1} g_{r\theta}^{I} + K_{II}^o x^{\lambda_{II} - 1} g_{r\theta}^{II}, \tag{4.26b}$$

where

$$K_I^o = K_I f_{\theta\theta}^{I}\left(\frac{\pi-\varphi}{2}\right), \tag{4.27a}$$

$$K_{II}^o = K_{II} f_{\theta\theta}^{II}\left(\frac{\pi-\varphi}{2}\right), \tag{4.27b}$$

$$g_{r\theta}^{I} = \frac{f_{r\theta}^{I}\left(\frac{\pi-\varphi}{2}\right)}{f_{\theta\theta}^{I}\left(\frac{\pi-\varphi}{2}\right)}, \tag{4.27c}$$

$$g_{r\theta}^{II} = \frac{f_{r\theta}^{II}\left(\frac{\pi-\varphi}{2}\right)}{f_{\theta\theta}^{II}\left(\frac{\pi-\varphi}{2}\right)}. \tag{4.27d}$$

The functions $g_{r\theta}^{I}$ and $g_{r\theta}^{II}$ may be written in closed form by combining equations (4.12) with the identities found from equation (4.8), giving

$$g_{r\theta}^{I} = \frac{\sin\left[(\lambda_I+1)(\pi-\varphi)/2\right] - \Gamma_I^s \sin\left[(\lambda_I-1)(\pi-\varphi)/2\right]}{\cos\left[(\lambda_I+1)(\pi-\varphi)/2\right] - \Gamma_I^c \cos\left[(\lambda_I-1)(\pi-\varphi)/2\right]}, \tag{4.28a}$$

$$g_{r\theta}^{II} = \frac{-\cos\left[(\lambda_{II}+1)(\pi-\varphi)/2\right] + \Gamma_{II}^c \cos\left[(\lambda_{II}-1)(\pi-\varphi)/2\right]}{\sin\left[(\lambda_{II}+1)(\pi-\varphi)/2\right] - \Gamma_{II}^s \sin\left[(\lambda_{II}-1)(\pi-\varphi)/2\right]}, \tag{4.28b}$$

where

$$\Gamma_i^s = \frac{\sin\left[(\lambda_i+1)(\pi+\varphi)/2\right]}{\sin\left[(\lambda_i-1)(\pi+\varphi)/2\right]}, \quad \Gamma_i^c = \frac{\cos\left[(\lambda_i+1)(\pi+\varphi)/2\right]}{\cos\left[(\lambda_i-1)(\pi+\varphi)/2\right]}. \tag{4.29}$$

4.3 Wedge sliding on a half-plane

The semi-infinite sliding wedge problem has been extensively studied by Gdoutos and Theocaris (1975) and by Comninou (1976). In this section a summary of that study will be briefly presented. The geometry of the problem solved is shown in Figure 4.5. It consists of a half-plane (Body 1) with modulus of rigidity μ_1 and Poisson's ratio ν_1 onto which a semi-infinite wedge (Body 2) of internal included angle φ and with corresponding properties μ_2, ν_2 is allowed to slide. The coefficient of friction f in this problem is given a sign. A positive value of f corresponds to the wedge slipping away from the apex (the sense of slip one observes at a trailing edge) whilst a negative value of f corresponds to the wedge slipping towards the apex (the sense of slip one observes at a leading edge), when $\sigma_{\theta\theta} < 0$.

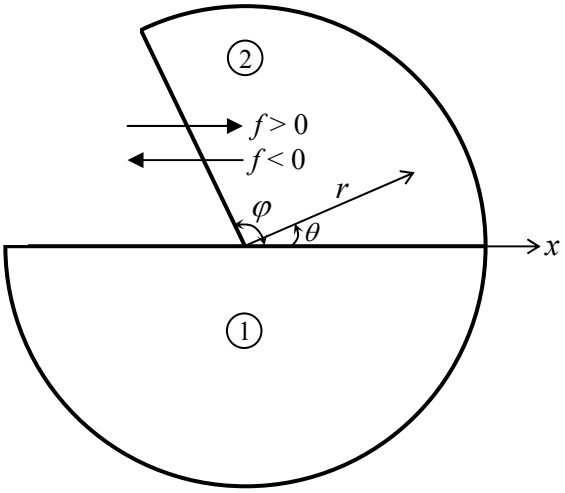

Figure 4.5 : Wedge of angle φ (Body 2) sliding on a semi-infinite half plane (Body 1)

The appropriate Airy stress functions for this problem are of the form used in the Williams solution. Two stress functions ϕ_1 and ϕ_2 which correspond to body 1 and body 2, respectively, are required. These functions are similar to those in equations (4.15a) and (4.15b). The stress components for this problem are again determined by substituting these Airy stress functions into equations (4.3a) – (4.3c) .

The eight constants from equations (4.15a) and (4.15b) are determined by satisfying eight independent boundary conditions. The first four boundary conditions are from the requirements that the free surfaces remain traction-free giving

$$\sigma_{r\theta 1}(r,-\pi) = \sigma_{\theta\theta 1}(r,-\pi) = 0\,, \tag{4.30a}$$

$$\sigma_{r\theta 2}(r,\varphi) = \sigma_{\theta\theta 2}(r,\varphi) = 0\,. \tag{4.30b}$$

Continuity of traction and displacement at the common boundary give the remaining four boundary conditions

$$\sigma_{\theta\theta 1}(r,0) = \sigma_{\theta\theta 2}(r,0)\,, \tag{4.31a}$$

$$\sigma_{r\theta 1}(r,0) = -f\sigma_{\theta\theta 1}(r,0)\,, \tag{4.31b}$$

$$\sigma_{r\theta 2}(r,0) = -f\sigma_{\theta\theta 2}(r,0)\,, \tag{4.31c}$$

$$u_{\theta 1}(r,0) = u_{\theta 2}(r,0)\,. \tag{4.31d}$$

In addition, the stress components of the two stress fields have to satisfy the regularity conditions (Bogy, 1971)

$$\sigma_{rr},\ \sigma_{\theta\theta},\ \sigma_{r\theta}\ = 0\left(r^{\delta-1}\right) \quad \text{as } r \to \infty \ \text{ for every } \delta > 0\,. \tag{4.32}$$

Application of the boundary conditions in equations (4.30) and (4.31) produces a homogenous set of eight equations with eight unknowns which has a non-trivial solution if

$$\begin{aligned}\nabla(\varphi, f, \alpha, \beta; \lambda) = {} & (1+\alpha)\cos\lambda\pi\,(\sin^2\lambda\varphi - \lambda^2\sin^2\varphi) + 0.5(1-\alpha)\sin\lambda\pi(\sin 2\lambda\varphi + \lambda\sin 2\varphi) \\ & + f\sin\lambda\pi\left\{(1-\alpha)\lambda(1+\lambda)\sin^2\varphi - 2\beta(\sin^2\lambda\varphi - \lambda^2\sin^2\varphi)\right\} = 0\,,\end{aligned} \tag{4.33}$$

where $\nabla(\varphi, f, \alpha, \beta; \lambda)$ is the determinant of the boundary conditions matrix, φ is the internal wedge angle, f is the coefficient of friction and α, β are the Dundurs parameters which describe the elastic mismatch between the wedge and half-plane.

Bogy (1971) suggested that, if λ is a zero of $\nabla(\varphi, f, \alpha, \beta; \lambda)$ in $0 < \mathrm{Re}(\lambda) < 1$ that has the smallest real part, the orders of the singularity in the stresses as $r \to 0$ are

$$\begin{aligned}\sigma_{ij} &= 0\left(r^{\lambda-1}\right) \quad \text{if } \lambda \text{ is real} \\ &= 0\left(r^{\zeta-1}\cos(\eta\log r)\right) \text{ or } \left(r^{\zeta-1}\sin(\eta\log r)\right) \quad \text{if } \lambda = \zeta + i\eta \text{ is complex} \\ &= 0\left(\log r\right) \quad \text{if no zero of } \nabla(\lambda) \text{ occurs in } 0 < \mathrm{Re}(\lambda) < 1 \text{ but } \partial\nabla(\lambda)/\partial\lambda = 0 \text{ at } \lambda = 1 \\ &= 0(1) \quad \text{if no zero of } \nabla(\lambda) \text{ occurs in } 0 < \mathrm{Re}(\lambda) < 1 \text{ and } \partial\nabla(\lambda)/\partial\lambda \neq 0 \text{ at } \lambda = 1\,.\end{aligned} \tag{4.34}$$

For elastically similar contacts, the Dundurs parameters are equal to zero and therefore equation (4.33) will be simplified to

$$\nabla(\varphi, f, 0, 0; \lambda) = \cos\lambda\pi\left(\sin^2\lambda\varphi - \lambda^2\sin^2\varphi\right) + 0.5\sin\lambda\pi(\sin 2\lambda\varphi + \lambda\sin 2\varphi)$$
$$+ f\sin\lambda\pi(\lambda(1+\lambda)\sin^2\varphi) = 0. \qquad (4.35)$$

This equation will be used extensively in chapters 6, 7 and 8 where elastically similar contacts are investigated in detail.

4.3.1 Example problems

The problem of a square punch sliding on a half-plane is discussed in detail in chapter 6. It was found that, from the eigenvalue plot for a square punch ($\varphi = \pi/2$), there are three distinct regions (see Figure 6.2). In this section, the asymptotic stress components near the corner of the contact within the half-plane for three examples cases, f = 0.2 (region I), f = 0.35 (region II) and f = 0.8 (region III), using the technique described in sections 4.1 and 4.3, will be summarised. These results are used for the full-field asymptotic stress plots in sections 6.4.1 and 6.4.2.

f = 0.2 (trailing edge)

$$\sigma_{rr}(r,\theta) = \frac{-K_s}{r^{0.1055}}\begin{pmatrix} 0.441\cos(0.106\theta) - 0.603\cos(1.894\theta) \\ +3.269\sin(0.106\theta) - 0.036\sin(1.894\theta) \end{pmatrix}, \qquad (4.36a)$$

$$\sigma_{\theta\theta}(r,\theta) = \frac{-K_s}{r^{0.1055}}\begin{pmatrix} 0.397\cos(0.106\theta) + 0.603\cos(1.894\theta) \\ +2.941\sin(0.106\theta) + 0.036\sin(1.894\theta) \end{pmatrix}, \qquad (4.36b)$$

$$\sigma_{r\theta}(r,\theta) = \frac{-K_s}{r^{0.1055}}\begin{pmatrix} -0.164\cos(0.106\theta) - 0.036\cos(1.894\theta) \\ +0.022\sin(0.106\theta) + 0.603\sin(1.894\theta) \end{pmatrix}. \qquad (4.36c)$$

***f* = 0.35 (trailing edge)**

$$\sigma_{rr}(r,\theta) = -K_{b1} r^{0.042} \begin{pmatrix} 3.562\cos(0.042\theta) + 2.715\cos(2.042\theta) \\ +\,7.037\sin(0.042\theta) - 0.199\sin(2.042\theta) \end{pmatrix} + \\ - K_{b2} r^{0.3048} \begin{pmatrix} 1.056\cos(0.305\theta) + 0.436\cos(2.305\theta) \\ +\,0.3\sin(0.305\theta) - 0.296\sin(2.305\theta) \end{pmatrix}, \tag{4.37a}$$

$$\sigma_{\theta\theta}(r,\theta) = -K_{b1} r^{0.042} \begin{pmatrix} 3.715\cos(0.042\theta) - 2.715\cos(2.042\theta) \\ +\,7.339\sin(0.042\theta) + 0.199\sin(2.042\theta) \end{pmatrix} + \\ - K_{b2} r^{0.3048} \begin{pmatrix} 1.436\cos(0.305\theta) - 0.436\cos(2.305\theta) \\ +\,0.407\sin(0.305\theta) + 0.296\sin(2.305\theta) \end{pmatrix}, \tag{4.37b}$$

$$\sigma_{r\theta}(r,\theta) = -K_{b1} r^{0.042} \begin{pmatrix} -0.151\cos(0.042\theta) - 0.199\cos(2.042\theta) \\ +\,0.076\sin(0.042\theta) - 2.715\sin(2.042\theta) \end{pmatrix} + \\ - K_{b2} r^{0.3048} \begin{pmatrix} -0.054\cos(0.305\theta) - 0.296\cos(2.305\theta) \\ +\,0.19\sin(0.305\theta) - 0.436\sin(2.305\theta) \end{pmatrix}. \tag{4.37c}$$

***f* = 0.8 (trailing edge)**

$$\sigma_{jk}(r,\theta) = 2H\hat{r}^{0.161} \left| f_{jk}(\theta) \right| \cos\left(0.403\ln\hat{r} + \phi_{jk}(\theta)\right), \tag{4.38}$$

where

$$f_{rr}(\theta) = (4.131 - 3.382i)\cos[(0.161 + 0.403i)\theta] + (2.033 - 2.506i)\cos[(2.161 + 0.403i)\theta] \\ - (2.59 + 4.005i)\sin[(0.161 + 0.403i)\theta] - (2.347 + 1.339i)\sin[(2.161 + 0.403i)\theta]$$

$$f_{\theta\theta}(\theta) = (5.983 - 1.758i)\cos[(0.161 + 0.403i)\theta] - (2.033 - 2.506i)\cos[(2.161 + 0.403i)\theta] \\ - (0.964 + 5.486i)\sin[(0.161 + 0.403i)\theta] + (2.347 + 1.339i)\sin[(2.161 + 0.403i)\theta]$$

$$f_{r\theta}(\theta) = (-0.813 + 0.741i)\cos[(0.161 + 0.403i)\theta] - (2.347 + 1.339i)\cos[(2.161 + 0.403i)\theta] \\ + (0.926 + 0.812i)\sin[(0.161 + 0.403i)\theta] - (2.033 - 2.506i)\sin[(2.161 + 0.403i)\theta] \tag{4.39}$$

$\phi_{jk}(\theta)$ is the argument of $f_{jk}(\theta)$, and

$\hat{r} = r / a_o$ (a_o is an arbitrary length scale).

Collocation of these results to a finite problem is described in sections 6.2.3 and 6.4.2.

Chapter 5

An edge dislocation in a semi-infinite elastic wedge

5.1 Introduction

The main object of this chapter is to describe a technique for the deduction of the complete state of stress induced by an edge dislocation present in a semi-infinite wedge of arbitrary internal angle, and to display the results, for the specific cases of wedges with internal angles of $4\pi/3$ and $5\pi/3$ radians, in an efficient form suitable for inclusion in other calculations. The motivation for this is not to study crystalline defects, but to use the dislocations as strain nuclei for modelling slip and separation at the edge of a complete contact (see section 5.5), and for the representation of a crack in the neighbourhood of a semi-infinite (or, indeed, finite) notch, particularly for bonded components. Churchman *et al.* (2006) have recently published the results for a dislocation in a three quarter plane, which is clearly a special case of the problem presently under consideration, but there are several additional features in the present calculation. These extend beyond the most obvious aspects of transforming the state of stress in order to ensure that the traction components of stress vanish on the free-surfaces, to obtaining better convergence near the notch root, by careful application of the Williams asymptote (1952) to the solution itself.

The basic strategy to be followed follows the same pattern as before (Churchman *et al.*, 2006). The starting point is the solution for an edge dislocation in an infinite plane. This is exact and available in closed form (Hills *et al.*, 1996), and correctly describes the state of stress adjacent to the dislocation itself, i.e. at observation points which are close to the 'object' dislocation but remote from the free boundaries of the wedge. To model the boundaries arrays of dislocations are deployed along both free edges of the wedge,

Figure 5.1. These have their Burgers vectors arranged in the *x* and *y* directions along the free surfaces, and thus enable both components of traction to be annulled. In practice continuous arrays of dislocations are employed, whose densities are represented by families of Chebyshev polynomials; these are used within an integral equation formulation, and enable a corrective solution for the presence of the semi-infinite free boundaries to be represented effectively.

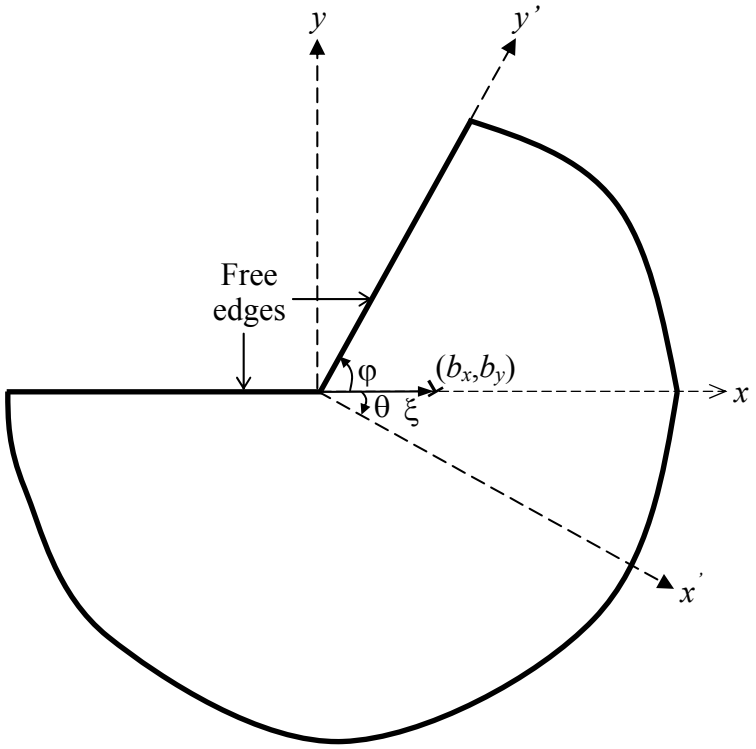

Figure 5.1 : Geometry of the problem solved – an edge dislocation (at $x = \xi$), with components b_x and by, along the projection of the horizontal free-surface

5.2 Formulation

The state of stress at a general point, $\sigma_{ij}(x,y)$ in an infinite plane induced by an edge dislocation, having Burgers vector components b_x, b_y located at (x_d, y_d) is given by

$$\sigma_{ij}(x,y,x_d,y_d) = \frac{2\mu}{\pi(\kappa+1)}\left\{b_x(x_d,y_d)G_{xij}(x,y,x_d,y_d) + b_y(x_d,y_d)G_{yij}(x,y,x_d,y_d)\right\}, \quad (5.1)$$

where

$$G_{xxx}(x,y,x_d,y_d) = -\frac{(y-y_d)}{r^4}\left[3(x-x_d)^2 + (y-y_d)^2\right], \tag{5.2a}$$

$$G_{yxx}(x,y,x_d,y_d) = \frac{(x-x_d)}{r^4}\left[(x-x_d)^2 - (y-y_d)^2\right], \tag{5.2b}$$

$$G_{xyy}(x,y,x_d,y_d) = \frac{(y-y_d)}{r^4}\left[(x-x_d)^2 - (y-y_d)^2\right], \tag{5.2c}$$

$$G_{yyy}(x,y,x_d,y_d) = \frac{(x-x_d)}{r^4}\left[(x-x_d)^2 + 3(y-y_d)^2\right], \tag{5.2d}$$

$$G_{xxy}(x,y,x_d,y_d) = \frac{(x-x_d)}{r^4}\left[(x-x_d)^2 - (y-y_d)^2\right], \tag{5.2e}$$

$$G_{yxy}(x,y,x_d,y_d) = \frac{(y-y_d)}{r^4}\left[(x-x_d)^2 - (y-y_d)^2\right], \tag{5.2f}$$

$r = \sqrt{(x-x_d)^2 + (y-y_d)^2}$, μ is the modulus of rigidity and κ is Kolosov's constant. We require to clear the half line $-\infty < x < 0$, $y = 0$ of tractions, in order to establish one free surface of the wedge, and this is expressed by the following two pairs of integral equations

$$\begin{aligned}
&\frac{2\mu}{\pi(\kappa+1)}\int_{-\infty}^{0}\left\{B_x(x_d)\,G_{xmy}(x,0,x_d,0) + B_y(x_d)\,G_{ymy}(x,0,x_d,0)\right\}dx_d + \\
&\frac{2\mu}{\pi(\kappa+1)}\int_{0}^{\infty}\left\{\begin{matrix} B_x(y'_d)\,G_{xmy}(x,0,y'_d\cos\varphi, y'_d\sin\varphi) \\ + B_y(y'_d)\,G_{ymy}(x,0,y'_d\cos\varphi, y'_d\sin\varphi)\end{matrix}\right\}dy'_d \\
&= -\frac{2\mu}{\pi(\kappa+1)}b_l\left(G_{lmy}(x,0,\xi,0)\right)
\end{aligned} \tag{5.3}$$

for $l = x, y$, i.e. the two kinds of object dislocation, and where

$m = y$ corresponds to $\sigma_{yy} = 0$ for $-\infty < x < 0$,

$m = x$ corresponds to $\sigma_{xy} = 0$ for $-\infty < x < 0$, and

$B_i(\chi_d)$ is the dislocation density (= $db_i/d\chi_d$).

Similarly, the other wedge face $0 < y' < \infty$, $x' = 0$ is cleared of tractions by the following two pairs of integral equations, which are written out here in full, because they explicitly include the transformation equations to enable the traction components to be evaluated in the rotated (x', y') coordinate set

$$\frac{2\mu}{\pi(\kappa+1)}\int_{-\infty}^{0} B_x(x_d)\begin{Bmatrix} G_{xyy}(y'\cos\varphi, y'\sin\varphi, x_d, 0)\sin^2\theta \\ +G_{xxx}(y'\cos\varphi, y'\sin\varphi, x_d, 0)\cos^2\theta \\ +G_{xxy}(y'\cos\varphi, y'\sin\varphi, x_d, 0)2\sin\theta\cos\theta \end{Bmatrix} dx_d +$$

$$\frac{2\mu}{\pi(\kappa+1)}\int_{-\infty}^{0} B_y(x_d)\begin{Bmatrix} G_{yyy}(y'\cos\varphi, y'\sin\varphi, x_d, 0)\sin^2\theta \\ +G_{yxx}(y'\cos\varphi, y'\sin\varphi, x_d, 0)\cos^2\theta \\ +G_{yxy}(y'\cos\varphi, y'\sin\varphi, x_d, 0)2\sin\theta\cos\theta \end{Bmatrix} dx_d +$$

$$\frac{2\mu}{\pi(\kappa+1)}\int_{0}^{\infty} B_x(y'_d)\begin{Bmatrix} G_{xyy}(y'\cos\varphi, y'\sin\varphi, y'_d\cos\varphi, y'_d\sin\varphi)\sin^2\theta \\ +G_{xxx}(y'\cos\varphi, y'\sin\varphi, y'_d\cos\varphi, y'_d\sin\varphi)\cos^2\theta \\ +G_{xxy}(y'\cos\varphi, y'\sin\varphi, y'_d\cos\varphi, y'_d\sin\varphi)2\sin\theta\cos\theta \end{Bmatrix} dy'_d +$$

$$\frac{2\mu}{\pi(\kappa+1)}\int_{0}^{\infty} B_y(y'_d)\begin{Bmatrix} G_{yyy}(y'\cos\varphi, y'\sin\varphi, y'_d\cos\varphi, y'_d\sin\varphi)\sin^2\theta \\ +G_{yxx}(y'\cos\varphi, y'\sin\varphi, y'_d\cos\varphi, y'_d\sin\varphi)\cos^2\theta \\ +G_{yxy}(y'\cos\varphi, y'\sin\varphi, y'_d\cos\varphi, y'_d\sin\varphi)2\sin\theta\cos\theta \end{Bmatrix} dy'_d +$$

$$= -\frac{2\mu}{\pi(\kappa+1)} b_l \begin{Bmatrix} G_{lyy}(y'\cos\varphi, y'\sin\varphi, \xi, 0)\sin^2\theta \\ +G_{lxx}(y'\cos\varphi, y'\sin\varphi, \xi, 0)\cos^2\theta \\ G_{lxy}(y'\cos\varphi, y'\sin\varphi, \xi, 0)2\sin\theta\cos\theta \end{Bmatrix} \qquad \text{for } l = x, y \tag{5.4}$$

which ensures that

$$\sigma_{x'x'} = 0 \quad \text{for} \quad 0 < y' < \infty \tag{5.5}$$

and

$$\frac{2\mu}{\pi(\kappa+1)}\int_{-\infty}^{0} B_x(x_d)\begin{Bmatrix} G_{xyy}(y'\cos\varphi, y'\sin\varphi, x_d, 0)\sin\theta\cos\theta \\ -G_{xxx}(y'\cos\varphi, y'\sin\varphi, x_d, 0)\sin\theta\cos\theta \\ +G_{xxy}(y'\cos\varphi, y'\sin\varphi, x_d, 0)(\cos^2\theta-\sin^2\theta)\end{Bmatrix} dx_d +$$

$$\frac{2\mu}{\pi(\kappa+1)}\int_{-\infty}^{0} B_y(x_d)\begin{Bmatrix} G_{yyy}(y'\cos\varphi, y'\sin\varphi, x_d, 0)\sin\theta\cos\theta \\ -G_{yxx}(y'\cos\varphi, y'\sin\varphi, x_d, 0)\sin\theta\cos\theta \\ +G_{yxy}(y'\cos\varphi, y'\sin\varphi, x_d, 0)(\cos^2\theta-\sin^2\theta)\end{Bmatrix} dx_d +$$

$$\frac{2\mu}{\pi(\kappa+1)}\int_{0}^{\infty} B_x(y'_d)\begin{Bmatrix} G_{xyy}(y'\cos\varphi, y'\sin\varphi, y'_d\cos\varphi, y'_d\sin\varphi)\sin\theta\cos\theta \\ -G_{xxx}(y'\cos\varphi, y'\sin\varphi, y'_d\cos\varphi, y'_d\sin\varphi)\sin\theta\cos\theta \\ +G_{xxy}(y'\cos\varphi, y'\sin\varphi, y'_d\cos\varphi, y'_d\sin\varphi)(\cos^2\theta-\sin^2\theta)\end{Bmatrix} dy'_d +$$

$$\frac{2\mu}{\pi(\kappa+1)}\int_{0}^{\infty} B_y(y'_d)\begin{Bmatrix} G_{yyy}(y'\cos\varphi, y'\sin\varphi, y'_d\cos\varphi, y'_d\sin\varphi)\sin\theta\cos\theta \\ -G_{yxx}(y'\cos\varphi, y'\sin\varphi, y'_d\cos\varphi, y'_d\sin\varphi)\sin\theta\cos\theta \\ +G_{yxy}(y'\cos\varphi, y'\sin\varphi, y'_d\cos\varphi, y'_d\sin\varphi)(\cos^2\theta-\sin^2\theta)\end{Bmatrix} dy'_d +$$

$$= -\frac{2\mu}{\pi(\kappa+1)} b_l \begin{Bmatrix} G_{lyy}(y'\cos\varphi, y'\sin\varphi, \xi, 0)\sin\theta\cos\theta \\ -G_{lxx}(y'\cos\varphi, y'\sin\varphi, \xi, 0)\sin\theta\cos\theta \\ G_{lxy}(y'\cos\varphi, y'\sin\varphi, \xi, 0)(\cos^2\theta-\sin^2\theta)\end{Bmatrix} \qquad \text{for } l = x, y \tag{5.6}$$

which imposes the condition

$$\sigma_{x'y'} = 0 \quad \text{for} \quad 0 < y' < \infty\,. \tag{5.7}$$

5.3 Solution

A small refinement, here, over the original paper by Churchman *et al*. (2006) is that we shall require that the dislocations generating the free edges be distributed over semi-infinite intervals (*viz.* $-\infty < x_d < 0$, $\infty > y'_d > 0$, rather than simply truncating the range of imposition). In order to re-express the conditions over finite intervals ($-1 < u_x,\ u_{y'},\ v_x,\ v_{y'} < 1$) the following transformations were employed

$$u_x = 2\exp\left(\frac{x_d}{A}\right) - 1\,, \tag{5.8a}$$

$$u_{y'} = 2\exp\left(-\frac{y'_d}{A}\right) - 1\,, \tag{5.8b}$$

$$v_x = 2\exp\left(\frac{x}{A}\right) - 1, \tag{5.8c}$$

$$v_{y'} = 2\exp\left(-\frac{y'}{A}\right) - 1, \tag{5.8d}$$

where u_x and $u_{y'}$ are the normalised integration points, v_x and $v_{y'}$ are the normalised collocation points and A is a constant which was set as 50 for this problem. As we expect the dislocation densities needed to be singular at the origin but to decay remotely we can represent them as the products of a fundamental solution $w(u_j)$ and unknown but well-behaved functions $\phi(u_j)$, i.e.

$$B_k(u_j) = w(u_j)\phi(u_j) \quad \text{for} \quad j = x, y' \quad \text{and} \quad k = x, y \tag{5.9a}$$

where

$$w(u_j) = \sqrt{\frac{1+u_j}{1-u_j}} \quad \text{for} \quad j = x, y'. \tag{5.9b}$$

The integral equations (eqs. (5.3), (5.4) and (5.6)) can be reduced to families of linear algebraic equations. As an example, equation (5.3) is now written as

$$\int_{-1}^{1} \left\{ \begin{array}{l} \hat{B}_x(u_x) G_{xmy}\left(-A\ln\left(\frac{2}{1+v_x}\right), 0, -A\ln\left(\frac{2}{1+u_x}\right), 0\right) \\ + \hat{B}_y(u_x) G_{ymy}\left(-A\ln\left(\frac{2}{1+v_x}\right), 0, -A\ln\left(\frac{2}{1+u_x}\right), 0\right) \end{array} \right\} \frac{A}{1+u_x} du_x +$$

$$\int_{-1}^{1} \left\{ \begin{array}{l} \hat{B}_x(u_{y'}) G_{xmy}\left(-A\ln\left(\frac{2}{1+v_x}\right), 0, A\ln\left(\frac{2}{1+u_{y'}}\right)\cos\varphi, A\ln\left(\frac{2}{1+u_{y'}}\right)\sin\varphi\right) \\ + \hat{B}_y(u_{y'}) G_{xmy}\left(-A\ln\left(\frac{2}{1+v_x}\right), 0, A\ln\left(\frac{2}{1+u_{y'}}\right)\cos\varphi, A\ln\left(\frac{2}{1+u_{y'}}\right)\sin\varphi\right) \end{array} \right\} \frac{A}{1+u_{y'}} du_{y'}$$

$$= -G_{lmy}\left(-A\ln\left(\frac{2}{1+v_x}\right), 0, \xi, 0\right) \quad \text{for} \quad m = x, y \quad \text{and} \quad l = x, y \tag{5.10}$$

where

$$\hat{B}_k(u_j) = \frac{B_k(u_j)}{b_l} \quad \text{for } j = x, y';\ k = x, y;\ l = x, y \tag{5.11}$$

or, in a discretized form the integrals become

$$\left\{ \begin{array}{l} \displaystyle\sum_{i=1}^{n} G_{xmy}\left(-A\ln\left(\frac{2}{1+v_{xk}}\right), 0, -A\ln\left(\frac{2}{1+u_{xi}}\right), 0 \right) \hat{W}(u_{xi})\phi_x(u_{xi}) \\ \displaystyle + \sum_{i=1}^{n} G_{ymy}\left(-A\ln\left(\frac{2}{1+v_{xk}}\right), 0, -A\ln\left(\frac{2}{1+u_{xi}}\right), 0 \right) \hat{W}(u_{xi})\phi_y(u_{xi}) \end{array} \right\} +$$

$$\left\{ \begin{array}{l} \displaystyle\sum_{i=1}^{n} G_{xmy}\left(-A\ln\left(\frac{2}{1+v_{xk}}\right), 0, A\ln\left(\frac{2}{1+u_{y'i}}\right)\cos\varphi, A\ln\left(\frac{2}{1+u_{y'i}}\right)\sin\varphi \right) \hat{W}(u_{y'i})\phi_x(u_{y'i}) \\ \displaystyle + \sum_{i=1}^{n} G_{ymy}\left(-A\ln\left(\frac{2}{1+v_{xk}}\right), 0, A\ln\left(\frac{2}{1+u_{y'i}}\right)\cos\varphi, A\ln\left(\frac{2}{1+u_{y'i}}\right)\sin\varphi \right) \hat{W}(u_{y'i})\phi_y(u_{y'i}) \end{array} \right\}$$

$$= -G_{lmy}\left(-A\ln\left(\frac{2}{1+v_{xk}}\right), 0, \xi, 0 \right) \quad \text{for } m = x, y \text{ and } l = x, y \tag{5.12}$$

where

$$\hat{W}(u_{ji}) = \frac{2\pi A}{2n+1} \quad \text{for } j = x, y' \tag{5.13a}$$

$$u_{xi} = u_{y'i} = \cos\left(\pi \frac{2i-1}{2n+1} \right) \quad \text{for } i = 1, \ldots, n \tag{5.13b}$$

$$v_{xk} = v_{y'k} = \cos\left(\pi \frac{2k}{2n+1} \right) \quad \text{for } k = 1, \ldots, n \tag{5.13c}$$

These integrals are solved to find the dislocation densities. It was found that the numerical convergence of the quadrature is extremely rapid and a value of n = 500 is an appropriate choice.

5.4 Results

When once the dislocation densities have been found it is possible to find the complete state of stress within the wedge. It would be perfectly possible to evaluate the state of stress at any point, but we shall concentrate on the projection line from the free surface, ($y = 0$, $x > 0$) for the reasons explained earlier. The stress along the projection line due to both the dislocation at (ξ,0) and the presence of the free boundaries, can be expressed as

$$\tilde{\sigma}_{ij}(x,0) = \frac{2\mu}{\pi(\kappa+1)}\left\{b_x\left(G_{xij}(x,0,\xi,0)+F_{xij}(x,\xi)\right)+b_y\left(G_{yij}(x,0,\xi,0)+F_{yij}(x,\xi)\right)\right\}, \qquad (5.14)$$

where the influence functions for the object dislocation at (ξ,0) along the projection line simplify to

$$G_{xyy}(x,0,\xi,0) = G_{yxy}(x,0,\xi,0) = 0 \qquad (5.15a)$$

$$G_{xxy}(x,0,\xi,0) = G_{yyy}(x,0,\xi,0) = \frac{1}{x-\xi}. \qquad (5.15b)$$

The modification state of stress found due to the presence of the free boundaries, F_{kij}, is displayed in Figure 5.2. In order to emphasize the universal nature of the solution found, these functions are plotted in coordinates normalised with respect to the position of the object dislocation (x/ξ). It was found that the rate of convergence of the various components of stress, particularly as the origin (wedge corner) was approached varied enormously, and great care was needed to attain a reliable set of results. It is known, from the classical Williams analysis, that the state of stress as the wedge corner is approached must vary as $\sigma_{ij}(r) \sim r^{\lambda_I - 1}$, where the eigenvalue, λ_I, corresponds to a symmetrical solution of the biharmonic equation, and is given by

$$\lambda_I \sin[\pi+\varphi] + \sin[\lambda_I(\pi+\varphi)] = 0. \qquad (5.16)$$

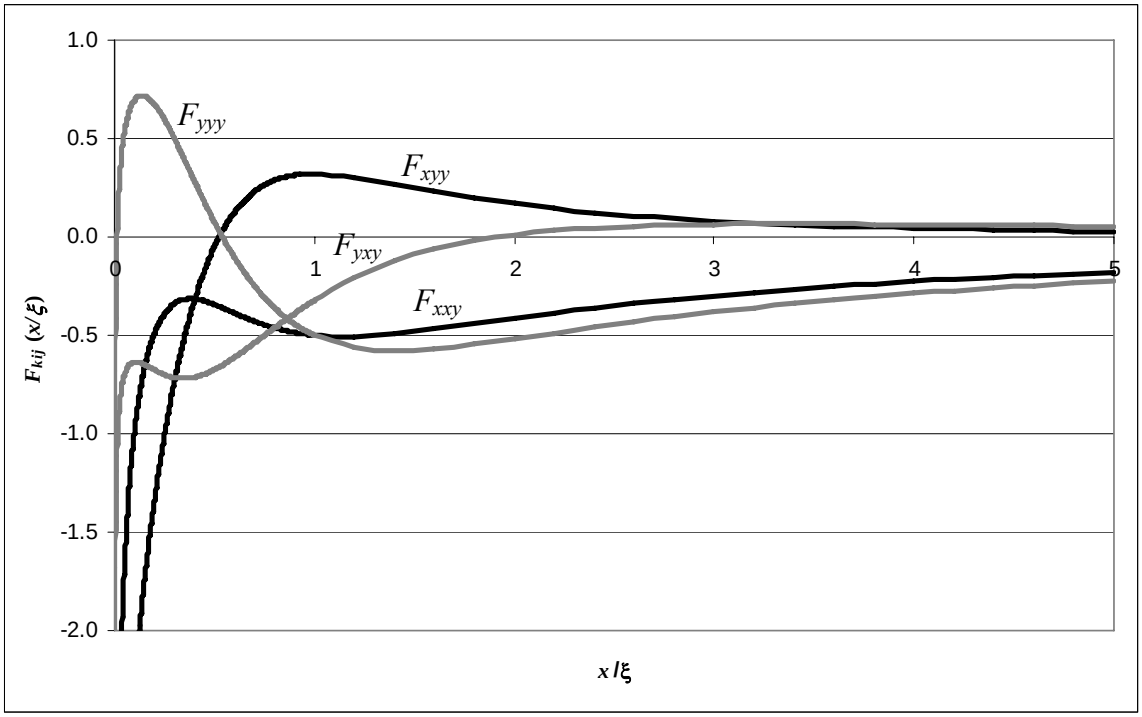

(a)

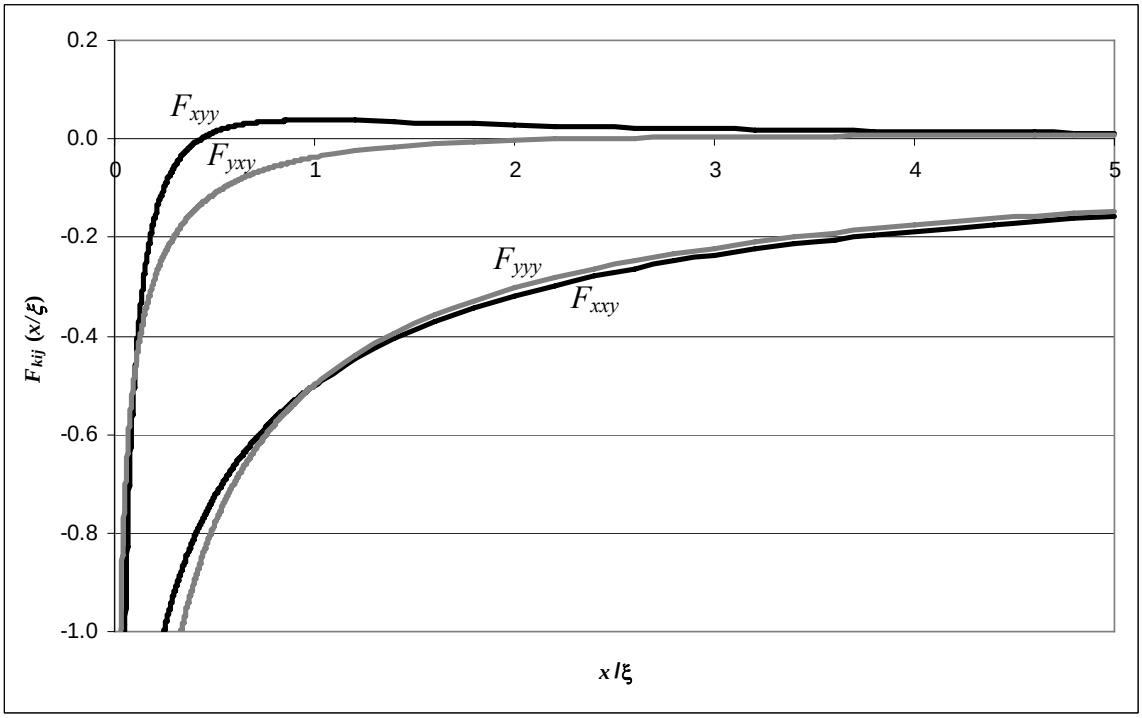

(b)

Figure 5.2 : Linear plot of the influence functions F_{xxy}, F_{xyy}, F_{yxy} and F_{yyy} against normalized distance, x/ξ for an edge dislocation in (a) a 240^0 wedge (b) a 300^0 wedge

For the two wedge geometries studied here the eigenvalues are given by $\varphi = \pi/3$; $\lambda_I = 0.6157$ (for the 240^0 wedge) and $\varphi = 2\pi/3$; $\lambda_I = 0.5122$ (for the 300^0 wedge). By plotting out the stress variation on a logarithmic scale it was possible to observe the radial extent for which this dependence was followed. It should be noted that the absolute values of F_{kij} have been considered to facilitate the use of the logarithm. It was found that, for both wedge angles under consideration here, all the stress components followed the expected form as shown in Figures 5.3 and 5.4 for the 240^0 wedge and the 300^0 wedge, respectively. However, it should be noted that, for some stress components, the state of stress was dictated by the asymptotic form over a much smaller radial distance than the others. As expected, the state of stress in the neighbourhood of the origin is dominated by the geometric singularity (given by the Williams solution), and then at very large distances from the wedge corner (well beyond the object dislocation), the state of stress is found to decay as $1/\hat{x}^t$. With these observations in mind, in order to provide a useful representation of the state of stress for subsequent computation, the following function was collocated with the numerical values obtained

$$F_{kij}(\hat{x}) = \frac{1}{\hat{x}^{1-\lambda_I} + \hat{x}^t} \sum_{m=0}^{m=n} C_m \left(\frac{\hat{x}}{1+\hat{x}} \right)^m . \tag{5.17}$$

For $\hat{x} << 1$, equation (5.17) reduces to

$$F_{kij}(\hat{x}) = \frac{C_0}{\hat{x}^{1-\lambda_I}} , \tag{5.18a}$$

and for $\hat{x} >> 1$, equation (5.17) reduces to

$$F_{kij}(\hat{x}) = \frac{1}{\hat{x}^t} \sum_{m=0}^{m=n} C_m . \tag{5.18b}$$

(a)

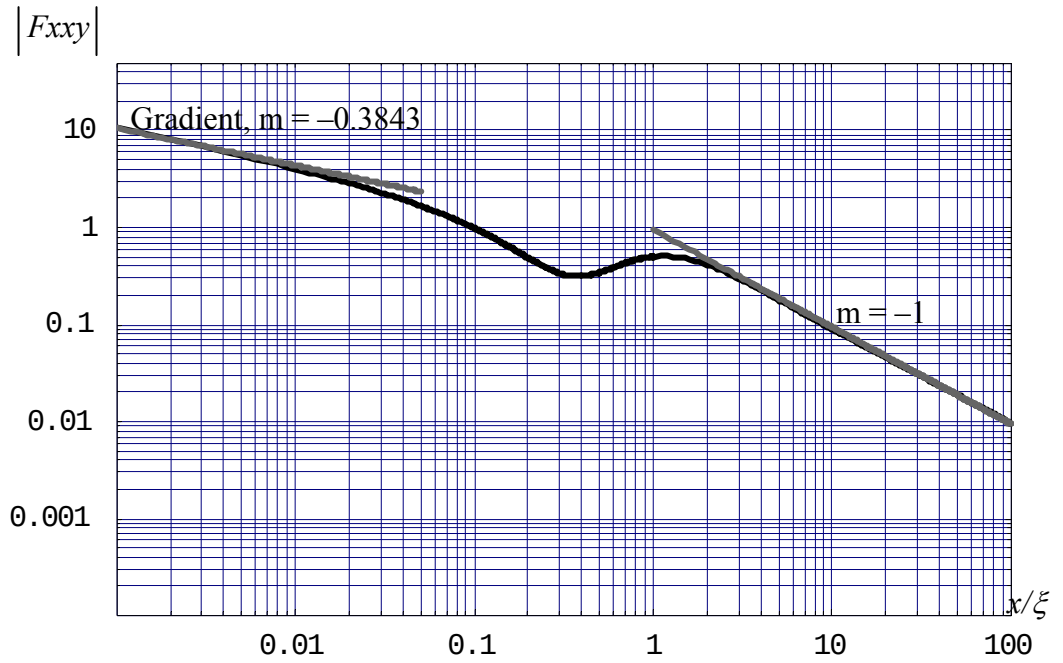
|Fxxy|
Gradient, m = –0.3843
m = –1
10
1
0.1
0.01
0.001
0.01
0.1
1
10
100
x/ξ

(b)

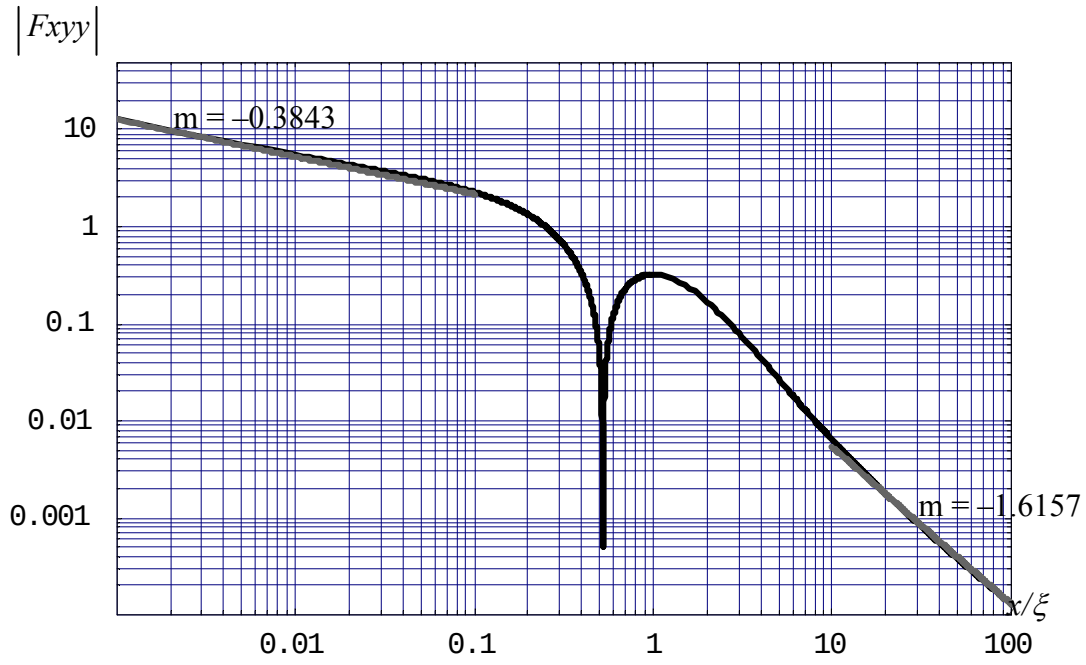
|Fxyy|
m = –0.3843
m = –1.6157
10
1
0.1
0.01
0.001
0.01
0.1
1
10
100
x/ξ

(c)

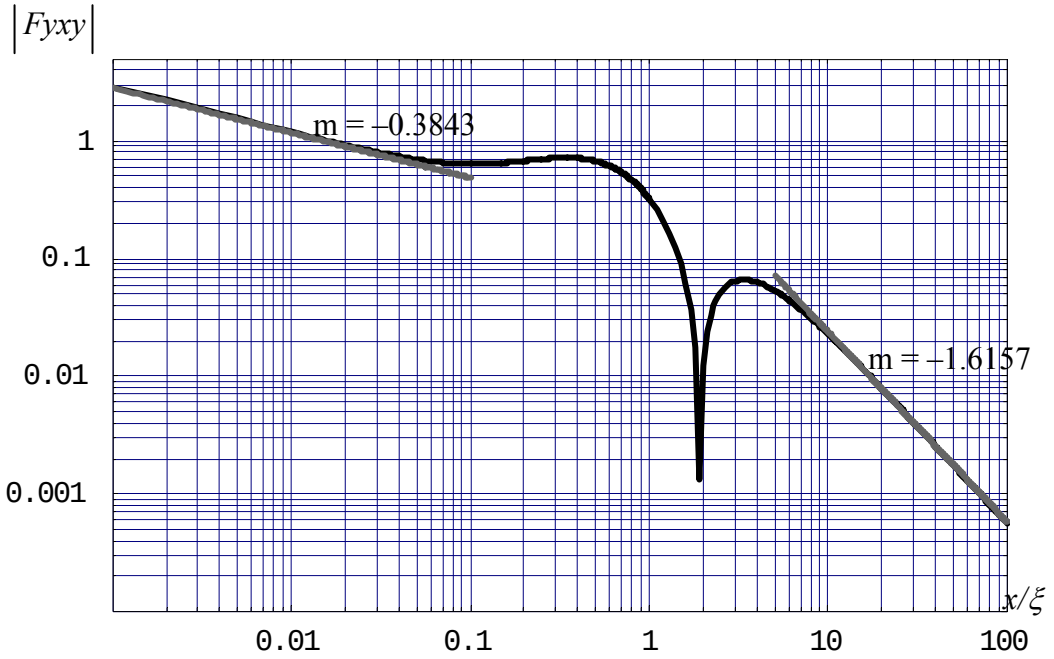

(d)

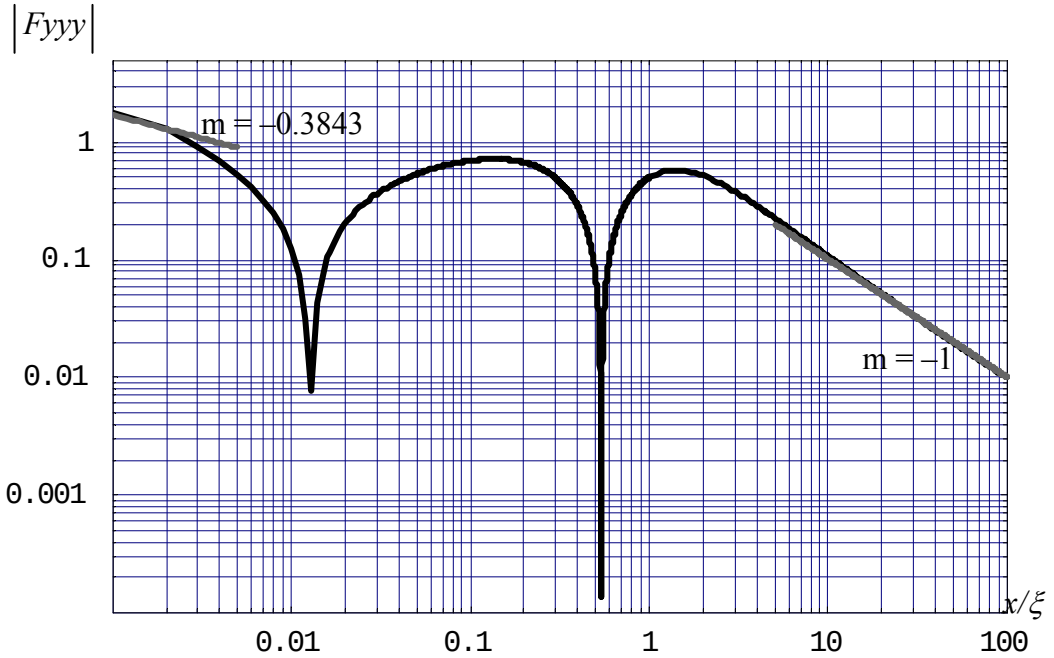

Figure 5.3 : Log-Log plots of the magnitudes of (a) F_{xxy} (b) F_{xyy} (c) F_{yxy} (d) F_{yyy} for an edge dislocation in a 240^0 wedge showing the asymptotes (grey lines) derived from the analytical approximation

(a)

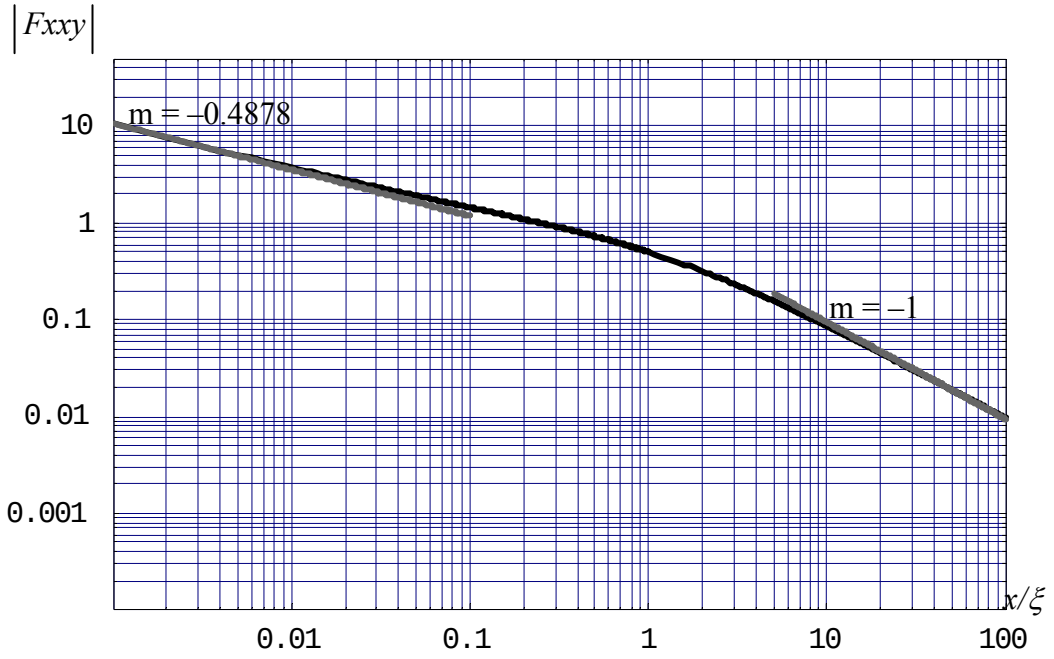
|Fxxy|
m = –0.4878
m = –1
10
1
0.1
0.01
0.001
x/ξ
0.01
0.1
1
10
100

(b)

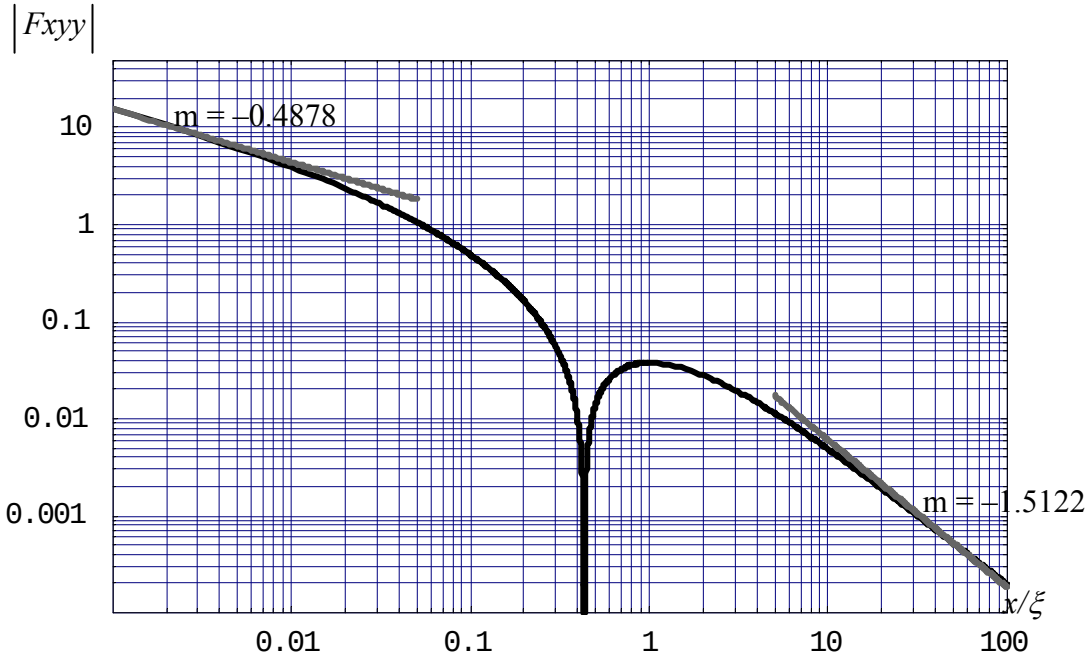
|Fxyy|
m = –0.4878
m = –1.5122
10
1
0.1
0.01
0.001
x/ξ
0.01
0.1
1
10
100

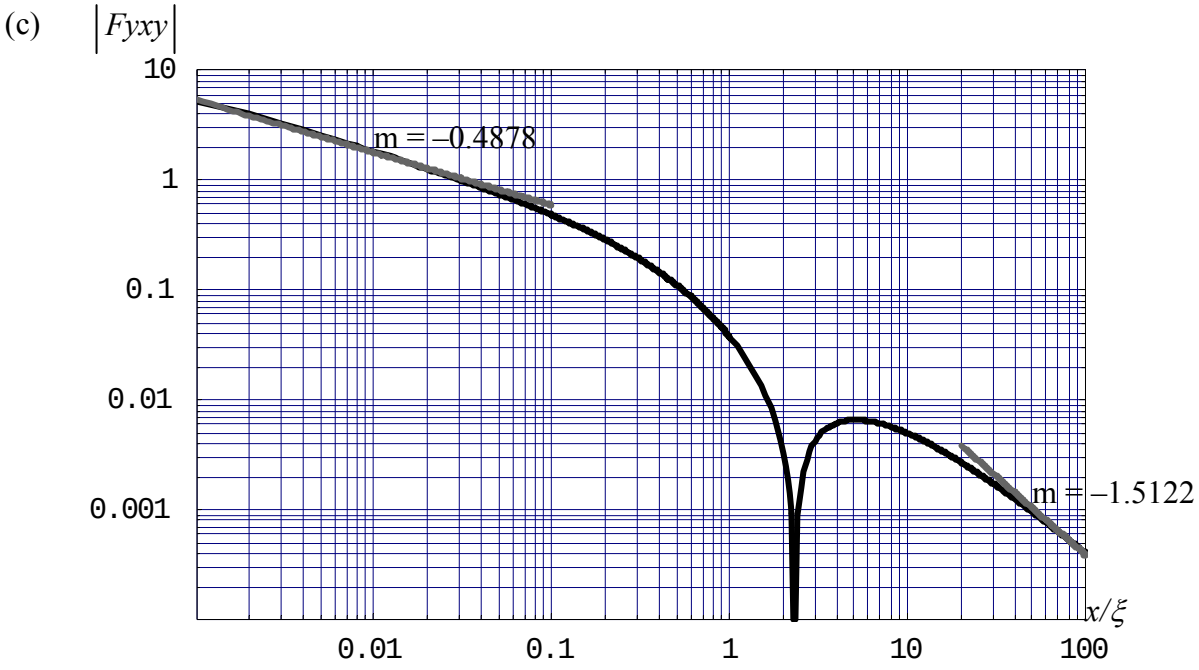

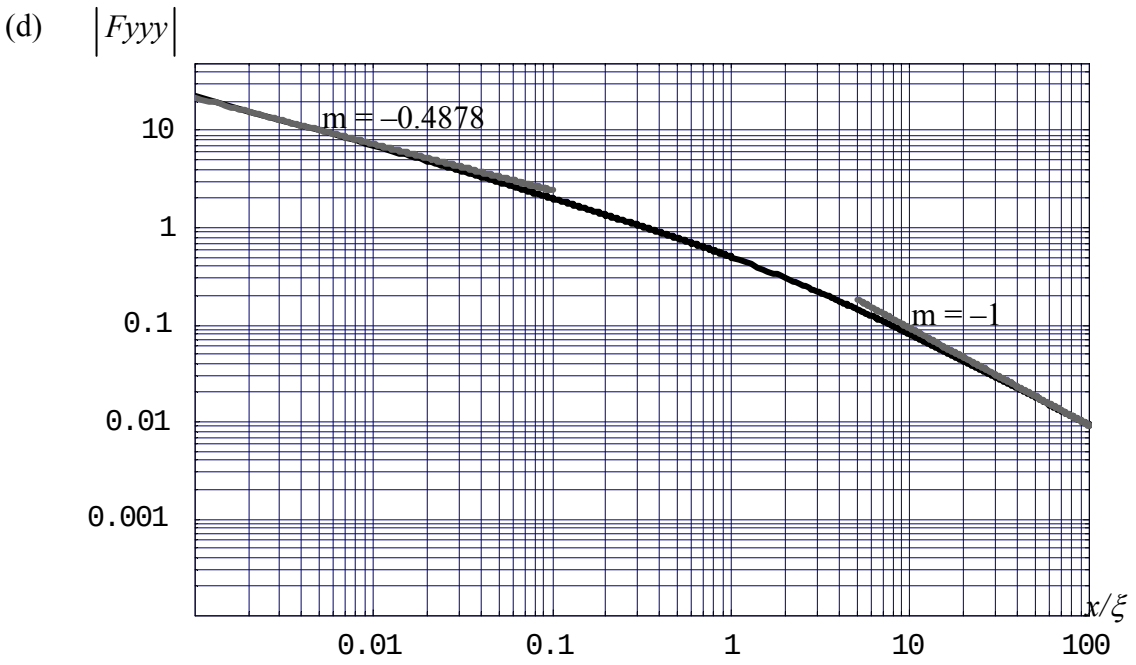

Figure 5.4 : Log-Log plots of the magnitudes of (a) F_{xxy} (b) F_{xyy} (c) F_{yxy} (d) F_{yyy} for an edge dislocation in a 300^0 wedge showing the asymptotes (grey lines) derived from the analytical approximation

The value of the far-field asymptote exponent t and the coefficients C_0, ..., C_n are given in Tables 5.1 and 5.2 for the 240^0 wedge and the 300^0 wedge, respectively. The far-field asymptote exponent t for F_{xxy} and F_{yyy} is found to be 1 whilst for F_{xyy} and F_{yxy} is found to be $(1+\lambda_1)$. The influence functions for the 240^0 wedge (Figure 5.2(a)) are slightly more complicated compared to the influence functions for the 300^0 wedge (Figure 5.2(b)), and therefore require 5 terms in equation (5.17) to define them completely, as compared to 4 terms for the 300^0 wedge.

Table 5.1 : Constants in equation (5.17) for 240^0 wedge

F_{kij}	t	C_0	C_1	C_2	C_3	C_4	$\sum_{m=0}^{4} C_m$
F_{xxy}	1	–0.8019	5.84	–22.77	25.19	–8.43	–0.9719
F_{xyy}	1.6157	–0.9253	–3.70	34.58	–54.35	24.63	0.2347
F_{yxy}	1.6157	–0.2030	0.14	–15.74	38.87	–22.14	0.9270
F_{yyy}	1	–0.1360	10.06	–46.66	55.67	–19.95	–1.0160

Table 5.2 : Constants in equation (5.17) for 300^0 wedge

F_{kij}	t	C_0	C_1	C_2	C_3	$\sum_{m=0}^{3} C_m$
F_{xxy}	1	–0.4308	–2.0979	2.4762	–1.0632	–1.1157
F_{xyy}	1.5122	–0.3385	1.7110	–2.2816	1.1184	0.2093
F_{yxy}	1.5122	–0.1964	0.6025	–2.0214	2.0567	0.4414
F_{yyy}	1	–0.8127	–0.2864	–0.5850	0.6832	–1.0009

The collocated form of the solutions agrees very well with the numerical values, and has proved an efficient way to make use of the solution found.

5.5 Applications

5.5.1 Introduction

As mentioned in the main introduction section, the solutions found for the dislocation in a wedge can be used to model slip and separation at the edge of complete contacts. In chapter 6, it will be shown how the solutions found for a 270^0 wedge were used to find the separation extent at the edge of a square punch sliding on an elastically similar half-plane. However, it transpires that for sliding 60^0 punch and 120^0 punch problems, the solutions seem to be of little practical use for finding the separation extent. This is because, for 60^0 punch problem, the separation extent is often quite large and therefore can be found directly from the finite element analysis. For 120^0 punch problem, on the other hand, separation at the edge of the sliding contact occurs only at a friction value greater than 1.28, which is not of practical use.

The slip region size at the edge of contact, subject to normal load and subsequently to increasing shear load, for values of the coefficient of friction close to $g_{r\theta}^{I}$ (equation (4.28a)) is relatively small. Therefore, it is difficult to achieve convergence using the finite element method. Churchman and Hills (2006b) proposed an alternative approach to tackle this kind of problem. In the following sections the technique proposed by them will be briefly described and will be used for an example problem.

5.5.2 Formulation

The problem solved within the context of a semi-infinite asymptote is shown in Figure 5.5. It consists of an elastic wedge of an arbitrary angle (body 2), pressed onto an elastically similar half plane (body 1), and subsequently subject to shear load. The entire contact interface is adhered save for a small slip region adjacent to the contact corner, whose extent c is to be determined. The extent c is found by distributing glide dislocations along the interface within this interval, giving the following expressions for the normal and shear tractions, $N(x)$ and $S(x)$,

$$N(x) = K_I^o x^{\lambda_I - 1} + K_{II}^o x^{\lambda_{II} - 1} + \frac{2\mu}{\pi(\kappa+1)} \int_0^c B_x(\xi) F_{xyy}(x,\xi)\, d\xi \,, \tag{5.19a}$$

$$S(x) = K_I^o g_{r\theta}^I x^{\lambda_I - 1} + K_{II}^o g_{r\theta}^{II} x^{\lambda_{II} - 1} + \frac{2\mu}{\pi(\kappa+1)} \int_0^c B_x(\xi) \left[F_{xxy}(x,\xi) + \frac{1}{x-\xi} \right] d\xi \,, \tag{5.19b}$$

where $B_x(\xi) = db_x/dx$ is the dislocation density.

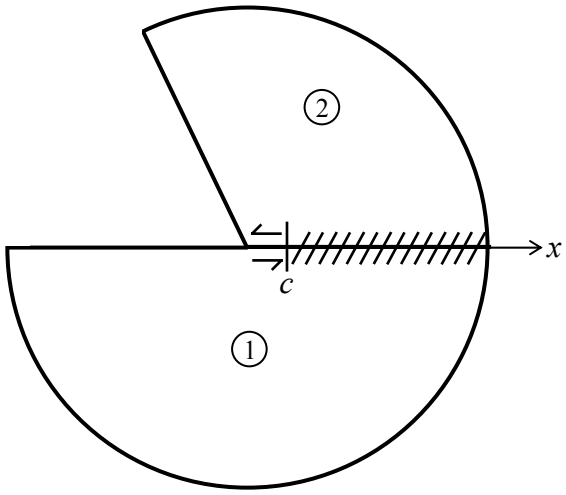

Figure 5.5 : Geometry of the problem solved – slip zone extent at the edge of an arbitrary wedge on a half-plane

If we impose the following friction law, i.e.,

$$\begin{aligned} S(x) &= -fN(x) \qquad 0 \le x \le c \\ &< -fN(x) \qquad x > c, \end{aligned} \tag{5.20}$$

we will arrive at the following Cauchy singular integral equation

$$(f + g_{r\theta}^I)\left(\frac{x}{d_o}\right)^{\lambda_I - 1} + (f + g_{r\theta}^{II})\left(\frac{x}{d_o}\right)^{\lambda_{II} - 1} + \int_0^c \hat{B}_x(\xi) F_T(f,x,\xi)\, d\xi = 0 \quad \text{for } 0 \le x \le c \tag{5.21}$$

where

$$F_T(f,x,\xi) = fF_{xyy}(x,\xi) + F_{xxy}(x,\xi) + \frac{1}{x-\xi} \,, \tag{5.22a}$$

$$\hat{B}_x(\xi) = \frac{2\mu}{\pi(\kappa+1)} \frac{B_x(\xi)}{K_I^o d_o^{\lambda_I - 1}}, \text{ and} \tag{5.22b}$$

$$d_o = \left(\frac{K_I^o}{K_{II}^o} \right)^{\frac{1}{\lambda_{II} - \lambda_I}}. \tag{5.22c}$$

Now, let

$$\hat{x} = \frac{x}{d_o}, \quad \hat{c} = \frac{c}{d_o}, \quad \hat{\xi} = \frac{\xi}{d_o}, \tag{5.23}$$

so that equation (5.21) becomes

$$(f + g_{r\theta}^I)\hat{x}^{\lambda_I - 1} + (f + g_{r\theta}^{II})\hat{x}^{\lambda_{II} - 1} + \int_0^{\hat{c}} \hat{B}_x(\hat{\xi}) F_T(f, \hat{x}, \hat{\xi}) d\hat{\xi} = 0 \quad \text{for } 0 \le \hat{x} \le \hat{c}, \tag{5.24}$$

and carry out a further change of variables by setting:

$$\hat{\xi} = \frac{\hat{c}}{2}(u+1), \text{ and} \tag{5.25a}$$

$$\hat{x} = \frac{\hat{c}}{2}(v+1). \tag{5.25b}$$

Equation (5.24) is now finally written as:

$$\begin{aligned} &\int_{-1}^{1} \hat{B}_x(u) F_T(f, v, u) du = \\ &-(f + g_{r\theta}^I)\left(\frac{\hat{c}}{2}\right)^{\lambda_I - 1} (v+1)^{\lambda_I - 1} - (f + g_{r\theta}^{II})\left(\frac{\hat{c}}{2}\right)^{\lambda_{II} - 1} (v+1)^{\lambda_{II} - 1} \quad \text{for } -1 \le v \le 1 \end{aligned} \tag{5.26}$$

5.5.3 Solution

It is assumed that the transition from slip to stick region is smooth, and therefore the dislocation densities are expected to display bounded behaviour adjacent to the transition point $(u \to +1)$ and singular behaviour near the corner $(u \to -1)$. We may write the unknown dislocation densities as the product of fundamental functions ($w(u)$) and well-behaved smooth functions ($\phi_x(u)$),

$$\hat{B}_x(u) = w(u)\phi_x(u) \tag{5.27a}$$

where

$$w(u) = \sqrt{\frac{1-u}{1+u}}\,. \tag{5.27b}$$

The integral equation (5.26) in discretized form is written as

$$\begin{aligned}&\sum_{i=1}^{n} W(u_i) F_T(f, v_k, u_i) \phi_x(u_i) = \\ &-(f + g^I_{r\theta})\left(\frac{\hat{c}}{2}\right)^{\lambda_I - 1} (v_k + 1)^{\lambda_I - 1} - (f + g^{II}_{r\theta})\left(\frac{\hat{c}}{2}\right)^{\lambda_{II} - 1} (v_k + 1)^{\lambda_{II} - 1} \quad \text{for } k = 0,....,n\end{aligned} \tag{5.28}$$

where

$$W(u_i) = \frac{2\pi(1-u_i)}{2n+1} \tag{5.29a}$$

$$u_i = \cos\left(\pi \frac{2i}{2n+1}\right) \quad \text{for } i = 1, ..., n, \tag{5.29b}$$

$$v_k = \cos\left(\pi \frac{2k-1}{2n+1}\right) \quad \text{for } k = 1, ..., n. \tag{5.29c}$$

The extent of the slip region $\hat{c}$ is determined by checking the results to ensure that the following inequalities are satisfied

$$S(x) < \left| -fN(x) \right| \quad \text{for} \quad x > c\,, \tag{5.30a}$$

$$\text{sgn}(h(x)) = \text{sgn}(S(x)) \quad \text{for} \quad x \le c\,, \tag{5.30b}$$

where $h(x)$ is the tangential slip displacement

$$h(x) = \int_{x/c}^{1} B_x(\xi)\, d\xi\,. \tag{5.30c}$$

Another condition which can be used to establish the slip interval is that the traction distribution near the contact edge must follow the form given by the slipping asymptote (Comninou, 1976). We can therefore expect that

$$N(x) = K_s x^{\lambda_s - 1} \quad \text{for} \quad 0 < x/c < 1 \quad \text{or} \tag{5.31a}$$

$$K_s = \frac{N(x)}{x^{\lambda_s - 1}} \quad \text{as} \quad x/c \to 0 . \tag{5.31b}$$

5.5.4 Results

The size of the slip zone, $\hat{c}\,(c/d_o)$ is found by solving the integral equation (5.28). These results are then compared with the approximate solution

$$\frac{c_o}{d_o} = \left\{ -\frac{(f + g^I_{r\theta})}{(f + g^{II}_{r\theta})} \right\}^{\frac{1}{\lambda_{II} - \lambda_I}}, \tag{5.32}$$

which is found from the adhered solution alone (by setting $S(c_o) = -fN(c_o)$ and by substituting equations (5.19a) and (5.19b) - minus the corrective dislocation term).

The results found from two different routes are plotted in Figures 5.6 and 5.7, for wedge of internal angles 60^0 and 120^0, respectively.

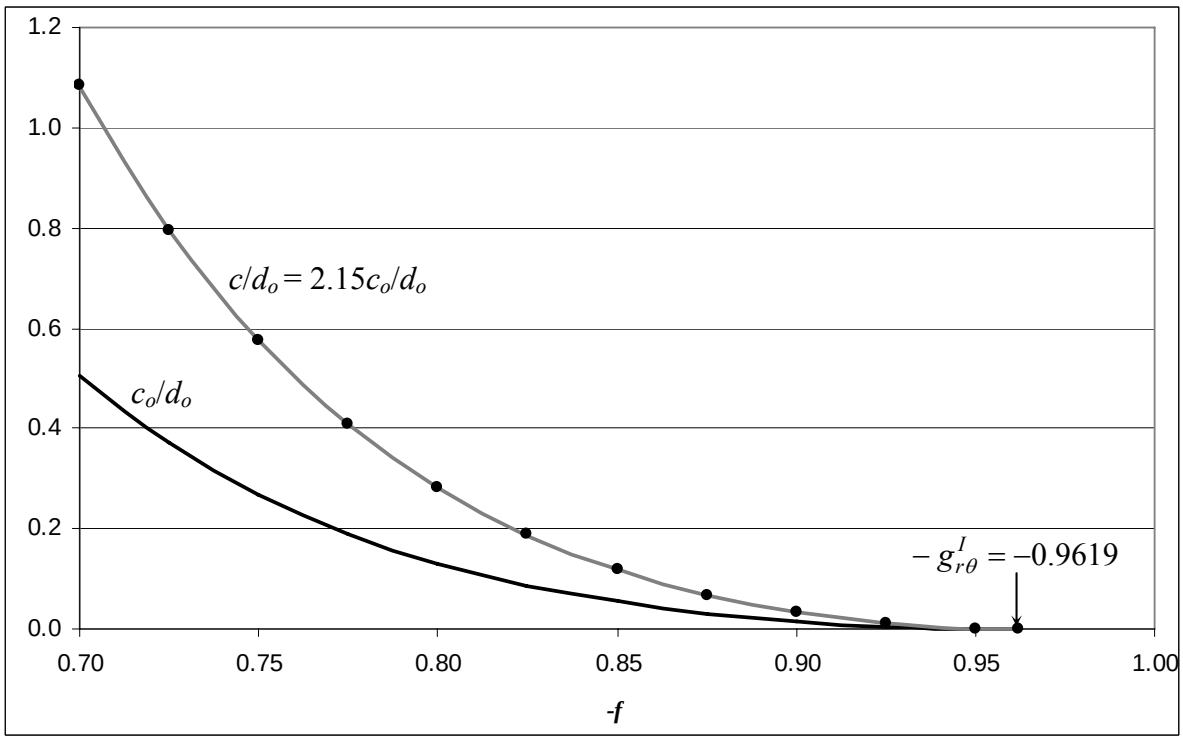

Figure 5.6 : Plot showing both c_o/d_o (dark line, bilateral solution) and c/d_o (dark dots, unilateral solution) as a function of the coefficient of friction, f, for the 60^0 wedge slipping away from the apex

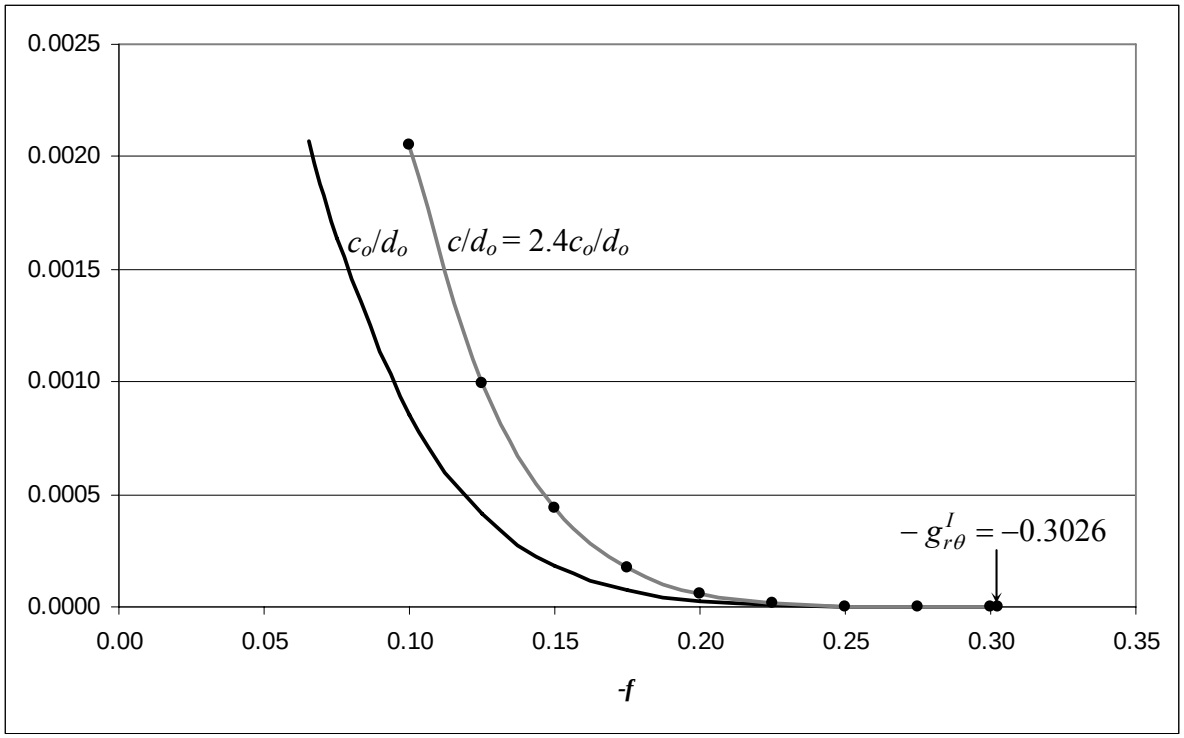

Figure 5.7 : Plot showing both c_o/d_o (dark line) and c/d_o (dark dots) as a function of the coefficient of friction, f, for the 120^0 wedge slipping away from the apex

It was found that the true slip distance is a multiple of approximate solution and follows these relationships

$$\frac{c}{d_o} = 2.15\frac{c_o}{d_o} \quad \text{for the } 60^0 \text{ wedge problem, and} \tag{5.33a}$$

$$\frac{c}{d_o} = 2.4\frac{c_o}{d_o} \quad \text{for the } 120^0 \text{ wedge problem.} \tag{5.33b}$$

The results found may be applied to finite problems provided that the generalised stress intensity factors have been calibrated for the geometry under consideration. As an example, consider the 60^0 trapezium punch (see section 8.4.4). Substituting generalised stress intensity factors for this problem (equation (8.20)) into equation (5.33a), gives

$$c/a = 2.15\left\{-\frac{(f+0.9619)}{(f+0.3224)}\left(\frac{-0.197+0.360(Q/P)}{-0.407-0.173(Q/P)}\right)\right\}^{\frac{1}{0.5332}}. \tag{5.34}$$

Figure 5.8 provides a comparison of the slip zone size, c/a, found from the finite element analysis and those predicted from the asymptotes, and the correlation found is excellent.

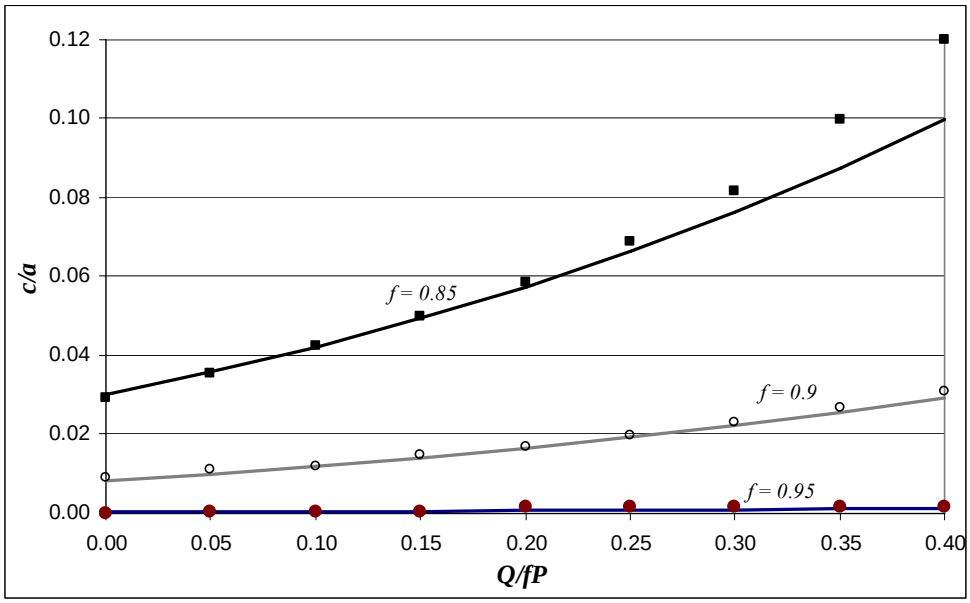

Figure 5.8 : Slip zone size, c/a, as a function of Q/fP showing the correlation between the prediction derived from the asymptotes (solid lines) and the finite element output (discrete markers). Note that $c/a = 0$ if $f > g^{I}_{r\theta}(0.9619)$.

5.6 Conclusions

The state of stress produced by an edge dislocation in a wedge has been analysed, for the general case, and with particular attention paid to the cases of internal wedge angles of 240^0 and 300^0, and with both the dislocation and the observation points lying on projection lines from one of the free surfaces. Application of the Williams eigensolution permits a thorough check on convergence of all stress components near the apex to be made, and it was found that convergence of the numerical solution was obtained with the order of numerical integration set to $n = 500$. A simple function containing 5 coefficients for the 240^0 wedge and 4 coefficients for the 300^0 wedge has been collocated with the numerical values, and, because the form of the terms has been chosen carefully to coincide with the expected form of the behaviour in the key regions, an excellent representation is found efficiently. Finally the solutions found were used to find the size of the slip zone emanating from the edge of an example case of complete contact, which showed a very good agreement between the predicted results and the finite element results.

Chapter 6

Sliding of a square punch

6.1 Introduction

It is often asserted that the presence of interfacial frictional shearing tractions has only a very small effect on contact pressure distribution, and that, under sliding conditions, the frictionless contact pressure distribution may be taken, for practical purposes, as always applying. This claim may stem from several results found from half-plane contact theory; incomplete contacts which are sliding have a traction distribution which is independent of the coefficient of friction if the bodies are elastically similar, or are only weakly dependent on friction when there is elastic mismatch. Complete contacts studied using these principles are restricted to cases where the body defining the size of the contact is rigid. If the contacting body is incompressible the solution is again independent of the coefficient of friction, whilst, if it is compressible, the solution varies fairly weakly with Poisson's ratio. However, if both bodies are elastically similar and the contact is complete, which is the problem under consideration here and arises frequently in practice, conditions are very different, and it will be shown that the contact pressure adjacent to the trailing edge, in particular, is profoundly affected by the value of the coefficient of friction.

Problems of this class cannot be solved analytically, and details of the contact traction distribution depend on the overall geometry of the body, though only relatively weakly. Here, the specific case of a square punch, of side $2a$, pressed normally onto an elastically similar half-plane by a normal force, P, and pushed along by a shearing force, Q, sufficient to cause sliding, and where the coefficient of friction is f, is treated, Figure 6.1. Although this problem may appear to be simple, as the entire interface is in a state of slip, it will transpire that there are several new features which are difficult to quantify. At the contact corners the problem may be locally idealised by using an elasticity formulation

appropriate to a semi-infinite wedge sliding on an elastically similar half-plane (see Figure 4.5). This development enables great detail to be added, whilst providing an easy and straightforward way to generalise the solution to other geometries, where the general features found here are expected still to be present.

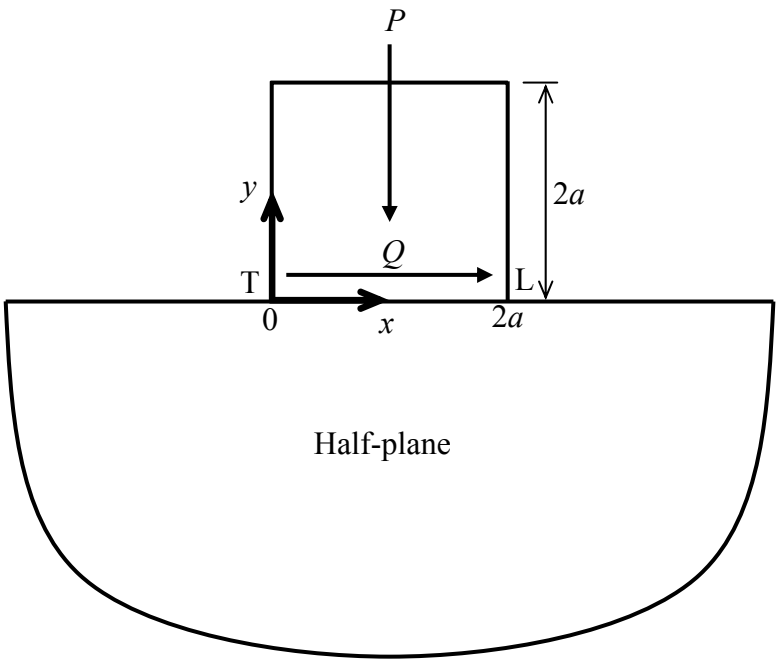

Figure 6.1 : Geometry of the problem solved - an elastic square punch, of side 2*a*, sliding on an elastically similar half-plane

6.2 Sliding asymptote (bilateral)

The semi-infinite wedge problem to be considered for this problem, and studied by Gdoutos and Theocaris (1975), and by Comninou (1976), is described in detail in section 4.3. The procedure employed is to see what restrictions are placed on the form of the elasticity field solution by the requirements that the free surface of the half-plane exterior to the contact, and the inclined face of the contact remain traction-free, and that the following continuity conditions exist at the interface:

$$u_\theta^1 = u_\theta^2, \text{ and} \tag{6.1}$$

$$\sigma_{r\theta} = -f\sigma_{\theta\theta}. \tag{6.2}$$

Although these appear to be conventional frictional contact requirements, it should be recognised that they do not encompass the Signorini conditions (i.e. in the region of separation: $u_\theta^1 - u_\theta^2 > 0$ and $\sigma_{r\theta} = \sigma_{\theta\theta} = 0$), so that the two bodies are required to remain in contact, even if $\sigma_{\theta\theta} > 0$. Also, the coefficient of friction, f, is a signed parameter. If $\sigma_{\theta\theta} < 0$, implying compressive contact, a positive value of f suggests the kind of slip which is experienced at a trailing edge, Figure 4.5, whilst a negative value of f implies the kind of slip seen at the leading edge of a contact. In asymptotic expansions of problems of this type, based on the pioneering solution of Williams (1952), the state of stress near the apex is captured by terms having the form

$$\sigma_{ij} \sim r^{\lambda-1} f_{ij}(\theta) . \tag{6.3}$$

The value of λ is determined by substituting $\varphi = \pi/2$ into the characteristic equation (equation (4.35)) giving

$$\left(\sin^2\left[\frac{\lambda\pi}{2}\right] - \lambda^2 \right) \cos[\lambda\pi] + 0.5\sin^2[\lambda\pi] + f\lambda(1+\lambda)\sin[\lambda\pi] = 0 . \tag{6.4}$$

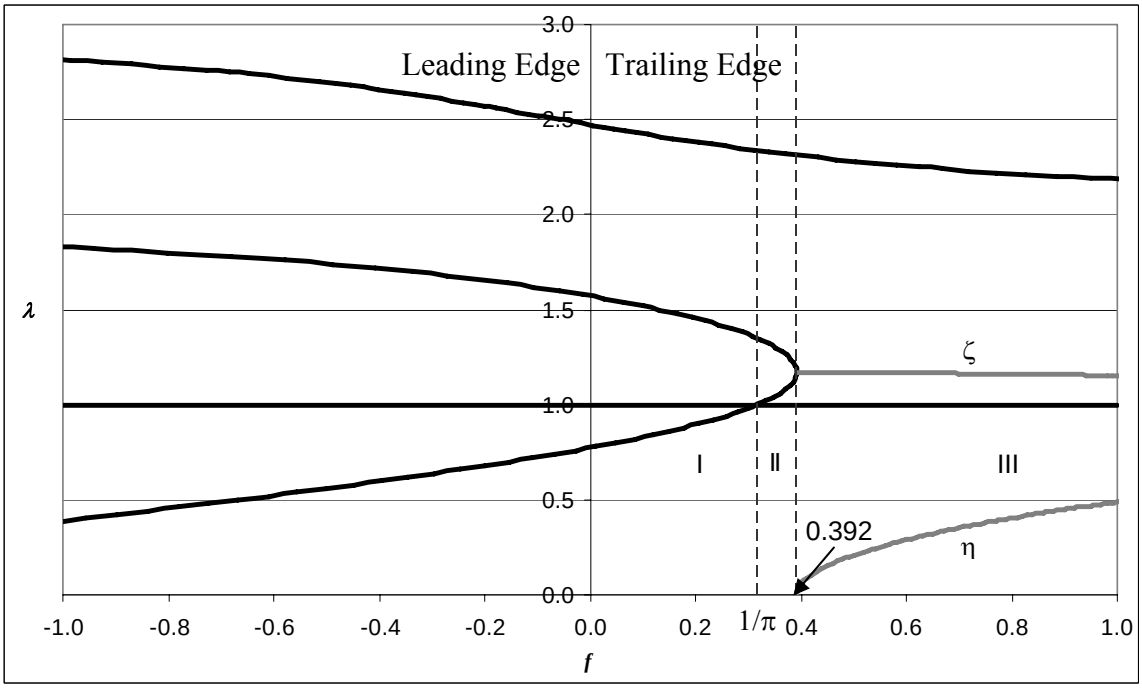

Figure 6.2 : The slipping eigenvalues, λ as a function of the coefficient of friction, f

The roots of equation (6.4) are plotted out in Figure 6.2. This plot displays several features which are worthy of comment. First, assuming, for the time being, that contact is maintained everywhere (and therefore that $\sigma_{\theta\theta} < 0$), the left hand half of the figure relates to the leading edge (for which $f < 0$), whereas the right hand half of the figure relates to the trailing edge (for which $f > 0$). Also there are three distinct regions; each exhibits different behaviour which will be discussed in detail in the following subsections.

6.2.1 Region I ($f < 1/\pi$)

In this region, the state of stress varies as $r^{\lambda_s - 1}$, where r is a polar coordinate measured from the contact edge. It follows that, as the lowest root is always less than unity, the dominant behaviour is given by this root, and is power order singular in nature. Therefore, the contact pressure may be written in the form

$$p(r) = -\sigma_{\theta\theta}(r,0) = K_s r^{\lambda_s - 1} \tag{6.5}$$

where K_s is the generalised stress intensity factor found by collocating the solution to whatever finite problem is being studied. However, if the coefficient of friction is greater than this value the problem seems much more complex. In fact, there is always a root $\lambda = 1$, but the corresponding eigenvector is of zero amplitude, so that this solution does not contribute to the possible asymptotic forms which might arise.

6.2.2 Region II ($1/\pi \leq f \leq 0.392$)

For a coefficient of friction in this range, there are two wholly real roots in the interval $1 < \lambda < 2$, and these correspond to a local pressure distribution which is bounded but where $dp/dr \to \infty$ as $r \to 0$. In this region the contact pressure may be written in the form

$$p(r) = -\sigma_{\theta\theta}(r,0) = K_{b1} r^{\lambda_{b1} - 1} + K_{b2} r^{\lambda_{b2} - 1}. \tag{6.6}$$

where K_{b1} and K_{b2} are the power order bounded stress intensity factors.

6.2.3 Region III (f > 0.392)

If the coefficient of friction exceeds 0.392 the lowest wholly real root lies in the interval $2 < \lambda < 3$, so that, as $r \to 0$ not only does the pressure fall to zero, but also $dp/dr \to 0$. Therefore, the appropriate eigenvalue in this region is a complex one, whose real branch originates at the point where the locus folds back (Figure 6.2), and an imaginary part also develops. The contact pressure in this region may be written in the form

$$p(r) = -\sigma_{\theta\theta}(r,0) = K_c r^{\zeta-1} \sin\left(\eta \ln\left(\frac{r}{r_o}\right)\right), \quad 1 < \zeta < 2,\ 0 < \eta < 1, \tag{6.7}$$

where K_c is the stress intensity factor, ζ and η are the real and imaginary parts of the eigenvalue respectively, and r_o denotes the position from the contact edge where the argument of the logarithm passes through unity. It is clear that, if $\sigma_{\theta\theta} < 0$ when $r > r_o$, the contact pressure must become tensile close to the contact corner, i.e. when $r < r_o$.

The solutions in regions I and II are physically reasonable, but that in region III clearly does not satisfy the normal Signorini boundary conditions, and a correction to the Comninou solution is needed in order to permit the wedge and half-plane to separate in a region where there is implied interfacial tension. It will be shown later how the separation condition can be restored within the asymptote. When this happens the contact pressure falls smoothly to zero, and is square-root bounded.

The general state of stress in Region III can be expressed in the following form

$$\begin{aligned} \sigma_{jk}(r,\theta) &= H\,\hat{r}^{\zeta+i\eta-1} f_{jk}(\theta) \\ &= H\,\hat{r}^{\zeta-1} \exp\left[i\eta \ln \hat{r}\right] \left|f_{jk}(\theta)\right| \exp\left[i\phi_{jk}(\theta)\right], \end{aligned} \tag{6.8}$$

where H is an arbitrary multiplier, $\hat{r}$ is a normalised coordinate (implicitly $\hat{r} = r/a_o$), a_o is an arbitrary length scale, $i = \sqrt{-1}$, $f_{jk}(\theta)$ is the eigenvector corresponding to the complex eigenvalue ($\zeta + i\eta$) with magnitude $\left|f_{jk}(\theta)\right|$ and phase $\phi_{jk}(\theta)$ when written in complex polar

form. The solution of the characteristic equation for $f > 0.392$ has complex conjugate pairs which are simultaneously excited, so

$$\begin{aligned}\sigma_{jk}(r,\theta) &= H\,\hat{r}^{\zeta-1}\left|f_{jk}(\theta)\right|\left\{\exp\left[i\left(\eta\ln\hat{r}+\phi_{jk}(\theta)\right)\right]+\exp\left[-i\left(\eta\ln\hat{r}+\phi_{jk}(\theta)\right)\right]\right\}\\ &= 2H\hat{r}^{\zeta-1}\left|f_{jk}(\theta)\right|\cos\left(\eta\ln\hat{r}+\phi_{jk}(\theta)\right),\end{aligned} \tag{6.9}$$

where it has been noted that the conjugate eigenvectors have the same magnitude but opposite sign phase. The $\sigma_{\theta\theta}$ stress along the interface, from equation (6.9), can be expressed as

$$\sigma_{\theta\theta}(x,0) = 2H\left|f_{\theta\theta}(0)\right|\left(\frac{x}{a_o}\right)^{\zeta-1}\sin\left(\eta\ln\left(\frac{x}{a_o}\right)+\phi_{\theta\theta}(0)+\frac{\pi}{2}\right). \tag{6.10}$$

If we define $\sigma_{\theta\theta}$ stress along the interface in a finite problem as

$$\sigma_{\theta\theta}(x,0) = -K_c x^{\zeta-1}\sin\left(\eta\ln\left(\frac{x}{x_o}\right)\right), \tag{6.11}$$

we can find the multiplier H and the ratio x_o/a_o by comparing equations (6.10) and (6.11) giving

$$H = \frac{-K_c}{2\left|f_{\theta\theta}(0)\right|}\,a_o^{\zeta-1}, \tag{6.12a}$$

$$\frac{x_o}{a_o} = \exp\left(\frac{-\left(\phi_{\theta\theta}(0)+\pi/2\right)}{\eta}\right). \tag{6.12b}$$

Therefore, the general state of stress incorporating a length scale, a, taken from any finite problem under consideration may be written as

$$\frac{\sigma_{jk}(r,\theta)}{p_o} = \left(\frac{-K_c a^{\zeta-1}}{p_o}\right)\frac{\left|f_{jk}(\theta)\right|}{\left|f_{\theta\theta}(0)\right|}\left(\frac{r}{a}\right)^{\zeta-1}\cos\left(\eta\ln\left(\frac{r}{a}\frac{a}{a_o}\right)+\phi_{jk}(\theta)\right), \tag{6.13}$$

where a is contact half-width, $p_o = P/2a$ is the applied normal mean pressure and a/a_o is a constant which scales the semi-infinite asymptote into the finite problem. This scaling ratio, a/a_o is found by the following relationship

$$\frac{a}{a_o} = \frac{x_o / a_o}{x_o / a}, \tag{6.14}$$

where x_o/a_o is from equation (6.12b) and x_o/a is found from a model of the finite problem with bilateral boundary conditions.

6.3 Sliding asymptote (unilateral)

The bilateral form of the asymptote must be modified for case III solutions, where there is an implied interfacial tension. This may be done by distributing climb dislocations to permit separation. However, there is no solution in the literature for a climb dislocation along the interface between a slipping wedge and an elastically similar half-plane, and so the problem must be tackled slightly differently. The solution is known for glide and climb dislocations along the projection line of the free surface in a three quarter plane (Churchman *et al.*, 2006), Figure 6.3, and so we may obtain the Comninou asymptotic solutions from the Williams solution for a monolithic three quarter plane in the following way.

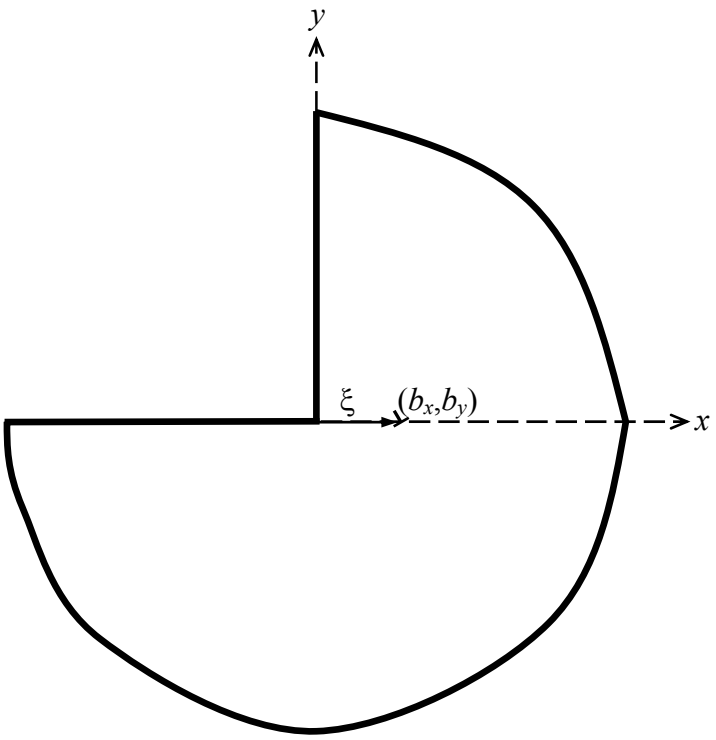

Figure 6.3 : An edge dislocation along the projection line of the free surface in a three quarter plane.

The direct, $N_1(x)$, and shear, $S_1(x)$, tractions along the slipping interface shown are given by the dominant Williams solution, viz. $\sigma_{\theta\theta}(x) = K_I^o x^{\lambda_I - 1} + K_{II}^o x^{\lambda_{II} - 1}$, $\sigma_{r\theta}(x) = g_{r\theta}^I K_I^o x^{\lambda_I - 1} + g_{r\theta}^{II} K_{II}^o x^{\lambda_{II} - 1}$, where K_I^o, K_{II}^o, λ_I, λ_{II}, $g_{r\theta}^I$, $g_{r\theta}^{II}$ are the generalised stress intensity factors, eigenvalues and eigenvectors for a wedge of total internal angle $3\pi/2$, together with the influence of a distribution of glide dislocations of density $B_x(\xi)$, as

$$N_1(x) = K_I^o x^{\lambda_I - 1} + K_{II}^o x^{\lambda_{II} - 1} + \int_0^\infty B_x(\xi) G_{xyy}(x,\xi) d\xi \,, \tag{6.15a}$$

$$S_1(x) = g_{r\theta}^I K_I^o x^{\lambda_I - 1} + g_{r\theta}^{II} K_{II}^o x^{\lambda_{II} - 1} + \int_0^\infty B_x(\xi) G_{xxy}(x,\xi) d\xi \,, \tag{6.15b}$$

where $G_{xky}(x,\xi)$ are the influence functions for a glide dislocation in a three quarter plane (see Churchman *et al.*, 2006, and section 6.7) and the slipping condition, bilaterally imposed, is given by

$$S_1(x) = -fN_1(x), \quad 0 < x < \infty \,. \tag{6.16}$$

The resulting tractions given by inversion of this integral equation are precisely those implied by the Comninou solution, and for $f > 0.392$, a solution of the form of equation (6.11) results. We can then add further distributions of dislocations, of both the glide and climb type, *in the same domain*, to give

$$N_2(x) = N_1(x) + \int_0^\infty B_x(\xi) G_{xyy}(x,\xi) d\xi + \int_0^c B_y(\xi) G_{yyy}(x,\xi) d\xi \,, \tag{6.17a}$$

$$S_2(x) = S_1(x) + \int_0^\infty B_x(\xi) G_{xxy}(x,\xi) d\xi + \int_0^c B_y(\xi) G_{yxy}(x,\xi) d\xi \,, \tag{6.17b}$$

where

$$N_1(x) = \frac{S_1(x)}{-f} = -K_c x^{\zeta - 1} \sin\left(\eta \ln\left(\frac{x}{x_o}\right)\right). \tag{6.18}$$

The standard unilateral (Signorini) conditions are now imposed, by setting

$$N_2(x) = 0, \qquad 0 < x < c, \tag{6.19a}$$

$$S_2(x) = -fN_2(x), \quad 0 < x < \infty, \tag{6.19b}$$

where c is the point of closure. As the tractions fall continuously to zero as $x \to c^+$, a bounded quadrature is required to simulate $B_y(\xi)$, and the additional condition that the contact pressure must be square root bounded provides the means of defining c, the point of separation. Thus, in practice, we do not need to solve the first pair of integral equations (6.15a), (6.15b), but simply employ the second pair (6.17a), (6.17b). The details of this calculation are given in section 6.7, and the results in Figure 6.4.

Figure 6.4(a) shows the normalised traction distributions adjacent to the edge of the three quarter plane when the bilateral form of the tractions is present, and when separation is permitted (the 'unilateral' solution), for an example case of $f = 0.6$. The true location of the separation point (c), normalised with respect to the location of the point where the direct traction changes sign in the bilateral solution (x_o), is shown in Figure 6.4(b). The contact pressure must be square root bounded in form close to the contact edge, and we may therefore define a dimensional multiplier, analogous to a stress intensity factor, from the relation

$$p(x) = K_B\sqrt{x-c}, \quad Lt \;\; x \to c^+, \tag{6.20}$$

and this is related to the multiplier on the bilateral form of the solution by

$$\Lambda(f) = \frac{K_B}{K_c x_o^{\zeta-3/2}}. \tag{6.21}$$

The function $\Lambda(f)$ is plotted out in Figure 6.4(c). Finally, the 'asymptotes to the asymptote' displaying the characteristic forms of the solution very close to the point of separation (defined in equation (6.20)), and well away from it (defined in equation (6.11)), are included in Figure 6.4(d).

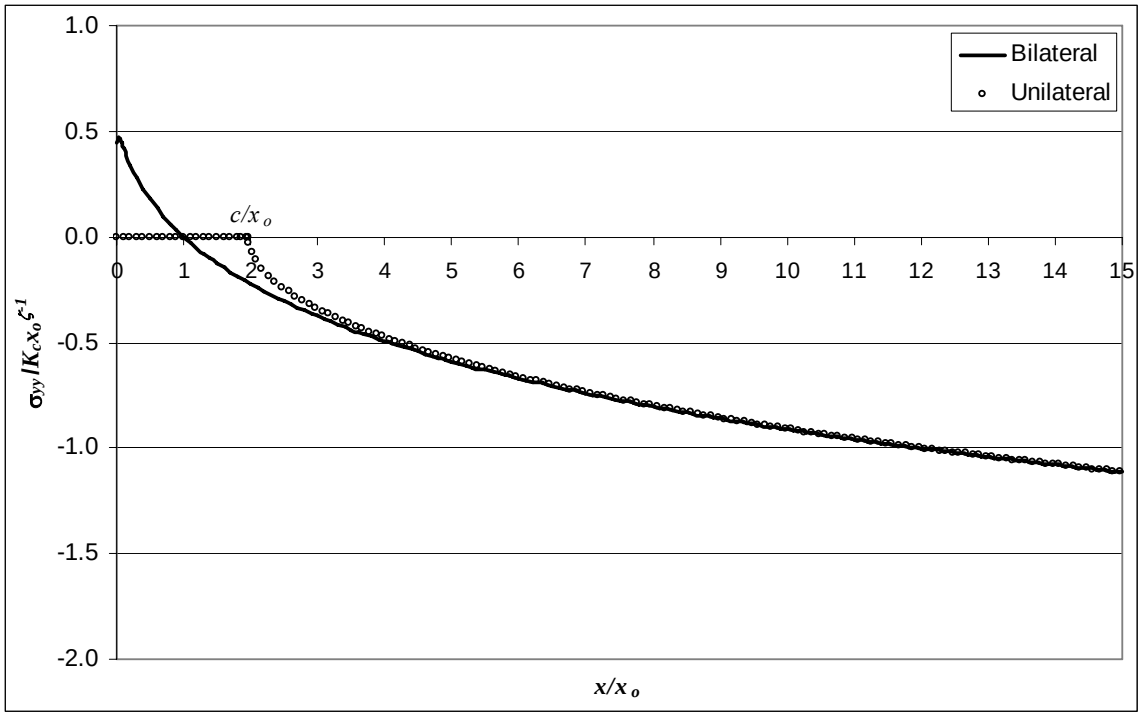

Figure 6.4(a) : Normalized traction distributions adjacent to the edge of the three quarter plane, for the example case $f = 0.6$.

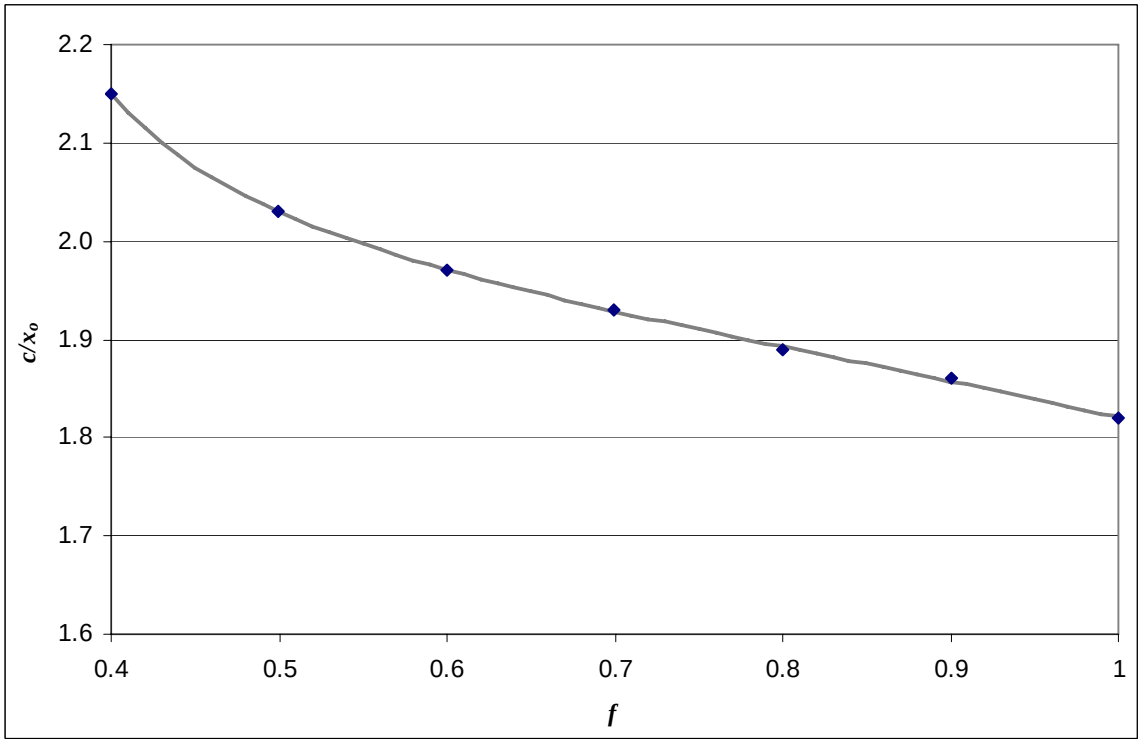

Figure 6.4(b) : The location of the separation point normalized with respect to the location of the point where the direct traction changes sign in the bilateral solution, c/x_o as a function of the coefficient of friction, f.

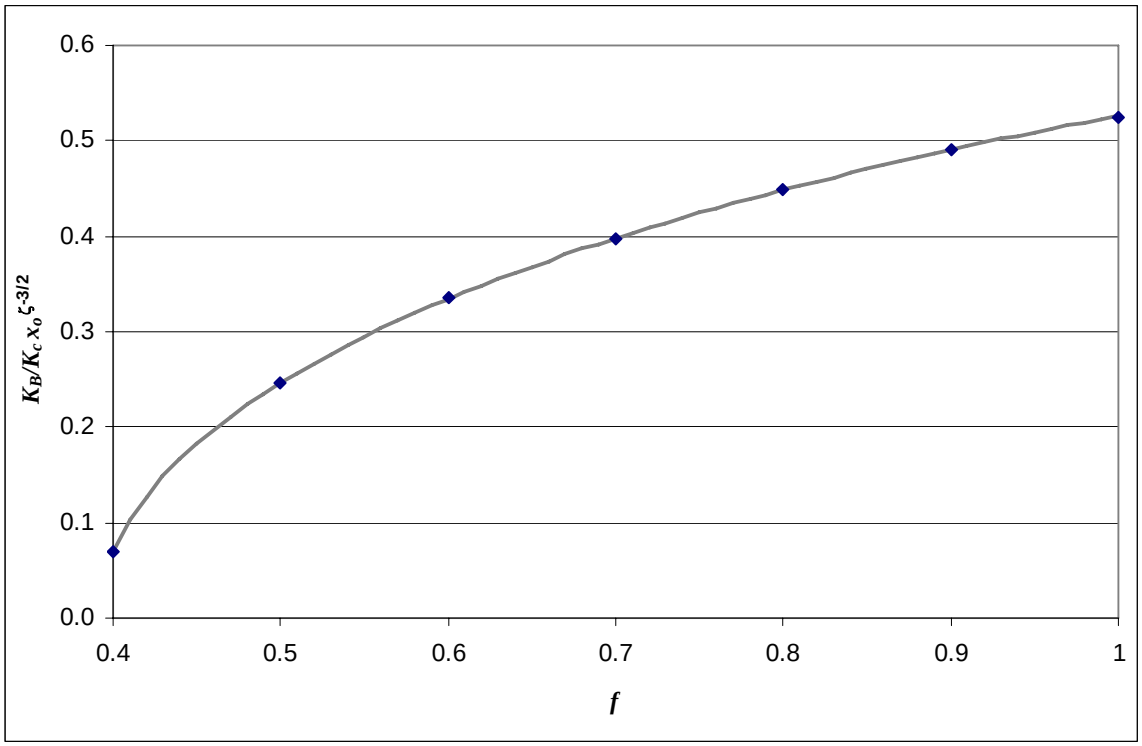

Figure 6.4(c): Normalised inner asymptote multiplier, $K_B/K_c x_o^{\zeta-3/2}$ as a function of the coefficient of friction, f.

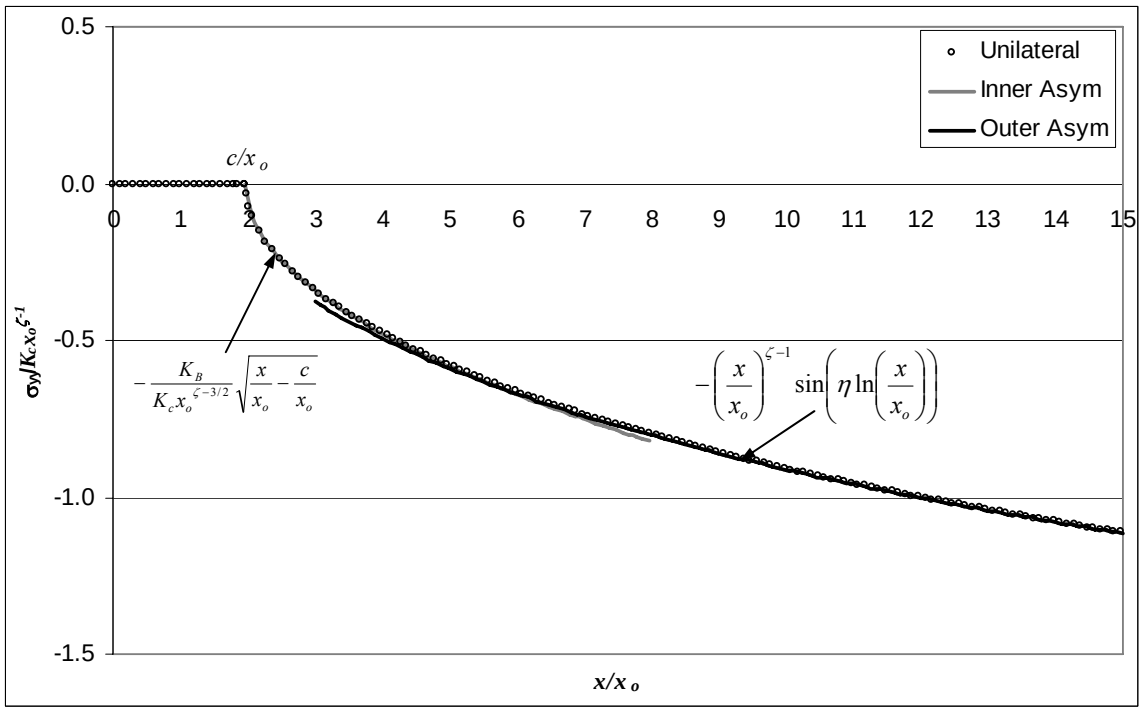

Figure 6.4(d) : The unilateral solution, together with the inner asymptote (square root bounded behaviour) and outer asymptote, for an example case of $f = 0.6$.

6.4 Finite element analysis

The problem under consideration, shown in Figure 6.1, was analysed using the finite element method. The model employed is shown schematically in Figure 6.5(a). It was investigated using the commercial programme *ABAQUS*. The normal force P was applied as a distributed load p_o ($p_o = P/2a$) along the upper surface of the punch. The shearing force Q was then applied as a distributed shearing traction q_o ($q_o = Q/2a$) at the upper surface of the punch, together with a distributed anticlockwise moment, of resultant magnitude $2Qa$, in order to render the shearing force statically equivalent to one applied in the plane of the contact, and therefore to remove any overturning moment. This procedure was adopted so as to remove any spurious local effects caused by the details of the way in which the force was applied. A total of approximately 122,000 elements (with slightly over 122,000 nodes) were used, giving nearly 244,000 degrees of freedom. There were 600 first order (linear) four-noded quadrilateral elements along the line of the contact interface, with the length of element at the contact edge reduced to $1 \times 10^{-3}a$. The quality of the mesh used for the whole model and at the contact edges for this problem is shown in Figures 6.5(b) and 6.5(c), respectively. Two forms of the model were employed: the first used conventional Signorini contact conditions and the second used bilateral 'contact' conditions, i.e. no separation was permitted. The results of these computations are given in the following sections.

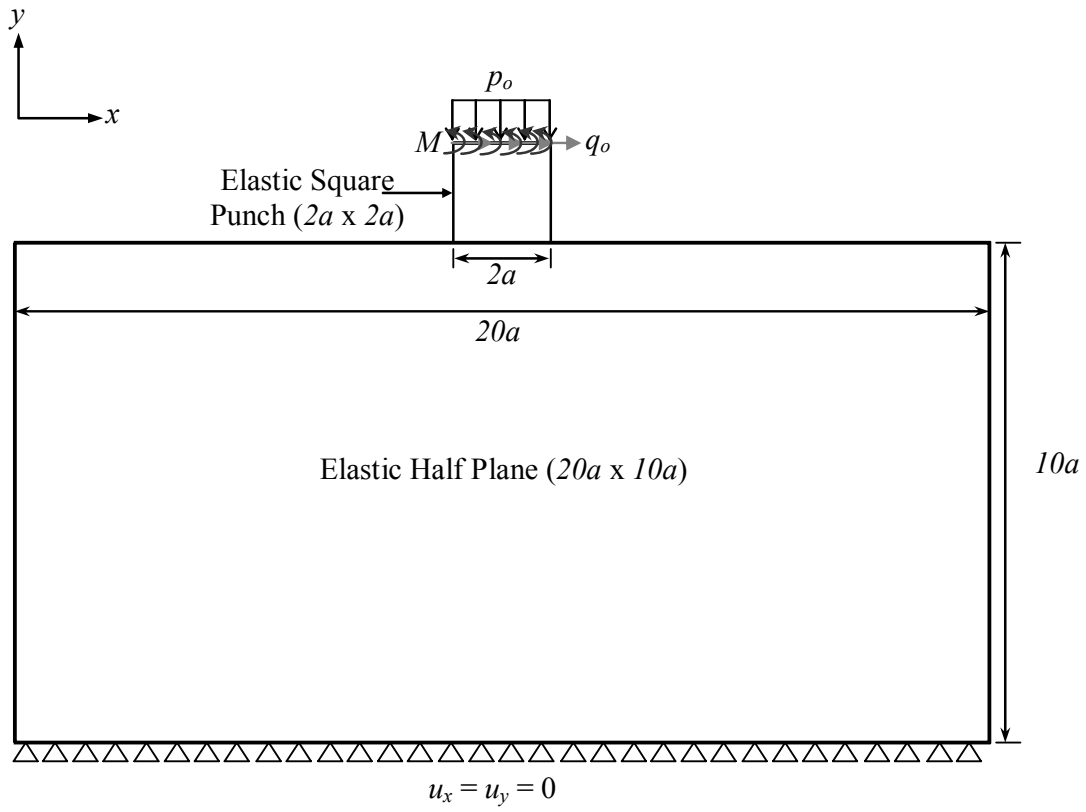
y
x
p_o
M
q_o
Elastic Square
Punch (2a x 2a)
2a
20a
Elastic Half Plane (20a x 10a)
10a
$u_x = u_y = 0$

(a)

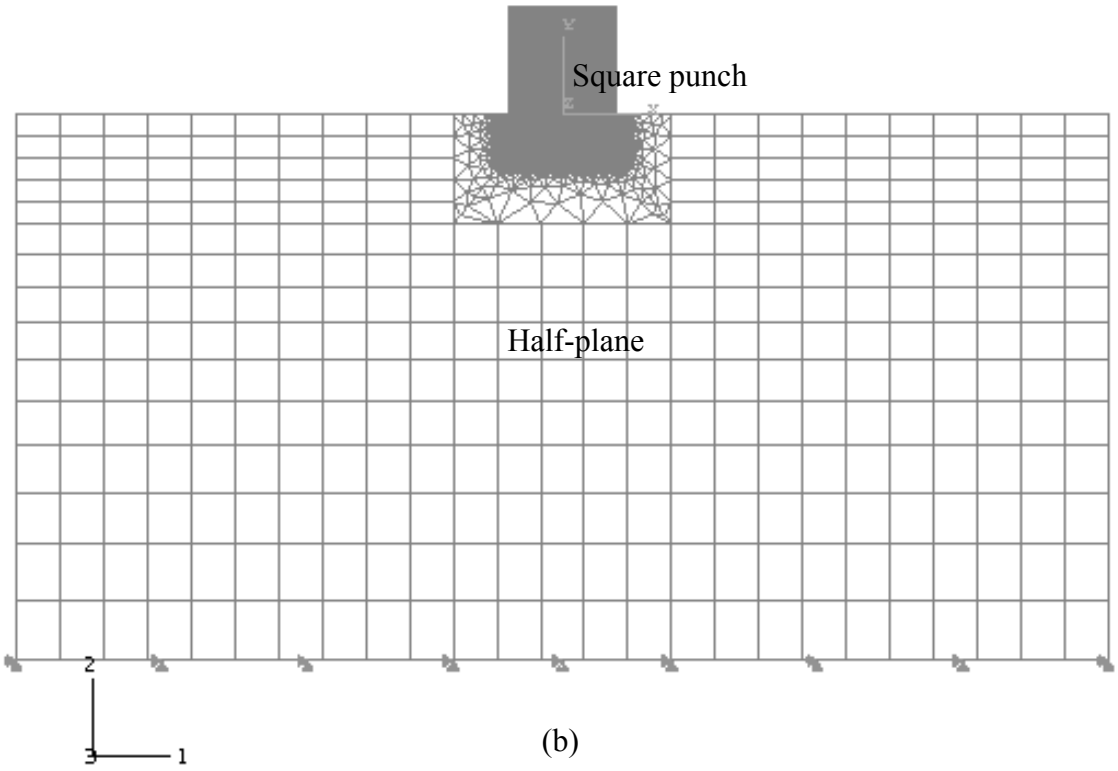
Square punch
Half-plane
2
3
1

(b)

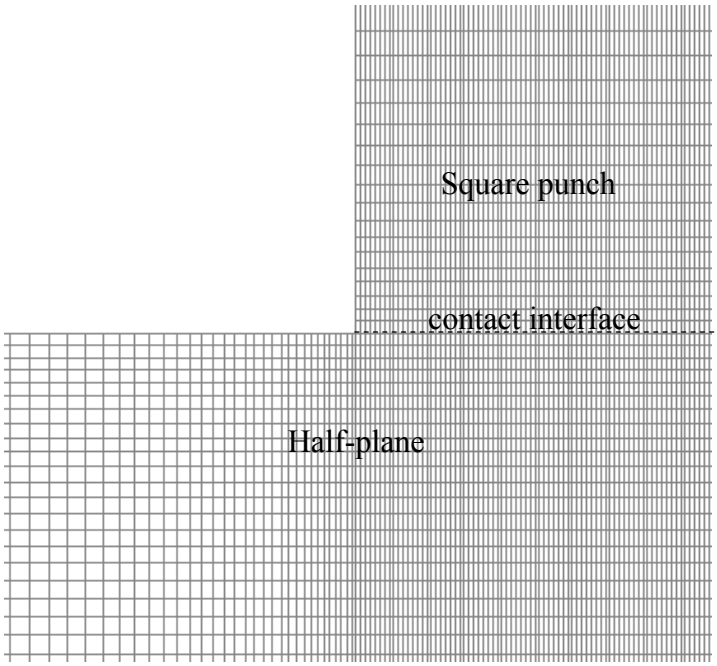

(c)

Figure 6.5 : (a) Geometry of the FE model for the square punch problem (b) Quality of the mesh for the whole model (c) Quality of the mesh at the contact edges

6.4.1 Finite element analysis with conventional interface conditions

Results for the contact pressure distribution along the interface found from the model are shown in Figure 6.6(a). The results at the trailing edge are very difficult to resolve at this scale, and are re-plotted, enlarged, in Figure 6.6(b) for an improvement in clarity. As expected, the contact pressure was invariably singular at the leading edge, regardless of the coefficient of friction. At the trailing edge the contact pressure is also seen to be power order singular for low coefficients of friction (up to $1/\pi$). This region is denoted region I in Figure 6.2. Figure 6.7(a) shows the calibration found for the multiplier, K_s, on the power-order asymptotic form at the leading and, where relevant, trailing edge positions. It is defined by

$$K_s = \frac{p(x)}{x^{\lambda_s - 1}} \qquad Lt \;\; x \to 0, \tag{6.22}$$

where x is a local coordinate measured inwards from the contact edge, and $\lambda_s < 1$.

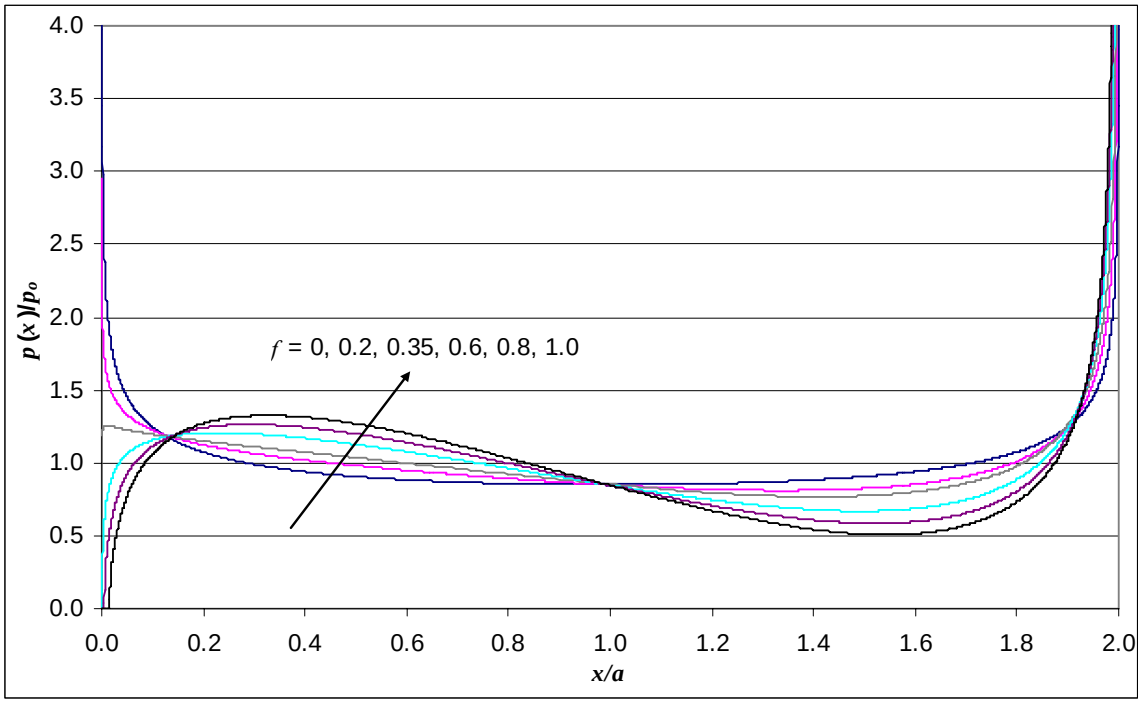

Figure 6.6(a) : Normalised contact pressure distribution along the interface

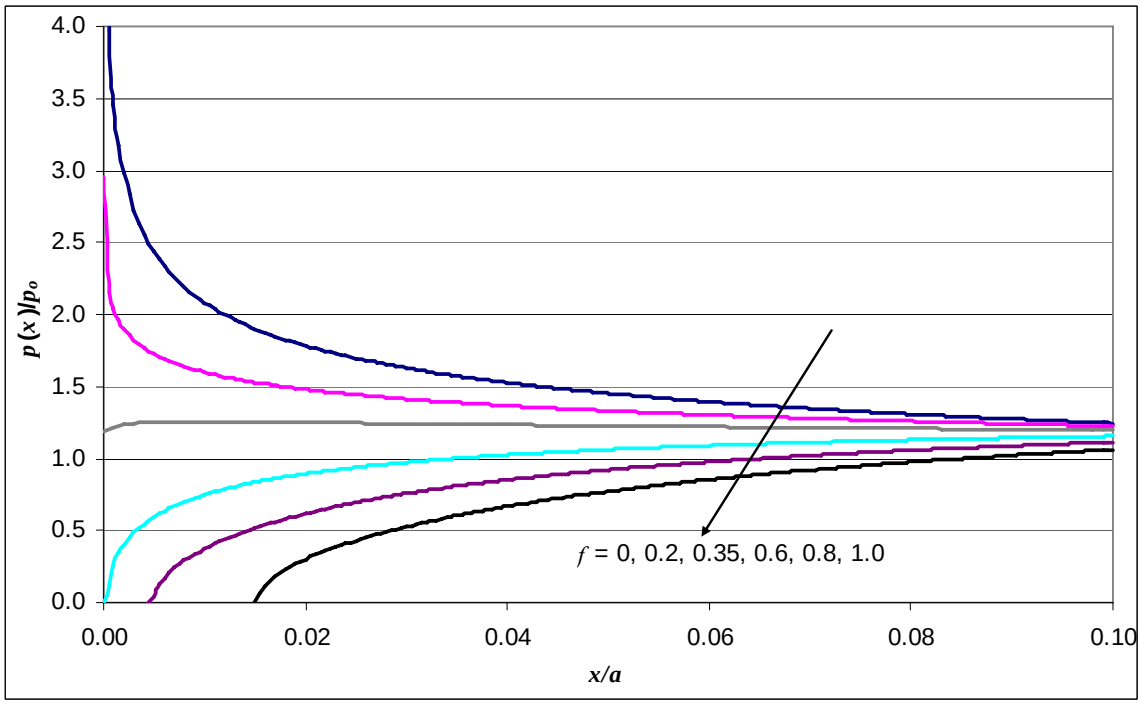

Figure 6.6(b) : Normalised contact pressure distribution at the trailing edge.

A comparison of the normal full-field stress, σ_{yy}/p_o near the corner of the contact within the half-plane between the asymptotic solution and the finite element solution, for an example

case f = 0.2, is as shown in Figure 6.7(b), showing a very good agreement which qualifies the proposed asymptotic form.

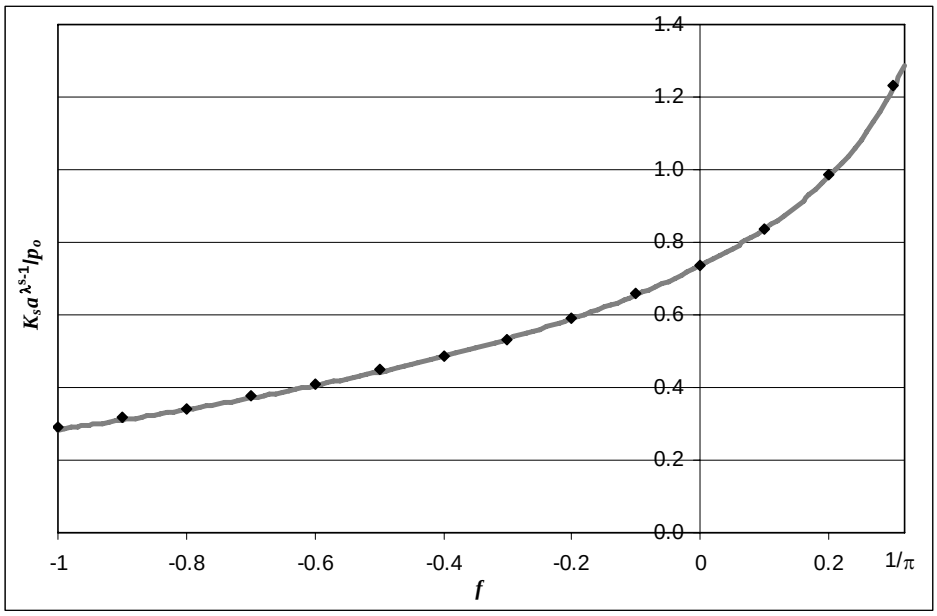

Figure 6.7(a) : Generalised stress intensity factor, $K_S a^{\lambda s-1}/p_o$ as a function of the coefficient of friction, f.

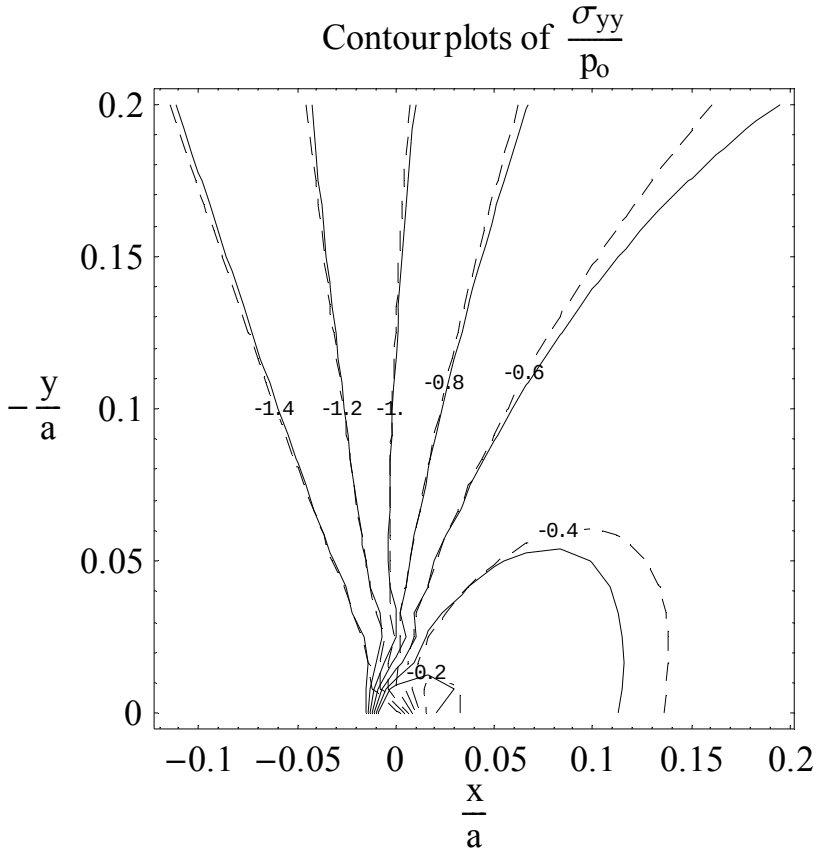

Figure 6.7(b) : Normal stress component comparison between the finite element solution (solid lines) and the asymptotic solution (dashed lines), for an example problem of f = 0.2.

If $f \geq 1/\pi$ the contact pressure at the trailing edge appears to fall to zero either at the extreme contact edge, or just inside it - the latter implies a small region of separation. In region II ($1/\pi \leq f \leq 0.392$), the contact pressure exhibits power order bounded behaviour. The power order bounded asymptotic multipliers are shown in Figure 6.8(a). Figure 6.8(b) shows the normal stress component, σ_{yy}/p_o, and provides a comparison near the contact edge within the half-plane between the finite element solution (solid lines) and the asymptotic solution (dashed lines), for an example case in this region (f = 0.35). The results are in very good agreement suggesting that the asymptotic form of solution using two eigenvalues in the range $1 < \lambda < 2$, is sufficient to describe the stress state near the vicinity of the contact edge. In region III ($f > 0.392$), square root bounded behaviour is expected due to separation, and it will be explored in detail in the following sections.

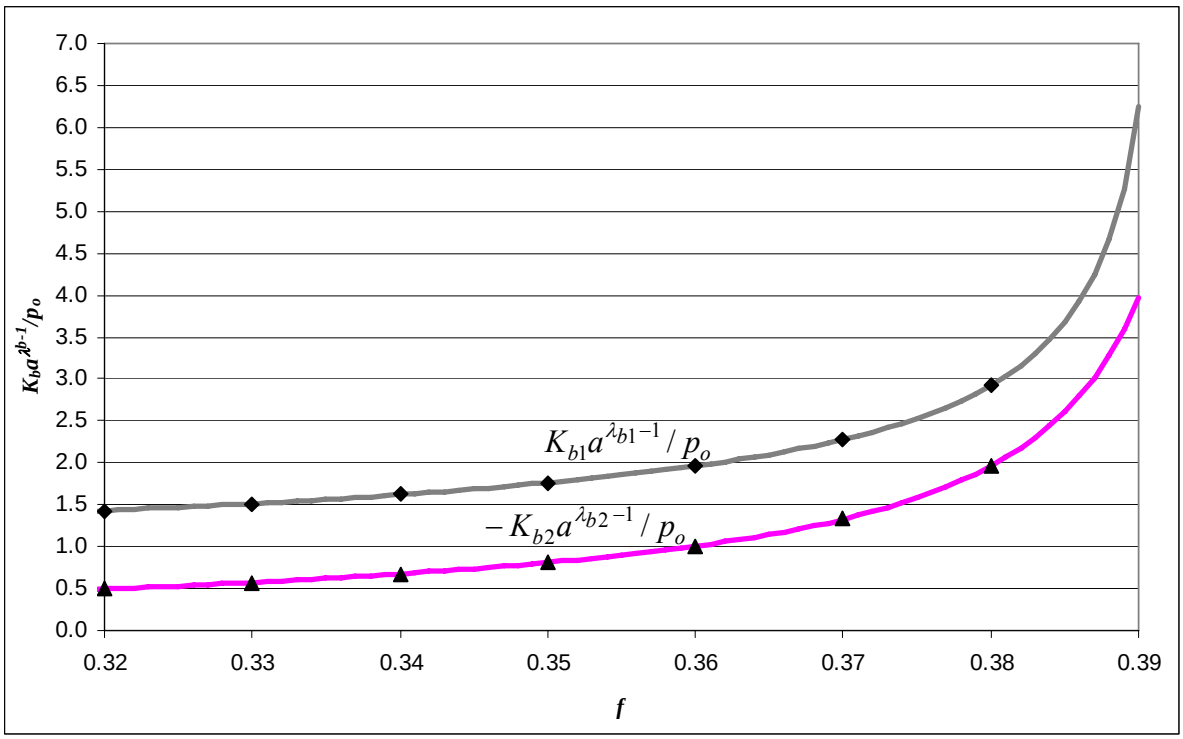

Figure 6.8(a) : Normalised power order bounded asymptotic multipliers as a function of the coefficient of friction, f for the square punch problem.

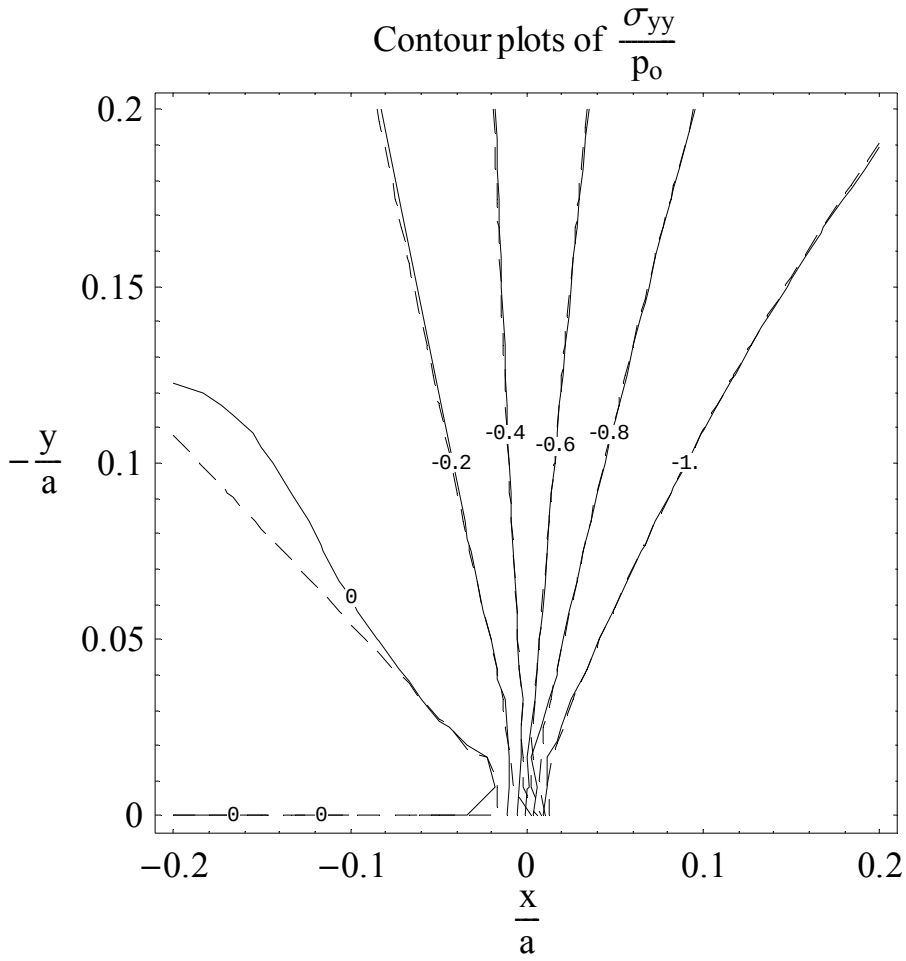

Figure 6.8(b) : Normal stress component comparison between the finite element solution (solid lines) and the asymptotic solution (dashed lines), for an example problem of $f = 0.35$.

6.4.2 Finite element analysis with bilateral interface conditions

From a consideration of the asymptote, at the trailing edge, if the coefficient of friction exceeds $1/\pi$, the contact pressure will be bounded, and the finite element model using conventional contact elements seems to corroborate this, although it is hard to refine the solution locally in sufficient detail. We also know that, if the coefficient of friction exceeds about 0.392, the contact patch will recede from the punch edge, but only slightly, at realistic coefficients of friction. The unilateral form of the asymptote is capable of giving the details of both the recession and the local contact pressure but, in order to match it with the finite

problem, we need to re-do the finite element problem with bilateral 'contact' conditions, i.e. we require the normal surface displacement to be continuous across the interface ($u_{y1} - u_{y2} = 0$), and we also impose a strict ratio between the direct and shear tractions, viz. $\sigma_{xy} = -f\sigma_{yy}$. A special friction formulation which defines the required boundary conditions is imposed along the contact interface by programming a user subroutine in the finite element code *ABAQUS* (see Appendix *B* for details) and modifying the appropriate contact controls. Note that one consequence of imposing the strict ratio between shear and direct traction is that where the direct traction is tensile the shear traction actually pushes the punch in the direction of the applied shear force, Q. Thus, over this small region, and under these conditions, the 'frictional' force is actually doing work on the punch.*

The output from this calculation was processed to find the value of the multiplier, K_c, on the region III solution. This was done by scaling the asymptotic form of solution to fit the finite element pressure at the contact edge, and the results are displayed in Figure 6.9(a). The second important result from the bilateral form of the finite element solution is the point where the direct traction changes sign, x_o/a, and this is shown in Figure 6.9(b). Finally, the state of stress adjacent to the contact edge was determined by using the formulation established in section 6.2.3. A comparison of the normalised full-field stress component, σ_{yy}/p_o in the vicinity of the corner within the half-plane between the asymptotic solution and the finite element solution, for an example case of $f = 0.8$, is shown in Figure 6.9(c). This comparison is very good suggesting that the asymptotic form of solution developed in section 6.2.3 is indeed the major eigensolution excited.

* Note that, because both tractions reverse sign here, the singular asymptotic forms associated with the *leading* edge (Figure 6.2) cannot be excited at the trailing edge: if these eigensolutions are assigned a negative multiplier they would produce tensile direct tractions, but the shear traction would still be in a sense which resists the motion of the punch.

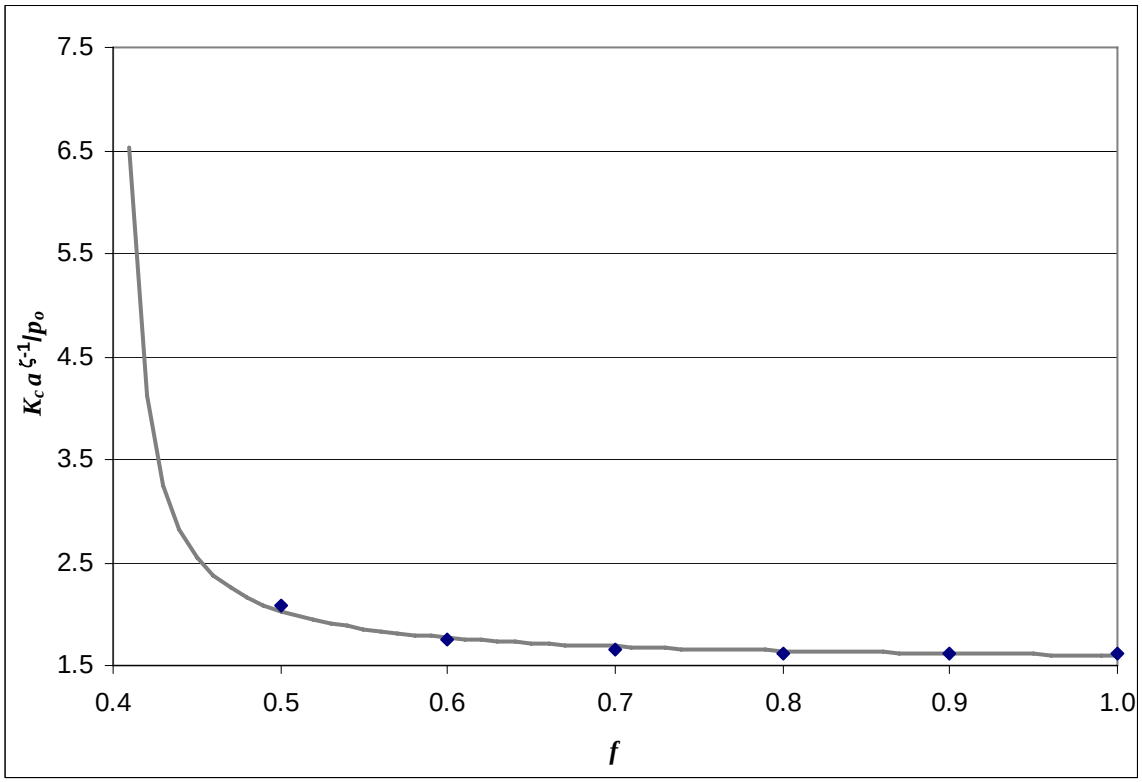

Figure 6.9(a) : Normalised outer asymptotic multiplier, $K_c a^{\zeta-1}/p_o$ for the bilateral finite element solution as a function of the coefficient of friction, f.

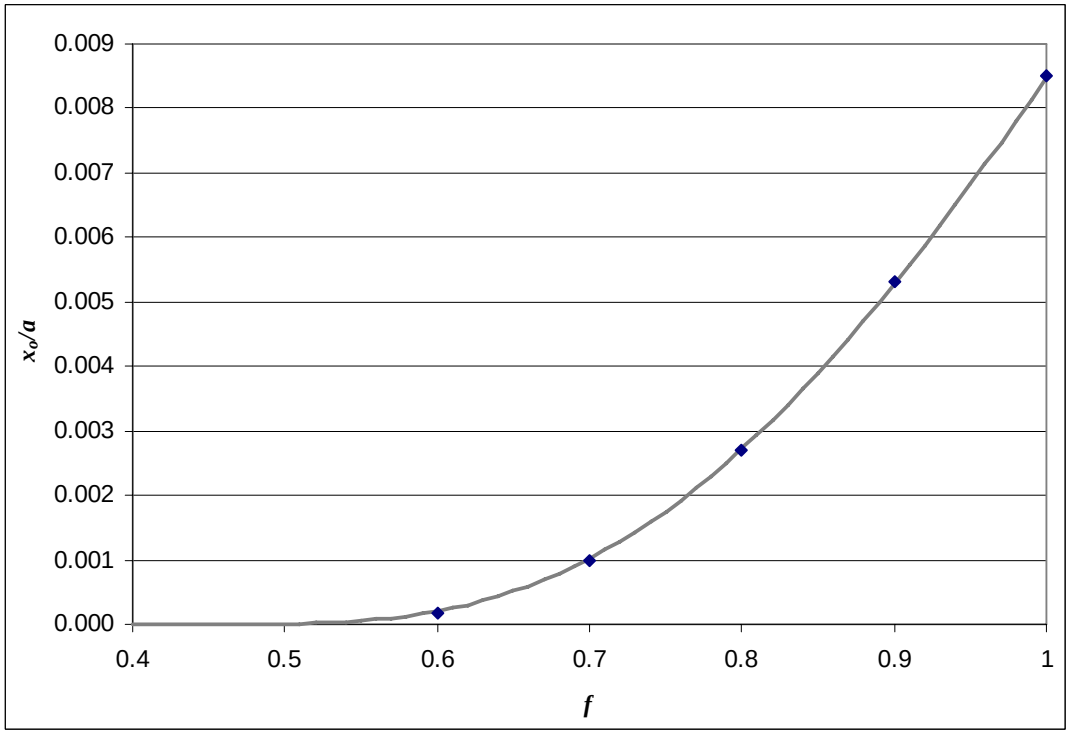

Figure 6.9(b) : The location of the point where the direct traction changes sign normalized with respect to the contact half-width, x_o/a as a function of the coefficient of friction, f.

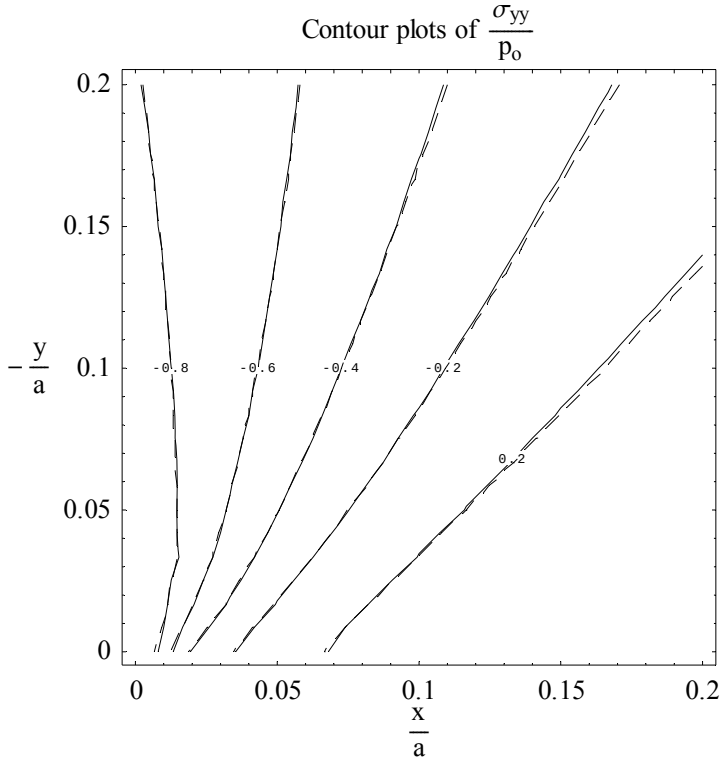

Figure 6.9(c) : A comparison of the normalized normal full-field stress component, σ_{yy}/p_o in the vicinity of the corner within the half-plane between the bilateral finite element solution (solid lines) and the asymptotic solution (dashed lines), for an example case of $f = 0.8$.

6.5 Collocation of asymptotic solution with finite element solution

We are now in a position to compare the unilateral form of the asymptote with the unilateral finite element solution for the example finite problem. First, the point of separation may be found by combining the correction within the asymptote, c/x_o (Figure 6.4(b)) with the position of change in sign in the direct traction, x_o/a from *bilateral* finite element solution (Figure 6.9(b)) using

$$\frac{c}{a} = \left(\frac{c}{x_o}\right)\left(\frac{x_o}{a}\right), \tag{6.23}$$

to give the point of separation, c/a. This is shown in Figure 6.10(a), where it is compared with the estimate of separation found directly from the unilateral form of the finite element solution, and with which there is excellent agreement. Secondly, the normalised square root bounded asymptotic multiplier for the contact pressure distribution at the edge of the 'lifted off' contact is determined from the following expression

$$\frac{K_B\sqrt{a}}{p_o} = \left(\frac{K_c a^{\zeta-1}}{p_o}\right)\left(\frac{K_B\sqrt{x_o}}{K_c x_o^{\zeta-1}}\right)\left(\frac{x_o}{a}\right)^{\zeta-3/2}, \tag{6.24}$$

where $K_c a^{\zeta-1}/p_o$ is the asymptotic solution multiplier from the bilateral finite element calculation, as plotted in Figure 6.9(a), $K_B\sqrt{x_o}\,/\,K_c x_o^{\zeta-1}$ is the calibration for the bounded asymptotic form given by the correction to the asymptote as in Figure 6.4(c) and (x_o/a) is the point where the direct traction changes sign in the bilateral finite element solution (Figure 6.9(b)). A comparison plot of $K_B\sqrt{a}\,/\,p_o$ found by two routes is shown in Figure 6.10(b). One set of symbols is for results found this way and the second found directly from the unilateral form of the finite element solution. This is also in a very good agreement.

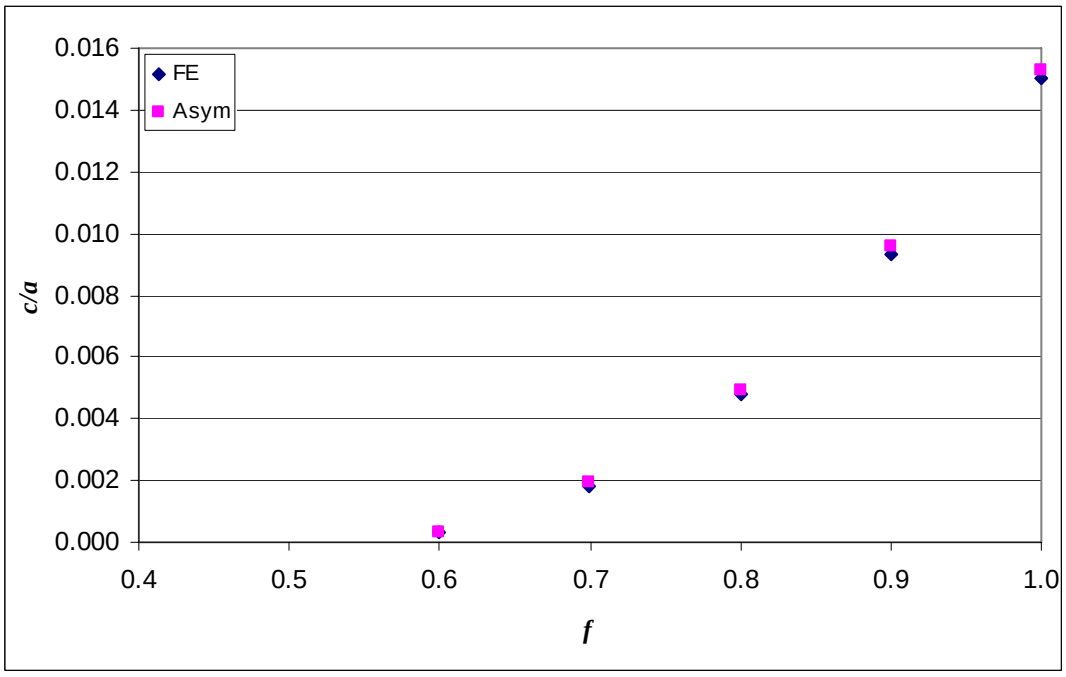

(a)

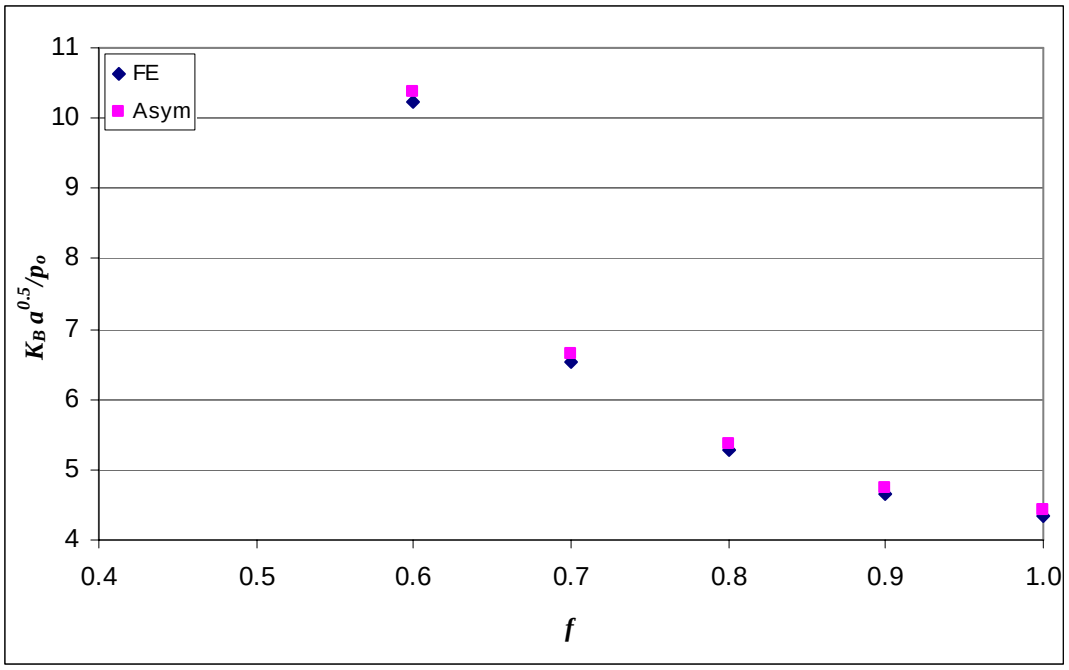

(b)

Figure 6.10 : (a) Normalised separation extent, c/a as a function of the coefficient of friction, f predicted from the asymptotes and the finite element output. (b) Normalised square root bounded asymptote multiplier, $K_B a^{0.5}/p_o$ as a function of the coefficient of friction, f predicted from the asymptotes and the finite element output.

6.6 Conclusions

The most important practical result from this analysis is that, when a square block is slid along an elastically similar half-plane, the leading edge always displays a power order singularity in the tractions, and so does the trailing edge if the coefficient of friction is less than $1/\pi$. If the coefficient of friction exceeds this value (but is still less than 0.392) the contact pressure at the trailing edge becomes power order bounded. Finally, if the coefficient of friction exceeds 0.392 the trailing edge of the contact lifts off and, more importantly, the contact pressure becomes locally square root bounded. The amount of contact lifted is very small, and probably not of practical significance, but the completely changed character of the traction distribution certainly is important. An asymptotic form has

been derived which describes the local behaviour, and which may be readily scaled to fit the solution found from a conventional finite element solution, and considerable detail added. The true local edge traction distribution may be found without further calculation. It has also been shown that the extent of separation at the trailing edge of the contact may be accurately predicted with the benefit of adding detail to a 'rough and ready' finite element solution. The problem, though geometrically very simple, provides another example of a contact which seems, *prima facie*, to be complete in character, but which becomes incomplete when the loading is applied. Indeed, at the true trailing edge point, the local state of stress present is actually similar in form to that at a Hertzian contact. The results also have implications for a 'pin on disk' wear test where, in the early stages, the initial geometry of the pin is preserved, and the contact pressure, along the central plane, is as deduced here.

6.7 Details of calculation described in section 6.3

The tractions at the trailing edge of a sliding punch deduced from the bilateral form of the asymptote are given by:

$$N_1(x) = \sigma^o_{yy}(x,0) = -K_c x^{\zeta-1} \sin\left(\eta \ln\left(\frac{x}{x_o}\right)\right), \tag{6.25a}$$

$$S_1(x) = \sigma^o_{xy}(x,0) = fK_c x^{\zeta-1} \sin\left(\eta \ln\left(\frac{x}{x_o}\right)\right). \tag{6.25b}$$

The state of stress induced along the projection line by an edge dislocation lying in a three-quarter plane, is given by

$$\overline{\sigma}_{yy}(x,\xi) = \frac{2\mu}{\pi(\kappa+1)}\left(\frac{b_x}{\xi} G_{xyy}(\overline{x}) + \frac{b_y}{\xi} G_{yyy}(\overline{x})\right), \tag{6.26a}$$

$$\overline{\sigma}_{xy}(x,\xi) = \frac{2\mu}{\pi(\kappa+1)}\left(\frac{b_x}{\xi} G_{xxy}(\overline{x}) + \frac{b_y}{\xi} G_{yxy}(\overline{x})\right), \tag{6.26b}$$

where

$$G_{xyy}(x,\xi)=\frac{1}{(\bar{x})^{0.4555}+(\bar{x})^{1.45}}\left\{\begin{array}{l}-0.8416+3.602\left(\dfrac{\bar{x}}{1+\bar{x}}\right)\\ -3.146\left(\dfrac{\bar{x}}{1+\bar{x}}\right)^2+0.6288\left(\dfrac{\bar{x}}{1+\bar{x}}\right)^3\end{array}\right\}, \tag{6.27a}$$

$$G_{xxy}(x,\xi)=G_{yyy}(x,\xi)=\frac{1}{\bar{x}-1}+\frac{1}{(\bar{x})^{0.4555}+(\bar{x})^{1}}\left\{\begin{array}{l}-0.365-0.1416\left(\dfrac{\bar{x}}{1+\bar{x}}\right)\\ -3.942\left(\dfrac{\bar{x}}{1+\bar{x}}\right)^2+3.45\left(\dfrac{\bar{x}}{1+\bar{x}}\right)^3\end{array}\right\}, \tag{6.27b}$$

$$G_{yxy}(x,\xi)=\frac{1}{(\bar{x})^{0.4555}+(\bar{x})^{1.45}}\left\{\begin{array}{l}-0.2726-1.016\left(\dfrac{\bar{x}}{1+\bar{x}}\right)\\ +2.333\left(\dfrac{\bar{x}}{1+\bar{x}}\right)^2-0.3687\left(\dfrac{\bar{x}}{1+\bar{x}}\right)^3\end{array}\right\}, \tag{6.27c}$$

$$\bar{x}=\frac{x}{\xi}, \tag{6.27d}$$

b_x, b_y are the components of the Burgers vector, μ is the modulus of rigidity, κ is Kolosov's constant, G_{ijk} are stress influence functions, and ξ is the position of the dislocation. We note that, when conventional frictional contact boundary conditions are restored, separation will be over a length c, which is to be found but is expected to be greater than x_o. Glide dislocations are therefore distributed over the region $0 \le x < \infty$, whilst climb dislocations are distributed only over the interval $0 \le x \le c$, and hence the resultant tractions are

$$\tilde{\sigma}_{yy}=\frac{2\mu}{\pi(\kappa+1)}\left(\int_0^{\infty}\frac{B_x(\xi)G_{xyy}(x,\xi)d\xi}{\xi}+\int_0^{c}\frac{B_y(\xi)G_{yyy}(x,\xi)d\xi}{\xi}\right), \tag{6.28a}$$

$$\tilde{\sigma}_{xy}=\frac{2\mu}{\pi(\kappa+1)}\left(\int_0^{\infty}\frac{B_x(\xi)G_{xxy}(x,\xi)d\xi}{\xi}+\int_0^{c}\frac{B_y(\xi)G_{yxy}(x,\xi)d\xi}{\xi}\right). \tag{6.28b}$$

If we now impose the following boundary conditions

$$\sigma_{yy}(x,0)=\sigma_{yy}^{o}+\tilde{\sigma}_{yy}=0, \qquad 0\le x\le c, \tag{6.29a}$$

$$\sigma_{xy}(x,0) = \sigma_{xy}^{o} + \tilde{\sigma}_{xy} = -f\sigma_{yy}, \quad 0 \le x \le \infty, \tag{6.29b}$$

we arrive at the following pair of coupled Cauchy singular integral equations of the first kind with generalised kernels

$$-K_c x^{\zeta-1}\sin\left(\eta\ln\left(\frac{x}{x_o}\right)\right) + \frac{2\mu}{\pi(\kappa+1)}\left(\begin{array}{l}\displaystyle\int_0^{\infty}\frac{B_x(\xi)G_{xyy}(x,\xi)d\xi}{\xi} \\ \displaystyle+\int_0^{c}\frac{B_y(\xi)G_{yyy}(x,\xi)d\xi}{\xi}\end{array}\right) = 0, \tag{6.30a}$$

$$\begin{aligned} &fK_c x^{\zeta-1}\sin\left(\eta\ln\left(\frac{x}{x_o}\right)\right) + \frac{2\mu}{\pi(\kappa+1)}\left(\int_0^{\infty}\frac{B_x(\xi)G_{xxy}(x,\xi)d\xi}{\xi} + \int_0^{c}\frac{B_y(\xi)G_{yxy}(x,\xi)d\xi}{\xi}\right) \\ &= f\left(K_c x^{\zeta-1}\sin\left(\eta\ln\left(\frac{x}{x_o}\right)\right) - \frac{2\mu}{\pi(\kappa+1)}\left(\begin{array}{l}\displaystyle\int_0^{\infty}\frac{B_x(\xi)G_{xyy}(x,\xi)d\xi}{\xi} \\ \displaystyle+\int_0^{c}\frac{B_y(\xi)G_{yyy}(x,\xi)d\xi}{\xi}\end{array}\right)\right)\times[H(x-c)], \end{aligned} \tag{6.30b}$$

where $H(\cdot)$ is the Heaviside step function. Problems of this type (with slip over a finite interval) have been considered before by Schmueser (Schmueser and Comninou, 1980), whose papers should be consulted for details of their treatment. In order to normalise the intervals involved let

$$\hat{x} = \frac{x}{x_o};\ \hat{c} = \frac{c}{x_o};\ \hat{\xi} = \frac{\xi}{x_o};\ \hat{B}_x\left(\hat{\xi}\right) = \frac{2\mu}{\pi(\kappa+1)}\frac{B_x\left(\hat{\xi}\right)}{K_c x_o^{\zeta-1}};\ \hat{B}_y\left(\hat{\xi}\right) = \frac{2\mu}{\pi(\kappa+1)}\frac{B_y\left(\hat{\xi}\right)}{K_c x_o^{\zeta-1}} \tag{6.31}$$

so that

$$\int_0^{\infty}\frac{\hat{B}_x(\hat{\xi})G_{xyy}(\hat{x},\hat{\xi})d\hat{\xi}}{\hat{\xi}} + \int_0^{\hat{c}}\frac{\hat{B}_y(\hat{\xi})G_{yyy}(\hat{x},\hat{\xi})d\hat{\xi}}{\hat{\xi}} = (\hat{x})^{\zeta-1}\sin\left(\eta\ln\left(\hat{x}\right)\right) \tag{6.32}$$

and

$$\begin{aligned} &\int_0^{\infty}\frac{\hat{B}_x(\hat{\xi})\left(G_{xxy}(\hat{x},\hat{\xi}) + fG_{xyy}(\hat{x},\hat{\xi})H(\hat{x}-\hat{c})\right)d\hat{\xi}}{\hat{\xi}} + \int_0^{\hat{c}}\frac{\hat{B}_y(\hat{\xi})\left(G_{yxy}(\hat{x},\hat{\xi}) + fG_{yyy}(\hat{x},\hat{\xi})H(\hat{x}-\hat{c})\right)d\hat{\xi}}{\hat{\xi}} \\ &= -f(\hat{x})^{\zeta-1}\sin\left(\eta\ln\left(\hat{x}\right)\right) + f(\hat{x})^{\zeta-1}\sin\left(\eta\ln\left(\hat{x}\right)\right)H(\hat{x}-\hat{c}), \end{aligned} \tag{6.33}$$

and carry out a further change of variables by setting:

$$u = \frac{2\hat{\xi}}{\hat{c}} - 1, \tag{6.34a}$$

$$u_1 = 1 - \frac{2}{e^{\hat{\xi}/A}}, \tag{6.34b}$$

$$v = \frac{2\hat{x}}{\hat{c}} - 1, \tag{6.34c}$$

$$v_1 = 1 - \frac{2}{e^{\hat{x}/A}}, \tag{6.34d}$$

where A is a constant. Equations (6.32) and (6.33) are now finally written as:

$$\int_{-1}^{1} \frac{\hat{B}_x(u_1) G_{xyy}(\hat{c}, v, u_1) du_1}{(1-u_1)\ln\left(2/(1-u_1)\right)} + \int_{-1}^{1} \frac{\hat{B}_y(u) G_{yyy}(v, u) du}{u+1} = \left(\frac{\hat{c}}{2}(v+1)\right)^{\zeta-1} \sin\left(\eta \ln\left(\frac{\hat{c}}{2}(v+1)\right)\right), \tag{6.35}$$

$$\begin{aligned}
&\int_{-1}^{1} \frac{\hat{B}_x(u_1)\left(G_{xxy}(v_1, u_1) + fG_{xyy}(v_1, u_1) H(A\ln(2/(1-v_1)) - \hat{c})\right) du_1}{(1-u_1)\ln\left(2/(1-u_1)\right)} \\
&+ \int_{-1}^{1} \frac{\hat{B}_y(u)\left(G_{yxy}(\hat{c}, v_1, u) + fG_{yyy}(\hat{c}, v_1, u) H(A\ln(2/(1-v_1)) - \hat{c})\right) du}{u+1} \\
&= -f\left(A\ln\left(\frac{2}{1-v_1}\right)\right)^{\zeta-1} \sin\left(\eta \ln\left(A\ln\left(\frac{2}{1-v_1}\right)\right)\right) \\
&+ f\left(A\ln\left(\frac{2}{1-v_1}\right)\right)^{\zeta-1} \sin\left(\eta \ln\left(A\ln\left(\frac{2}{1-v_1}\right)\right)\right) H\left(A\ln\left(\frac{2}{1-v_1}\right) - \hat{c}\right).
\end{aligned} \tag{6.36}$$

It is assumed that, adjacent to the contact edge, the dislocation densities display a square root singular form (which is slightly stronger than that actually present), whilst, adjacent to the separation point, the contact pressure must be square root bounded. This is an important consideration, and is consistent with results found for local separation of contact faces in crack problems. Also, the tractions decay in a power order manner, remote from the contact edge. These assumptions mean that we may write the unknown dislocation densities down as the product of fundamental functions incorporating the required characteristics, and well-behaved smooth functions, ϕ_i. Thus, we let

$$\hat{B}_x(u_1) = \phi_x(u_1)\sqrt{\frac{1-u_1}{1+u_1}}, \tag{6.37}$$

$$\hat{B}_y(u) = \phi_y(u)\sqrt{\frac{1-u}{1+u}}\,. \tag{6.38}$$

The discretized form of equations (6.35) and (6.36) are:

$$\begin{aligned}&\sum_{i=1}^{n} W(u_{1i})G_{xyy}(\hat{c}, v_k, u_{1i})\phi_x(u_{1i}) + \sum_{i=1}^{n} W(u_i)G_{yyy}(v_k, u_i)\phi_y(u_i)\\ &= \left(\frac{\hat{c}}{2}(v_k+1)\right)^{\zeta-1} \sin\left(\eta \ln\left(\frac{\hat{c}}{2}(v_k+1)\right)\right),\end{aligned} \tag{6.39}$$

$$\begin{aligned}&\sum_{i=1}^{n} W(u_{1i})\left(G_{xxy}(v_{1k}, u_{1i}) + fG_{xyy}(v_{1k}, u_{1i})H(A\ln(2/(1-v_{1k})) - \hat{c})\right)\phi_x(u_{1i})\\ &+ \sum_{i=1}^{n} W(u_i)\left(G_{yxy}(\hat{c}, v_{1k}, u_i) + fG_{yyy}(\hat{c}, v_{1k}, u_i)H(A\ln(2/(1-v_{1k})) - \hat{c})\right)\phi_y(u_i)\\ &= -f\left(A\ln\left(\frac{2}{1-v_{1k}}\right)\right)^{\zeta-1} \sin\left(\eta\ln\left(A\ln\left(\frac{2}{1-v_{1k}}\right)\right)\right)\\ &+ f\left(A\ln\left(\frac{2}{1-v_{1k}}\right)\right)^{\zeta-1} \sin\left(\eta\ln\left(A\ln\left(\frac{2}{1-v_{1k}}\right)\right)\right) H\left(A\ln\left(\frac{2}{1-v_{1k}}\right) - \hat{c}\right),\end{aligned} \tag{6.40}$$

where

$$u_i = u_{1i} = \cos\left(\pi\frac{2i}{2n+1}\right) \quad \text{for} \quad i = 1,.....,n, \tag{6.41a}$$

$$v_k = v_{1k} = \cos\left(\pi\frac{2k-1}{2n+1}\right) \quad \text{for} \quad k = 1,.....,n, \tag{6.41b}$$

$$W(u_{1i}) = \frac{2\pi}{(2n+1)\ln(2/(1-u_{1i}))}\,, \tag{6.41c}$$

$$W(u_i) = \frac{2\pi(1-u_i)}{(2n+1)(1+u_i)}\,. \tag{6.41d}$$

There are therefore $2n$ simultaneous linear algebraic equations in terms of the $2n$ unknowns $\phi_x(u_{1i})$, $\phi_y(u_i)$. However, there are no additional requirements within the quadrature which enable the ratio c/x_o to be found, and this must be done by imposing additional physical side conditions. The most obvious ones are that, just within the contact, at $x = c + \varepsilon$, the contact pressure must be compressive, and this may be checked whilst, just

exterior to the contact point, at $x = c - \varepsilon$, there must be a positive gap. In fact, the gradient of the relative separation must be positive, i.e. $(dv_1 - dv_2)/dx > 0$. This may be checked from the sign of B_y at this point. In practice these were not found to be particularly sensitive requirements, and the most suitable condition proved to be the imposition of a truly square root bounded traction distribution as the separation point was approached from within the contact.

Chapter 7

Sliding of general frictional complete contacts

7.1 Introduction

An intrinsic feature of any complete contact problem is that it is impossible to separate out the contact problem itself from the stiffness of the remainder of the body, in the way that convex contact problems usually can, and this hampers obtaining a geometry-independent solution in which only the contact front face profile features in the solution. It turns out that the geometry well 'behind' the contact enters the problem only weakly, although the angle the ends of the contact make with the front face has a first order effect. Therefore, only the example problems displayed in Figure 7.1, viz. trapezium shaped plane bodies with internal angles of 60^0, 90^0 and 120^0 will be examined in detail.

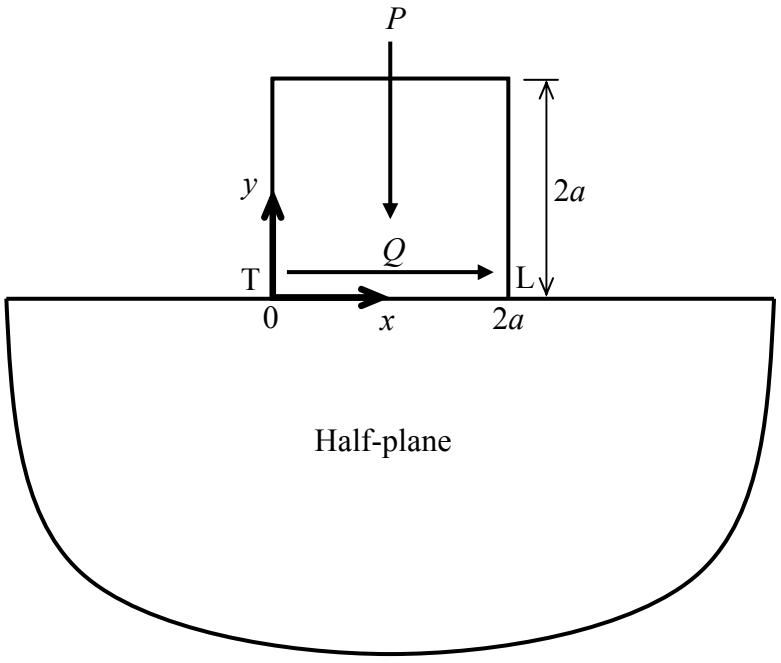

(a)

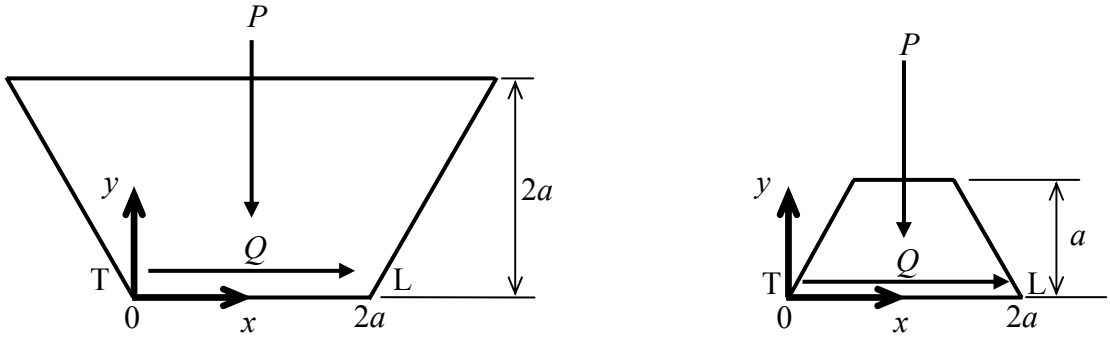

(b) (c)

Figure 7.1 : Geometry of the problem solved - elastic punches of internal angles (a) 90^0 (b) 120^0 (c) 60^0, of contact length *2a*, sliding on an elastically similar half-plane.

In fact, the 90^0 punch has already been studied in great detail in chapter 6 and will not be repeated here. The purpose of this chapter is to build upon the results developed there, to understand how the contact angle, φ, and coefficient of friction, f, determine the characteristics of the resulting pressure distribution.

7.2 Asymptotic solution

The key equations from the sliding semi-infinite wedge problem, studied by Gdoutos and Theocaris (1975), and by Comninou (1976), will be briefly described here. The state of stress near the edge of a contact is in the form

$$\sigma_{ij} \sim r^{\lambda-1} f_{ij}(\theta)\,. \tag{7.1}$$

The value of λ is determined from the characteristic equation given below

$$\begin{aligned}\nabla(\varphi, f, \alpha, \beta; \lambda) = (1+\alpha)\cos\lambda\pi(\sin^2\lambda\varphi - \lambda^2\sin^2\varphi) + 0.5(1-\alpha)\sin\lambda\pi(\sin 2\lambda\varphi + \lambda\sin 2\varphi) \\ + f\sin\lambda\pi\left\{(1-\alpha)\lambda(1+\lambda)\sin^2\varphi - 2\beta(\sin^2\lambda\varphi - \lambda^2\sin^2\varphi)\right\} = 0\,.\end{aligned} \tag{7.2}$$

This equation is a function of the internal wedge angle, φ, coefficient of friction f and Dundurs parameters α, β that describe the elastic mismatch between the wedge and

half-plane. For the case where the wedge and the half-plane have the same elastic constants (and this is the only case considered here), the Dundurs parameters are equal to zero and the characteristic equation therefore becomes

$$\nabla(\varphi, f, 0, 0; \lambda) = \cos\lambda\pi\,(\sin^2\lambda\varphi - \lambda^2\sin^2\varphi) + 0.5\sin\lambda\pi(\sin 2\lambda\varphi + \lambda\sin 2\varphi) + f\sin\lambda\pi\,(\lambda(1+\lambda)\sin^2\varphi) = 0\,. \tag{7.3}$$

The most useful property of the contact to emerge from this analysis is the dominant behaviour of the contact stress field and, in particular, the local contact pressure distribution, which is governed by the smallest value of λ which satisfies equation (7.3).

7.2.1 120^0 punch

The eigenvalues for a 120^0 punch, shown in Figure 7.1(b), are determined by substituting $\varphi = 2\pi/3$ into equation (7.3) giving

$$\cos\lambda\pi\left(\sin^2\left[\lambda\frac{2\pi}{3}\right] - \lambda^2\sin^2\left[\frac{2\pi}{3}\right]\right) + 0.5\sin\lambda\pi\left(\sin\left[\frac{4\pi\lambda}{3}\right] + \lambda\sin\left[\frac{4\pi}{3}\right]\right) + f\lambda(1+\lambda)\sin[\lambda\pi]\sin^2\left[\frac{2\pi}{3}\right] = 0\,. \tag{7.4}$$

These eigenvalues are given in Figure 7.2. Thus, for practically arising coefficients of friction there is always power order singular behaviour at both edges of the contact, and this is therefore a much more straightforward problem to understand than the 90^0 punch.

.

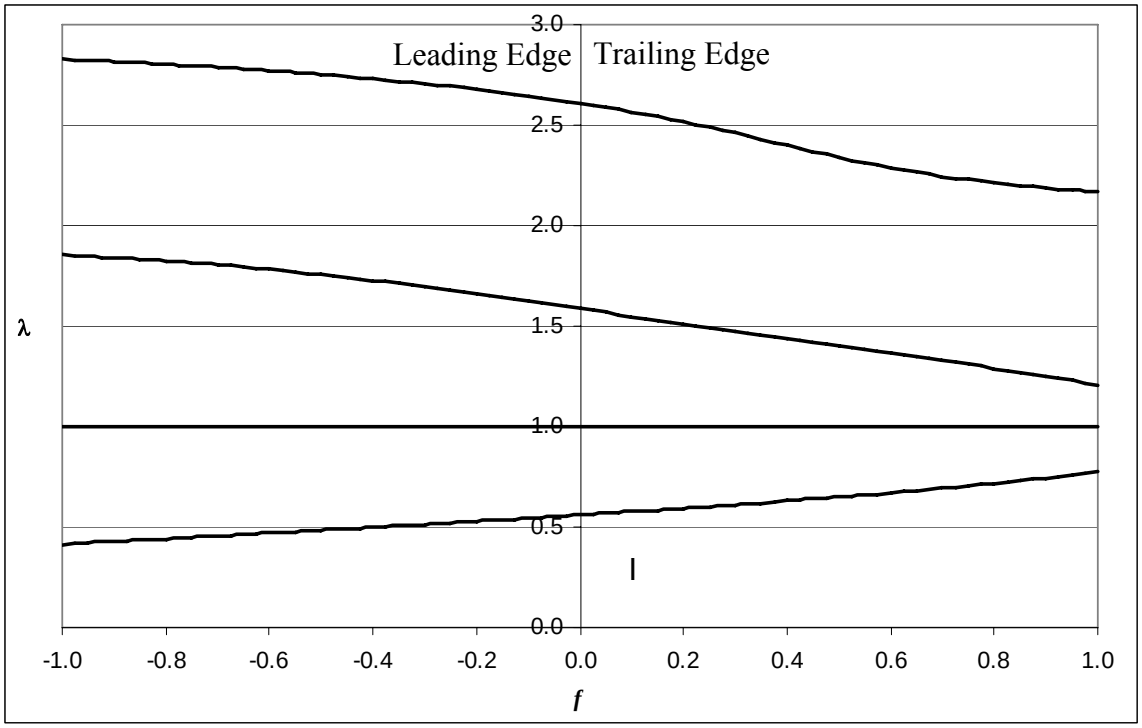

Figure 7.2 : The slipping eigenvalues, λ as a function of the coefficient of friction, f for a 120^0 wedge.

7.2.2 60^0 punch

This punch, shown in Figure 7.1(c), has the dominant eigenvalue characteristic displayed in Figure 7.3. These eigenvalues are determined by substituting $\varphi = \pi/3$ into equation (7.3) giving

$$\begin{aligned}&\cos\lambda\pi\left(\sin^2\left[\lambda\frac{\pi}{3}\right]-\lambda^2\sin^2\left[\frac{\pi}{3}\right]\right)+0.5\sin\lambda\pi\left(\sin\left[\frac{2\pi\lambda}{3}\right]+\lambda\sin\left[\frac{2\pi}{3}\right]\right)\\&+f\lambda(1+\lambda)\sin[\lambda\pi]\sin^2\left[\frac{\pi}{3}\right]=0\end{aligned}\quad . \qquad (7.5)$$

It should be compared with the ones for the 90^0 and 120^0 cases to establish the trend in movement of the roots, and we shall return to this point more fully later. Here, power order singular behaviour at the *leading* edge occurs only if the coefficient of friction is moderately large ($|f| \gtrsim 0.451$), whilst for slightly lower coefficients of friction ($0.219 \lesssim |f| \lesssim 0.451$) the behaviour is power order bounded. For lower coefficients of friction the eigenvalue is

complex, implying separation. At the *trailing* edge (positive values of the coefficent of friction), the dominant root is always complex, implying oscillatory behaviour within the framework of bilateral boundary conditions and hence, when the unilateral (Signorini) conditions are restored, separation and square root bounded behaviour are expected.

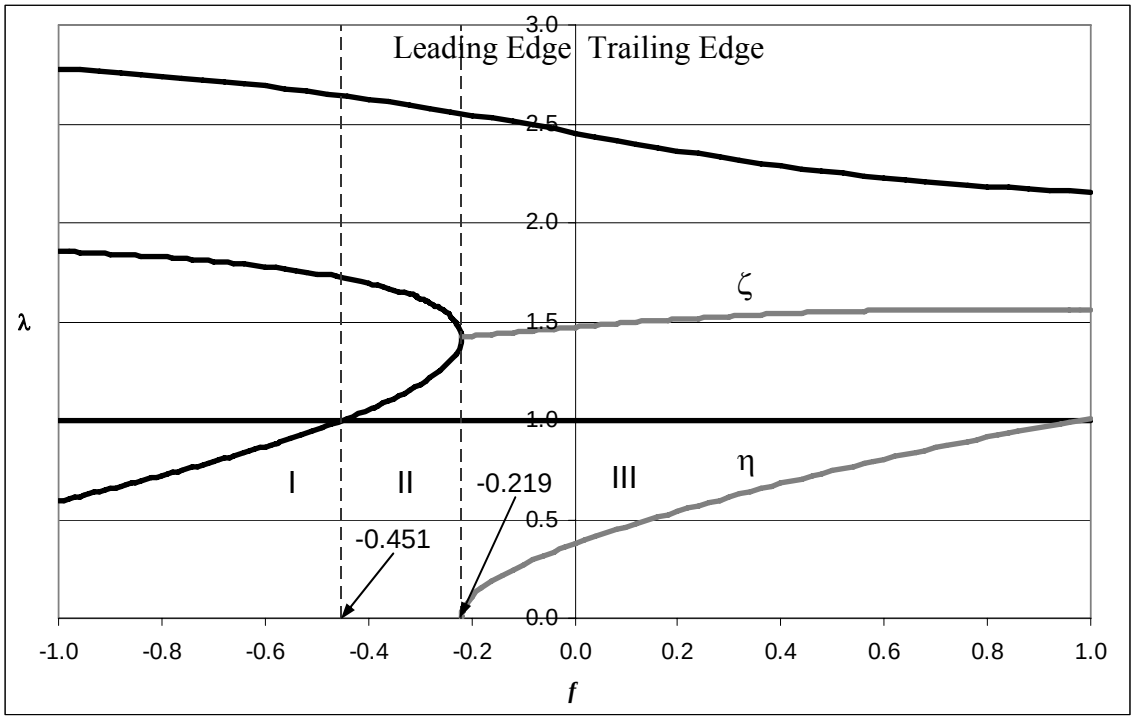

Figure 7.3 : The slipping eigenvalues, λ as a function of the coefficient of friction, f for a 60^0 wedge.

7.3 Finite element analysis

7.3.1 120^0 punch

The problem under consideration, shown in Figure 7.1(b), was analysed using the commercial finite element programme *ABAQUS*. The finite element model employed is shown schematically in Figure 7.4(a). The normal force P was applied as a distributed load p_o ($p_o = P/2a$) along the upper surface of the punch. The distribution of the normal load was confined to a length $2a$ which is parallel to and directly above the contact interface. This was done to avoid any unwanted bending in the punch caused if the load was applied along the 'wings'. The shearing force Q was then applied as a distributed shearing traction q_o ($q_o = Q/2a$) at the upper surface of the punch, together with a distributed anticlockwise moment, of resultant magnitude $2Qa$, in order to render the shearing force statically equivalent to one applied in the plane of the contact, and therefore to remove any overturning moment. These loads were also confined to a length $2a$ in order to be consistent with the normal load.

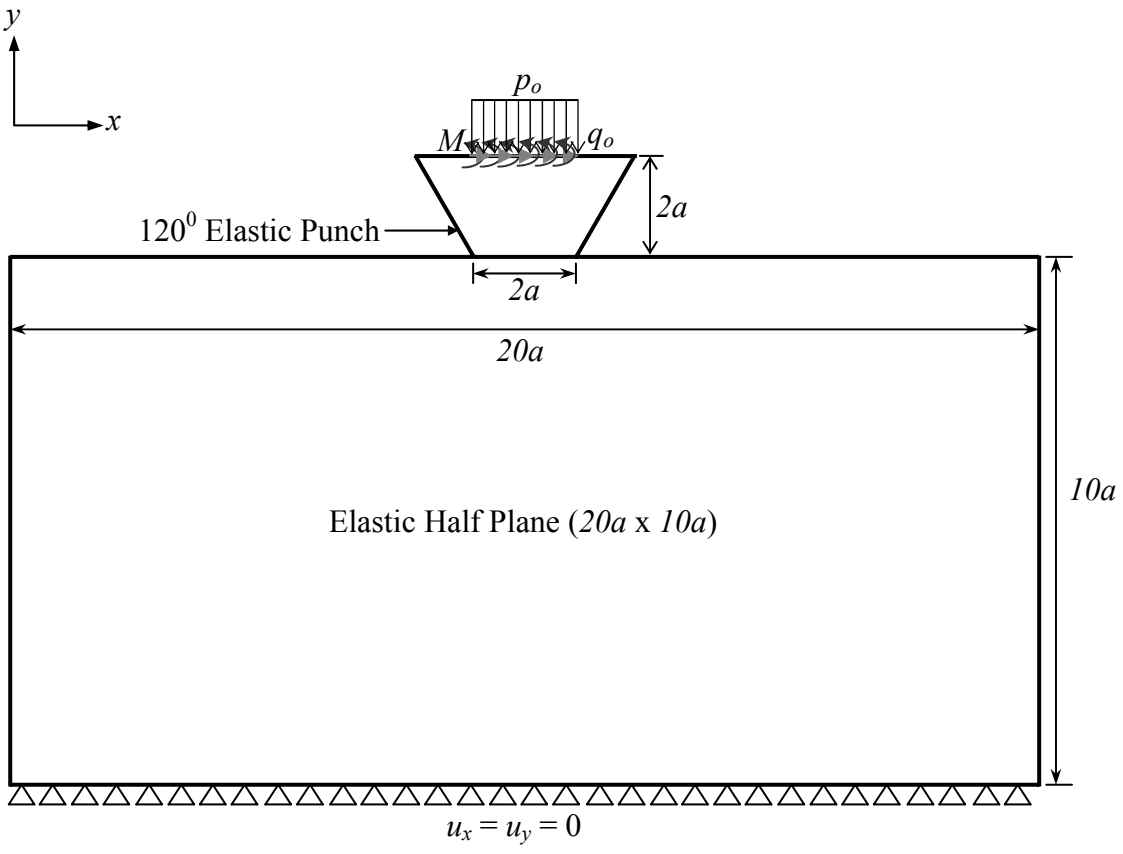

(a)

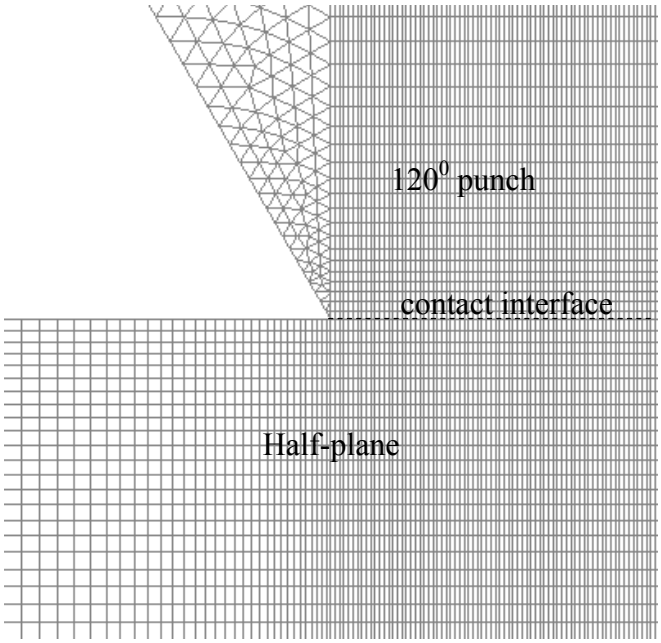

(b)

Figure 7.4 : (a) Geometry of the FE model for the 120^0 punch problem (b) Quality of the mesh at the contact edges

A total of approximately 124,000 elements (with slightly over 124,000 nodes) were used, giving nearly 248,000 degrees of freedom. There were 600 first order (linear) four-noded quadrilateral elements along the line of the contact interface, with the length of element at the contact edge reduced to $1 \times 10^{-3}a$. The quality of the mesh used at the contact edges for this problem is shown in Figure 7.4(b).

The results for the pressure distribution found are shown in Figure 7.5(a). This displays the power order singular behaviour anticipated, at both ends of the contact. Figure 7.5(b) shows the calibration found for the multiplier, K_s, on the power-order asymptotic form at the edges of the contact.

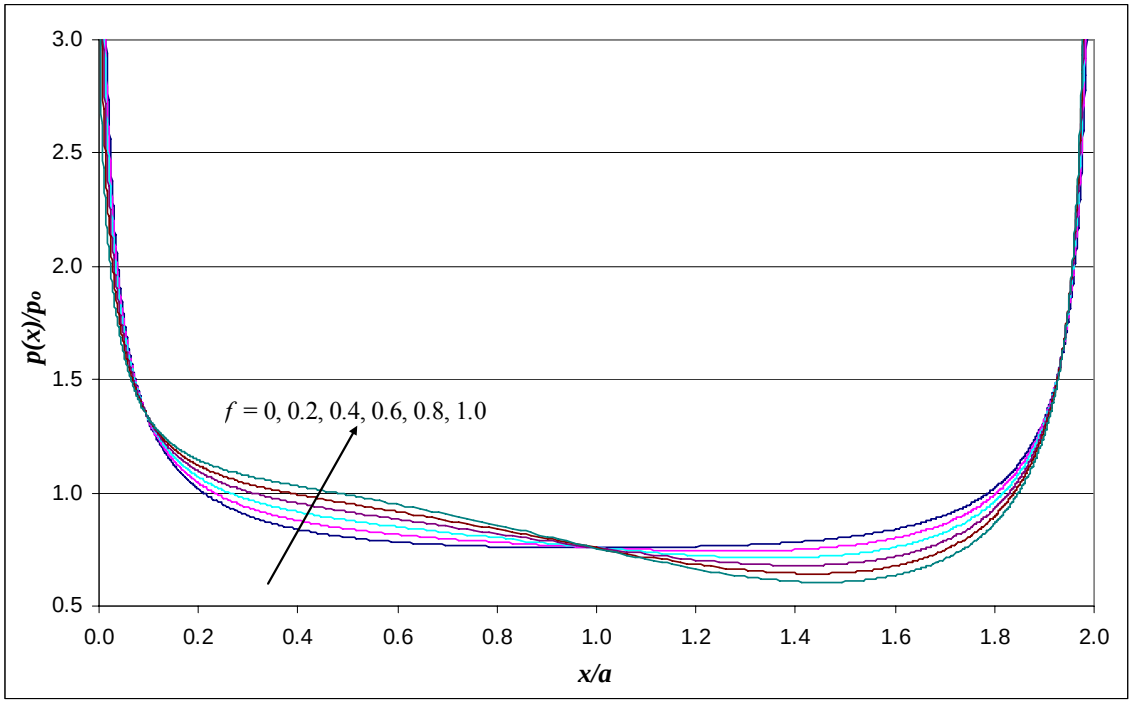

(a)

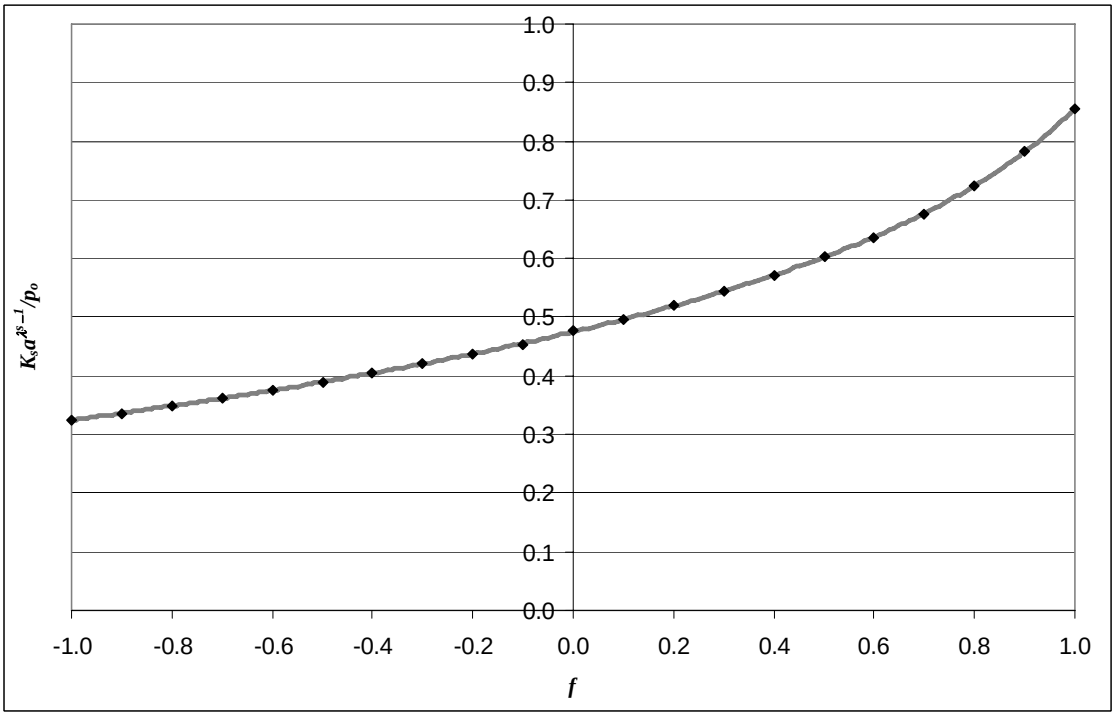

(b)

Figure 7.5 : (a) Normalised contact pressure distribution along the interface for the 120^0 punch problem. (b) Generalised stress intensity factor as a function of the coefficient of friction, f for the 120^0 punch problem.

7.3.2 60^0 punch

A finite element model of the problem, shown in Figure 7.1(c), was constructed within *ABAQUS*, and as shown schematically in Figure 7.6(a). As for the case of 120^0 punch problem, the normal force, P, and the shearing force, Q, sufficient to cause sliding, were applied as distributed loads p_o ($p_o = P/2a(1-\cot(\pi/3))$ and q_o ($q_o = Q/2a(1-\cot(\pi/3))$, respectively, along the upper surface of the punch. A distributed anticlockwise moment, of resultant magnitude Qa, was again applied along the upper surface of the punch, to ensure the shearing force is statically equivalent to one applied in the plane of the contact, and therefore to remove any overturning moment. A total of approximately 122,000 elements (with slightly over 122,000 nodes) were used, giving nearly 244,000 degrees of freedom. There were 600 first order (linear) four-noded quadrilateral elements along the line of the contact interface, with the length of element at the contact edge reduced to $1 \times 10^{-3}a$. Figure 7.6(b) shows the quality of the mesh used at the contact edges for this problem.

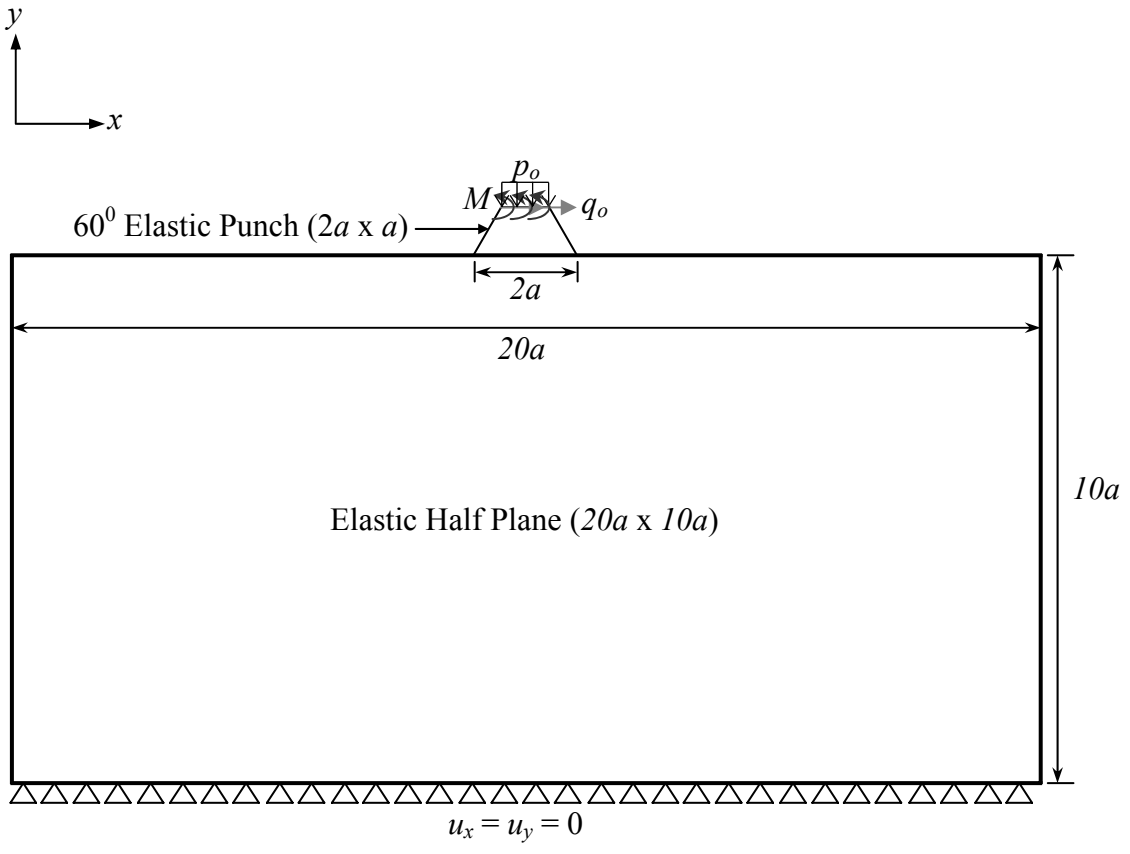

(a)

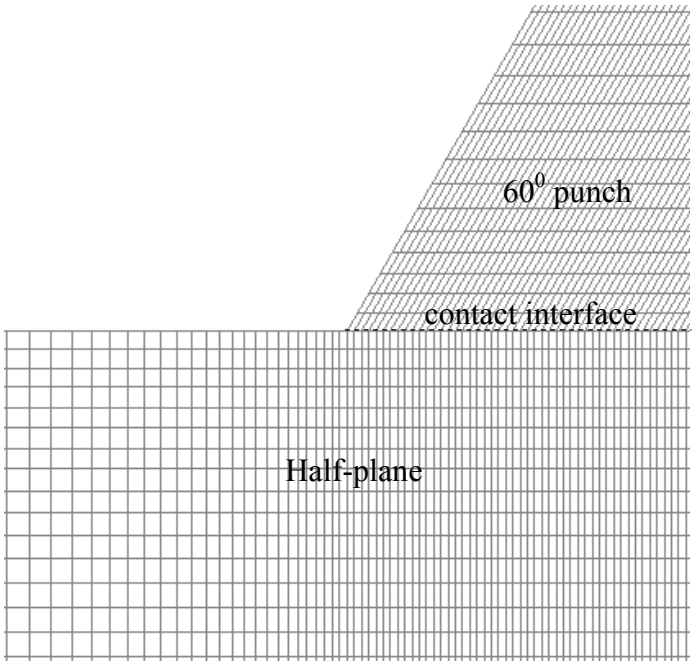

(b)

Figure 7.6 : (a) Geometry of the FE model for the 60^0 punch problem (b) Quality of the mesh at the contact edges

Figure 7.7 shows the results of the contact pressure distribution found, displaying the behaviour which is as anticipated. In region I, the power order singular behaviour is found and the calibration for the multiplier, K_s, on the power-order asymptotic form, is shown in Figure 7.8. In region II, the power order bounded behaviour is found and the normalised asymptotic multipliers, $K_{b1}a^{\lambda_{b1}-1}/p_o$ and $K_{b2}a^{\lambda_{b2}-1}/p_o$, are shown in Figure 7.9. Finally in region III, separation near the contact edge is found, and therefore square root bounded behaviour is expected. The normalised inner asymptotic multiplier, $K_B\sqrt{a}/p_o$, and also the normalised outer asymptotic multiplier, $K_c a^{\zeta-1}/p_o$, for this problem are shown in Figure 7.10(a) and Figure 7.10(b), respectively. In Figure 7.10(c), the extent of separation found from the unilateral finite element solution is shown. It would be entirely possible to use a bilateral finite element model (requiring the two bodies to remain in contact throughout their entire length), followed by the procedure to restore separation condition within the asymptote, as was done for the 90^0 punch problem in chapter 6. However, here the

separation distances are often quite large, particularly at the trailing edge, as can be seen, and there therefore seems little point in pursuing this refinement.

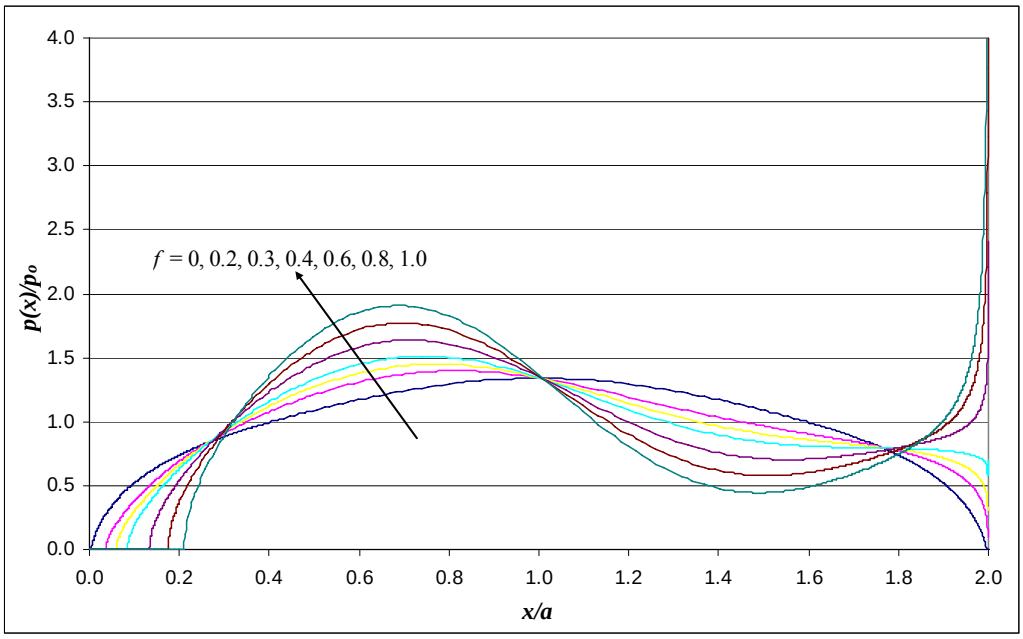

Figure 7.7 : Normalised contact pressure distribution along the interface for the 60^0 punch problem

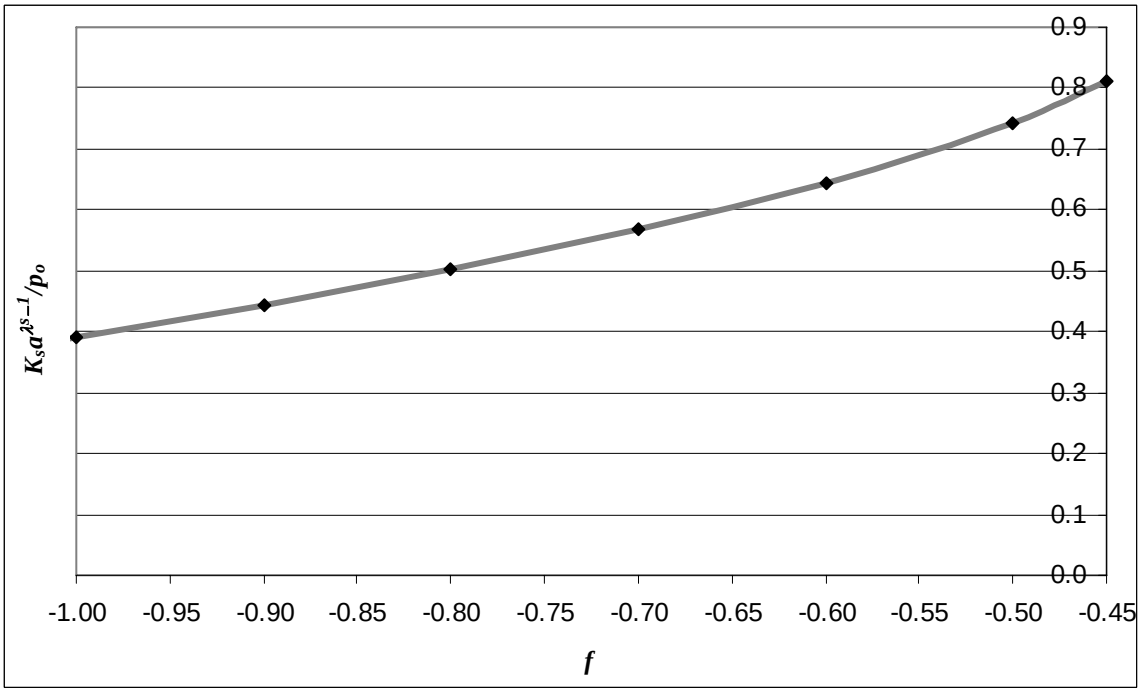

Figure 7.8 : Generalised stress intensity factor as a function of the coefficient of friction, f for the 60^0 punch problem.

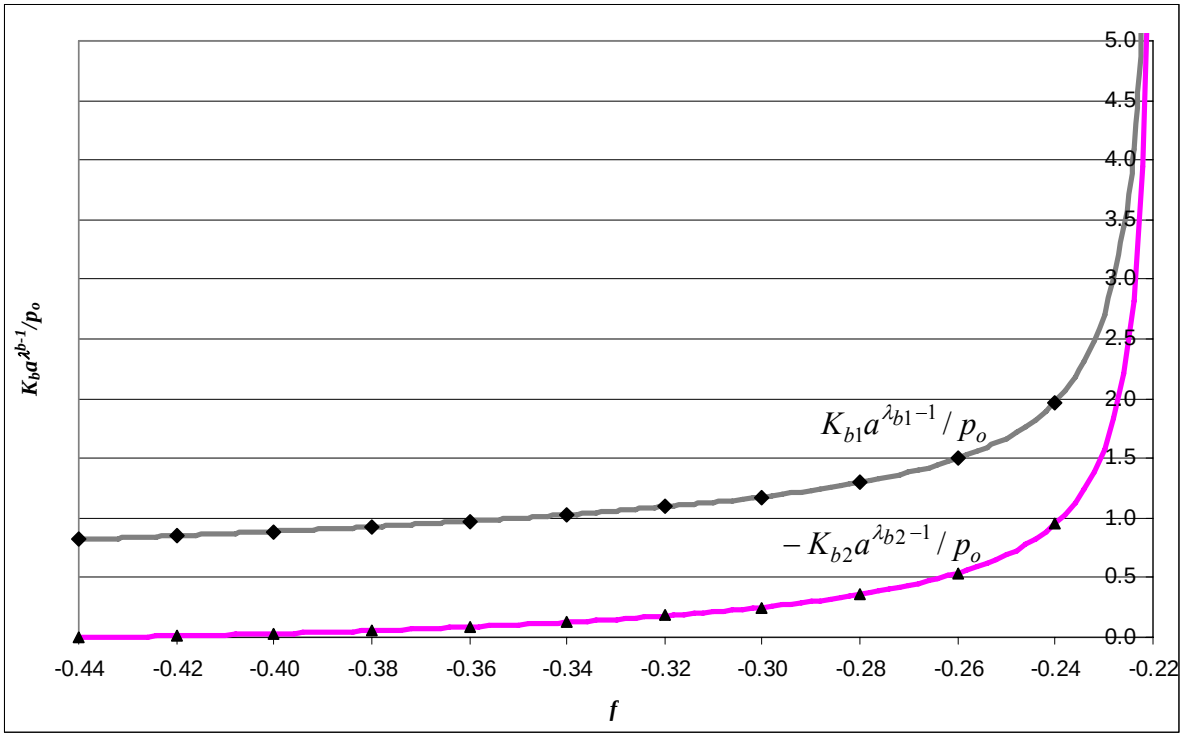

Figure 7.9 : Normalised power order bounded asymptotic multipliers as a function of the coefficient of friction, f for the 60^0 punch problem.

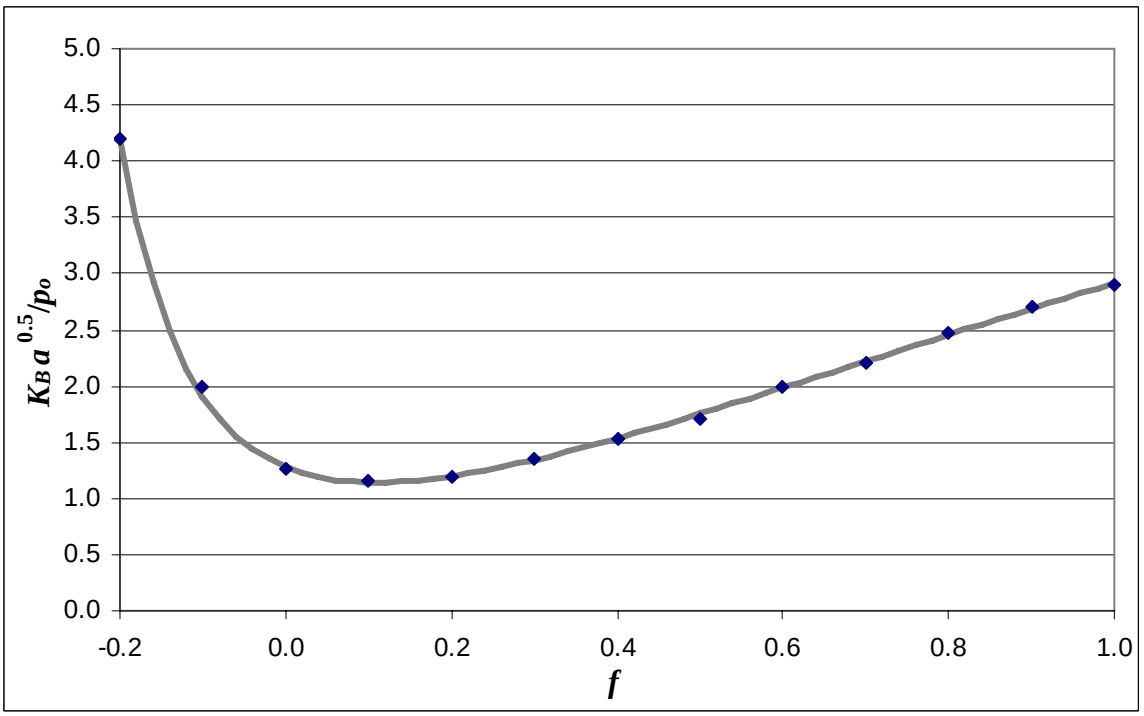

Figure 7.10(a) : Normalised inner asymptotic multiplier as a function of the coefficient of friction, f for the 60^0 punch problem.

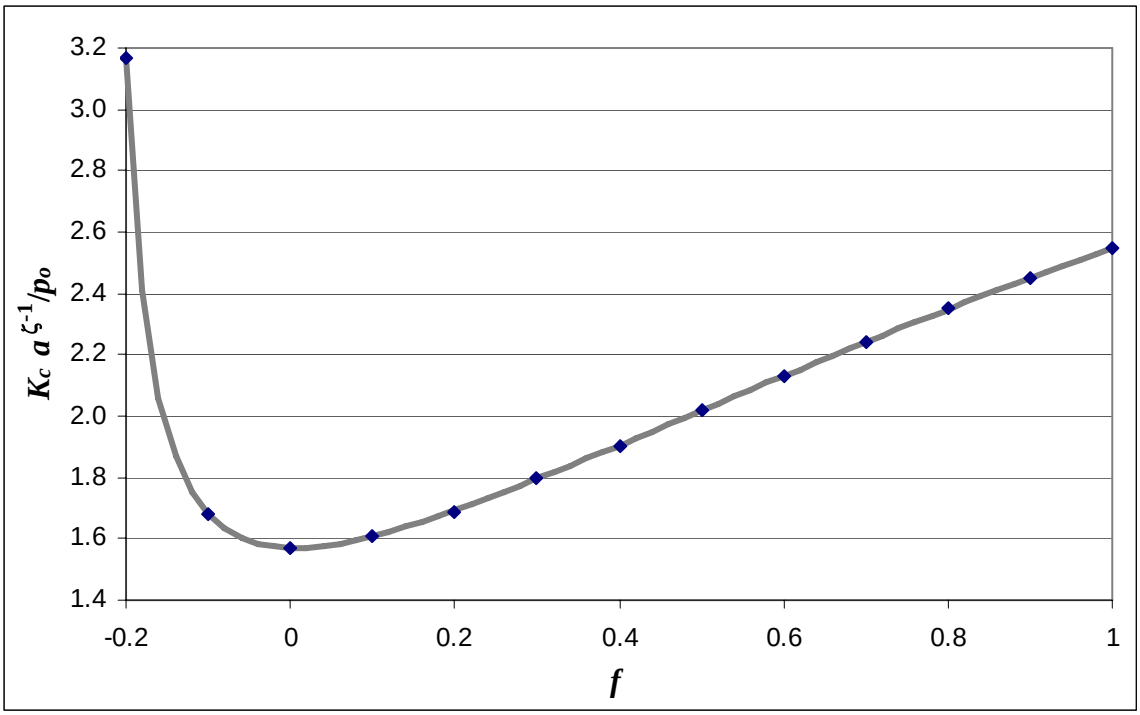

Figure 7.10(b) : Normalised outer asymptotic multiplier as a function of the coefficient of friction, f for the 60^0 punch problem.

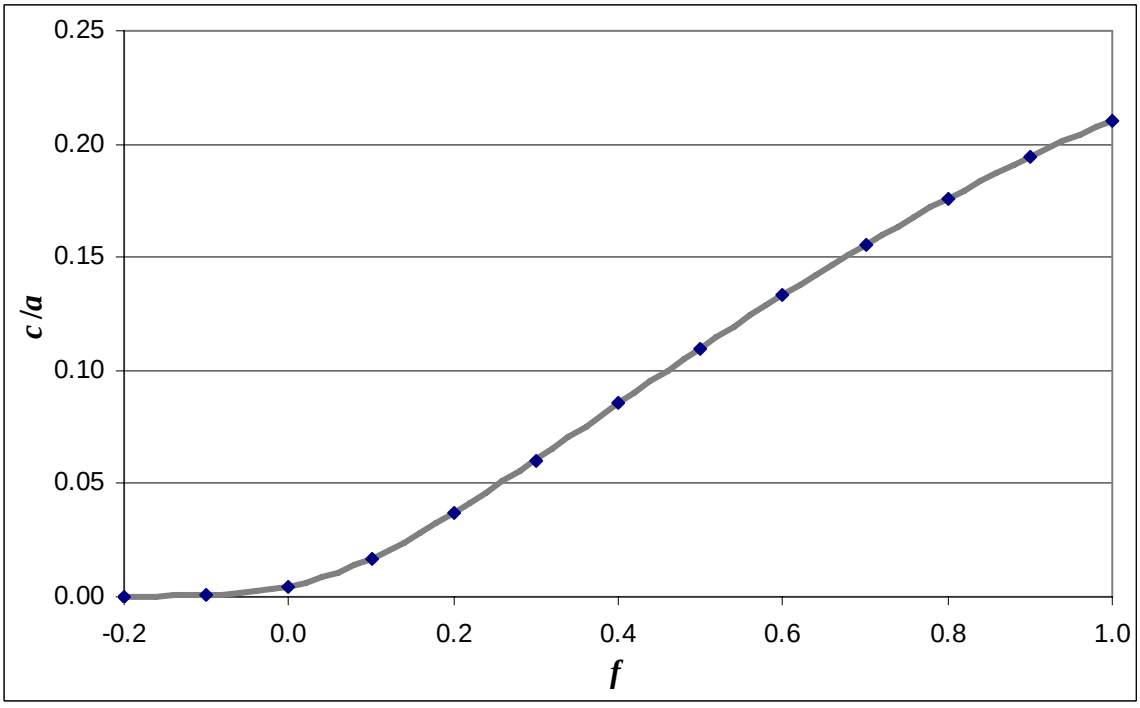

Figure 7.10(c) : Normalised separation extent as a function of the coefficient of friction, f from the unilateral finite element output for the 60^0 punch problem.

7.4 General solution and behaviour

Guided by the results already found, the behaviour to be expected over a wide range of wedge contact angles and coefficients of friction is now investigated, by considering the properties of the roots of the characteristic equation more fully. Figure 7.11(a) shows the type of eigenvector and edge behaviour found for a range of wedge angles, and with a coefficient of friction less than unity. Above the dark line the dominant root is in the range $0 < \lambda < 1$, giving singular behaviour, between the dark and the grey line the dominant root is in the range $1 < \lambda < 2$ and is wholly real, giving power order bounded behaviour, whilst below the grey line the dominant root is complex, leading to separation. It is helpful to consider the graph in this form first, but we can then fold it in half to obtain the overall 'map' of responses shown in Figure 7.11(b), and the key to this, Figure 7.11(c). It is apparent that there are a total of six possible regimes which may exist, as any of the three possible kinds of edge behaviour may arise at either the leading or trailing edge.

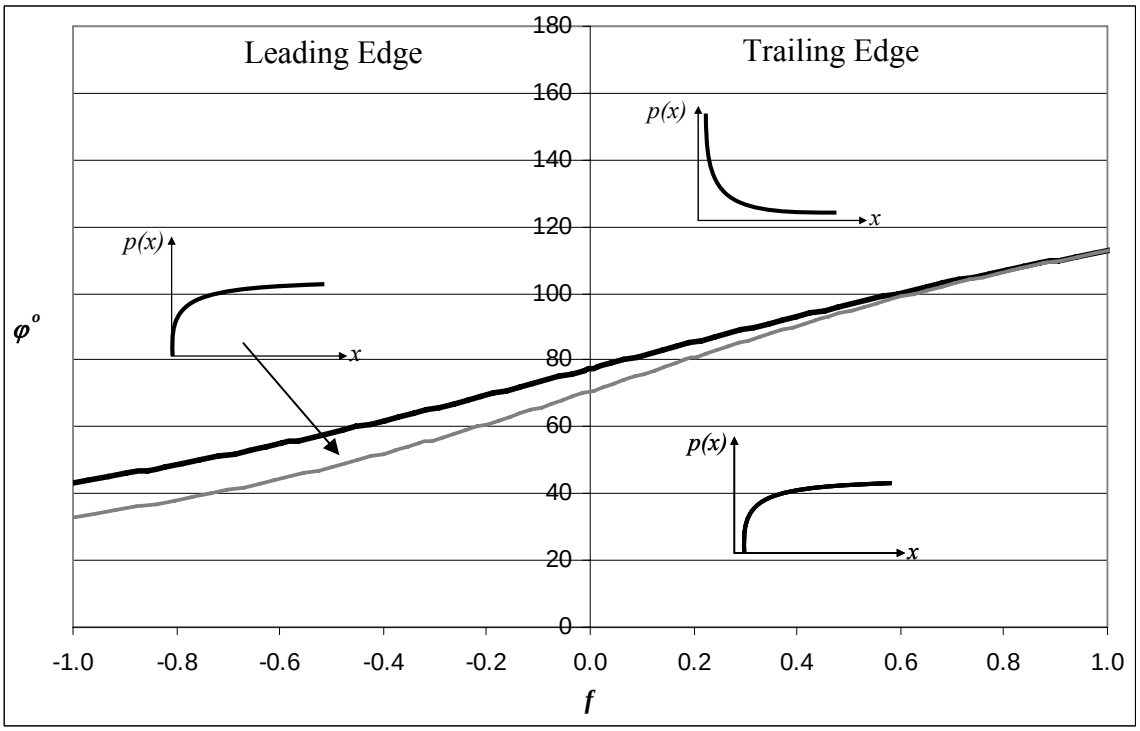

Figure 7.11(a) : Type of eigenvector and edge behaviour for a range of wedge angles, φ^o

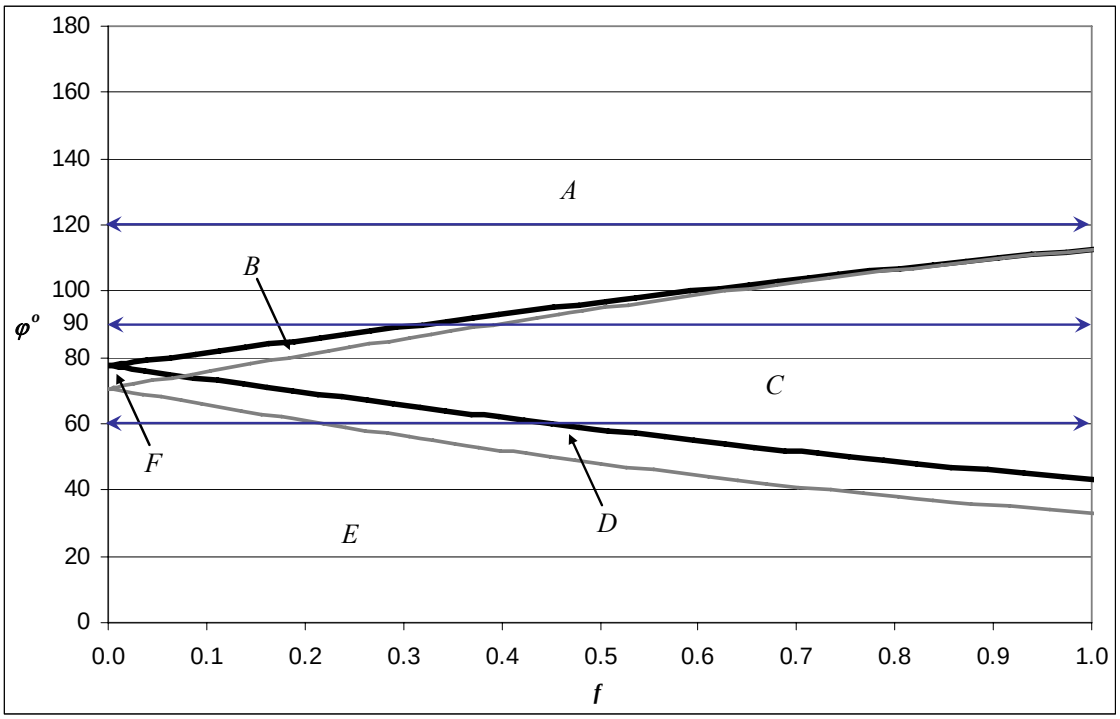

Figure 7.11(b) : Overall map of the contact edge responses showing 6 distinct regions

In Region *A*, the traction behaviour at both contact edges is singular with a stronger singularity at the leading edge. For the range of *f* considered here, this type of behaviour is expected for wedge angle $\varphi \gtrsim 113^0$. In Region *B*, the trailing edge tractions behaviour is power order bounded whilst singular behaviour is still expected at the leading edge. In Region *C*, the trailing edge of the contact lifts off and, more importantly, the tractions become locally square root bounded whilst singular behaviour is retained at the leading edge. In Region *D*, the trailing edge of the contact lifts off but power order bounded behaviour is expected at the leading edge. In Region *E*, both contact edges lift off with trailing edge lifting off over a greater distance. For the range of *f* considered here, this type of behaviour is expected for wedge angle $\varphi \lesssim 33^0$. Finally in Region *F*, both contact edges are expected to exhibit power order bounded behaviour. Also highlighted on Figure 7.11(b) are the three angles studied in detail, showing that; (a) the 120^0 punch exhibits only Region *A* behaviour, (b) the 90^0 punch exhibits Region *A*, *B* or *C* behaviour, as the coefficient of friction is increased, and (c) the 60^0 punch exhibits Region *E*, *D* or *C* behaviour with increasing friction. This covers all the kinds of possible response save for Region *F* which is

confined to extremely low coefficients of friction and an internal contact angle of about 75^0, so it is unlikely to arise very frequently.

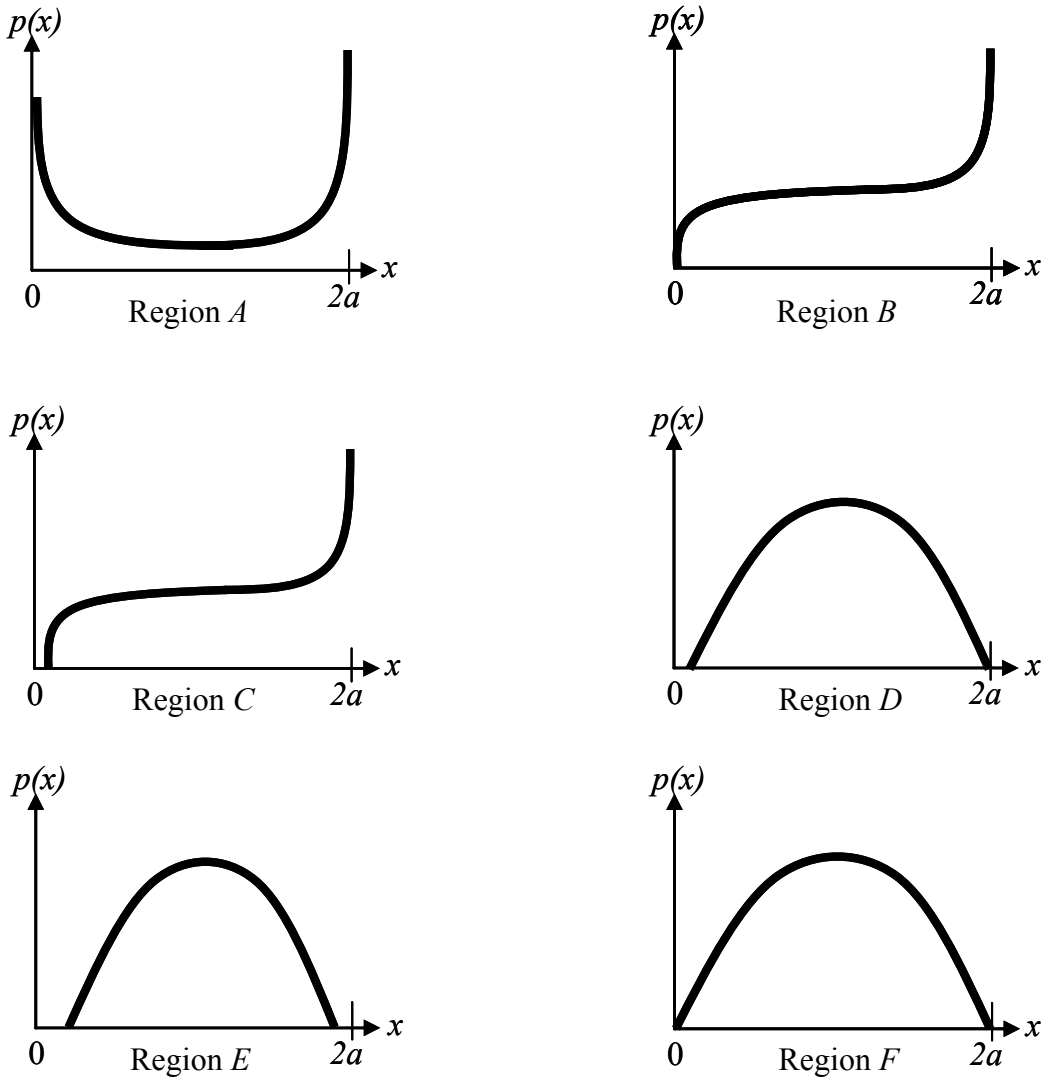

Figure 7.11(c) : Various types of contact pressure behaviour at the edge of complete contacts

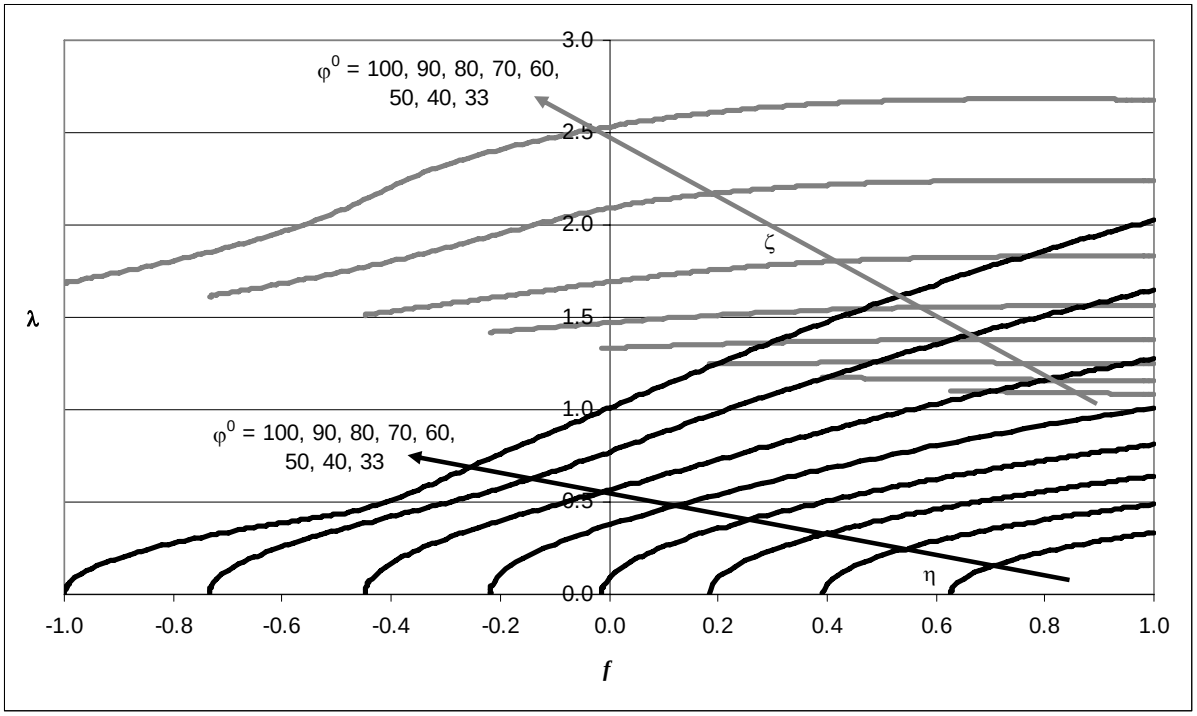

Figure 7.12 : Real and imaginary parts plot for complex roots

Lastly, in Figure 7.12 the real (ζ) and imaginary (η) parts of the root of the characteristic equation are displayed when the dominant root is complex. When the internal angle is large the real part of the root remains almost constant as the coefficient of friction is increased, whilst for smaller internal angles the real part increases with the value of f. The imaginary part of the complex roots increases rapidly with decreasing wedge angle. The extent of separation is proportional to the value of η, and is therefore greater, in general terms, for smaller values of φ.

7.5 Conclusions

The interfacial contact pressure distribution beneath a complete sliding contact between elastically similar components has been studied, with particular reference to contacts whose edge angles are 60^0, 90^0 (see chapter 6) and 120^0. These display a range of responses, depending on the coefficient of friction. In general terms, for angles near the centre of the

range studied, the leading edge will be singular whilst the trailing edge will exhibit singular behaviour if the coefficient of friction is low, but will tend to separate at higher coefficients of friction. The details of the behaviour require a careful study of the characteristic equation, but these results show that the kinds of pressure distribution to be anticipated can vary very markedly, and are quite different from what would be expected if the body defining the size of the contact were rigid, and simple half-plane theory were used.

Chapter 8

Monotonic and cyclic loading of static frictional complete contacts

8.1 Introduction

Fretting fatigue is concerned with the nucleation of a crack by small amounts of differential motion between contacting bodies. It is one of the more insidious ways in which cracks can form, because there may be no apparent slip taking place, and yet cracks may originate much sooner than anticipated. It is therefore important to have a detailed knowledge of the precise interface conditions: if the contact is adhered (particularly adjacent to the edges) there can be no fretting damage, and thus the role of contact in accelerating nucleation is merely because it acts as a stress concentration (if the contact is incomplete in nature) or almost certainly as a stress intensification if the contact is complete. A full understanding of the behaviour of an incomplete contact, exemplified by the Hertz geometry, has been known under conditions of sequential normal and tangential loading for about seventy years (Cattaneo, 1938), and the simpler case of proportional loading has been analysed by Maw *et al.* (1976), as well as being described in Johnson's book (1985). The corresponding problems for complete contact have received little attention because, as described in previous chapters, if the bodies are elastically similar, it is not possible to represent the contact-defining body as a half-plane, and hence it is tricky to obtain an analytical solution. It might be thought that the use of a finite element model would make good this deficiency, and in principle this is so, but because there is often an implied singularity in the state of stress at the contact edges it is not easy to obtain the necessary resolution, and obtain convergence, without taking precautions. An alternative way of handling the contact-edge conditions is to employ asymptotic solutions; the relevant ones in this field are the classic

Williams solution (1952), appropriate when the bodies are adhered, and the more recent results found by Theocaris and Gdoutos (1975) and by Comninou (1976), when the contact edge slips. When the latter were discovered it was not completely clear what they implied for finite bodies, and it is only by combining the two approaches that a full understanding of how example finite complete contacts do respond to sequential normal and shear loading has become possible.

Recently, the response when a square block is pressed normally onto a half-plane, and subsequently subjected to monotonically increasing, (and reversing) shear was considered in some detail by Churchman and Hills (2006a). This type of contact problem was also been studied independently by Bohorquez and Dominguez (2005, 2007). A feature of complete contacts is that, because the half-plane idealisation cannot be applied to one of the bodies, the contact problem cannot, formally, be separated from a consideration of the load path in the rest of the body. However, it is normally assumed that the details of the geometry remote from the contact front face will have only a weak effect on the solution, and this may be exploited by ensuring that the applied forces are imposed as distributed tractions along the top face of component, remote from the contact interface, with a distributed moment to make the shear statically equivalent to one passing through the plane of the contact interface. One property of the geometry which does have a first order effect on the solution is the angle which the end faces of the contact make, as this materially affects the properties of the asymptotic solutions. To avoid the problems of having two local length scales which would occur if the contacts were chamfered, we will, here, concentrate on the cases where the contact ends are plane, and hence the contacting body is trapezium in form[*]. The trapezium shaped bodies under consideration here are similar to those shown in Figure 7.1 (so it is not repeated here). They were analysed using the commercial finite

[*] If the contact is chamfered the local contact edge chamfer angle can be expected to control the state of stress over a length less than the length of the chamfer, whilst the angle of the end faces beyond will have a correspondingly longer range influence.

element programme *ABAQUS*. In this chapter, the monotonically increasing shear problem is addressed first, followed by the cyclic shear problem.

8.2 Asymptotic solution

The basic asymptotic forms needed for the analysis that will follow have already been described in detail in chapter 4. Here, a summary of the key equations will be given for convenience.

8.2.1 Adhered asymptote

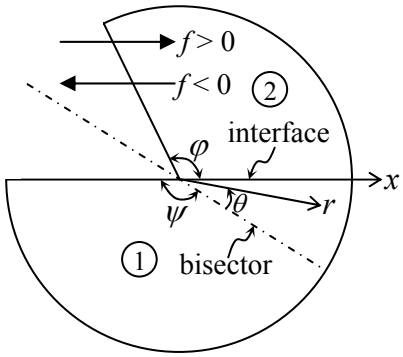

Figure 8.1 : Semi-infinite wedge geometry

First, assume that the whole of the contact interface is adhered. It follows that, adjacent to the contact edges, the state of stress may be represented by Williams solution for a wedge of total internal angle $\pi + \varphi$ radians, where φ is the contact internal angle (Figure 8.1). The direct ($p(x)$) and shear ($q(x)$) tractions in this neighbourhood may be written down as

$$-p(x) = \sigma_{\theta\theta}\left(r, \frac{\pi-\varphi}{2}\right) = K_I^o x^{\lambda_I - 1} + K_{II}^o x^{\lambda_{II} - 1}, \tag{8.1a}$$

$$q(x) = \sigma_{r\theta}\left(r, \frac{\pi-\varphi}{2}\right) = K_I^o x^{\lambda_I - 1} g_{r\theta}^I + K_{II}^o x^{\lambda_{II} - 1} g_{r\theta}^{II}, \tag{8.1b}$$

where λ_I, λ_{II} are solutions of the following characteristic equations

$$\lambda_I \sin[\pi+\varphi]+\sin[\lambda_I(\pi+\varphi)]=0\,, \tag{8.2a}$$

$$\lambda_{II} \sin[\pi+\varphi]-\sin[\lambda_{II}(\pi+\varphi)]=0\,, \tag{8.2b}$$

and the functions $g^I_{r\theta}$, $g^{II}_{r\theta}$, which effectively define the eigenvectors, are given in closed form by

$$g^I_{r\theta}=\frac{\sin[(\lambda_I+1)(\pi-\varphi)/2]-\Gamma^s_I\sin[(\lambda_I-1)(\pi-\varphi)/2]}{\cos[(\lambda_I+1)(\pi-\varphi)/2]-\Gamma^c_I\cos[(\lambda_I-1)(\pi-\varphi)/2]}, \tag{8.3a}$$

$$g^{II}_{r\theta}=\frac{-\cos[(\lambda_{II}+1)(\pi-\varphi)/2]+\Gamma^c_{II}\cos[(\lambda_{II}-1)(\pi-\varphi)/2]}{\sin[(\lambda_{II}+1)(\pi-\varphi)/2]-\Gamma^s_{II}\sin[(\lambda_{II}-1)(\pi-\varphi)/2]}, \tag{8.3b}$$

where

$$\Gamma^s_i=\frac{\sin[(\lambda_i+1)(\pi+\varphi)/2]}{\sin[(\lambda_i-1)(\pi+\varphi)/2]},\quad \Gamma^c_i=\frac{\cos[(\lambda_i+1)(\pi+\varphi)/2]}{\cos[(\lambda_i-1)(\pi+\varphi)/2]}. \tag{8.4}$$

K^o_I and K^o_{II} are the generalised stress intensity factors given by

$$K^o_I=K_I\frac{\cos[(\lambda_I+1)(\pi-\varphi)/2]\cos[(\lambda_I-1)\psi]-\cos[(\lambda_I+1)\psi]\cos[(\lambda_I-1)(\pi-\varphi)/2]}{\cos[(\lambda_I-1)\psi]-\cos[(\lambda_I+1)\psi]} \tag{8.5a}$$

$$K^o_{II}=K_{II}\frac{\sin[(\lambda_{II}+1)(\pi-\varphi)/2]\sin[(\lambda_{II}-1)\psi]-\sin[(\lambda_{II}+1)\psi]\sin[(\lambda_{II}-1)(\pi-\varphi)/2]}{-\sin[(\lambda_{II}-1)\psi]+\dfrac{(\lambda_{II}-1)}{(\lambda_{II}+1)}\sin[(\lambda_{II}+1)\psi]} \tag{8.5b}$$

where K_I and K_{II} are the more usual mode I and mode II stress intensity factors found by collocating the solution to whatever finite problem is being studied along the 'notch' bisector, and are defined as

$$K_I=\frac{\sigma_{\theta\theta}(r,0)}{r^{\lambda_I-1}}\quad Lt\quad r\to 0\ \text{ and} \tag{8.6a}$$

$$K_{II}=\frac{\sigma_{r\theta}(r,0)}{r^{\lambda_{II}-1}}\quad Lt\quad r\to 0\,. \tag{8.6b}$$

8.2.2 Slipping asymptote

Now, consider a problem where the contacting, semi-infinite, bodies are slipping relative to each other (Gdoutus and Theocaris, 1975; Comninou, 1976). The direct and shear tractions along the interface at the contact edge may be written down as (Karuppanan and Hills, 2007)

$$p(x) = \frac{q(x)}{f} = K_s x^{\lambda_s - 1} \quad \text{for} \quad 0 < \lambda < 1 \tag{8.7a}$$

$$p(x) = \frac{q(x)}{f} = K_{b1} x^{\lambda_{b1} - 1} + K_{b2} x^{\lambda_{b2} - 1} \quad \text{for} \quad 1 < \lambda < 2 \tag{8.7b}$$

$$p(x) = \frac{q(x)}{f} = K_c x^{\zeta - 1} \sin\left(\eta \ln\left(\frac{x}{x_o} \right) \right) \quad \text{for} \quad 2 < \lambda < 3 \quad (1 < \zeta < 2 \,\&\, 0 < \eta < 1) \tag{8.7c}$$

where K_s, K_{b1}, K_{b2}, K_c are generalised stress intensity factors, ζ and η are the real and imaginary parts of the eigenvalue used in equation (8.7c) and x_o denotes the position from the contact edge where the argument of the logarithm passes through unity. The value of λ for the problem under consideration here (where the wedge and the half-plane have the same elastic constants) is given by a root of the following characteristic equation

$$\begin{aligned} \nabla(\varphi, f; \lambda) = {} & \cos\lambda\pi\,(\sin^2\lambda\varphi - \lambda^2 \sin^2\varphi) + 0.5 \sin\lambda\pi\,(\sin 2\lambda\varphi + \lambda \sin 2\varphi) \\ & + f \sin\lambda\pi\,(\lambda(1+\lambda)\sin^2\varphi) = 0\,. \end{aligned} \tag{8.8}$$

Also note that the coefficient of friction is given a sign in the slipping asymptotic solution: a positive value of f suggests the kind of slip which is experienced at a trailing edge ('inward' slip), Figure 8.1, whilst a negative value of f implies the kind of slip seen at the leading edge of a contact ('outward' slip).

8.3 Normal load application

The aim of this section is not only to investigate in detail the response of trapezium-shaped punches with internal angles of 60^0, 90^0 and 120^0 (as shown in Figure 7.1), but also to look at the general characteristics of the solution for all values of punch internal angle in a realistic range. Under a range of conditions the interface will be mainly or entirely adhered, so it is appropriate to consider, first, conditions for complete adhesion. The two basic requirements for adhesion at the contact edges are

$$K_I^o < 0 \tag{8.9a}$$

$$f > g_{r\theta}^I \tag{8.9b}$$

and the first of these will certainly be fulfilled under normal loading alone, so that the second is sufficient, and follows directly from the characteristic equation, i.e.

$$f > \frac{\sin\left[(\lambda_I+1)(\pi-\varphi)/2\right]-\Gamma_I^s\sin\left[(\lambda_I-1)(\pi-\varphi)/2\right]}{\cos\left[(\lambda_I+1)(\pi-\varphi)/2\right]-\Gamma_I^c\cos\left[(\lambda_I-1)(\pi-\varphi)/2\right]}. \tag{8.10}$$

This describes the behaviour in region *A*, Figure 8.2(a) which provides an overall response map with primary parameters f, φ. When this inequality is not satisfied slip will ensue and, in general terms, the punch will tend to 'spread' relative to the half-plane, and give rise to the possibility of subsequent damage. In order to investigate further what happens in this regime, the magnification of the microscope with which we are looking at the contact edges must be turned up, so that we can now think of a slipping asymptote applying at the very edges of the contact, within the slipping regions. It was noted that the sense of slip is the same at both edges, and that this is the same as that prevalent at the leading edge of a sliding contact. The sense of slip is important because, in the case of the slipping asymptote, the characteristic equation and the nature of the eigensolution depend on this. In region *B* (Figure 8.2(a)), where $\lambda < 1$, the tractions will be power-order singular and are given by equation (8.7a). If the lowest root lies in the range $1 < \lambda < 2$, and is wholly real, the tractions will be power order bounded (region *C*) and are described by equation (8.7b), whilst if the

relevant root is complex, local separation will occur, with square-root bounded behaviour at the true contact edge (region *D*). The procedure to restore the separation condition within the asymptote is described in detail by Karuppanan *et al*. (2007b) and is included in chapter 6. Also highlighted on Figure 8.2(a) are the three angles studied in detail, showing that; (a) the 120^0 and 90^0 punches exhibit region *A* and *B* behaviour, and (b) the 60^0 punch exhibits region *D*, *C*, *B* and *A* behaviour with increasing friction. Figure 8.2(b) provides a set of schematics to illustrate the response anticipated in all regions of Figure 8.2(a). These example problems (60^0, 90^0 and 120^0 punch problems) were analysed using the commercial finite element programme *ABAQUS*. However, only the results for the 60^0 punch problem will be reported since it covers all four regions. Figure 8.3(a) shows the results for the normalised pressure distribution found. These results are re-plotted enlarged at the trailing edge in Figure 8.3(b) for an improvement in clarity, and it displays the kind of behaviour which is as anticipated.

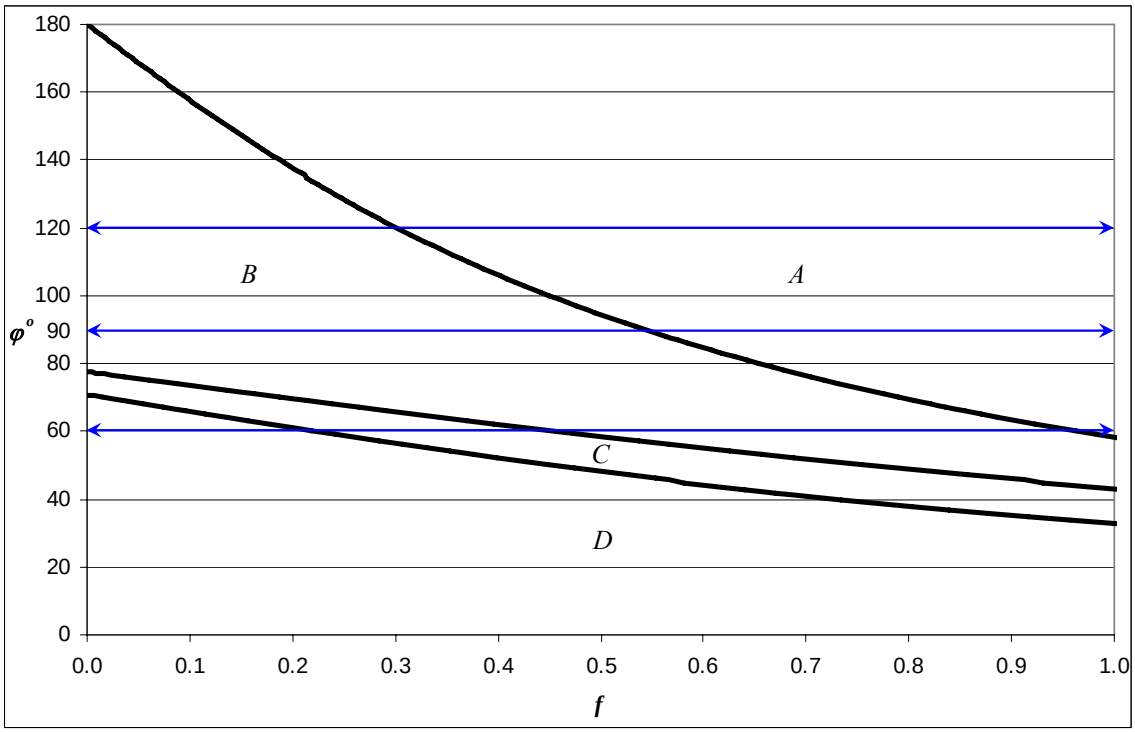

Figure 8.2(a) : Overall map of the contact edge responses due to the normal load only showing 4 distinct regions

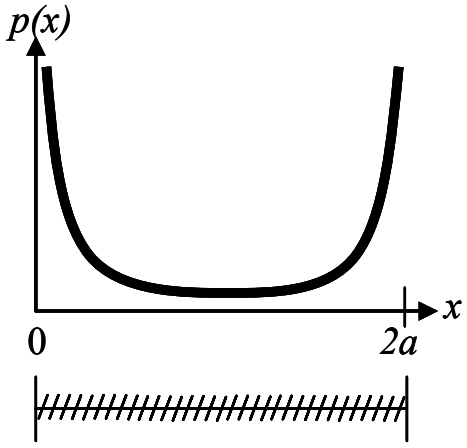

Region *A*

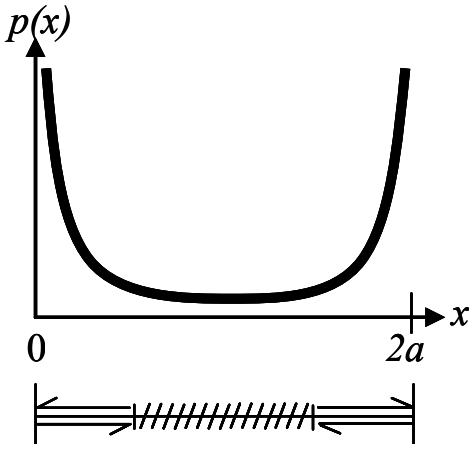

Region *B*

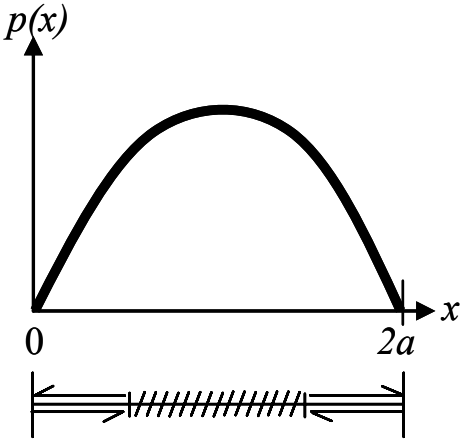

Region *C*

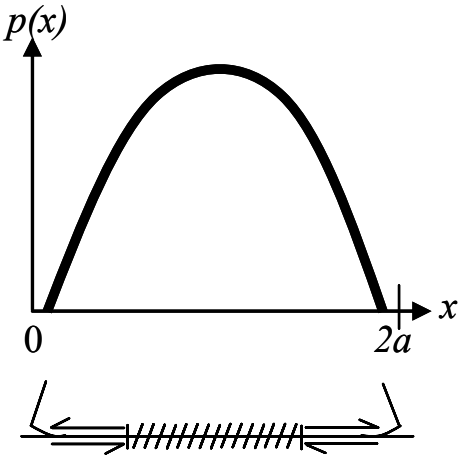

Region *D*

Figure 8.2(b) : Various types of contact pressure and surface behaviour of complete contacts subject to normal load *P*

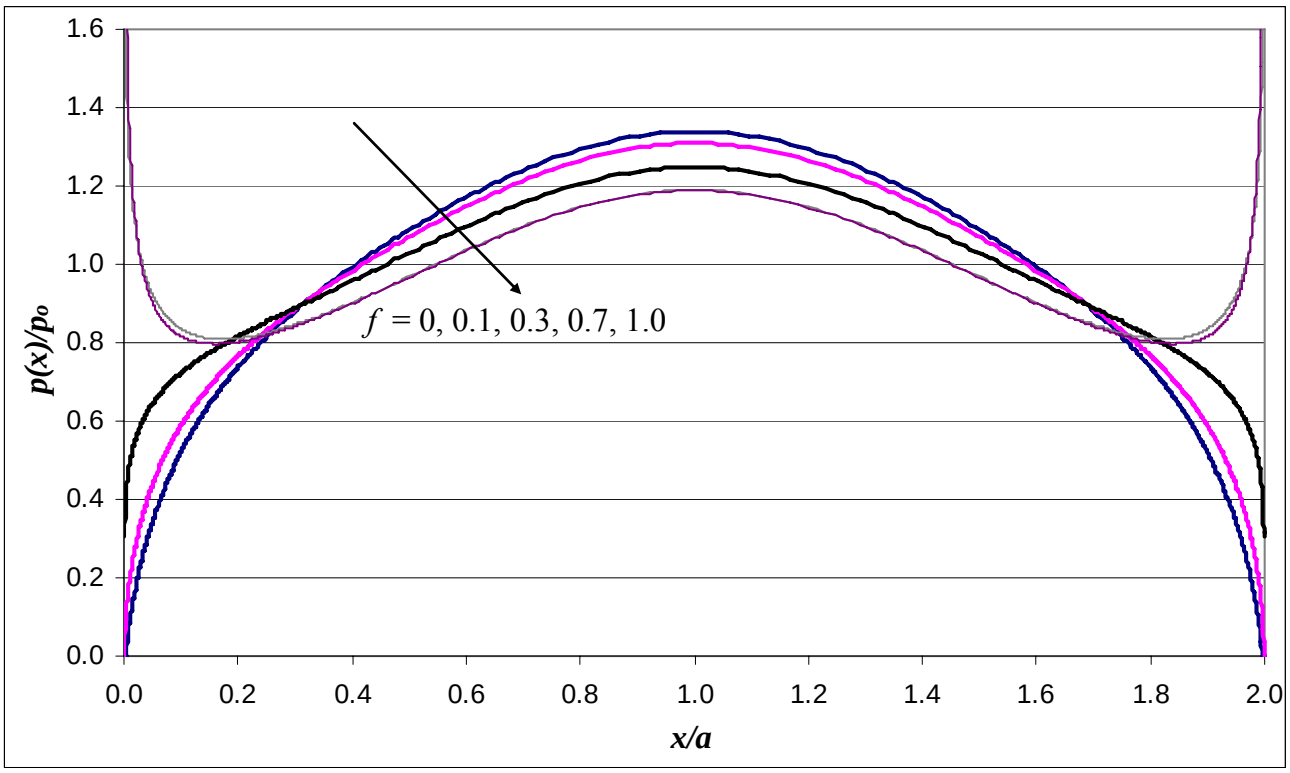

(a)

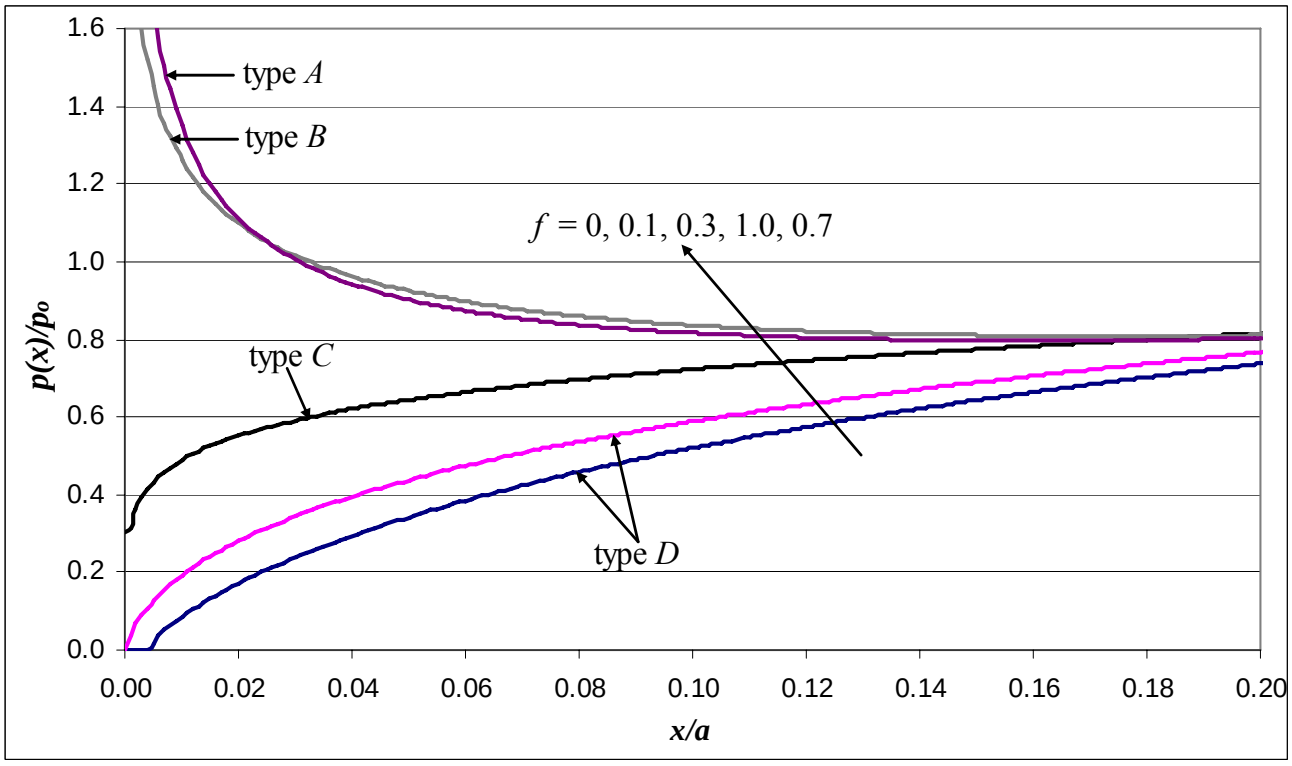

(b)

Figure 8.3: Normalised contact pressure distribution (a) along the interface (b) at the trailing edge; for a 60^0 punch due to the application of normal load only.

8.4 Monotonic shear loading

8.4.1 Square punch solution

The procedure adopted by Churchman and Hills (2006a), for the problem shown in Figure 7.1(a), will be briefly summarised in this section. In their attempt to understand the general interfacial characteristics of complete contacts in partial slip (for a monotonically increasing shearing force) a map, shown in Figure 8.4, was developed. For a square punch problem, i.e. when $\varphi = \pi/2$, the eigensolution in the adhered regime is characterised by

$$\lambda_I = 0.5445; \quad \lambda_{II} = 0.9085; \quad g^I_{r\theta} = 0.5431; \quad g^{II}_{r\theta} = -0.2189 . \tag{8.11}$$

As $0 > \lambda_I - 1 < \lambda_{II} - 1$, the state of stress is singular and, furthermore, the traction ratio is given by the dominant eigensolution, so that

$$\frac{q(x)}{p(x)} = g^I_{r\theta} \qquad Lt \quad x \to 0 . \tag{8.12}$$

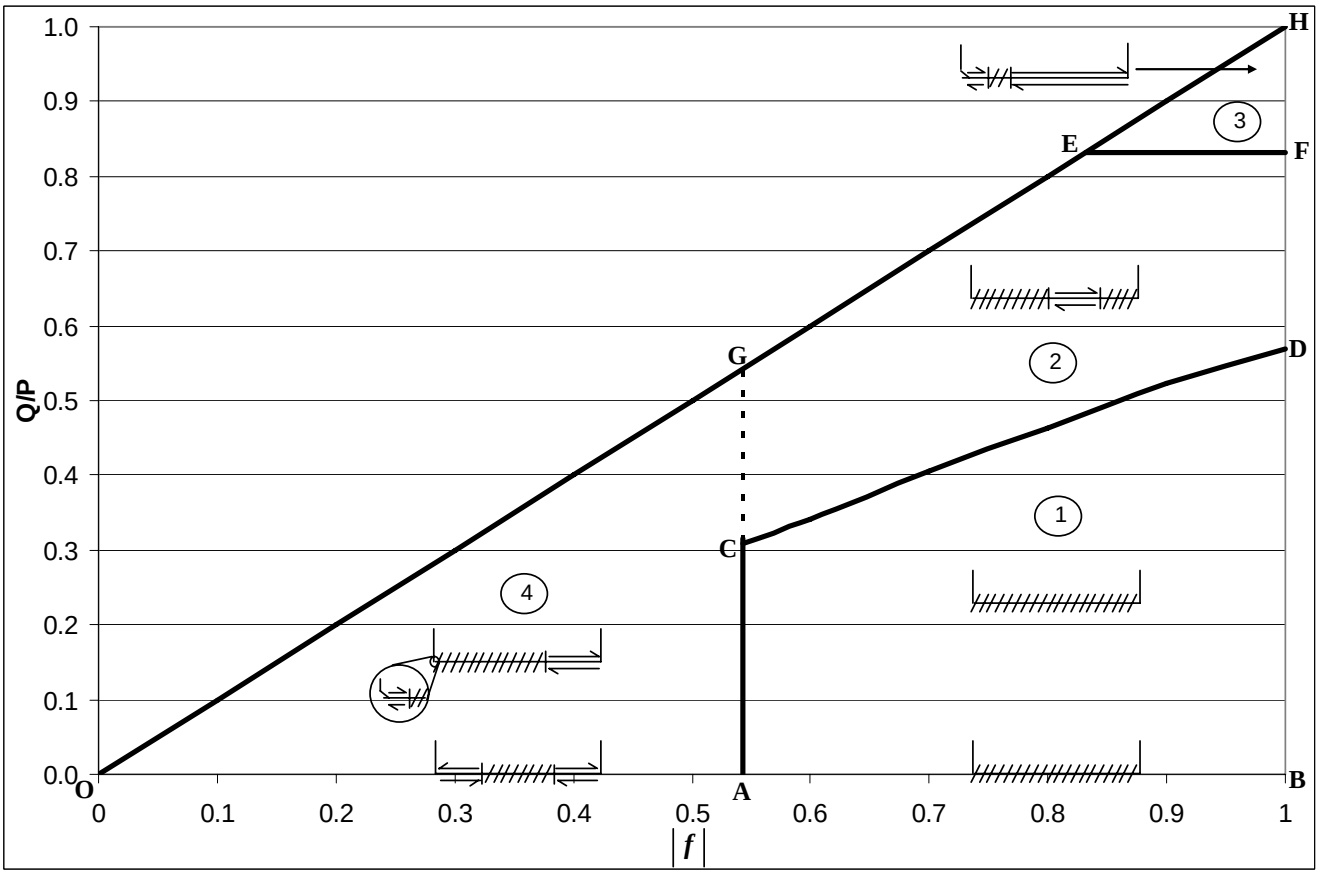

Figure 8.4 : Behaviour map for a square punch by Churchman and Hills (2006a)

It follows that, provided the coefficient of friction, f, exceeds this value (= f_{crit}, say), the contact edge will certainly adhere (region 1 in Figure 8.4). Furthermore, the traction ratio is *independent* of the ratio Q/P, where P is the applied contact normal force and Q the applied shearing force. Thus, providing only that $f > f_{crit}$ the contact corner will remain stuck, but the traction-ratio (q/p) within the interior of the contact will increase as a shearing force is developed, and, at some value of Q/P will exceed $g^I_{r\theta}$. This point must be found by a finite element analysis, but is easy to locate because the tractions at interior points are finite, and hence the ratio may easily be found reliably. When q/p exceeds f interior slip starts, and this condition corresponds to the line ***CD*** given in Figure 8.4. A further increase in the value of Q/P beyond the point of first slip will result in a growing region of slip (region 2). Note that the condition for sustained edge adhesion is not only independent of the applied load, but also of the geometry of the problem (save for the value of φ which has a first order effect).

In a sliding contact the trailing edge has a propensity to lift, whereas the leading edge tends to 'dig in', and an important characteristic of the solution is to determine the conditions for initial separation. A calibration for the generalised stress intensity factors scaling the trailing edge solution under conditions of full adhesion with the applied loads, using a finite element analysis, is given by[*]

$$\begin{Bmatrix} K_I^o a^{\lambda_I - 1} \\ K_{II}^o a^{\lambda_{II} - 1} \end{Bmatrix} = \begin{bmatrix} -0.307 & 0.369 \\ -0.283 & -0.542 \end{bmatrix} \begin{Bmatrix} P/2a \\ Q/2a \end{Bmatrix}, \tag{8.13}$$

where a is the contact semi-width. As stated above, the solution adjacent to the contact edge is dominated by the symmetric (mode I) eigensolution, and the contact pressure will be negative at the trailing edge provided only that the value of $K_I^o < 0$. Thus, from the first row of the matrix given, this will be true provided that

$$\frac{Q}{P} < \frac{0.307}{0.369} = 0.832. \tag{8.14}$$

[*] These figures differ slightly from those in Churchman and Hills (2006a) because there were small differences in the way in which the load was applied.

Churchman and Hills took this to be the ruling separation condition, but, of course, it holds exactly only if it is not preceded by any slip, and it becomes approximate if the coefficient of friction, f, only moderately exceeds the critical value: this aspect of the Churchman figure (region 3) merits refinement by further application of the finite element method.

When $f < f_{crit}$ the application of a normal load alone causes two small fringes of outward slip to appear at the edges of the contact (region 4). Their extent may be found by finite element calculation or, if the coefficient of friction is only slightly less than $g^{I}_{r\theta}$ (for cases where the slip size is difficult to resolve by finite element analysis), it may be found approximately from the adhered eigensolution by checking the extent over which violation of the friction law occurs within the asymptote (Churchman and Hills, 2006a). A first-order approximation to the size of the slip zone, c_o is given in a closed form by

$$c_o = \left\{ \left(-\frac{f + g^{I}_{r\theta}}{f + g^{II}_{r\theta}} \right) \frac{K^o_I}{K^o_{II}} \right\}^{\frac{1}{\lambda_{II} - \lambda_I}} . \tag{8.15}$$

If, now, a monotonically increasing shearing force is applied (region 4), the leading edge slip zone will grow in extent because the applied shear is consistent with the direction of pre-existing slip. At the trailing edge, the implied increment of shearing traction is in the opposite sense to the slip displacement due to the application of normal load, and will give way, instantaneously, to stick. This will be followed by edge slip and separation as the shear force is increased. The normal traction at the trailing edge is given by

$$\sigma_{\theta\theta}(x,0) = K_s\, x^{\lambda_s - 1} + \Delta K^o_I x^{\lambda_I - 1} + \Delta K^o_{II} x^{\lambda_{II} - 1} \tag{8.16}$$

where the first term corresponds to the residual locked-in tractions, and the other two terms correspond to the adhered correction due to the *change* in load. The adhered correction is expected to dominate the solution at the edge because the mode *I* singularity is always stronger than the slipping singularity, $\lambda_I < \lambda_s$. Therefore, if a small increment of shear load is applied (with P kept constant), $\Delta K^o_I > 0$ (from equation (8.13)) implying separation at the

edge. A first-order approximation to the extent of the separation zone, d_s and accompanying slip distance, e_s, found from the bilateral solution, are given in closed form by

$$d_s = \left(-\frac{\Delta K_I^o}{K_s} \right)^{\frac{1}{\lambda_s - \lambda_I}}, \tag{8.17}$$

$$e_s = \left(\frac{f - g_{r\theta}^I}{2f} \left(-\frac{\Delta K_I^o}{K_s} \right) \right)^{\frac{1}{\lambda_s - \lambda_I}}. \tag{8.18}$$

This technique is appropriate when the trailing edge slip zone is small, but clearly it will become inaccurate when the shearing force approaches the sliding value, and this was not investigated in Churchman's thesis (2006).

Notwithstanding the limitations of the solution near to sliding, the basic ideas in Churchman's solution are sound, and permit a precise investigation of the contact's behaviour under small to moderate shearing forces.

8.4.2 Square punch solution refinements

The general form of the solution to this problem, previously investigated by Churchman and Hills (2006a), has already been described. The results merit refinement near incipient sliding, and this can really only be achieved by careful finite elements analysis. In this part of the diagram, assuming a monotonically increasing shearing force, the slip zones are increasing in size, and so no history effects are present. The regimes discovered and refinements to the original map are shown in Figure 8.5. The various regimes on the behaviour map are labelled based on the edge behaviour at two extreme conditions, i.e. the first letter represents the type of behaviour due to normal load only and the second letter represents the type of behaviour in sliding condition (Karuppanan and Hills, 2007; section 7.4). As an example, region *BA* indicates singular traction behaviour at the edges with fringes of slip at both ends when normal load is applied (region *B* in Figure 8.2) and singular

traction behaviour at both edges in sliding condition (region *A* in Figure 7.11(b)). This labelling format is also extended to other punch angles, i.e. 60^0 and 120^0 punch. Lines ***ON***, ***NLP*** and ***KLM*** were found by careful finite element analysis where simulations were carried out for different values of f at small increments of Q/P ratios, especially at the boundaries between two regions. Line ***IJ*** was found from finite element analysis using a monolithic model whilst line ***CIKNG*** was inferred from a consideration of adhered asymptotes (equation (4.28a)).

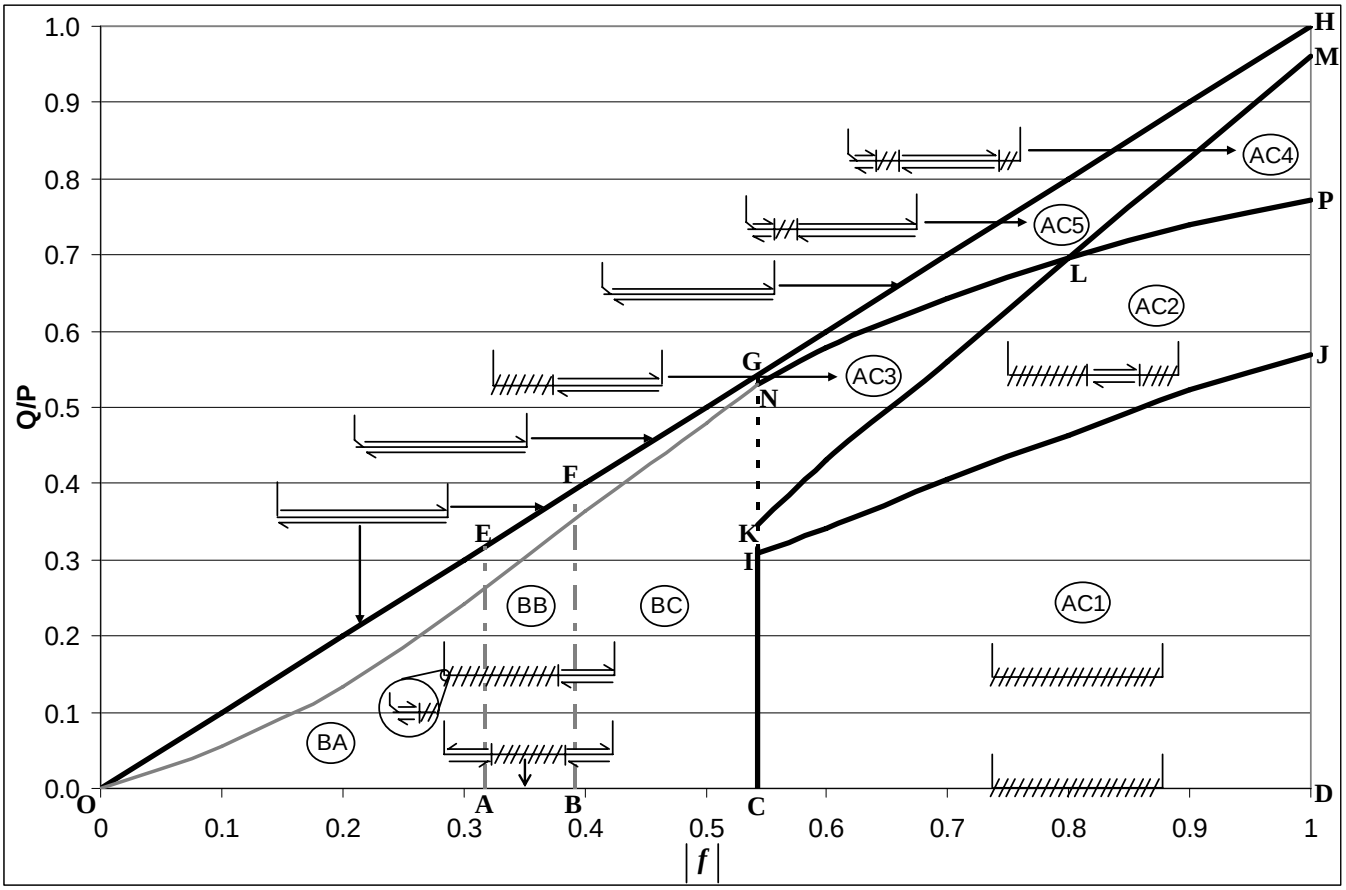

Figure 8.5 : Refined behaviour map for a square punch, on a half-plane subject to a constant normal load *P* and a monotonically increasing shear load *Q*, and with coefficient of friction, *f*

First, consider the case where $f > g^I_{r\theta}$. The solution already described is correct in region *AC*1 but requires modification in region *AC*2. If the traction-ratio (q/p) within the contact reaches $g^I_{r\theta}$ value (line ***IJ***), interior slip starts to develop. A further increase of

shearing force will result in a growing slip zone within the contact (region $AC2$). For $g^I_{r\theta} < f \lesssim 0.8$, as the shear force is increased region $AC2$ will give way to region $AC3$ where the growing interior slip reaches the leading edge. If the shearing force is increased further a second forward slip zone will develop at the trailing edge as the contact recedes in size (the trailing edge lifts off), region $AC5$. For $f > 0.8$, region $AC5$ is preceded by region $AC4$ in which a small forward slip zone and separation develops at the trailing edge prior to the interior slip reaching the leading edge. Finally when $Q/fP = 1$, the entire contact interface will be slipping save a small region at the trailing edge which lifts off, line ***GH***. Also note that line ***NLP*** which indicates the boundary above which trailing edge forward slip and separation occurs approaches Churchman's separation rule, equation (8.14) ($Q/P = 0.832$) with increasing friction.

If $f < g^I_{r\theta}$, the application of normal load alone causes outward slip of same size at both edges, line ***OABC***. Subsequent application of a shear load will increase the extent of slip at the leading edge, whilst the trailing edge will instantaneously be stuck followed by the development of a minute region of forward slip and separation at the edge, regions BA, BB and BC. In region BA ($0 < f < 1/\pi$), when the grey line is reached (line ***ON***), the forward slip at the trailing edge will have the tendency to grow rapidly as the contact edge falls continuously to resume contact before the entire contact interface slips when line ***OE*** is reached, where the traction behaviour is singular at both contact edges. In region BB ($1/\pi < f < 0.392$), similar behaviour to that found in region BA is expected, except that the tractions are bounded at the trailing edge and singular at the leading edge when line ***EF*** is reached. Finally in region BC ($0.392 < f < g^I_{r\theta}$), the forward slip zone at the trailing edge will grow rapidly if Q/P ratio lies above the grey line, as does the separation distance. When the gross sliding condition is achieved, line ***FG***, the tractions exhibit square root bounded behaviour at the trailing edge and singular behaviour at the leading edge.

8.4.3 120^0 trapezium punch

The geometry of the problem studied here is given in Figure 7.1(b). A practical problem having a contact edge condition very close to the one studied here is the involute spline used in split shafts within some gas turbines, and the map giving the overall response to applied loads is shown in Figure 8.6. In this problem, the normal load is applied first, held constant, and then a monotonically increasing shear load imposed.

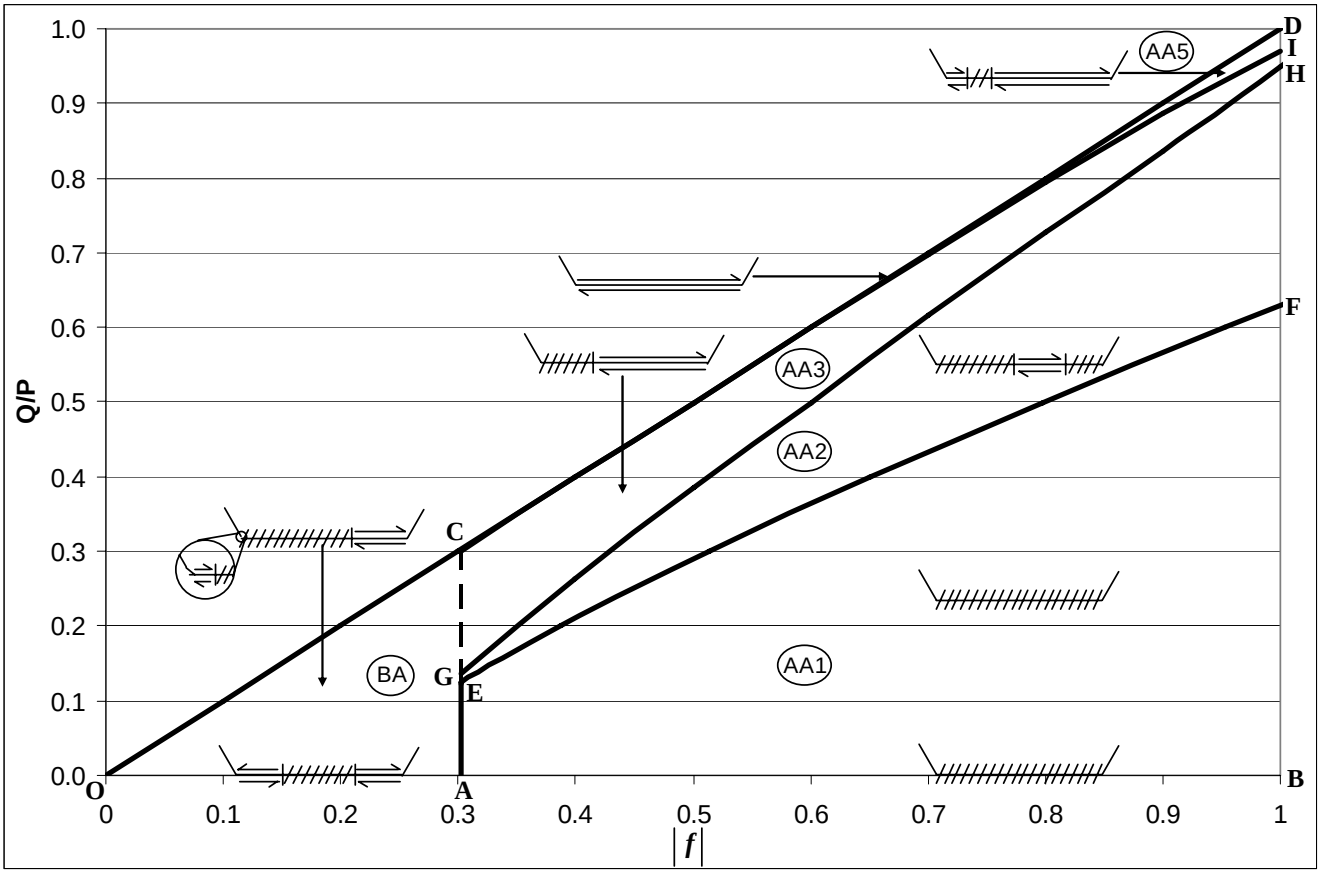

Figure 8.6 : Behaviour map for a 120^0 punch, on a half-plane subject to a constant normal load P and a monotonically increasing shear load Q, and with coefficient of friction, f.

If $f > g_{r\theta}^{I}$ the application of normal load will ensure full adhesion of the contact interface, line ***AB***. This condition will hold with a finite shear load, region $AA1$, until line ***EF*** is reached. In the nomenclature developed earlier, the two eigenvalues describing the order of singular behaviour under adhered conditions in region $AA1$ are $\lambda_I = 0.5122$,

λ_{II} = 0.7309, and the two key coefficients defining the eigenvector are $g^{I}_{r\theta}$ = 0.3026, $g^{II}_{r\theta}$ = –0.8500 so that the minimum friction needed to sustain full adhesion is 0.3026. A calibration for the generalised stress intensity factors scaling the trailing edge asymptotic solution, using a finite element analysis, is given by

$$\begin{Bmatrix} K^{o}_{I} a^{\lambda_I - 1} \\ K^{o}_{II} a^{\lambda_{II} - 1} \end{Bmatrix} = \begin{bmatrix} -0.370 & 0.291 \\ -0.087 & -0.432 \end{bmatrix} \begin{Bmatrix} P/2a \\ Q/2a \end{Bmatrix}. \tag{8.19}$$

The tractions at the trailing edge of the contact can therefore be determined from equations (8.1a) and (8.1b). When the line ***EF*** is reached, the application of an increasing shearing force leads, as before, to interior slip, bounded by two regions of stick, region *AA*2. A further increase in the value of the shearing force causes the interior slip zone to grow, until it reaches the leading edge, region *AA*3. The stick zone subsequently recedes further until a subsidiary forward slip zone develops, attached to the trailing edge, region *AA*5 prior to gross sliding of the contact interface when $Q/fP = 1$ is achieved, line *CD*, where the tractions exhibit singular behaviour at both edges.

If $f < g^{I}_{r\theta}$ the response is generally the same as that observed for the 90^0 case. Outward slip at both edges will develop due to the application of normal load alone, line ***OA***. Subsequent application of a shear load will increase the size of slip zone at the leading edge, whilst the trailing edge experiences instantaneous stick followed by a minute forward slip and separation region attached to the edge, due to the influence of locked-in residual tractions, region *BA*. As we move in region *BA* closer to gross sliding condition (line ***OC***), the influence of the sliding eigenvalue becomes increasingly important and the minute amounts of separation which occurs earlier will gradually diminish. Finally a gross sliding condition is achieved when line ***OC*** is reached, where the tractions exhibit singular behaviour at both edges.

8.4.4 60^0 trapezium punch

The geometry of the problem studied here is given in Figure 7.1(c). This kind of geometry also occurs, in a modified way, in a gas turbine engine. It is the overall shape of the dovetail lug fastening in a fanblade. Of course the fanblade normally has rounded edges, but the solution to be discussed shows what might be expected if that radius were reduced to a very small value. For a 60^0 punch problem, i.e. when $\varphi = \pi/3$

$$\lambda_I = 0.6157; \quad \lambda_{II} = 1.1489; \quad g^I_{r\theta} = 0.9619; \quad g^{II}_{r\theta} = 0.3224 . \tag{8.20}$$

The new overall response map is as in Figure 8.7 showing a more complicated response than the first two geometries.

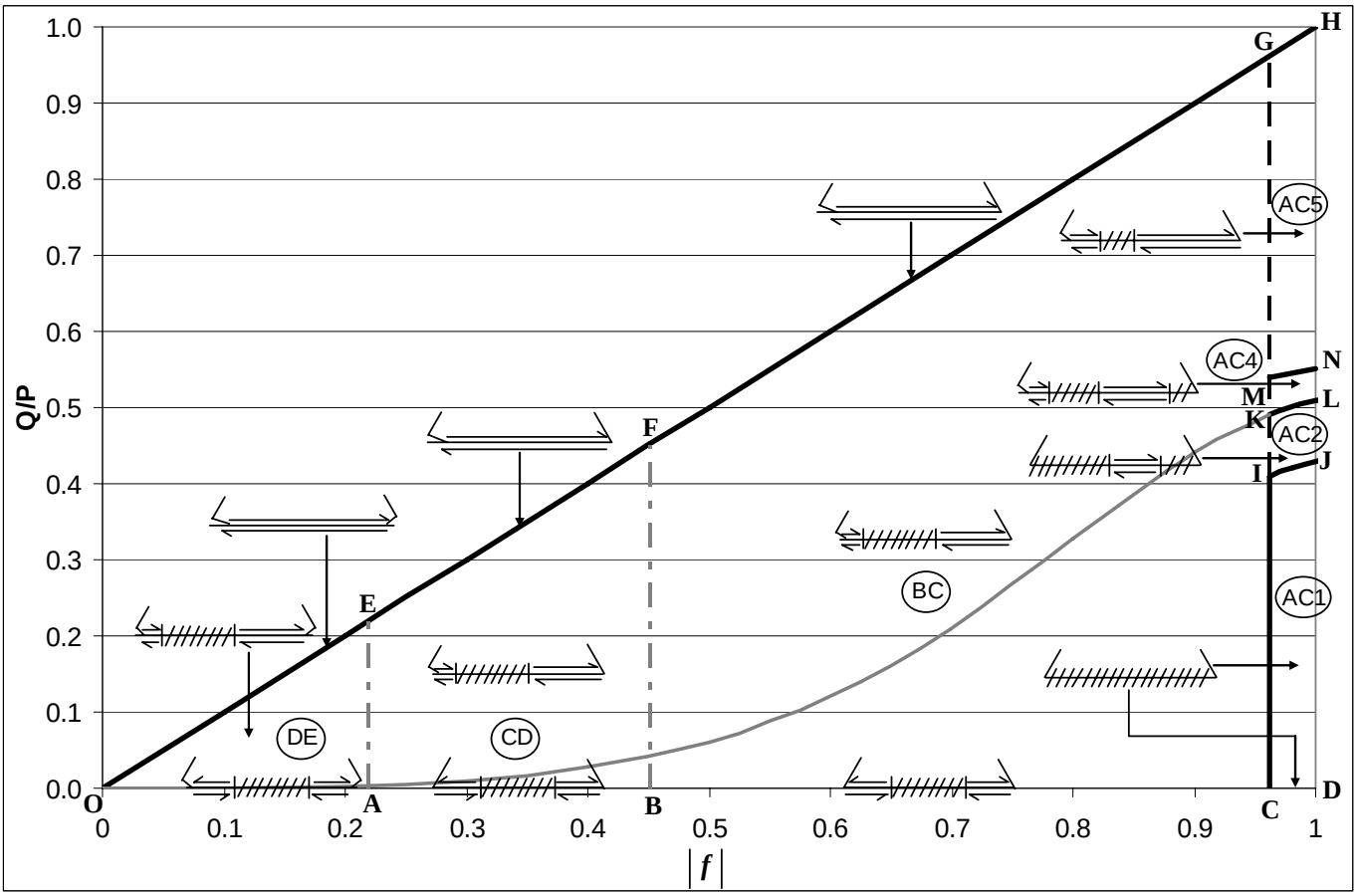

Figure 8.7 : Behaviour map for a 60^0 punch, on a half-plane subject to a constant normal load P and a monotonically increasing shear load Q, and with coefficient of friction, f.

If $f > g^I_{r\theta}$ a fully adhered interface is expected, due to the application of normal load (line ***CD***) and subsequently shearing load (region *AC*1) until line ***IJ*** is reached. The tractions in this region are singular in nature at the edges and the adhered generalised stress intensity calibration is given by

$$\begin{Bmatrix} K^o_I a^{\lambda_I - 1} \\ K^o_{II} a^{\lambda_{II} - 1} \end{Bmatrix} = \begin{bmatrix} -0.197 & 0.360 \\ -0.407 & -0.173 \end{bmatrix} \begin{Bmatrix} P/2a \\ Q/2a \end{Bmatrix} \tag{8.21}$$

A further increase of shearing force above line ***IJ*** causes interior slip to develop (region *AC*2). As we move along a vertical trajectory from region *AC*2, forward slip and separation will occur at the trailing edge as line ***KL*** is passed (region *AC*4). Finally the interior slip zone reaches the leading edge (region *AC*5) prior to full sliding when line ***GH*** is reached, where the trailing edge remains separated giving square root bounded traction behaviour, whilst the leading edge exhibits singular-traction behaviour. Even though these regions are unlikely to be important for practical cases, they are included here so that we get a clearer picture of the expected behaviour of the contact interface for different wedge angles.

If $f < g^I_{r\theta}$ we again expect fringes of slip of opposite sign bordering adhered interface at the centre of the contact due to the application of normal load alone, but the tractions adjacent to the edges will exhibit different behaviour. For $0 < f < 0.219$, when the normal load is applied, the contact edges will lift off so that the traction behaviour is square root bounded, line ***OA***. A subsequent application of shear load will cause the trailing edge to adhere instantaneously save for a small region of separation which arose earlier, before the development of a forward slip zone accompanying separation, whilst the slip zone at the leading edge increases in size, region *DE*. When the sliding condition is achieved, line ***OE***, the entire contact interface will slip with the edges lifted off. The amount of lift off at the trailing edge is greater than that at the leading edge. For $0.219 < f < 0.451$, when the normal load is applied, the contact edges will exhibit a power order bounded traction behaviour, line ***AB***. When the shear load is applied the trailing edge will instantaneously adhere before

a forward slip region, accompanying separation, develops whilst the slip zone at the leading edge increases in size, region *CD*. When the grey line (line ***OK***), is reached, the slip zone and separation region at the trailing edge will have a tendency to grow rapidly and the change in tractions behaviour is expected whilst the leading edge tractions behaviour is maintained. Finally when the sliding condition is achieved, line ***EF***, the entire contact interface will slip with the trailing edge lifting off exhibiting square root bounded traction behaviour but the leading edge traction behaviour is still power order bounded. For $0.451 < f < g^{I}_{r\theta}$, when the normal load is applied, the contact edges will exhibit a singular traction behaviour, line ***BC***. As before the application of shear load will initially cause the trailing edge to adhere instantaneously, prior to the development of a forward slip zone accompanying separation, whereas the leading edge slip zone increases in size (region *BC*). When the grey line is reached the extent of forward slip and separation at the trailing edge increases rapidly and the traction behaviour changes to square root bounded. Finally, when the sliding condition is achieved, line ***FG***, the entire contact interface will slip with the trailing edge lifting off exhibiting square root bounded traction behaviour whereas the leading edge still exhibits singular behaviour.

8.5 Cyclic shear loading

The preceding sections have all been concerned with the influence of a monotonically increasing shearing force on the interfacial behaviour, but, in most practical problems, contacts are subject to a reversing shearing force. Potentially, this could give rise to a more complicated calculation, but in practice what is often needed is simply a knowledge of whether or not the contact will 'shake down', i.e. whether a self-developing interfacial residual shearing traction distribution will arise which, together with the applied load, will mean that the limiting friction will not be achieved at any point within the contact. If the contact does shake down completely there will be no steady-state slip, and hence fretting

damage will cease, so that, as explained in section 8.1, the contact edges will simply become points of stress intensification, rather like a notch. It is, perhaps, worth noting that, if the contact edges do lift off, the local behaviour is formally incomplete, and, as in many incomplete contacts subject to this mode of loading, because the contact pressure goes uniformly to zero at such points it is impossible to sustain any residual shearing traction, and hence no shakedown can occur. However, in many cases the regions in which this cyclic lift and reversing shear occur are very small indeed (Churchman and Hills, 2006a), so that the region in which fretting damage occurs is likely to be extremely small, with correspondingly small slip displacements, and the damage which results will also be very small indeed compared with that usually observed in conventional incomplete contacts.

Instead of tracking out the loading history as a function of time using the finite element method, a lower bound technique for determining the shakedown limit was speculated in Churchman's paper (Churchman and Hills, 2006a), and verified in 'spot' cases using a finite element simulation. The shakedown limit using this technique is achieved provided that

$$|f| > \left| \frac{\tilde{q}^{Q}\left(\frac{Q}{P}\right)_{\max}[\gamma - 1]}{2\tilde{p}^{P} + \tilde{p}^{Q}\left(\frac{Q}{P}\right)_{\max}[\gamma + 1]} \right|_{\max} \qquad \forall x \tag{8.22}$$

where

$$\tilde{p}^{P} = \frac{p^{P}(x)}{(P/2a)}, \quad \tilde{p}^{Q} = \frac{p^{Q}(x)}{(Q/2a)}, \quad \tilde{q}^{Q} = \frac{q^{Q}(x)}{(Q/2a)}, \tag{8.23}$$

and $p^{P}(x)$ is the traction along the interface under normal load only (P) whilst $p^{Q}(x)$, $q^{Q}(x)$ are the tractions resulting from pure shear load only (Q). These traction values are determined from adhered finite element analysis.

The loading condition for this problem is as shown in Figure 8.8. It is assumed that the contact is first subjected to a normal load, P, whose value is increased steadily from zero

and subsequently held constant. It is then loaded by shear up to some value, Q_{max}. It is then reduced to a value $Q_{min} = \gamma Q_{max}$ ($-1 < \gamma < 1$), and is subsequently cycled between these limits. In very general terms, the closer γ lies to +1 (so that the range of shear is small), the more likely the contact is to shakedown.

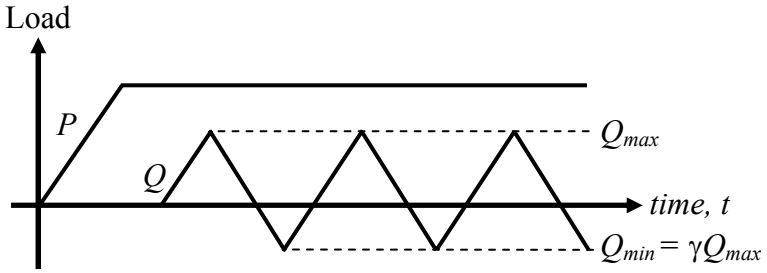

Figure 8.8 : Loading history

8.5.1 Square punch

The steady state response map for the square punch problem is shown in Figure 8.9(a). It was developed by using the monotonic shear load map as a reference and employing the lower bound technique (section 8.5). These results are then certified with the finite element results at various locations on the map. The boundary between shakedown (below, to the right) and cyclic slip (above, to the left) for a fully reversing shear case ($\gamma = -1$) is represented by a thick dark line. The full description of the steady state contact response will be based on this example case.

If $f > g^{I}_{r\theta}$, in region $AC1$, the contact interface will be fully adhered from outset. In region $AC2$, if a location below (or to the right of) the dark line is considered, the contact interface will be fully adhered in the steady state, due to frictional shakedown. A cyclic slip region at the centre of an otherwise adhered contact is expected if the contact is represented by a point above or to the left of this dark line. In region $AC3$, an adhered interface or a cyclic slip region in the middle of this adhered interface, together with a minute slip region

at the leading edge is expected depending on its exact position on the map relative to the dark line. In region *AC*4, an adhered interface with a small region of forward slip and separation at the trailing edge, together with interior cyclic slip, is expected. The same behaviour is expected in region *AC*5 with an additional minute forward slip region at the leading edge being the only difference. The interior cyclic slip occurring in these regions is shifted from the centre towards the leading edge. For load cases where the dark line is shifted closer to the gross sliding condition (line ***OH***), the interior cyclic slip in regions *AC*4 and *AC*5 will vanish, but the forward slip and separation attached to the edges are still maintained, if a position below or to the right of the dark line is considered.

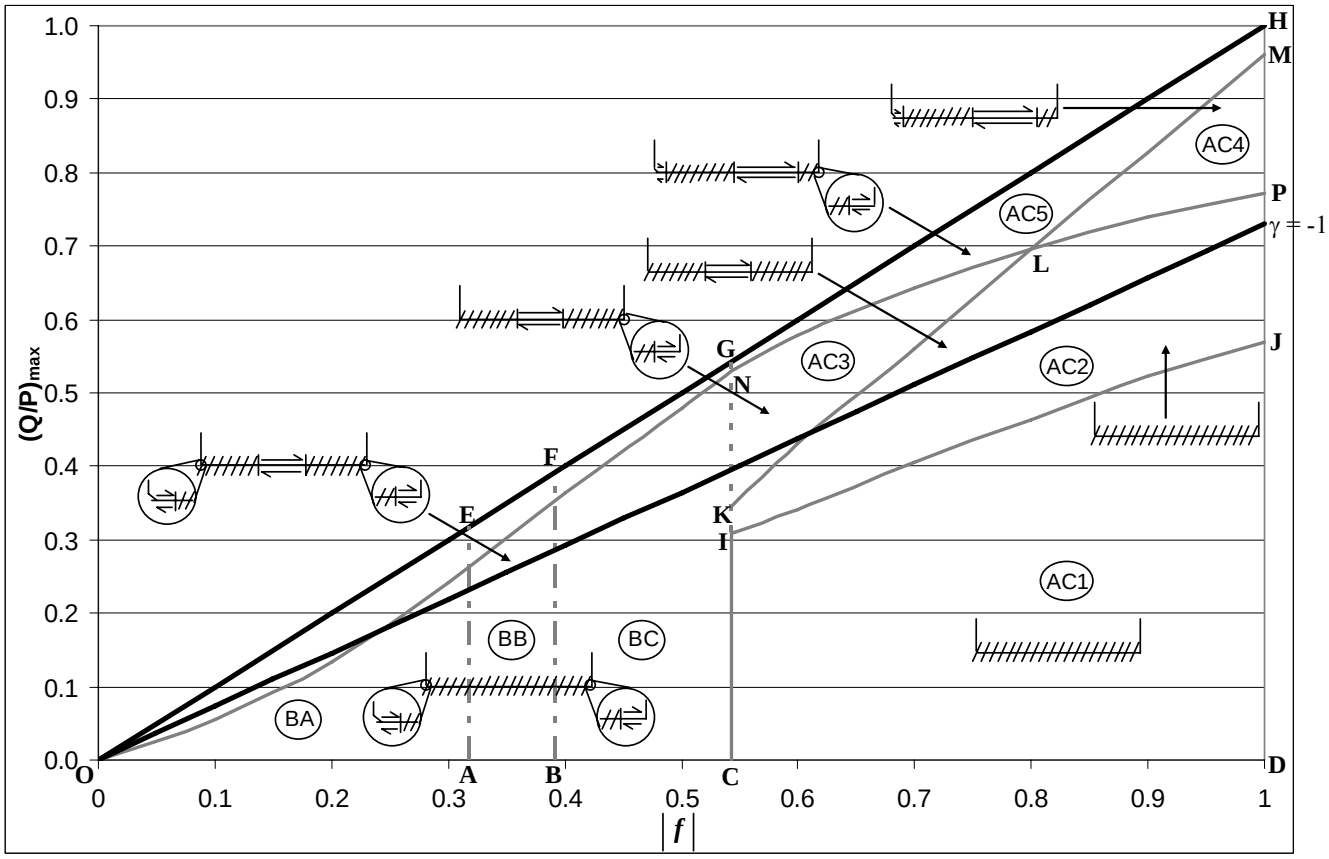

Figure 8.9(a) : Behaviour map for a square punch, on a half-plane subject to a constant normal load *P* and a cyclic shear load *Q*, and with coefficient of friction, *f*.

If $f < g^{I}_{r\theta}$, the entire contact interface in regions *BA*, *BB* and BC will shake down to an adhered state, save for a small forward slip and separation region at the trailing edge, and additionally, a forward slip region at the leading edge for a point below and to the right of the dark line. If a point above and to the left of the dark line is considered, an additional interior cyclic slip region near the middle of the contact is expected. The difference between regions *BA*, *BB* and *BC* is in the traction behaviour at the contact edges, as described in the monotonic loading section.

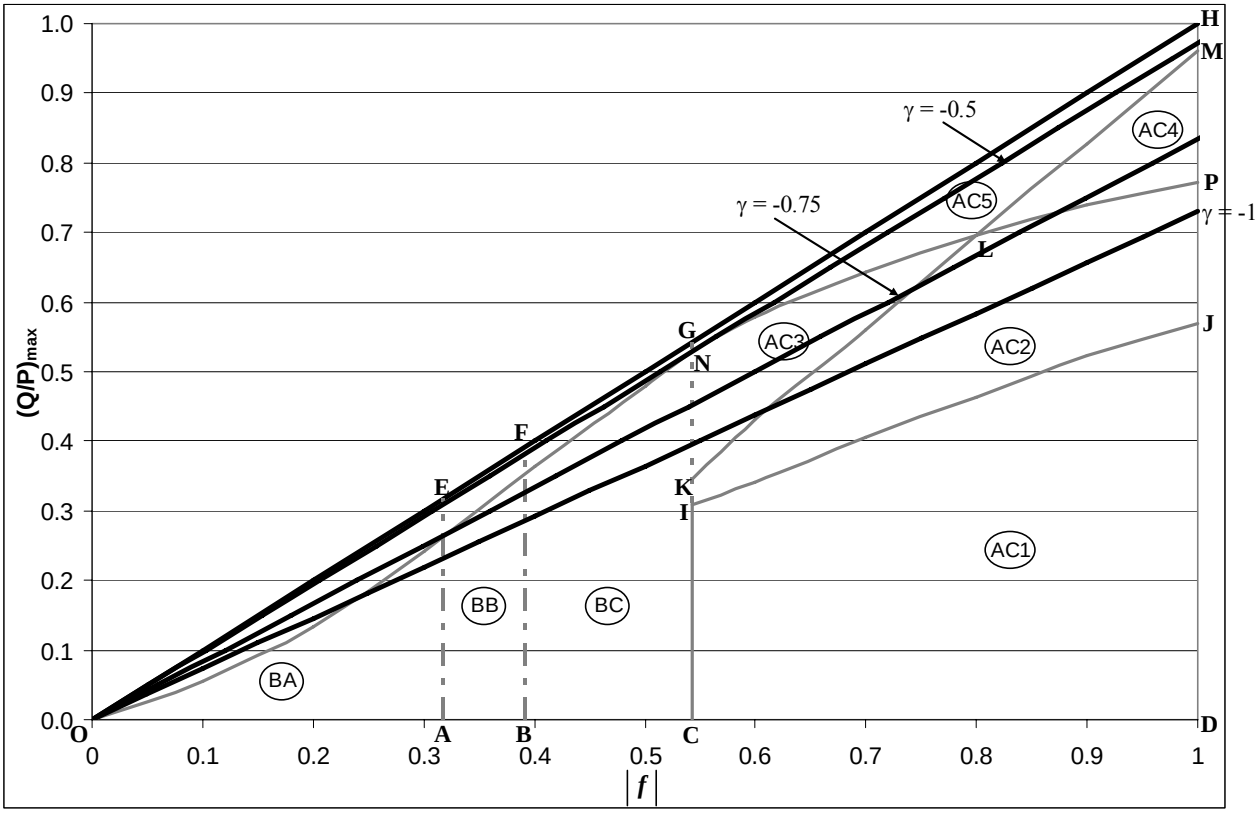

Figure 8.9(b) : Steady state response map for a square punch, for example load cases

Figure 8.9(b) shows the steady state response map for the square punch problem which includes the boundaries for other load cases, i.e. $\gamma = -0.75$ and $\gamma = -0.5$. The concept used to describe $\gamma = -1$ example case applies here, i.e. the contact interface characteristic depends on (a) the region on the map, and (b) the exact position relative to the thick dark line. For this square punch, in the region of interest $0 < |f| < 1$, the contact interface will always shake down if $\gamma \gtrsim -0.45$.

8.5.2 120^0 trapezium punch

The steady state response map for the 120^0 punch problem is shown in Figure 8.10(a). A thick dark line representing the boundary between shakedown and cyclic slip for a fully reversing shear case ($\gamma = -1$) is included.

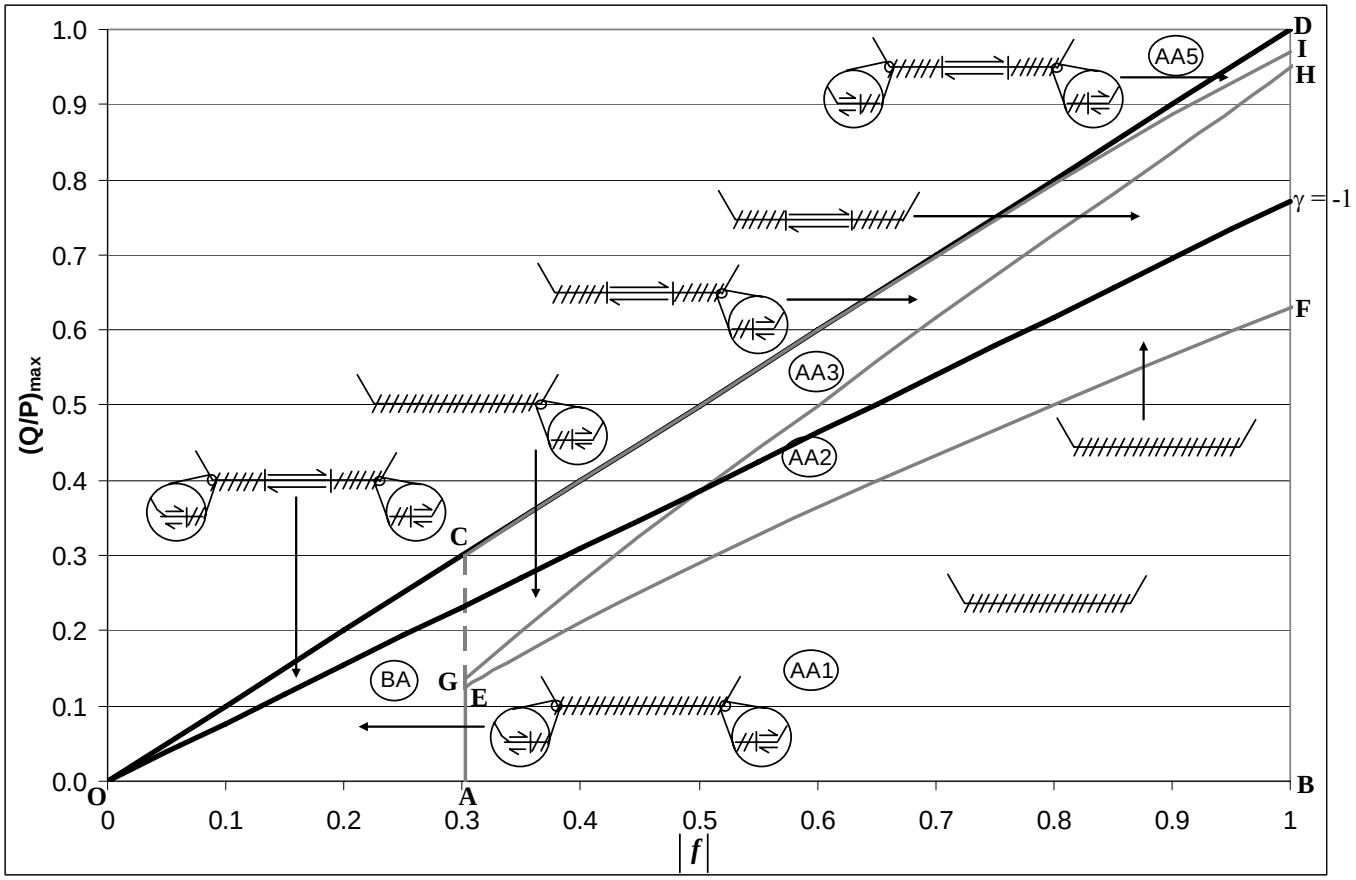

Figure 8.10(a) : Behaviour map for a 120^0 punch, on a half-plane subject to a constant normal load P and a cyclic shear load Q, and with coefficient of friction, f.

If $f > g^I_{r\theta}$, in region $AA1$, a fully adhered interface from the outset is expected. In region $AA2$, at a location below or to the right of this dark line, the contact interface will shake down to a fully adhered state. A detached cyclic slip region in the middle of the contact is expected above or to the left of this dark line. In region $AA3$, the contact will either shake down to a fully adhered state with a minute amount of forward slip at the leading edge or an additional cyclic slip region in the middle of the contact is expected. A cyclic detached

slip zone in the middle of an adhered interface together with minute forward slip regions at both edges is expected in region *AA*5. If $f < g^I_{r\theta}$, the entire contact interface in region *BA* will shakedown to an adhered state save a minute forward slip and separation region at the trailing edge and a forward slip region at the leading edge, or an additional interior slip is expected depending on the position relative to the dark line. The detached cyclic slip in regions *AA*2, *AA*3, *AA*5 and *BA* will vanish if a different load case is used provided that the point considered on the steady state map is always below or to the right of the corresponding dark line. Figure 8.10(b) shows the steady state response map for the 120^0 punch problem which includes the boundaries for other load cases, i.e. $\gamma = -0.75$ and $\gamma = -0.6$. As for the square punch problem, the concept used to describe $\gamma = -1$ example case also applies here. In the region of interest $0 < |f| < 1$, the contact interface will always shake down if $\gamma \gtrsim -0.55$.

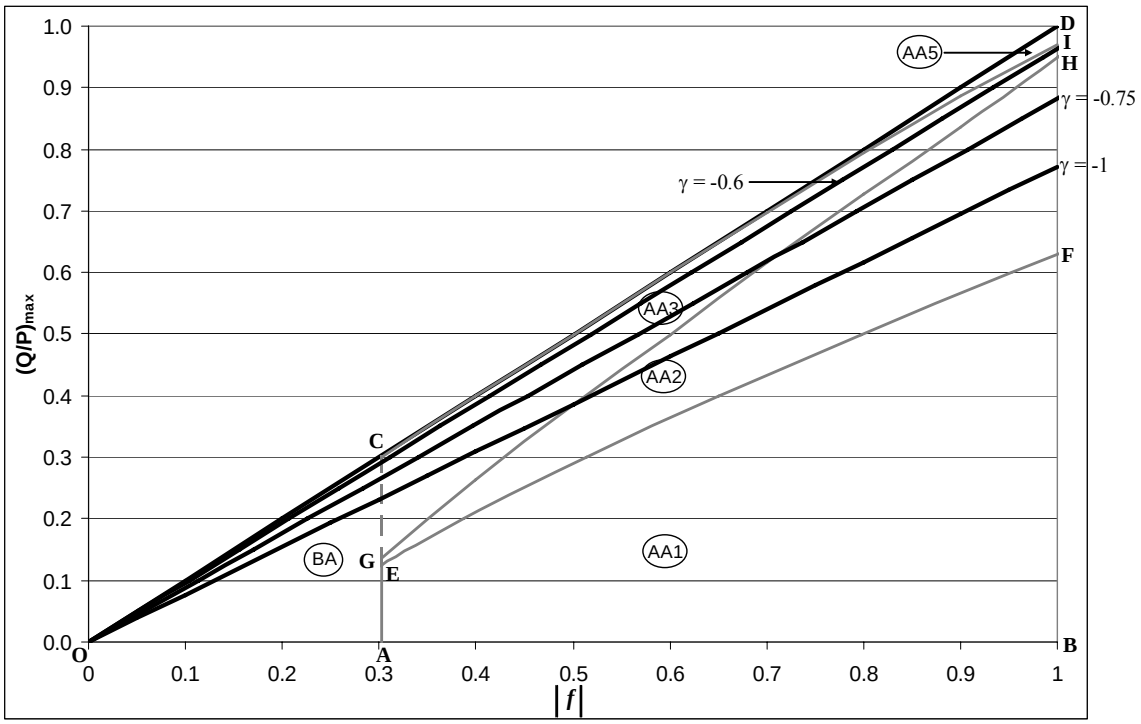

Figure 8.10(b) : Steady state response map for a 120^0 punch, for example load cases

8.5.3 60^0 trapezium punch

The steady state response map for the 60^0 punch problem, together with a dark line representing the boundary between shakedown and cyclic slip for a fully reversing shear case ($\gamma = -1$), is shown in Figure 8.11(a).

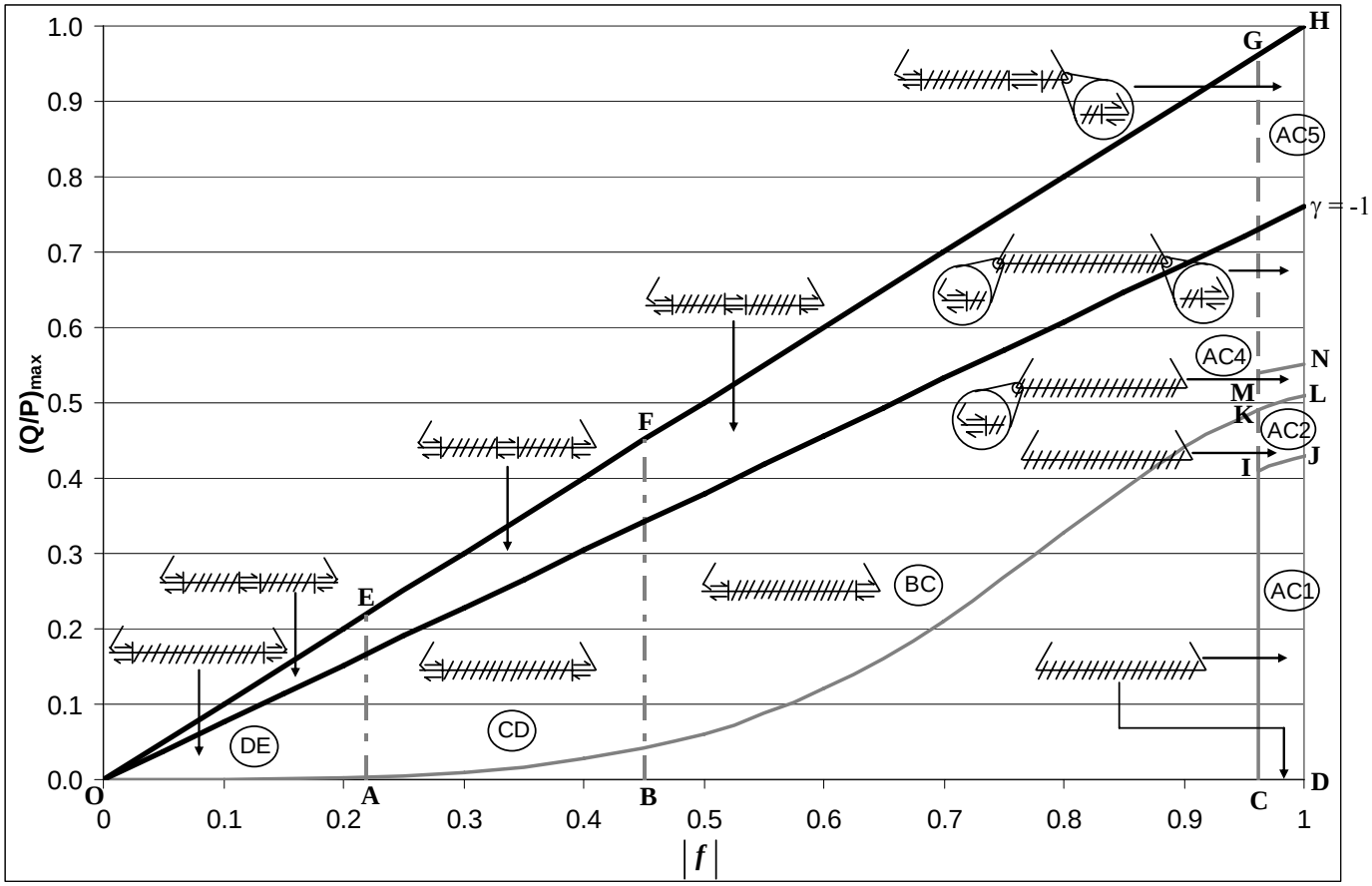

Figure 8.11(a) : Behaviour map for a 60^0 punch, on a half-plane subject to a constant normal load P and a cyclic shear load Q, and with coefficient of friction, f.

If $f > g^I_{r\theta}$, a fully adhered contact interface is expected in regions $AC1$ (from outset) and $AC2$ (due to frictional shakedown). A minute region of forward slip and separation attached to the trailing edge of an adhered interface is expected in region $AC4$. In region $AC5$, an additional forward slip zone will develop at the leading edge and for a higher $(Q/P)_{max}$ value (above the dark line), a detached cyclic slip zone closer to the leading edge is also expected. If $f < g^I_{r\theta}$ and the position on the map is below or to the right of the dark line,

an adhered interface at the middle of the contact, bordered by a finite forward slip and separation region at the trailing edge and a forward slip region at the leading edge, is expected in regions *CD* and *BC*. In region *DE*, the same behaviour will occur but with leading edge lifting off, although the amount of lift off is less than that at the trailing edge. It is worth noting that the slip and separation region at the trailing edge in the steady state condition occurs over a greater distance than that in the monotonic loading condition. However, the slip region at the leading edge is smaller in the steady state condition due to frictional shake down of points near to the leading edge. If the position on the map is above or to the left of the dark line, a very small region of cyclic slip at the middle of the contact will also develop. Figure 8.11(b) shows the steady state response map for the 60^0 punch problem which includes the boundaries for other load cases, i.e. $\gamma = -0.5$ and $\gamma = 0$. In the region of interest $0 < |f| < 1$, the contact interface will never shake down except for high friction values ($f > g^I_{r\theta}$) at moderate $(Q/P)_{max}$ values. However, if $\gamma \gtrsim 0.2$, the interior cyclic slip zone in all regions is expected to vanish.

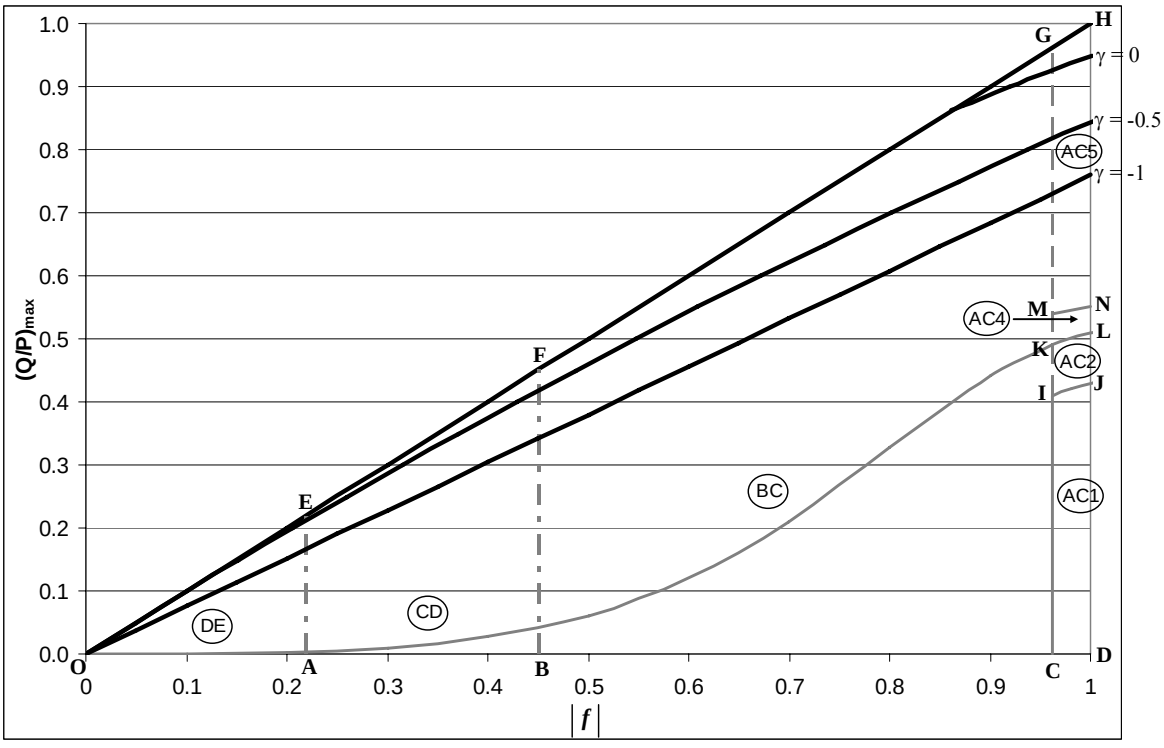

Figure 8.11(b) : Steady state response map for a 60^0 punch, for example load cases

8.6 Conclusions

Churchman's results for the interfacial response of a square block, pressed normally into a half-plane, and subject to subsequent shear, have been generalised to look at the important effect that different edge angles have on local behaviour. Detailed considerations have been given to the specific cases of 60^0 and 120^0 punches, and maps have been developed showing the interfacial response. A generalisation of the results for a wide range of contact angles has also been found, but the patterns of behaviour which emerge are extremely complicated. Consideration has also been given to the effects of cyclic shear between, in general, unequal values of the shearing force, to determine the steady state interface condition. Many contacts do exhibit at least some shakedown, and the shakedown limit (in the sense that all slip vanishes) is in some cases considerably higher than the load at which slip first occurs under monotonic loading, particularly when the internal contact angle, φ, is large.

Chapter 9

Conclusions and future work

9.1 Conclusions

Fretting fatigue, which is caused by oscillatory micro-slip that occurs between two components subjected to a clamping pressure and vibratory excitation or an oscillatory tangential force, remains as a major source of premature failure in a number of engineering assemblies. Fretting fatigue life is often divided into crack nucleation and crack propagation. The crack propagation phase is well understood and the life calculation involves application of fracture mechanics and universally accepted fatigue crack growth laws. However, the crack initiation phase remains elusive and is still predominantly tackled by an experimental approach. Quantifying crack nucleation in fretting fatigue is very important in order to reduce the conservatism involved in current component life prediction, and therefore one avenue for quantifying crack nucleation in fretting fatigue was pursued in the first part of this thesis.

As a starting point, the fretting fatigue test results employing Herzian contact, the results of which are available in the literature, conducted by Nowell (1988) and Szolwinski (1998), were analysed. First, a technique to find the internal stress state within a test specimen of moderate thickness is described. The internal stress state was found as a superposition of the stress state implied by a half-plane solution including bulk stress, and a corrective term to allow for the presence of the remote free boundary. Secondly, the solution for an edge dislocation in a strip is found in a very straightforward manner, using only the elementary solution for a dislocation in a half-plane. This was then employed to find the crack tip stress intensity factor for an edge crack in a strip subject to loading conditions including a severe stress gradient. Thirdly, asymptotic solutions were used to characterize

the state of stress in the neighbourhood of contact and it is noted that this approach is effective in encapsulating the whole local stress state. It also gives a simple means of comparing the fatigue strength measured in fretting tests and can be used to predict the strength of a complex prototype. The asymptotic solution provides an excellent measure of the boundary between finite and infinite lives, but has yet to be developed as a satisfactory parameter that can be used to correlate nucleation life in the 'finite life' regime.

In the second part of this thesis, attention was focused on complete contacts. This class of problems is very difficult to analyse in closed form and are mostly tackled by the use of a commercial finite element package. This is adequate for problems where the region of interest lies away from the contact edges, but the prospect of singular behaviour at the contact corners usually produces convergence difficulties. To circumvent this, and at the same time bring the possibility of at least some analytical treatment of the problem, results of asymptotic analysis have been used, by 'zooming in' on the corners, and using the solutions devised by Williams (1952) and Bogy (1968, 1971) for adhered problems, and by Gdoutos and Theocaris (1975) and Comninou (1976) for slipping problems. Therefore as a precursor to the analysis of complete contacts, an introduction to the wedge theory was briefly presented, followed by a technique to find the solution for an edge dislocation within a semi-infinite wedge.

The problem of complete contacts sliding along an elastically similar half-plane was considered first. A basic understanding for this type of problem was developed from the results found for the pressure distribution beneath a square block sliding along an elastically similar half-plane, in the presence of friction. The coefficient of friction was found to have a considerable effect on the edge pressure distribution, which exhibits one of three possible types of behaviour – namely power order singularity, power order bounded and square root bounded. A technique to restore local separation and bounded behaviour within the asymptotic field, when the coefficient of friction exceeds 0.392, was introduced. General frictional sliding of complete contacts were then considered, with particular reference to

contacts whose edge angles are 60^0, 90^0 and 120^0, and a general map for a reasonable range of coefficients of friction was constructed by exploiting the characteristic equation. This map, which is a function of contact edge angle and coefficient of friction, exhibits six distinct regions, each displaying different contact interface responses, from the three classes described above.

Finally, the problem of elastically similar complete contacts subjected to a normal load and subsequently monotonically increasing shear load or cyclic shear load was considered. Particular attention was given to the three specific cases of 60^0, 90^0 and 120^0 punches. Behaviour maps of the contact interface for a monotonically increasing shear load were constructed which comprised the mix of stick, slip and separation regions. The steady state response maps were then constructed for cyclic shear loading cases. It was found that all three types of contact experienced at least some shakedown. The contact interface will always shake down if the degree of reversal in shear load, $\gamma \gtrsim -0.45$ for square punch problem, $\gamma \gtrsim -0.55$ for 120^0 punch problem and $\gamma \gtrsim 0.2$ for 60^0 punch problem (for high coefficient of friction and moderate Q/P ratio). In general terms, the larger the internal contact angle, φ, the easier the contact is to shakedown.

In summary, fretting fatigue lives have been successfully correlated using an asymptotic approach and the behaviour of sharp-edged contacts pressed onto elastically similar half plane under sliding and partial slip conditions, the latter with a monotonically increasing and cyclic shear, have been successfully explained.

9.2 Future work

There are several pieces of work which merit further investigation prompted by this work which include the following:

1. Further analysis of fretting fatigue tests

Fretting fatigue test analysis can be extended to other contact geometries and materials. The first correlation which can be attempted is to find the boundary between finite and infinite lives for contact between different materials and geometries by using asymptotic approach. A second problem to be tackled would be to develop the asymptotic solution as a parameter to correlate nucleation life in the 'finite life' regime. A summary of the test results which are publicly available for analysis in the literature are given in Table 9.1.

Table 9.1 : A summary of tests for further analysis

No	Test	Contact geometry	Material
1	Cortez (1999)	Hertzian	Ti-6Al-4V
2	Lykins (2000)	Hertzian	Ti-6Al-4V
3	Mugadu (2002)	Complete	Ti-6Al-4V
4	Dini (2004)	Flat and rounded	Ti-6Al-4V
5	Navarro (2004)	Spherical	Al7075-T6

`

2. Effect of bulk load on the general response map under partial slip conditions

In chapter 8, general interfacial response maps have been developed for complete contacts with various edge angles, due to the application of normal load and subsequently to monotonically increasing (and also reversing) shear load. The application of a bulk load to one or both bodies in contact will change the interfacial response of the contact and it is therefore an important topic for investigation.

3. Proportional loading problem

The loading history often considered in fretting fatigue studies is where the normal load applied to establish contact is held constant, followed by the application of cyclic shear and bulk load. The specific case suggested for analysis is when these loads are increased in proportion, i.e. the normal and shear load remain in fixed proportion, as would any tension

developed in the surface of the contacting components. The intention of this work would be to provide a description of the interfacial response, for example on the contact lands of a fan blade dovetail when a gas turbine is started up.

4. Optimisation of contact problems

Fatigue remains as one of the major sources of premature engineering failures. Therefore, designing against fatigue failure is very important. One of the important quantities which might be optimised when designing against fretting fatigue failure is the contact geometry. The contact geometry could be optimised to give an improved resistance to fretting fatigue.

5. Frictional sliding contact of a circular cylinder over a half-plane

The contact pressure distribution and attendant local state of stress prevailing when a square-ended circular cylinder is slid, in the presence of friction, over a half-plane, could be determined. As a starting point, the problem where a rigid cylinder is slid on an incompressible half-plane could be analysed first. This is a relatively straightforward problem because it can be solved analytically and this will enable us to match the solution locally with the asymptotic solution developed. A second problem to be considered is when the cylinder and the half-space have similar elasticity. This problem, however, must be solved numerically, normally by the finite element method, because it would be very difficult to formulate an elasticity solution within either a finite or even semi-infinite cylinder. Even though it is a geometrically straightforward problem, it is still not easy to obtain a fully converged solution to the contact problem when there is both a singularity present and the frictional shearing traction has components both perpendicular to and parallel to the contact boundary. This is where asymptotic forms for the state of stress adjacent to the corner, for sliding contact between a semi-infinite wedge of internal angle $\pi/2$, i.e. a quarter plane and a half-plane, may profitably be used, to add detail, and give precision to the solution. The magnitude of the singularity in the pressure around the contact periphery will need to be found, and the trailing edge separation regime will have to be quantified, when the coefficient of friction exceeds 0.392.

References

Alic, J.A. and Kantimathi, A. (1979), Fretting fatigue, with reference to aircraft structures, SAE paper No. 790612.

Araujo, J.A. and Nowell, D. (2002), The effect of rapidly varying contact stress fields on fretting fatigue, *International Journal of Fatigue*, **24**, 763-775.

Banerjee, N. and Hills, D.A. (2006), Analysis of stick-slip and contact-edge behaviour in a simplified fretting fatigue test, *Journal of Strain Analysis*, **41**, 183-192.

Bogy, D.B. (1968), Edge-bonded dissimilar orthogonal elastic wedges under normal and shear loading, *J. Appl. Mech.*, **35**, Trans ASME, **90**, 460-466.

Bogy, D.B. (1971), Two edge-bonded elastic wedges of different materials and wedge angles under surface tractions, *J. Appl. Mech.*, **38**, 377-386.

Bohorquez, L. and Dominguez, J. (2005), Analysis of the elastic punch-substrate contact under fretting : Monotonic and cyclic loading of the punch, *International Journal of Mechanical Sciences*, **47**, 388-417.

Bohorquez, L. and Dominguez, J. (2007), Characterization of the contact between a punch and a half-infinite substrate in a fretting situation, *International Journal of Mechanical Sciences*, **49**, 608-621.

Bramhall, R. (1973), *Studies in fretting fatigue*, D.Phil. thesis, University of Oxford.

Brown, Jr.W.F. and Srawley, J.E. (1966), *Plane Strain Crack Toughness Testing of High Strength Metallic Materials*, ASTM STP 410, p.12.

Cattaneo, C. (1938), Sul contatto di due corpi elastici : distribuzione locale degli sforzi. Rc Accad. naz. Lincei, **27**, 342-348, 434-436, 474-478.

Churchman, C.M. (2006), *Asymptotic analysis of complete contacts*, D.Phil. thesis, University of Oxford.

Churchman, C.M. and Hills, D.A. (2006a), General results for complete contacts subject to oscillatory shear, *J. Mech. Phys. Solids*, **54 (6)**, 1186-1205.

Churchman, C.M. and Hills, D.A. (2006b), Slip zone length at the edge of a complete contact, *International Journal of Solids and Structures*, **43**, 2037-2049.

Churchman, C.M., Korsunsky, A.M. and Hills, D.A. (2006), The edge dislocation in a three-quarter plane-Part I : Influence functions, *Eur. J. Mech. A/Solids*, **25**, 42-50.

Comninou, M. (1976), Stress singularity at a sharp edge in contact problems with friction, *J. Appl. Math. Phys.*, **27**, 493-499.

Cortez, R., Mall, S. and Calcaterra, J.R (1999), Investigation of variable amplitude loading on fretting fatigue behavior of Ti-6Al-V, *International Journal of Fatigue*, **21**, 709-717.

Cortez, R., Mall, S. and Calcaterra, J.R. (2000), Interaction of high-cycle and low-cycle fatigue on fretting behaviour of Ti-6-V, in: Hoeppner, D.W., Chandrasekaran, V., Elliots, C.B. (Eds.), Fretting Fatigue: Current Technology and Practices, ASTM STP 1367, American Society for Testing and Materials, West Conshohocken, PA.

Dini, D. and Hills, D.A. (2004), Bounded asymptotic solutions for incomplete contacts in partial slip, *International Journal of Solids and Structures*, **41**, 7049-7062.

Dini, D. (2004), *Studies in fretting fatigue with particular application to almost complete contacts*, D.Phil. thesis, University of Oxford.

Dini, D., Sackfield, A. and Hills, D.A. (2005), Comprehensive bounded asymptotic solutions for incomplete contacts in partial slip, *Journal of Mechanics and Physics of Solids*, **53**, 437-454.

Eden, E.M., Rose, W.N. and Cunningham, F.L. (1911), The endurance of metals, *Proceedings of the Institute of Mechanical Engineers*, **4**, 68-76.

El Haddad, M.H., Smith, K.N. and Topper, T.H. (1979a), Fatigue Crack Propagation of Short Cracks, *Journal of Engineering Materials and Technology*, **101**, 42-46.

El Haddad, M.H., Topper, T.H. and Smith, K.N. (1979b), Prediction of Non Propagating Cracks, *Engineering Fracture Mechanics*, **11**, 573-584.

Endo, K. and Goto, H. (1976), Initiation and propagation of fretting fatigue cracks, *Wear*, **38**, 311-324.

Erdogan, F., Gupta, G.D. and Cook, T.S. (1973), *Numerical Solution of Singular Integral Equations, in Methods of Analysis and Solutions of Crack Problems*, Ed. G.C. Sih, Noordhoff, Leyden, 368-425.

Fatemi, A and Socie D.F. (1988), A critical plane approach to multiaxial fatigue damage including out of phase loading, *Fatigue Fract. Eng. Mater. Struct.*, **11**, 149-165.

Fellows, L.J., Nowell, D. and Hills, D.A. (1995), Contact stresses in a moderately thin strip (with particular reference to fretting experiments), *Wear*, **185**, 235-238.

Feng, I-Ming and Rightmire, B.G. (1952), The mechanism of fretting, Mass. Inst. of Tech., Cambridge, Mass., AD 4463.

Feng, I-Ming and Rightmire, B.G. (1953), The mechanism of fretting, *Lubrication Engineering*, **9**, 134-136 and 158-161.

Feng, I-Ming (1955), Fundamental study of the mechanism of fretting, MIT Lubrication Lab, Cambridge, Mass., Final Report AD59089.

Feng, I-Ming and Rightmire, B.G. (1956), An experimental study of fretting, *Proc. Inst. Mech. Engrs.,* London, **170**, 1055-1060.

Fridrici, V., Fouvry, S., Kapsa, P. and Perruchaut, P. (2005), Prediction of cracking in Ti-6A-4V alloy under fretting-wear : use of the SWT criterion, *Wear*, **259**, 300-308.

Gdoutos, E.E. and Theocaris, P.S. (1975), Stress concentrations at the apex of a plane interacting on an elastic half-plane, *J. Appl. Mech.*, **42**, 688-692.

Giannakopoulos, A.E., Lindley, T.C. and Suresh S. (1998), Aspects of equivalence between contact mechanics and fracture mechanics: theoretical connections and a life-prediction methodology for fretting-fatigue, *Acta Materialia*, **46(9)**, 2955-2968.

Godfrey, D. (1950), Investigation of fretting corrosion by microscopic observation, NACA Technical Note 2039.

Godfrey, D. and Bisson, E.E. (1952), NACA studies of mechanism of fretting (fretting corrosion) and principles of mitigation, *Lubrication Engineering*, **8**, 241-243.

Godfrey, D. and Bailey, J.M. (1953), Coefficient of friction and damage to contact area during the early stages of fretting-I. Glass, copper or steel against copper, NACA Technical Note 3011.

Godfrey, D. and Bailey, J.M. (1954), Early stages of fretting of copper, iron and steel, *Lubrication Engineering*, **10**, 155-159.

Godfrey, D. (1956), A study of fretting wear in mineral oil, *Lubrication Engineering*, **12**, 37-42.

Halliday, J.S. and Hirst, W. (1956), The fretting corrosion of mild steel, *Proc. Roy. Soc.,* London, **236A**, 411-425.

Hertz, H. (1882), Uber die Beruhrung fester elasticher Korper, *J. reine und angewandteMathematik.*, **92**, 156-171.

Hills, D.A., Nowell, D. and Sackfield, A. (1993), *Mechanics of Elastic Contacts*, Butterworth-Heinemann Ltd, Oxford.

Hills, D.A. and Nowell, D. (1994), *Mechanics of Fretting Fatigue*, Kluwer Academic Publishers, Dordrecht.

Hills, D.A., Kelly, P.A., Dai, D.N. and Korsunsky, A.M. (1996), *Solution of Crack Problems - The Distributed Dislocation Technique*, Kluwer Academic Publishers, Dordrecht, The Netherlands.

Hoeppner, D.W. and Goss, G.L. (1974), A fretting fatigue damage threshold concept, *Wear*, **27**, 61-70.

Johnson, K.L. (1985), *Contact Mechanics*, Cambridge University Press, Cambridge.

Karuppanan, S., Dini, D. and Hills, D. A. (2007a), Fretting fatigue test analysis of contact, *Fatigue Fract. Engng. Mater. Struct.*, **30(6)**, 499-509.

Karuppanan, S., Churchman, C.M., Hills, D.A. and Giner, E. (2007b), Sliding frictional contact between a square block and an elastically similar half-plane, *Eur. J. Mech. A/Solids*, in press.

Karuppanan, S. and Hills, D.A. (2007), Sliding of general frictional complete contacts, *International Journal of Mechanical Sciences*, under review.

Khadem, R. and O'Connor, J.J. (1969), Adhesive or frictionless compression of an elastic rectangle between two identical elastic half-spaces, *Int. J. Eng. Sci.*, **7**, 153-168.

Kitagawa, H. and Takahashi, S (1976), Applicability of fracture mechanics to very small cracks or cracks in the early stage, *Proceedings of the 2nd International Conference on Mechanical Behaviour of Materials*, 627-631.

Klarbring, A., Ciavarella, M. and Barber, J.R. (2007), Shakedown in elastic contact problems with Coulomb friction, *International Journal of Solids and Structures*, in press.

Kondo, Y. and Bodai, M. (2001), The fretting fatigue limit based on local stress at the contact edge, *Fatigue Fract. Eng. Mater. Struct.*, **24**, 791-801.

Kondo, Y., Sakae, C., Kubota, M., Nagasue, T. and Sato, S. (2004), Fretting fatigue limit as a short crack problem at the edge of contact, *Fatigue Fract. Eng. Mater. Struct.*, **27**, 361-368.

Kondo, Y., Sakae, C., Kubota, M. and Yanagihara, K. (2005), Non-propagating crack behaviour at giga-cycle fretting fatigue limit, *Fatigue Fract. Eng. Mater. Struct.*, **28**, 501-506.

Lampman, S.R. (1997), *ASM Handbook, Volume 19 : Fatigue and Fracture. The Materials Information Society*, ASM International.

Lin, K.Y. and Tong, P. (1980), Singular finite elements for the fracture analysis of V-notched plate, *Int. J. Numer. Meth. Eng.*, **15**, 1343-1354.

Lykins, C.D., Mall, S. and Jain, V. (2000), An evaluation of parameters for predicting fretting fatigue crack initiation, *International Journal of Fatigue*, **22**, 703-716.

Maw, N., Barber, J.R. and Fawcett, J.N. (1976), The oblique impact of elastic spheres, *Wear*, **38**, 110-114.

McDowell, J.R. (1953), Fretting corrosion tendencies and several combinations of materials, *Symposium on Fretting Corrosion*, **STP 144**, ASTM, Philadelphia, 24-39.

Miller, K.J. (1993), The two thresholds of fatigue behaviour, *Fatigue Fract. Eng. Mater. Struct.*, **16**, 931-939.

Mindlin, R.D. (1949), Compliance of elastic bodies in contact, *Journal of Applied Mechanics*, **16**, 259-268.

Mugadu, A.E.B. (2002), *Studies in fretting fatigue of complete contacts*, D.Phil. thesis, University of Oxford.

Mugadu, A., Hills, D.A. and Nowell, D. (2002a), Modifications to a fretting-fatigue testing apparatus based upon an analysis of contact stresses at complete and nearly complete contacts, *Wear*, **252**, 475-483.

Mugadu, A., Hills, D.A. and Limmer, L. (2002b), An asymptotic approach to crack initiation in fretting fatigue of complete contacts, *Journal of the Mechanics and Physics of Solids*, **50**, 531-547.

Mugadu, A. and Hills, D.A. (2003), The evolution of the process zone when a complete contact is subject to cyclically varying loads, *International Journal of Solids and Structures*, **40**, 4417-4435.

Murakami, Y. (1987), *Stress Intensity Factors Handbook*, Volume I, Pergamon Press.

Muskhelishvili, N.I. (1953), *Some Basic Problems of the Mathematical Theory of Elasticity*, Noordhoff, Groningen.

Navarro, C., Mugadu, A., Hills, D.A. and Dominguez, J. (2003), The influence of underlying tension on partial slip in complete and nearly complete contacts, *International Journal of Mechanical Sciences*, **45**, 757-773.

Navarro, C. and Dominguez, J. (2004), Initiation criteria in fretting fatigue with spherical contact, *International Journal of Fatigue*, **26**, 1253-1262.

Nishioka, K., Nishimura, S. and Hirakawa, K. (1968), Fundamental investigations of fretting fatigue–Part 1, On the relative slip amplitude of press-fitted axle assemblies, *Bulletin of JSME*, **11**, 45, 437-445.

Nishioka, K. and Hirakawa, K. (1969a), Fundamental investigations of fretting fatigue–Part 2, Fretting fatigue testing machine and some test results, *Bulletin of JSME*, **12**, 50, 180-187.

Nishioka, K. and Hirakawa, K. (1969b), Fundamental investigations of fretting fatigue–Part 3, Some phenomena and mechanisms of surface cracks, *Bulletin of JSME*, **12**, 51, 397-407.

Nishioka, K. and Hirakawa, K. (1969c), Fundamental investigations of fretting fatigue–Part 4, The effect of mean stress, *Bulletin of JSME*, **12**, 51, 408-414.

Nishioka, K. and Hirakawa, K. (1969d), Fundamental investigations of fretting fatigue–Part 5, The effect of relative slip amplitude, *Bulletin of JSME*, **12**, 52, 692-697.

Nishioka, K. and Hirakawa, K. (1972), Fundamental investigations of fretting fatigue–Part 6, Effects of contact pressure and hardness of materials, *Bulletin of JSME*, **15**, 80, 135-144.

Nowell, D. and Hills, D.A. (1987a), Mechanics of Fretting Fatigue Tests, *International Journal of Mechanical Sciences*, **29**, 355-365.

Nowell, D. and Hills, D.A. (1987b), Open Cracks at or Near Free Edges, *Journal of Strain Analysis*, **22**, 177-185.

Nowell, D. (1988), *An analysis of fretting fatigue*, D.Phil. thesis, University of Oxford.

Pape, J.A. and Neu, R.W. (1999), Influence of contact configuration in fretting fatigue testing, *Wear*, **225-229**, 1205-1214.

Paris, P.C. and Sih, G. (1965), *Stress Analysis of Cracks*, ASTM STP 381, 30-81.

Pearson, S. (1975), Initiation of fatigue cracks in commercial aluminum alloys and the subsequent propagation of very short cracks, *Engineering Fracture Mechanics*, **7**, 235-247.

Ruiz, C., Boddington, P.H.B. and Chen, K.C. (1984), An investigation of fatigue and fretting in a dovetail joint, *Experimental Mechanics*, **24**, 208-217.

Ruiz, C. and Chen, K.C. (1986), Life assessment of dovetail joints between blades and discs in aero-engines, *I MechE Conference Publications*, **1**, 187-194.

Schmueser, D. and Comninou, M. (1980), Separation and slip between a layer and a substrate caused by a tensile load, *Int. J. Eng. Sci.*, **18**, 1149-1155.

Sneddon, I.N. (1951), *Fourier Transforms*, McGraw-Hill, New York.

Socie, D. (1987), Multiaxial fatigue damage models, *Journal of Engineering Materials and Technology*, **109**, 293-298.

Szolwinski, M.P. and Farris, T.N. (1996), Mechanics of fretting fatigue crack formation, *Wear*, **198**, 93-107.

Szolwinski, M.P. and Farris, T.N. (1998), Observation, analysis and prediction of fretting fatigue in 2024-T351 aluminum alloy, *Wear*, **221**, 24-36.

Tanaka, T., Nakai, Y. and Yamashita, M. (1981), Fatigue growth threshold of small cracks, *International Journal of Fracture*, **17**, 519-533.

Tomlinson, G.A. (1927), The rusting of steel surfaces in contact, *Proc. Roy. Soc. Lond. Ser. A.*, **115A**, 472-483.

Tomlinson, G.A., Thorpe, P.L. and Gough, H.J. (1939), An investigation of the fretting corrosion of closely fitted surfaces, *Proc. Inst. Mech.Engs.*, **141**, 223-249.

Tur, M., Fuenmayor, J., Mugadu, A. and Hills, D.A. (2002), On the analysis of singular stress fields. Part 2: application to complete slipping contacts, *J. Strain Analysis*, **38(3)**, 207-217.

Uhlig, H.H., Feng, I-Ming, *et al.* (1953), Fundamental investigation of fretting corrosion, NACA Technical Note 3029.

Uhlig, H.H. (1954), Mechanism of fretting corrosion, *Journal of Applied Mechanics*, **21**, 401-407.

Warlow-Davies, E.J. (1941), Fretting corrosion and fatigue strength: brief results of preliminary experiments, *Proc. I. Mech. E.*, **146**, 33-38.

Waterhouse, R.B. (1955), Fretting corrosion, *Proc. Inst. Mech. Engrs.*, **169**, 1159-1172.

Waterhouse, R.B. (1972), *Fretting corrosion*, Pergamon Press, Oxford, England.

Waterhouse, R.B. (1981), *Fretting Fatigue*, Applied Science Publishers, London.

Williams, M.L. (1952), Stress singularities resulting from various boundary conditions in angular corners of plates in extension, *J. Appl. Mech.*, **19**, 526-528.

Wright, K.H.R. (1952a), An investigation of fretting corrosion, *Proc. Inst. Mech. Engrs.*, **1B**, 556-571.

Wright, K.H.R. (1952b), Discussion and communication on an investigation of fretting corrosion, *Proc. Inst. Mech. Engrs.*, **1B**, 571-574.

Xie, Y.J. and Hills, D.A. (2003), Crack initiation at contact surface, *Theoretical and Applied Fracture Mechanics*, **40**, 279-283.

Appendix A

Functions in equations (2.6) and (2.11b)

$$I_1(x,c,e) = -k[-\pi + \cos^{-1}(k_1)] - \sqrt{1-k_1^2} - \sqrt{1-k^2}\,\ln\left|\frac{\sqrt{\frac{1-k_1}{1+k_1}} - \sqrt{\frac{1-k}{1+k}}}{\sqrt{\frac{1-k_1}{1+k_1}} + \sqrt{\frac{1-k}{1+k}}}\right| \tag{A.1}$$

$$I_2(x,c,e) = k\cos^{-1}(k_2) + \sqrt{1-k_2^2} + \sqrt{1-k^2}\,\ln\left|\frac{\sqrt{\frac{1-k_2}{1+k_2}} - \sqrt{\frac{1-k}{1+k}}}{\sqrt{\frac{1-k_2}{1+k_2}} + \sqrt{\frac{1-k}{1+k}}}\right| \tag{A.2}$$

$$I_3(x,c,e) = (A+Bk)\ln\left(\frac{k-k_1}{k_2-k}\right) - B(k_2-k_1) \tag{A.3}$$

$$J_1(c,e) = \frac{a}{2}\left(\frac{\pi}{2} + k_1\sqrt{1-k_1^2} + \sin^{-1}(k_1)\right) \tag{A.4}$$

$$J_2(c,e) = \frac{a}{2}\left(\frac{\pi}{2} - k_2\sqrt{1-k_2^2} - \sin^{-1}(k_2)\right) \tag{A.5}$$

$$J_3(c,e) = \int_{e-c}^{e+c} q'(\xi)d\xi = a\int_{k_1}^{k_2} q'(t)dt \tag{A.6}$$

$$J_4(c,e) = a\left[A(k_2-k_1) + \frac{B}{2}(k_2^2-k_1^2)\right] \tag{A.7}$$

$$k = \frac{x}{a}; \quad k_1 = \frac{e-c}{a}; \quad k_2 = \frac{e+c}{a}; \tag{A.8}$$

$$A = \sqrt{1-k_1^2} + \frac{ak_1}{2c}\left(\sqrt{1-k_2^2} + \sqrt{1-k_1^2}\right) \tag{A.9}$$

$$B = -\frac{a}{2c}\left(\sqrt{1-k_2^2} + \sqrt{1-k_1^2}\right) \tag{A.10}$$

Appendix B

User subroutine which imposes bilateral boundary condition*

```
      subroutine fric(lm,tau,ddtddg,ddtddp,dslip,sed,spd,
     1 ddtdt,pnewdt,statev,dgam,taulm,press,dpress,ddpddh,
     2 slip,kstep,kinc,time,dtime,noel,ciname,slname,
     3 msname,npt,node,npatch,coords,rcoord,drot,temp,
     4 predef,nfdir,mcrd,npred,nstatv,chrlngth,props,nprops)
c
      include 'aba_param.inc'
c
      character*80 ciname,slname,msname
      dimension tau(nfdir),ddtddg(nfdir,nfdir),ddtddp(nfdir),
     1          dslip(nfdir),ddtdt(nfdir,2),statev(*),
     2          dgam(nfdir),taulm(nfdir),slip(nfdir),time(2),
     3          coords(mcrd),rcoord(mcrd),drot(2,2),temp(2),
     4          predef(2,*),props(nprops)
c
      parameter(zero=0.0D0)
c
      f=props(1)
c

      if (lm .eq. 2) return
c

     taucrit=f*(press)


     if (LM.eq.0) then
         if (dgam(1).eq.0)  then
            LM=1
            dslip(1)=0
         else
            tau(1)=dabs(dgam(1))/dgam(1)*taucrit
            dslip(1)=dgam(1)
         endif

     elseif (LM.eq.1) then

        if ((dabs(taulm(1)).ge.taucrit).and.(dabs(taulm(1)).gt.zero))then
            tau(1)=dabs(taulm(1))/taulm(1)*taucrit
            dslip(1)=dgam(1)
            LM=0
        endif

     endif

     return
     end
```

* This subroutine is written with the help of Professor E. Giner.